Imaging at the Quantum Noise Limit and Beyond:

Propagation Effects in the Generation of Multi-Spatial-Mode Squeezed Light and Optimised Detection of a Laser Beam Position

By

Ellie Fradgley

A thesis submitted to
the University of Birmingham
for the degree of
DOCTOR OF PHILOSOPHY

Cold Atoms Research Group
School of Physics and Astronomy
College of Engineering and Physical Sciences
University of Birmingham
June 2022

ABSTRACT

Light is commonly used as a measurement tool in both scientific and everyday applications. It is increasingly true that such measurements are limited by the quantum nature of light, which means there is fundamental minimum level of noise present on any measurement made using a classical beam. Typically, this limitation can be overcome by increasing the optical power, however this is not always possible: too much power can damage a system, or introduce other problems which dominate over the quantum noise. This thesis explores two ways of improving the signal to noise ratio (SNR) of a system limited by quantum intensity fluctuations, specifically where the spatial distribution of the light is also significant. The first method, explored in the first part of this thesis, concerns the use of the nonlinear optical process of 4 wave mixing (4WM) to generate twin beams which exhibit localised intensity correlations. A high quantum efficiency camera is used to capture images of the beams, allowing the correlations to be studied. Correlations at low spatial frequencies are observed, however a distortion effect caused by the matched propagation of the beams as they pass through the nonlinear media prevents correlations from being observed at higher spatial frequencies. The impact of this matched propagation on the ability to use the produced squeezed light to make sub-shot noise measurements, is explored. A simulation of the propagation of the twin beams through the cell is produced and verified experimentally. There is evidence to suggest a nontrivial transverse displacement of the spatially correlated modes in the twin beams occurs which impedes the ability to see squeezing in higher spatial modes. With the aid of the simulation and experimental data it should be possible to account for the displacements in future measurements and produce a mapping of the correlations between the two beams. The second method, explored in the second part of this thesis, investigates an optimised scheme for detecting small displacements of a Gaussian beam. This is particularly desirable in applications such as atomic force microscopy (AFM), which currently can operate at the shot noise limit. By using a detection mode which is maximally sensitive to the displacement, improvements can be seen in the SNR of a measurement limited by shot noise without the need for advanced optics setups. Rather, the conventional split photodetector used to detect small displacements is replaced with a photodetector with a detection mode which saturates the Cramer-Rao bound of the measurement. A theoretical improvement to the SNR of $\pi/2$ compared to the conventional method of using a split photodetector is calculated. This is verified experimentally by building the split and optimised detectors and measuring the displacement of an optical beam. An improvement in the SNR of $\pi/2$ is observed.

ACKNOWLEDGMENTS

First and foremost I would like to thank my supervisor, Dr. Vincent Boyer, for his support and guidance over the last few years. Thanks also to Dr. Plamen Petrov and Dr. Josh Rayne for passing on their knowledge of the experiment. To the PhD students in the Cold Atoms and Nuclear groups, thank you for providing me with friendship, entertainment, and most importantly people to walk to get lunch with. In particular my office companions: Joe Baker, Joe Kelly, Dr. Andy White, and for a short time our lodger Stuart Pirrie - you were all great fun to work with, and I learnt a lot from you! A special thanks to Carlton French, for being a great friend, coffee companion, and for ensuring I rarely had to suffer the last 5 minutes of my commute alone (definitely motivated by him not wanting to walk in...).

I would also like to thank my parents for all their encouragement throughout my life: they have always supported me in whatever I wanted to do (even when they had no idea what it was!), and for that I am incredibly grateful. Also to my brother Dale (who had somewhat more of an idea of what it was), for being someone to talk about science with. Finally, a huge thanks to my partner Chris for being such a great source of support and knowledge during my PhD.

I would also like to thank the School of Physics and Astronomy for providing the funding for my studies.

Abbreviations and Acronyms

1PD	One-Photon Detuning
2PD	Two-Photon Detuning
4WM	Four Wave Mixing
AFM	Atomic Force Microscopy
AOM	Acousto-Optical Modulator
BPD	Balanced Photodetector
CCD	Charge-Coupled Device
CMRR	Common Mode Rejection Ratio
COM	Centre of Mass
EM	Electromagnetic
FF	Far Field
GBP	Gain Bandwidth Product
GT	Glan Taylor (polariser)
MEMS	Micro-Electro-Mechanical Systems
MSM	Multi Spatial Mode (Squeezing)
NA	Numerical Aperture
NF	Near Field
OPO	Optical Parametric Oscillator
PBS	Polarising Beam Splitter
PD	Photodiode
PDC	Parametric Down Conversion
PID	Proportional-Integral-Derivative
PIN	Positive-Intrinsic-Negative
PSD	Position Sensing Detector
QCRB	Quantum Cramer-Rao Bound
RBW	Resolution Bandwidth
RF	Radio Frequency
SD	Split Detector
SNR	Signal to Noise Ratio
TA	Transimpedance Amplifier
TEM	Transverse Electromagnetic
TMSS	Two Mode Squeezed State
TTL	Transistor-Transistor Logic
VBW	Video Bandwidth

Table of Contents

Chapter One

Introduction

Light, and more widely EM radiation, has long been used as a tool for measurement and communication. Since the creation of the first lasers in 1960[1] they have proved invaluable tools, enabling the fields of cold atoms[2], atomic sensors[3] and gravitational waves[4] to emerge among many others. When the range of applications, such as fibre optic communications[5], medical treatments[6][7] and using LiDAR to help monitor the weather[8], are considered it's clear that lasers have had a great impact on our everyday lives. As a result, laser technology has advanced rapidly in terms of the available powers and wavelengths, and stable lasers are readily produced in compact packages optimised for different applications.

However, regardless of how stable the laser is, in the best case scenario with no technical noise sources it will generate a coherent state. Light in a coherent state possesses the minimum possible uncertainty product between the amplitude and phase variables, as required by the uncertainty principle. The result is measurable intensity fluctuations in a coherent beam at the quantum level, known as shot noise. A helpful qualitative description of this noise is reached by imaging a laser as a beam of single photons. When measuring the intensity of such a beam, i.e. the number of photons incident on the detector per second, small fluctuations will arise due to the random measured distribution of photons along the beam. This is illustrated in figure 1.1.

The distribution of the photons in a coherent state is described by Poissonian statistics[9]

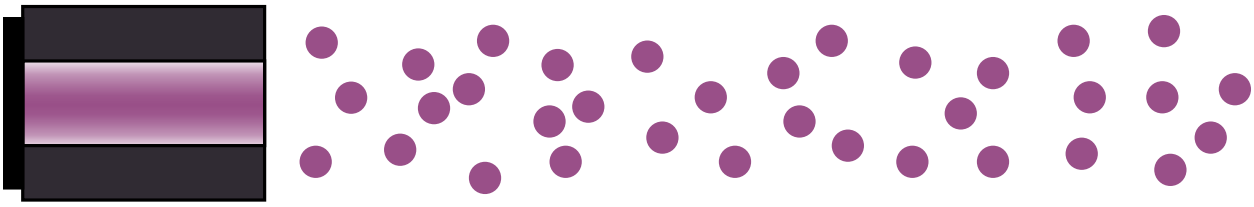

Figure 1.1 An illustration of the random distribution of photons in a laser beam which leads to intensity fluctuations on the quantum level.

and as such the variance in the number of photons detected per second is equal to the mean number of photons detected per second. From this we can obtain the signal to noise ratio (SNR), defined as the mean number of photons detected divided by the standard standard deviation:

$$\text{SNR} = \frac{N}{\sqrt{N}} = \sqrt{N}, \tag{1.1}$$

where N is the mean number of photons detected. While modelling a laser beam as a 2D stream of photons is not very realistic, the same principle applies to a beam made up of many photons distributed in space across a beam profile. Since the SNR is proportional to the number of photons, one way of improving the SNR is to increase the power of light used in the system, however in some situations this is not possible and other methods of increasing the SNR must be explored.

Since the discovery of shot noise, methods of improving a measurement limited by shot noise have been explored. Many of these involve reducing the noise by manipulating the quantum nature by generating special states of light using nonlinear atom-light interactions. This was first experimentally realised in 1985[10], and soon after similar techniques were used to make measurements beyond the shot noise limit[11]. One example is in the field of gravitational wave detection, where work to move past the shot noise limit is essential to the progress of the field due to the extremely high sensitivity of the detectors[12][13].

Alternatively, the detection scheme used can be optimised to ensure the information is extracted from the system in a way which gives the best possible SNR while still operating

at the shot noise limit by designing a detection scheme performs the best measurement theoretically possible in the presence of quantum noise; this limit is known as the Cramer-Rao Bound[14][15].

This thesis is split in two parts: the first explores the use of the nonlinear optical technique of 4 wave mixing (4WM) in a hot rubidium vapour to generate a pair of bright beams which display sub shot noise fluctuations in the difference of their intensities. When used with an appropriate imaging scheme, these can be used to enable measurements below the shot noise limit to be made for a range of applications. The second part of this thesis will focus on an optimised measurement technique for detecting small transverse displacements of a beam, thereby improving the measurement by increasing the SNR while remaining at the shot noise limit. The core theory behind the quantum noise limit, as well as optical theory relevant to the experimental techniques used in both parts of this theses, will first be covered.

Chapter Two

Theory

This chapter will describe theory relevant to both parts of this thesis. It will cover the fundamentals of optical design necessary to understand the optical systems discussed. It will also discuss the fundamentals of quantum optics and how the quantum nature of the EM field leads to a minimum noise on the light emitted by a laser. The theoretical and practical limitations which must be considered when using light as a measurement tool will be detailed: first experimental limitations imposed by the practicalities of optics, then fundamental limitations imposed by the quantum nature of the light itself. It will contain what may seen like a quite verbose approach to understanding how an imaging system works from relatively fundamental principles; this is due to the high level of overlap between conventional imaging and understanding some of the limitations in the quantum optics system described later on.

2.1 Quantum Optics

A concept essential to this thesis is that of shot noise: random fluctuations in the variables describing an electric field which is inherently due to the quantised nature of EM radiation. As high precision measurement techniques become more advanced these fluctuations are becoming the limiting factor in certain applications and it is increasingly desirable to have a way of reducing them.

2.1.1 Field Quantisation

The mathematical nature of these fluctuations can be more accurately described by first starting with the quantised nature of the EM field. An effort has been made to keep this brief, with key information only, as a more detailed derivation can be found in most quantum optics textbooks[16][17][18].

Our goal here is to simplify calculations by first writing expressions for the electric and magnetic fields in such a way that we can straightforwardly draw equivalences to the position and momentum of the well-understood case of the one-dimensional harmonic oscillator. These expressions must satisfy Maxwell's equations (without sources), given by

$$\nabla \times \underline{E} = \frac{\partial \underline{B}}{\partial t}, \tag{2.1}$$

$$\nabla \times \underline{B} = -\mu_0 \epsilon_0 \frac{\partial \underline{E}}{\partial t}, \tag{2.2}$$

$$\nabla \cdot \underline{B} = 0, \tag{2.3}$$

$$\nabla \cdot \underline{E} = 0, \tag{2.4}$$

$$\tag{2.5}$$

and have a Hamiltonian of the form

$$H = \frac{1}{2}\left(p(t)^2 + \omega^2 q(t)^2\right), \tag{2.6}$$

where $q(t)$ and $p(t) = \dot{q}(t)$ have the roles of canonical position and momentum respectively. In the simple case where the field is confined to a one-dimensional cavity along the z-axis with perfectly conducting walls at $z = 0$ and $z = L$ we find the following single-mode fields to satisfy these conditions:

$$E_x(z,t) = \left(\frac{2\omega^2}{V\epsilon_0}\right)^{\frac{1}{2}} q(t)\sin(kz) \tag{2.7}$$

$$B_y(z,t) = \left(\frac{\mu_0\epsilon_0}{k}\right)\left(\frac{2\omega^2}{V\epsilon_0}\right)^{\frac{1}{2}} p(t)\cos(kz), \tag{2.8}$$

where V is the effective volume of the cavity, ω is the frequency of the mode and $k = \omega/c$ is the wave number. The energy of such a field is given by

$$U(z,t) = \frac{1}{2}\int \epsilon_0 E^2 + \frac{1}{\mu_0} B^2 dV, \tag{2.9}$$

which has the same form as the Hamiltonian of the harmonic oscillator given in equation 2.6.

We may now use the correspondence principle to replace our canonical variables q and p by their operator equivalents $\hat{q}$ and $\hat{p}$, leading to the following expression for the Hamiltonian,

$$\hat{H} = \frac{1}{2}\left(\hat{p}^2 + \omega^2 \hat{q}\right). \tag{2.10}$$

Similarly from equations 2.7 and 2.8, the field operators are given by

$$\hat{E}_x(z,t) = \left(\frac{2\omega^2}{V\epsilon_0}\right)^{\frac{1}{2}} \hat{q}(t)\sin(kz) \tag{2.11}$$

$$\hat{B}_y(z,t) = \left(\frac{\mu_0\epsilon_0}{k}\right)\left(\frac{2\omega^2}{V\epsilon_0}\right)^{\frac{1}{2}} \hat{p}(t)\cos(kz). \tag{2.12}$$

From this we see a single mode field is formally equivalent to a harmonic oscillator of unit mass.

Having found this equivalence, we may now borrow some of the standard mathematics ubiquitous in physics concerning the quantum harmonic oscillator. First, we introduce the usual annihilation and creation operators,

$$\hat{a} = \frac{1}{\sqrt{2\hbar\omega}}\left(\omega\hat{q} + i\hat{p}\right), \tag{2.13}$$

$$\hat{a}^\dagger = \frac{1}{\sqrt{2\hbar\omega}}\left(\omega\hat{q} - i\hat{p}\right), \tag{2.14}$$

using which we may write the field operators as

$$\hat{E}_x = \epsilon_0\left(\hat{a} + \hat{a}^\dagger\right)\sin(kz) \tag{2.15}$$

$$\hat{B}_y = \beta_0 \frac{1}{i}\left(\hat{a} - \hat{a}^\dagger\right)\cos(kx). \tag{2.16}$$

Our Hamiltonian is given by

$$\hat{H} = \hbar\omega \left(\hat{a}^\dagger \hat{a} + \frac{1}{2} \right), \tag{2.17}$$

where $\hat{a}^\dagger \hat{a} = \hat{n}$, the number operator. Thus we have introduced a form of the EM field expressed, with the aid of formalisms used for the harmonic oscillator, such that the annihilation and creation operators act to add energy in quantised packets, or photons.

2.1.2 The Number State

Further following the usual case of the harmonic oscillator, we now introduce the number state vector, $|n\rangle$, which is an eigenvector of the hamiltonian such that

$$\hat{H} |n\rangle = \hbar\omega \left(\hat{n} + \frac{1}{2} \right) |n\rangle = E_n |n\rangle , \tag{2.18}$$

where $\hat{a} |n\rangle = \sqrt{n-1} |n-1\rangle$ and $\hat{a}^\dagger |n\rangle = \sqrt{n} |n+1\rangle$ describes how the annihilation and creation operators respectively act on the energy eigenstate. Using these definitions, we see that the general energy eigenstate may be generated from the ground state as follows:

$$|n\rangle = \frac{\left(\hat{a}^\dagger\right)^n}{\sqrt{n!}} |0\rangle , \tag{2.19}$$

where $|0\rangle$ is the minimum energy state, or the vacuum state.

Note that while $|n\rangle$ have well defined energy, the field is not well defined. We see this by calculating the mean field,

$$\langle n| \hat{E}_x |n\rangle = 0, \tag{2.20}$$

and also the variance of the field,

$$\Delta E_x = \sqrt{\langle n| \hat{E}_x^2 |n\rangle} = \sqrt{2}\epsilon_0 \sin(kz) \left(n + \frac{1}{2} \right)^{\frac{1}{2}} . \tag{2.21}$$

We see that despite the mean field being zero, there are still non-zero fluctuations. Crucially, these fluctuations are still present in the vacuum state ($n = 0$). This concept of fluctuations in the vacuum state is crucial to the idea of quantum noise: that even when on average the electric field is zero, there are still fluctuations around that average which means on the level of quantum noise some small field is always present.

While it may seem strange initially that the mean field is zero even for a non-zero number state, it is all in accordance with the uncertainty principle since the number operator and field operator do not commute:

$$\left[\hat{n}, \hat{E}_x\right] = \epsilon_0 \sin(kz) \left(\hat{a}^\dagger - \hat{a}\right). \tag{2.22}$$

This means $\hat{n}$ and $\hat{E}_x$ are complementary quantities with uncertainties obeying the inequality

$$\Delta n \Delta E_x \geq \frac{1}{2}\epsilon_0 |\sin(kz)| \|\langle\left(\hat{a}^\dagger - \hat{a}\right)\rangle|. \tag{2.23}$$

For a number state, $|n\rangle$, the uncertainty on the number of photons, n, is zero. However, the right side of the inequality is also equal to zero. Meanwhile, any knowledge about the field gives rise to uncertainty in the number of photons. While we do not use the uncertainty relation between the field and number operator directly, it is linked to the connection between the phase and amplitude of an electric field: while classically the two can be well known simultaneously this is not the case in quantum mechanics. While there is no convenient, universally accepted definition of a phase operator (although many attempts have been made[19]), we may take from equation 2.23 the idea that phase and number are complementary to one another and cannot both be well-known simultaneously. This concept of the photon number, or power, associated with an optical field and its phase being linked in their uncertainties will be important later.

2.1.3 The Coherent State

While the number state is helpful in understanding the special case of the vacuum state, $|0\rangle$, and showing that the energy fluctuations are non-zero, it has no well defined phase. Also, the expectation value of the field operator with a number state will always be zero.

In order to have a non-zero expectation of the field operator, we would need a superposition of many different number states. We will use such a concept to construct the coherent state: a quantum state which has a non-zero expectation value with the field operator. We shall construct this as a superposition of all the number states such that our coherent state, $|\alpha\rangle$ is defined as

$$|\alpha\rangle = \sum_{n=0}^{\infty} c_n |n\rangle , \tag{2.24}$$

where $\sum_{n=0}^{\infty} |c_n|^2 = 1$. Such states satisfy the relation

$$\hat{a} |\alpha\rangle = \alpha |\alpha\rangle , \tag{2.25}$$

where α is a complex number which we shall assign a physical meaning to later.

To determine an expression for the coefficients, c_n, we begin by multiplying both sides of equation 2.24 by $\hat{a}$:

$$\hat{a} |\alpha\rangle = \sum_{n=1}^{\infty} c_n \sqrt{n} |n-1\rangle = \alpha \sum_{n=0}^{\infty} c_n |n\rangle . \tag{2.26}$$

Equating coefficients on both sides gives $c_n\sqrt{n} = \alpha c_{n-1}$, and from this we see that the n^{th} coefficient can be expressed as

$$c_n = \frac{\alpha^n}{\sqrt{n!}} c_0, \tag{2.27}$$

and therefore

$$|\alpha\rangle = c_0 \sum_{n=0}^{\infty} \frac{\alpha^n}{\sqrt{n!}} |n\rangle \,. \tag{2.28}$$

To ensure normalisation we require $\langle\alpha|\alpha\rangle = 1$, therefore

$$|c_0|^2 \sum_{n=0}^{\infty} \frac{|\alpha|^{2n}}{n!} = |c_0|^2 e^{|\alpha|^2} = 1 \tag{2.29}$$

and so we find $c_0 = \exp\left(-\alpha^2/2\right)$. Hence the normalised coherent state is

$$|\alpha\rangle = e^{-\frac{1}{2}|\alpha|^2} \sum_{n=0}^{\infty} \frac{\alpha^n}{\sqrt{n!}} |n\rangle \,. \tag{2.30}$$

We now have a state constructed such that we will get a non-zero expectation value with the field operator:

$$\langle\alpha| \hat{E}_x |\alpha\rangle = 2|\alpha| \left(\frac{\hbar\omega}{2\epsilon_0 V}\right)^{\frac{1}{2}} \sin\left(\omega t - \underline{k}\cdot\underline{r} - \theta\right). \tag{2.31}$$

This looks a lot like a classical field. We can also find the fluctuations in $\hat{E}_x$:

$$\Delta E_x = \sqrt{\langle \hat{E}_x^2\rangle - \langle \hat{E}_x\rangle^2} = \left(\frac{\hbar\omega}{2\epsilon_0 v}\right)^{\frac{1}{2}}, \tag{2.32}$$

which is the same as the fluctuations in the vacuum state defined in equation 2.21. The coherent state is very close to a real laser beam, in that the expectation value of the field operator has the correct form. However a real beam would also have technical noise sources, at least at low frequencies.

To determine an expression for the noise on the field, as we inferred from Poissonian statistics earlier, we first determine the mean photon number in the field using the number operator, $\hat{n}$, defined earlier:

$$N = \langle\alpha| \hat{n} |\alpha\rangle = |\alpha|^2, \tag{2.33}$$

meaning $|\alpha|^2$ is simply the mean photon number of the field. This is consistent with equation 2.33, from which it is apparent that the physical meaning of α is related to the amplitude of the field.

The fluctuation in the photon number, or the noise, of the coherent state is given by

$$\Delta n = \sqrt{\langle \hat{n} \rangle - \langle \hat{n} \rangle^2} = N^{\frac{1}{2}}. \tag{2.34}$$

Therefore we see, as before, we obtain an SNR for a coherent state of light, such as that produced by a laser, of $\sqrt{N}$. This fundamental limit applies to all classical light sources, of which a laser is one. This limiting case assumes that classical noise sources have been eliminated and that an optimised detection scheme is being used.

2.2 Optics and Imaging

When using light as a measurement tool it is often the case that an 'image' of the 'object' being measured must be produced at a different spatial location, often at a detector. In the ideal case the intensity profile of the object will be reproduced in the image, potentially with some magnification, however a perfect reproduction is not possible experimentally.

The core of experimental work in this thesis will be performed using lasers, and as such it is essential to explore the basic principles of how coherent optical beams propagate and how imaging systems work. We will use Gaussian and Fourier optics to understand the propagation of light through our optical systems.

2.2.1 Gaussian Beams

For the work in this thesis, we will always be operating in the paraxial approximation[20]. We can compose a complete set of orthogonal modes which are solutions of the paraxial wave equation, for example the Transverse Electromagnetic (TEM_{mn}) or Hermite-Gaussian modes. As they form a complete set of eigenvalues, this set of modes can be used to construct

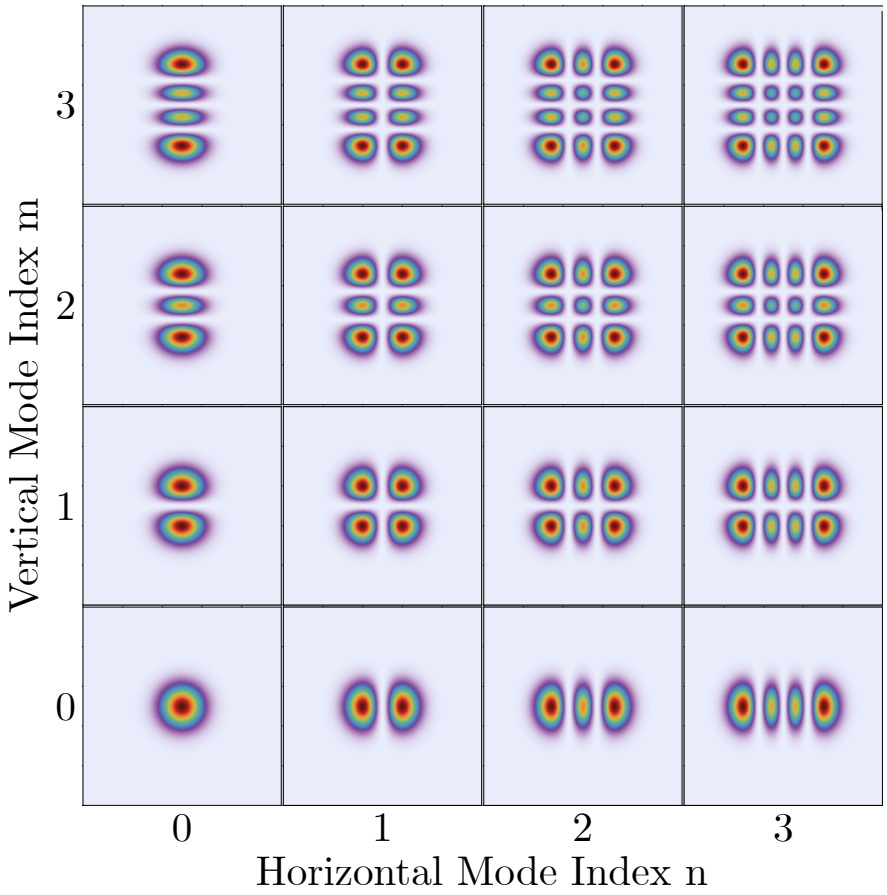

Figure 2.1 The first few orders of the Transverse Electromagnetic (TEM) modes. The TEM_{00} mode is the shape of the typical Gaussian beam used in optics experiments.

any beam shape or image in the paraxial approximation. The shape of any TEM mode, will remain constant through propagation, even though the overall scale will change.

The variables describing transverse space, x and y in the paraxial wave equation as written in Cartesian coordinates, are separable. The electric field amplitude of a TEM_{mn} mode with wavenumber k propagating in the z direction may be given as

$$E(x, y, z) = u_m(x, z)u_n(y, z)e^{-ikz}, \tag{2.35}$$

where the factors u_m and u_n are calculated from the Hermite polynomials, H_m and H_n[21][22]. The indices m and n determine the shape of the profile in the y and x direction respectively.

Figure 2.1 depicts the first few orders of the TEM_{mn} modes. The TEM_{00} mode is typically

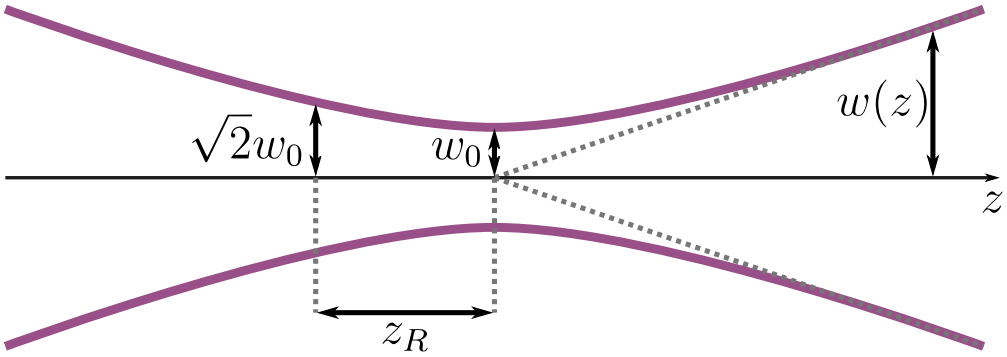

Figure 2.2 A Gaussian beam with waist w_0 propagating in the z direction. The Rayleigh range, indicated by z_R, is the distance travelled from the waist at which the width of the beam has increased by a factor of $\sqrt{2}$.

referred to simply as a Gaussian beam, and is the usual mode output by an ideal laser. In Gaussian optics, the shape of a Gaussian beam of a given wavelength, λ, is governed solely by the waist of the beam, w_0, which is the width of the beam at its focus. For a TEM00 profile, the width of the beam is half the diameter at the point where the intensity has dropped to $1/e^2$ of its maximum value. This is illustrated in figure 2.2.

As a function of distance travelled, z, in the direction of propagation, the beam width is given by

$$w(z) = w_0\sqrt{1 + \left(\frac{z}{z_R}\right)^2}, \tag{2.36}$$

where z_R is the Rayleigh range, given by

$$z_R = \frac{\pi w_0^2}{\lambda}. \tag{2.37}$$

The Rayleigh range is defined as the propagation distance from the waist over which the area of the cross section of the beam is doubled. It can be seen from equation 2.37 that beams with a smaller waist have a smaller Rayleigh range, and thus looking at equation 2.36 we see that the width of such beams will diverge more quickly than beams with larger waists.

From figure 2.1 it can be seen that higher order modes are comprised of more detail than the TEM_{00} mode, with several spots where a TEM_{00} mode beam has only one. This characteristic means small details in a Gaussian beam are intrinsically part of the higher

order modes. For a given family of TEM modes with waist w_0, the area of illumination of higher order modes is always larger than that of lower order modes[23]. The concept of fine details belonging to higher order modes, which are larger and also diverge more quickly, will be relevant in both parts of this thesis.

2.2.2 Imaging an Object

There are various limitations to our ability to accurately reproduce an EM field profile to produce an image. We will first discuss the (imaginary) case of perfect imaging, where the intensity profile of the field at the object is imaged perfectly at a different point in space i.e. a transverse amplitude profile which is mathematically similar is produced. To do this we must design an imaging system.

An optical imaging system typically consists of a set of lenses with particular focal lengths and diameters chosen to produce the desired outcome. If we assume all lenses to be perfect thin lenses, with no aberrations, the resolution of any imaging system is limited only by the finite diameter of the lenses used. Fourier optics is a useful tool for understanding much of the theory behind most imaging techniques, including how this limit arises. In Fourier optics, a beam is considered as being made up of a superposition of plane waves. Where Gaussian optics uses curved wavefronts, Fourier optics uses an infinite number of plane waves oriented in different propagation directions to produce a similarly curved wavefront, each with a different transverse momentum component/transverse k-vector. The mathematics behind Fourier optics has the same foundations as continuous Fourier transform theory for signal processing, except instead of time and its conjugate, frequency, Fourier optics makes use of real space and its conjugate, spatial frequency or transverse momentum space. A lens, which is the core component of any imaging system, maps plane waves with a given transverse k vector to a single point on a transverse plane one focal length away. The position of this point on this plane depends on the value of the transverse k vector of the plane wave. As

such, a lens allows us to move between these two spaces by forming a Fourier image one focal length behind the lens of the beam one focal length in front of it. In theory this transform is perfect, however experimentally there are several limitations we must consider when using a physical lens.

2.2.3 A Basic Imaging System

We will begin by considering a simple imaging system where two lenses are separated by the sum of their focal lengths, such as in figure 2.3a. This particular case if a $4f$ imaging system, however it is not necessarily the case that the lenses both have the same focal length. In the object plane our field has the shape of a top hat function. In the theoretical case with thin lenses which are infinite in the x-direction, the lens produces the Fourier transform of the object, a $\sin x/x$ function, in the Fourier plane. This is then transformed back into a perfect reproduction of the original object by the second infinite-thin lens in the imaging plane, one focal length away from the second lens. The ratio of the focal lengths of the two lenses, f_2/f_1 defines the magnification of the image.

Any loss of light which occurs at any point in the imaging system will degrade the quality of the image. In a real experiment, the lenses will never be infinite in extent. It is common to model a real lens as a theoretical infinite lens with an aperture placed in front to model the loss of light from the imaging system, as in figure 2.3b. Since $\sin x/x$ is infinite in extent some light will always be lost from the system, and it is impossible to reproduce the top hat function perfectly in the imaging plane.

The higher order spatial components, which correspond to the finest details in the image, diverge most quickly and it is these components which lost first from the imaging system. This causes sharp details, such as the edges of the imaging system, to be lost. The result is an oscillation in the transverse field profile, such as that shown in figure 2.3b, in the final image where these sharp details were in the object. If this is the case for an imaging system

it is said to be diffraction limited.

When designing a real imaging system it is important to consider how much of the light will be lost. Intuitively, using short focal lengths means the light will diverge less over the optical path length of the imaging system. Alternatively, using larger lenses will mean more light is captured and therefore sharper details can be retained. The ratio of these quantities is sufficiently important that it is given a name: the numerical aperture (NA). A lens has an NA given by

$$\mathrm{NA} = \frac{f}{D}, \tag{2.38}$$

where f is the focal length of the lens and D is its diameter, is often quoted as an important feature in an imaging system.

Using a lens with a larger numerical aperture (larger diameter or shorter focal length) will improve the resolution of an imaging system by decreasing the amount of light lost from higher order spatial modes. The concept of the light from higher spatial modes being lost from an imaging system if a sufficiently high numerical aperture is not used will be key to several aspects of the following experimental work.

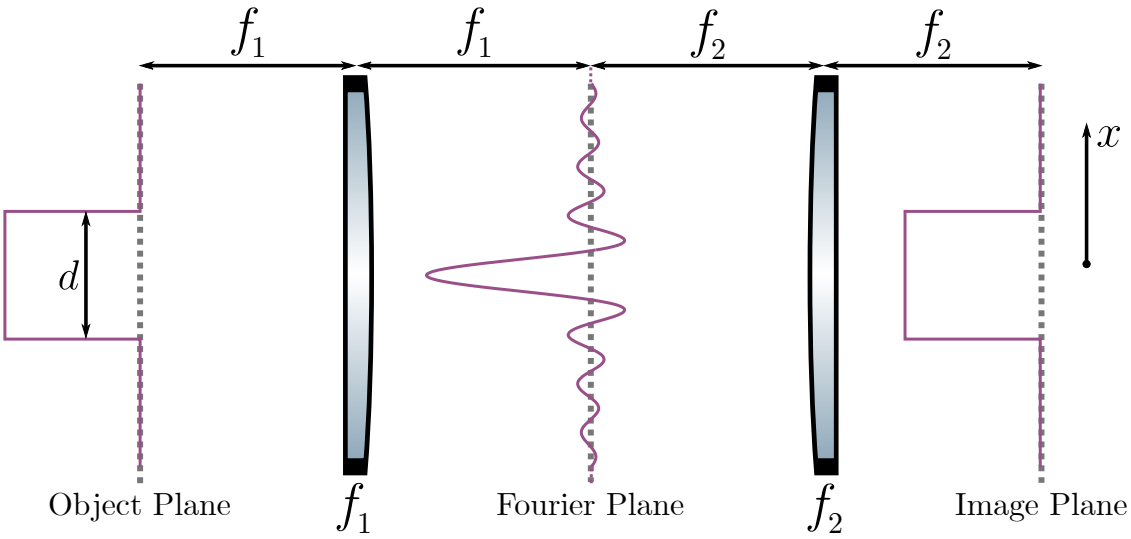

(a) The theoretical case of a perfect imaging system, reproducing an image of the object at the imaging plane with no light lost.

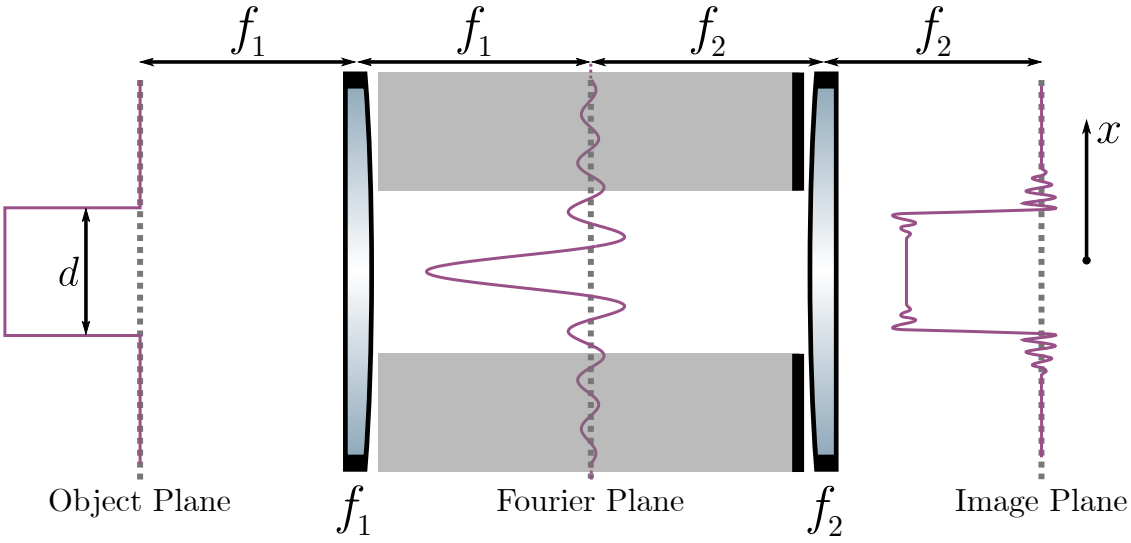

(b) The limitations of a real imaging system: an aperture is introduced in front of the second lens to simulate a real, finite lens. Higher spatial frequency components (i.e. sharp edges) of the object are lost, which leads to an imperfect image.

Figure 2.3 The perfect theoretical and realistic diffraction limited case of a $4f$ imaging system. All lenses are infinite in the x-direction, and the focal lengths of all lenses are f.

Part I

Four Wave Mixing

Chapter Three

Introduction and Literature Review

If we wish to improve the SNR of a measurement involving a laser which is limited only by shot noise there are two options: increase the mean number of photons, N, by using a more intense beam or reduce the noise on N. Increasing the number of photons used in a measurement is the simpler of these two options, and should be done where possible. However, there are many applications where it is not possible to use more power, or where using more power introduces other problems. For example, when imaging biological samples high optical powers can cause heating effects which damage or destroy living samples[24][25]. It is then necessary to instead reduce the noise if the SNR is to be improved.

Reducing the noise present on a single optical beam is useful, however it is also equivalent to produce a pair of beams with correlated quantum fluctuations. This way, one beam can be used as a reference while the other is used to make the measurement, and many experimental methods instead rely on this. Additionally, we should keep in mind that a reduction in optical power equates to a decrease in SNR. Therefore, when producing low noise light to be used in applications limited by quantum noise we should consider the power of the beams produced: this should be on the same order as the optical power typically used in current state of the art classical devices which are limited by quantum noise. This is usually the order of 1 mW for applications such as biological imaging. Finally, it is beneficial to some quantum metrology and quantum imaging applications for the noise to be reduced in

multiple spatial modes (MSM)[26]. This means the intensity profile is smoothed transversely (in space) as well as longitudinally (in time); i.e. the beams have localised correlations in their transverse profiles[27]. Such correlations could allow transverse spatial modes to be used to carry information with noise below the quantum limit, which is essential for imaging and also increases the capacity for information transfer in quantum information applications[28][29]. As a result, there is much interest in the generation of MSM squeezed light and its applications[30].

Unfortunately, it is not possible to remove the quantum fluctuations from a coherent state entirely without violating the uncertainty principle. However, it is possible to move them from one variable to another by taking advantage of nonlinear optics to introduce interaction (and therefore correlations) between photons. It is worth noting here that the field of quantum light is very wide with many different methods and the terminology is not always consistent between areas. It is therefore worth briefly discussing the field as a whole, and how this work fits in to the wider field, as well as clarifying the terminology which will be used for this thesis. For the purpose of this work, we will be interested only in reducing fluctuations in the intensity of the light. All information in the conjugate variable, phase, is lost in our measurement so this will not be discussed and noise/fluctuations should be taken to be on the intensity of the light unless otherwise specified. Finally, 'squeezing' will be used generally to refer to the reduction of noise on some variable. For a single beam this will be regarding the noise on the intensity of the light, but more commonly for a pair of correlated beams (as produced my many of the nonlinear processed discussed here) the squeezing will be in the intensity difference variable unless otherwise states, and 'squeezed light' should be considered in this case equivalent to beams with correlated intensity noise beyond the shot-noise level.

There are a range of techniques which can be used to manipulate the quantum noise on light, many of which involve an optical amplifier, which will now be discussed. The focus will be on methods capable of producing MSM squeezed light useful for the applications

we are interested in. Broadly, these methods can be categorised as either low-gain or high-gain (with 'high' typically meaning a gain greater than 2). Low-gain processes generate low numbers of photons over a vacuum background. They are used to induce correlations and entanglement of photons, and typically are discussed in the photon picture. High-gain processes introduce strong correlations between field quadratures which lead to squeezing of those field quadratures. Within these categories we also see spontaneous and stimulated processes, which can be either degenerate and non-degenerate. As mentioned previously, for this thesis a pair of correlated beams are considered to be squeezed in their intensity difference, and the language will be used interchangeably. For the low gain case, most experimental work sits in the non-degenerate spontaneous category and concerns the nonlinear process of spontaneous parametric downconversion (SPDC). SPDC, first demonstrated experimentally by Wu et.al.[31], uses a second-order nonlinear process to generate photon pairs from a single photon. The low gain inherent to the process can be attributed to limitations on the length of the nonlinear media used, non-centrosymmetric crystals which can only be grown to lengths of a few cm, and most importantly to the off-resonant nature of the interaction. Even so, pulsed beams containing as many as 6×10^5 photons have been generated via PDC[32], but typically far fewer photons are produced, and applications of SPDC are mostly concerned with heralded photon sources[33]. Despite the wide range of accessible angles in SPDC systems making it excellent for producing beams which are correlated across MSM[34][35][36][37], the photon numbers generated remain lower than desirable for our purposes.

To increase the gain of SPDC a resonant cavity can be placed around the gain medium to amplify the process. Such optical parametric oscillators (OPO) belong to the high gain regime, and both degenerate and non-degenerate versions have been realised. The cavity is typically operated below threshold, meaning the process remains spontaneous. Unfortunately, the addition of a cavity impairs the MSM nature of the produced correlations[38]. This can be mitigated with the use of a cavity designed to resonate simultaneously on more

than one mode[39], however typically it is difficult to do this for more than a few modes simultaneously. If one has a particular application in mind then the cavity can be tuned to resonate the appropriate mode[40]. Alternatively, self-imaging cavities in theory will resonate on many spatial modes. Practically this is difficult to achieve, and although some examples have been demonstrated it is difficult to realise many modes[41][42].

An alternative to SPDC and OPOs is the third order nonlinear process of four wave mixing (4WM). The first experimental demonstration of squeezing used 4WM in sodium vapour[10] to produce two degenerate correlated beams, and typically higher gains are achievable from 4WM than from SPDC without the aid of a cavity. As such, the MSM nature of the intensity correlations in the generated beams is preserved. The larger gains can be attributed in part to third order nonlinear media not being limited in length by the same constraints as the second order materials: for example, silica fibres can be used to generate bright squeezed beams[43], as well as atomic vapours[44], neither of which are limited by manufacturing capabilities. Additionally, 4WM processes can be constructed such that they are quasi resonant with atomic transitions (at least when compared to SPDC), which leads to far greater gains being possible from a single pass. Indeed, squeezing levels a high as 9 dB have been observed[45], and squeezing has been demonstrated at temporal frequencies as low as 4.5 kHz[46]. Additionally, MSM squeezed beams have been produced which exhibit localised spatial correlations[47][48][49] and have been used to make enhanced measurements[50][51][52], and the parameters impacting the gain of 4WM have been studied[53][54][55][56][57]. 4WM can be constructed such that the output is either degenerate (reverse 4WM) or non degenerate (forward 4WM) depending on the configuration of the beams. For the non-degenerate case, correlations in the Fourier plane of the vapour cell have been observed using a CCD camera, however this same measurement has not been achieved in the near field imaging plane of the cell. Additionally, the multimode nature of the generated squeezed beams has been studied using homodyne detection[58][59][60].

This thesis will focus on 4WM mixing as a method of generating bright beams which

are intensity difference squeezed in multiple spatial modes. It will build on the work done by previous PhD students Turnbull[61], Embrey[62] and Rayne[63] by studying the near field correlations produced via 4WM in a hot rubidium vapour. Through this, the matched propagation of the twin beams as they propagate through a vapour cell of finite lenth is studies, and the potential implications for the near field correlations are discussed.

Chapter Four

Theory of Squeezing and nonlinear Optics

Squeezing is a fairly generic term for reducing the quantum fluctuations on one variable (the squeezed variable) at the expense of increasing the fluctuations on it's conjugate (the anti-squeezed variable), thus avoiding violation of the uncertainty principle. For the purpose of this thesis, we will be concerned with squeezing the intensity difference between two beams at the expense of anti-squeezing the phase difference - although this will be of little relevance as we are interested only in the intensity profile for our measurements. The choice to move the noise to an unused parameter is key when optimising a measurement with squeezed light. This is an example of a two mode squeezed state (TMSS), as the squeezing exists between two bright beams which represent two distinct modes.

Generally, squeezing is achieved by manipulating the distribution of photons in a coherent state such that it is no longer random and therefore no longer follows Poissonian statistics. To do this it is necessary to induce interaction between the photons in the beam, and for this the aid of a nonlinear optical medium is needed. This is a medium whose polarisation has a nonlinear dependence on the elecric field.

4.1 Nonlinear Optics

In the case of linear optics, the polarisation of an isotropic medium, which is an expression of the electric dipole moment per unit volume, is linearly dependent on the applied electric field strength, $E(t)$:

$$P(t) = \epsilon_0 \chi^{(1)} E(t), \tag{4.1}$$

where ϵ_0 is the permittivity of free space and $\chi^{(1)}$ is the linear susceptibility of the medium and its value depends upon the properties of the medium itself.

However, in nonlinear optics the polarisation is instead expressed as a power series in $E(t)$:

$$P(t) = \epsilon_0 \left(\chi^{(1)} E(t) + \chi^{(2)} E^2(t) + \chi^{(3)} E^3(t) + ... \right), \tag{4.2}$$

where $\chi^{(2)}$ and $\chi^{(3)}$ are the second and third order nonlinear susceptibilities respectively and, as with $\chi^{(1)}$, have a value which depends on the properties of the medium. Typically these higher order susceptibilities are sufficiently small that the higher order components of the polarisation are negligible. However, with sufficiently high field strength, $E(t)$, and careful choice of medium these terms can become relevant.

This is important to the field of quantum optics, since the nonlinear polarisation can be considered a source term in the nonlinear wave equation[64],

$$\nabla^2 E(t) - \frac{n^2}{c^2} \frac{d^2 E}{\partial t^2} = \frac{1}{\epsilon_0 c^2} \frac{\partial^2 P_{\mathrm{NL}}}{dt}, \tag{4.3}$$

where n is the usual linear refractive index and c is the speed of light in vacuum. The right hand side is essentially an expression for the acceleration of the charges in the medium, and following Larmor's theorem this will generate EM radiation.

As an example, if we consider an input field of the form

$$E(t) = E_1 e^{-i\omega_1 t} + E_2 e^{-i\omega_2 t} + c.c., \tag{4.4}$$

then the second order ($\chi^{(2)}$) contribution to the nonlinear polarisation will be

$$P^{(2)}(t) = \epsilon_0 \chi^{(2)} E(t)^2 \tag{4.5}$$

$$\begin{aligned} P^{(2)}(t) = \epsilon_0 \chi^{(2)} (&E_1^2 e^{-2i\omega_1 t} + E_2^2 e^{-2i\omega_2 t} \\ &+ 2E_1 E_2 e^{-i(w_2+w_2)t} + 2E_1 E_2^* e^{-i(w_1-w_2)t} + c.c.) \\ &+ 2\epsilon_0 \chi^{(2)} \left(E_1 E_1^* + E_2 E_2^*\right) \end{aligned} \tag{4.6}$$

There are therefore components of the polarization which oscillate at some combination of ω_1 and ω_2 which give rise to different nonlinear processes. For example, the terms with frequency $\omega_1 + \omega_2$ and $\omega_1 - \omega_2$ are responsible for the physical processes of sum-frequency generation and difference-frequency generation, respectively. While there are 4 different frequency components present in equation 4.6, usually only one will be present with any significant intensity in the generated radiation from a particular nonlinear process. This is because the nonliear media is dispersive, which means the generated fields will not necessarily stay in phase with one another as they propagate along the z axis. Typically, the experimental parameters can be chosen such that one component will be correctly 'phase matched', and only this process occurs. Experimentally the dominant frequency component is selected by appropriately choosing the polarisation of the input field and the orientation of the nonlinear field. The phase matching condition will be discussed for a specific nonlinear process later.

4.1.1 Third Order Nonlinear Processes

When the symmetries of a nonlinear medium mean the $\chi^{(2)}$ component of the nonlinear susceptibility is zero, the $\chi^{(3)}$ component of the polarisation becomes the dominant nonlinear term. Such centro-symmetric materials, often atomic vapours, can be used to generate third

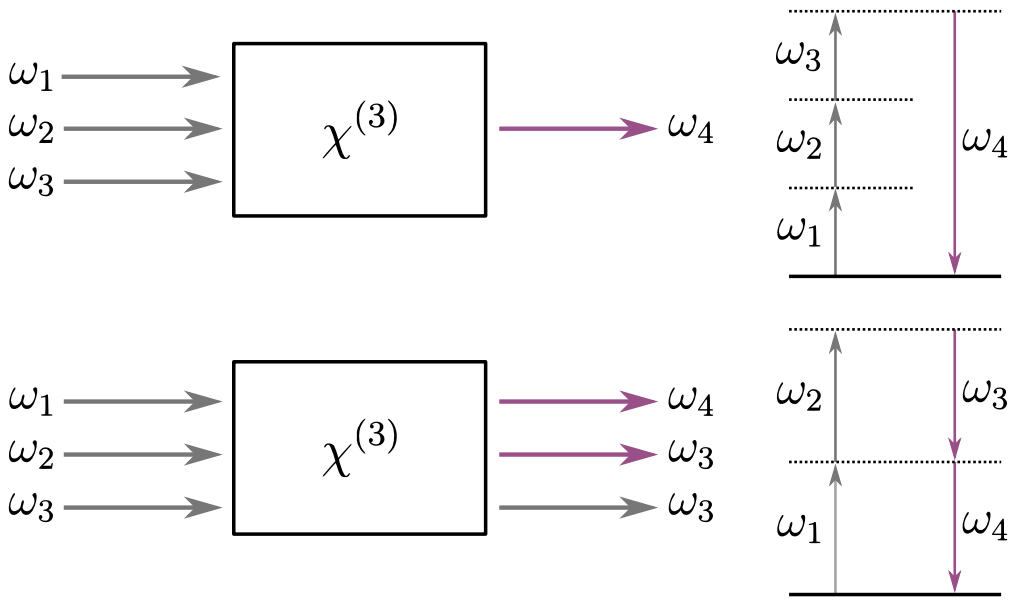

Figure 4.1 Two possible mixing processes possible when three input waves interact in a medium with a significant $\chi^{(3)}$ susceptibility. The fields indicated in purple are those created by the process, while those in grey are the input field. The dashed lines indicate virtual states.

order nonlinear processes which are governed by the third order nonlinear contribution to the polarisation:

$$P^{(3)}(t) = \epsilon_0 \chi^{(3)} E(t)^3. \tag{4.7}$$

The case of a third order nonlinear process is far more complex than that of the second order process described above. We shall consider the case where the applied field consists of three frequency components:

$$E(t) = E_1 e^{-i\omega_1 t} + E_2 e^{-i\omega_2 t} + E_3 e^{-i\omega_3} + c.c. \tag{4.8}$$

The nonlinear polarisation when this field is applied to the third order nonlinear medium contains 44 frequencies if positive and negative frequencies are considered separately. A more detailed description of this can be found in Boyd[64]. Some non-resonant examples of these processes are illustrated in figure 4.1: note that the generated frequency is dependent on the frequencies of the three input fields. Commonly, these processes are parametric, which means the initial and final quantum state of the atom are the same. Consequently, the photon

energy is always conserved in a parametric process. Theoretically, parametric processes can be described by a real susceptibility. However, it should be noted that experimentally when describing a nonlinear process undertaken by a whole system, absorption and other elements which are not the pure nonlinear process desired also come into play. This means that when describing what happens experimentally there will be an imaginary component to the susceptibility as the processes occurring in the medium include absorption as well as the desired nonlinear effect. This is more significant for more resonant nonlinear processes, where effects other than the wave mixing have a higher chance of occurring.

The nonlinear process used in this thesis to generate squeezed light is called four wave mixing (4WM)[65][66], and is similar to that illustrated in the bottom of figure 4.1 in that the generated field has frequency $\omega_1 + \omega_2 - \omega_3$, with complex amplitude

$$P(\omega_1 + \omega_2 - \omega_3) = 6\epsilon_0 \chi^{(3)} E_1 E_2 E_3^*. \tag{4.9}$$

However, the 4WM scheme used is a resonant process, meaning each atomic transition is 'close' to a real atomic level (at least when compared with those given in figure 4.1). The 4WM is performed using the D1 line of rubidium 85: a 4-level system. The frequencies of two of the input fields, ω_1 and ω_2, are the same and are used to 'pump' the atom into an excited state, while a weak 'probe' beam of frequency ω_3 seeds the process. A 'conjugate' beam of frequency ω_4 is generated by the process. The double lambda transition describing the 4WM process is shown in figure 4.2.

As with $\chi^{(2)}$ nonlinear processes, for 4WM to occur the dispersive nature of the nonlinear vapour must be taken into account, and the correct phase matching condition must be met. Again, the polarisation of the input radiation must be chosen correctly to ensure this is the case, however the orientation of the vapour does not matter as, unlike the crystals used in the $\chi^{(2)}$ processes, it is centrosymmetric. Instead, the angle between the direction of propagation of the input beams is relevant and must be chosen carefully. This, along with how 4WM is realised experimentally, is discussed in the next chapter.

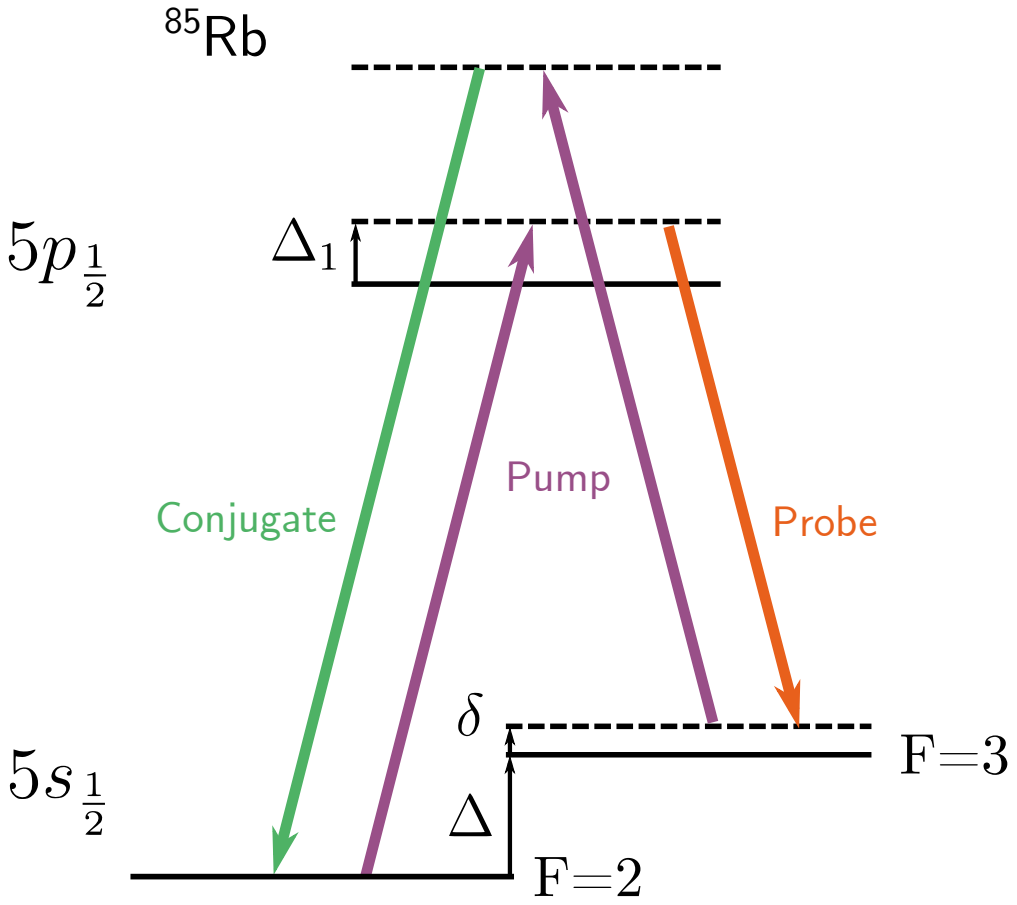

Figure 4.2 The double lambda transition on the D1 line of rubidium 85. An atom is excited from the F=3 ground state to the upper virtual excited state, detuned by $\Delta_2 = \Delta_1 + \delta + \Delta$, via the absorption of a pump photon. It immediately de-excites to the F=2 ground state, emitting a conjugate photon. It is then immediately excited to the lower virtual excited state via the absorption of a second pump photon, detuned by $\Delta_2 = \Delta_1 + \delta + \Delta$. Finally, it de-excites back to the F=3 ground state, emitting a probe photon.

Chapter Five

Experimental Four Wave Mixing

Following the theoretical scheme described in the previous section, to generate the squeezed light a strong pump beam is injected into a heated rubidium vapour cell. Two pump photons are absorbed and a probe and conjugate photon are emitted via the double lambda transition, described previously and illustrated in figure 4.2. This interaction takes place on the D1 line of rubidium 85[67]. A more detailed investigation, including simulations, of this process is undertaken in chapter 8.

5.1 Phase Matching

As 4WM is a parametric process, conservation of energy defines the frequency relation between our fields, which from here we shall refer exclusively to as the pump, probe and conjugate, as illustrated in figure 4.2. However, due to the dispersive nature of the rubidium vapour the three different frequency fields all experience different refractive indices as they pass through the cell. This effect is particularly prominent for the probe and pump beams, which are closer to resonance than the conjugate. In a vacuum the k-vectors are perfectly matched, as shown in figure 5.1a, however the slight difference in refractive index causes a mismatch in these k-vectors in the rubidium vapour, as shown in Figure 5.1b. This mismatch in phase accumulates as the beams propagate through the cell, and when a mismatch of π is

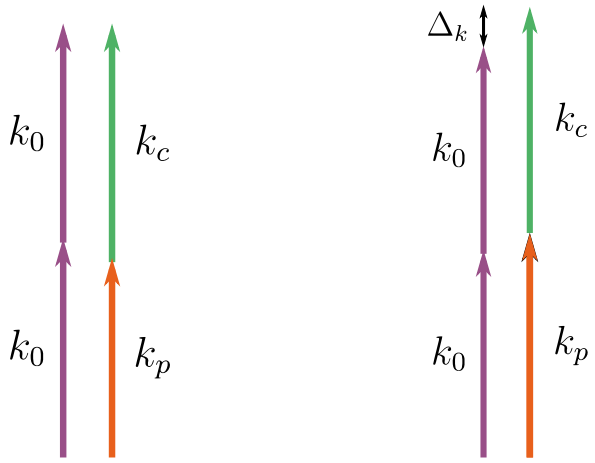

(a) Propagating colinearly in vacuum.

(b) Propagating colinearly in rubidium vapour.

(c) Critically phase matched in rubidium vapour.

Figure 5.1 The pump, probe and conjugate k-vectors as seen in vacuum and in rubidium vapour.

reached the 4WM process will begin to undo itself due to the fields being out of phase with one another. It is therefore essential that the relative phase difference between the pump beam and the probe and conjugate beams is kept to a minimum. For 4WM in rubidium vapour, the phase matching condition is met if the fields are incident at small angles to one another.

For a cell injected with a strong pump beam, the probe and conjugate photons will be emitted in an annulus, or halo, of light around the central axis. This is defined by the direction of the pump beam, such that the probe and conjugate photon positions in the annulus are radially symmetric. It can be thought of as the 4WM process being seeded by vacuum fluctuations, and as such is essentially an amplification of the vacuum field. The width of the annulus is representative of the tolerance in the phase matching requirements of the pump, probe and conjugate. A longer cell will lead to a thinner annulus as the tolerable phase mismatch between the beams decreases due to the longer propagation distance, and in the limit of an infinitesimally thin cell light would be emitted in all forward directions. In our current experimental setup, with a cell length of 12 mm, the angle range between the probe and pump for which we see gain is approximately 3-12 mrad[53].

The 4WM process can also be seeded with a probe seed beam. This stimulates the emission of probe and conjugate photons resulting in two bright beams. These are emitted in addition to the halo of light stimulated by vacuum fluctuations, which can be seen in figure 5.2. The gain of the process, G, is defined according to the ratio of the number of photons in the probe and probe seed, such that

$$N_{\text{probe}} = G \times N_{\text{seed}} \tag{5.1}$$

$$N_{\text{conj}} = (G-1) \times N_{\text{seed}}. \tag{5.2}$$

In the ideal case, the probe and conjugate photons are always produced in pairs, which means the beams have near perfect co-variance. The variance in the difference between the number of photons in the probe and conjugate in this ideal case is

$$\text{Var}(N_{\text{probe}} - N_{\text{conj}}) = \text{Var}(N_{\text{probe}}) + \text{Var}(N_{\text{conj}}) - \text{CoVar}(N_{\text{probe}} N_{\text{conj}}) \tag{5.3}$$

$$= \text{Var}(N_{\text{seed}}) = \sqrt{N_{\text{seed}}}, \tag{5.4}$$

assuming the seed beam is in a coherent state. We see that even in the ideal case of perfect pair production we are limited by the noise on the seed beam. Assuming no fluorescence and no absorption, the SNR of the intensity difference of a pair of probe and conjugate pulses produced by seeding with a pulse of N_{seed} photons is

$$\text{SNR}_{\text{coh}} = \frac{N_T}{\sqrt{N_T}} = \sqrt{(2G-1)N_{\text{seed}}}, \tag{5.5}$$

where the total photon number, N_T is the sum of equation 5.1 and equation 5.2.

Comparatively, the SNR of the intensity difference of a pair of equivalent coherent beams is

$$\text{SNR}_{\text{squ}} = \frac{N_T}{\sqrt{N_{\text{seed}}}} = (2G-1)\sqrt{N_{\text{seed}}}. \tag{5.6}$$

The SNR of the squeezed state is higher than that of the coherent state by a factor of $\sqrt{(2G-1)}$. Therefore maximising G will give maximal improvement in the SNR of the

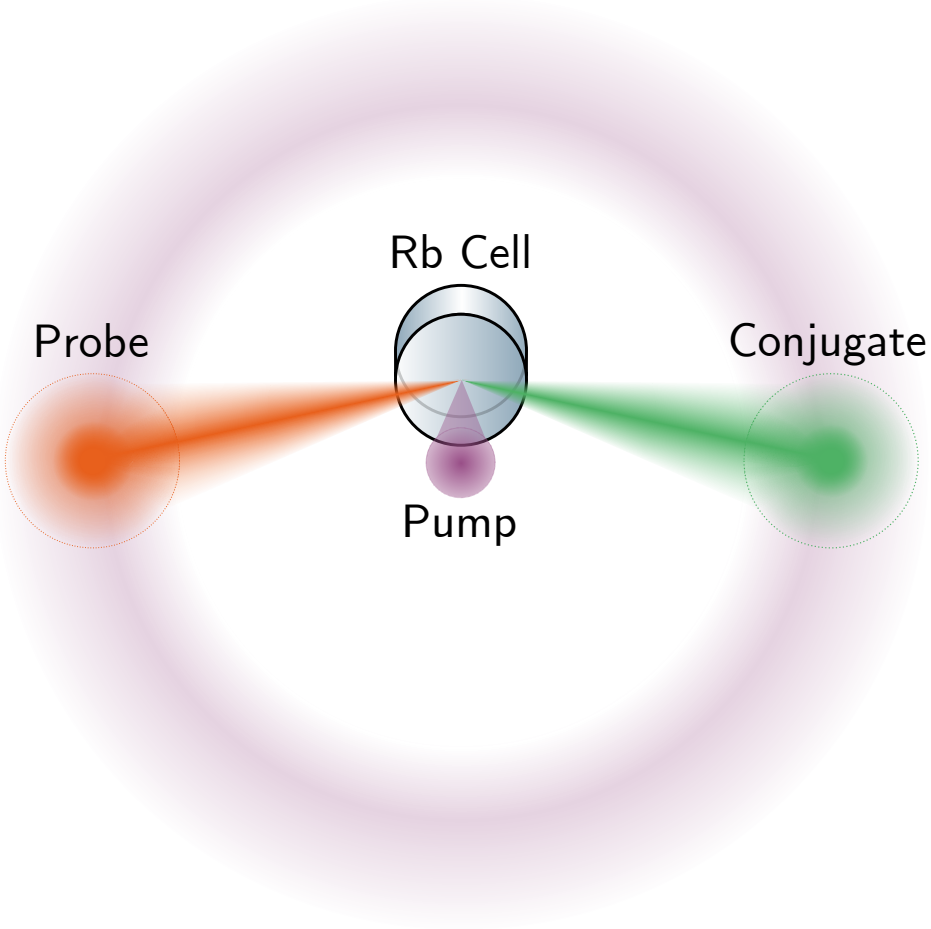

Figure 5.2 A halo of light is produced in the cell via 4WM stimulated by vacuum fluctuations. The probe seed produces probe and conjugate bright beams within this halo. In order to maintain high spatial resolution, all light within the 'area of interest' around the probe and conjugate beams should be captured by the imaging system.

squeezed state. Intuitively this makes sense as we know from equation 5.4 that the noise on the seed beam is the limiting factor in the level of squeezing in the theoretical case, therefore maximising the total power by increasing G minimises the effect of any noise in the seed beam.

There are several ways one can increase gain: the most intuitive is to increase the number of atoms by either increasing the temperature of the cell or increasing its length, both of which introduce new problems. As well as increasing the atom density, increasing the temperature also increases the average velocity of atoms in the cell, which in turn increases the number of collisions. This causes a decoherence of the atomic state which ultimately reduces the 4WM gain. Increasing the length of the cell creates a more restrictive phase matching condition which places limitations on the multimode nature of the squeezing. This will be discussed in detail later in section 5.3.1.

Ultimately there are many experimental parameters which must be tuned in order to maximise the gain, however this must be done while keeping other noise sources and distorting effects, such as absorption and Kerr lensing, to a minimum. Interestingly, the greatest levels of squeezing are not seen at the maximum gain. These effects will be discussed in more detail in chapters 8 and 9.

5.2 4WM Parameters

In our experiment, the polarisation of the pump and probe beam are chosen to be orthogonal as this allows relatively easy separation of the pump from the probe and conjugate (which has the same polarisation as the probe) despite the small angle separating them by using a Glan-Thompson polariser. The pump and probe beam are both linearly polarised orthogonally to one another. As a result the two virtual excited states in a single double-lambda transition are forced to occupy different m_F states. This choice means the double-lambda system is considered to have 4-levels, despite the value of Δ_1 typically being on the order of GHz

which is sufficiently large that it is not necessary to distinguish between the hyperfine levels of the excited state. For example, consider the pump beam to be π polarised and the probe and conjugate to be a linear superposition of $\sigma^{\pm}$ polarised light as determined by the quantisation axis of the atoms (since there are no dominant magnetic fields influencing the experiment there is no obvious sensible choice of quantisation axis, so this choice is arbitrary). Following the process illustrated in figure 5.3, an atom in the $F = 2, m_F = 0$ ground state will be excited by a pump photon with π-polarisation to the $m_F = 0$ virtual excited state (this could correspond to either excited F state with similar probability due to the large detuning). The atom will be stimulated by the $\sigma^{\pm}$ polarised probe beam to de-excite to the $F = 3, m_F = \mp 1$ ground state before being re-excited to the $m_F = \mp 1$ virtual excited state with the absorption of a second π polarised pump photon. Since the two virtual excited states will always occupy different m_F states, defined by the polarisations of the probe and pump beams, this defines the system as having 4-levels. Finally, since 4WM is a parametric process it must start and end in the same state. This means the atom must return to the $F = 2, m_F = 0$ state, which is achieved via the emission of a $\sigma^{\mp}$ conjugate photon, meaning the polarisation of the conjugate will be the opposite sigma to that of the probe. However, over many 4WM interactions both the probe and conjugate fields can be considered to be the same superposition of $\sigma^{\pm}$ light and as such have the same linear polarisation orthogonal to that of the pump.

There are only certain paths through the m_F states of the double lambda configuration which are possible, and these combined with the dipole matrix elements corresponding to various transitions defines a superposition of m_F states which the $F = 2$ ground state must be in for the 4WM to occur efficiently.

It takes a finite length of time for the atoms to be pumped into the described superposition of states and for a coherence to be established between the two ground states. During this time the gain of the 4WM increases as the correct superposition is established. It is useful to know how long this takes as the squeezing is limited during this time as the gain of the

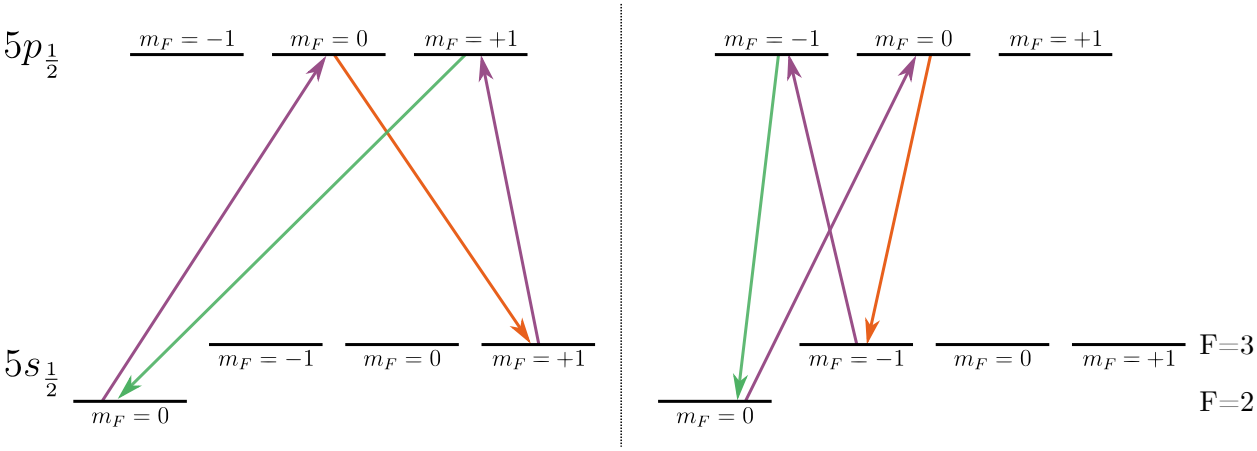

Figure 5.3 The two possible paths of an atom starting in the $m_F = 0$, $F = 2$ ground state to undergo 4WM. The pump (purple) is considered to be π polarised while the probe and conjugate (orange and green) are a superposition of $\sigma^{\pm}$ polarisations.

4WM is not yet at a maximum. This can be measured by monitoring the power of the seed beam after the pump is switched on, with the seed always on. Figure 5.4 shows such a measurement. The slight delay between the start of the TTL pulse controlling the pulse and the probe intensity increasing is due to delays in the electronics and in the acousto-optical modulator (AOM) used to switch the beams on and off. Note the AOM switching time should also be accounted for: it takes a finite amount of time for the RF wave to travel across the transverse profile of the pump beam in the AOM crystal, meaning the pump actually turns on gradually. The speed of the RF wave in the AOM is approximately 4.2 mm/µs[68], so for the beam size of approximately 2 mm used in this experiment one would expect the switching time of the pump beam to be on the order of 0.5 µs. The time taken for the probe to reach maximum gain is larger than this, therefore we assume the slow increase in the seed power is primarily due to the time taken for the ground state coherence to be established.

Figure 5.4 shows two different coherence pumping times, both with a similar final gain. These were taken for different one-photon detunings, Δ_1. The interplay between the 4WM and the amount of absorption experienced by the probe can lead to quite complex behaviour. As a result the parameters used in the 4WM experiment if squeezed light is to be generated must be precisely tuned to maximise overall gain while also considering absorption. The

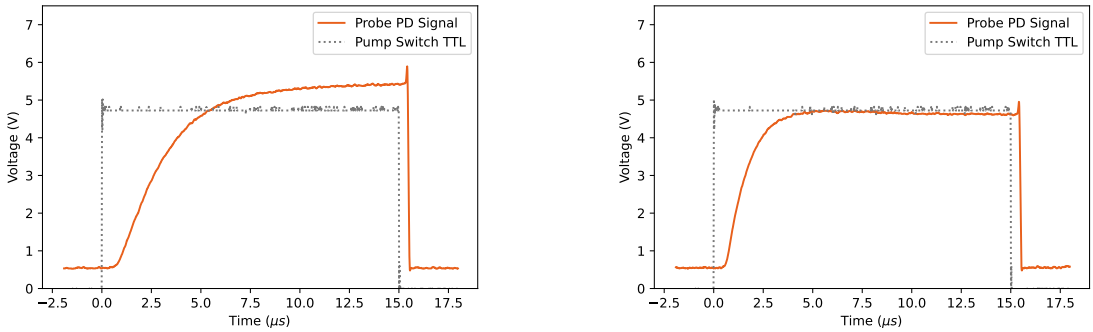

(a) Laser frequency set just above the 4WM resonance.

(b) Laser frequency set just below resonance (higher absorption).

Figure 5.4 The optical power of the probe beam as measured by a photodiode and the voltage used to switch the RF signal which controls the probe AOM. Note the voltage scale is arbitrary but consistent between the two plots.

two plots given in figure 5.4 correspond to values of Δ_1 which lie either side of the value which gives the greatest gain, with figure 5.4b corresponding to the value typically used when generating the greatest level of squeezing. These effects will be discussed in greater detail in chapter 8. One might think it would be preferable to choose the laser frequency which gives large gain with a short coherence pumping time, as in figure 5.4b. However, at this frequency there is a lot of absorption of the probe, which destroys correlations. Therefore it is necessary to accept the slightly longer coherence pumping time to operate in a region with less absorption.

5.3 Imaging Correlations

Since the 4WM photon pair production happens almost instantaneously from a single atom, the photon pairs can be considered to originate from the same place in the gain medium as there is no time for the atom to move between the probe and conjugate photons being emitted. Additionally, due to conservation of momentum the probe and conjugate pair produced will have equal and opposite transverse momenta. Therefore when we image the beams we expect to see correlations in small corresponding regions across the two beams. These corre-

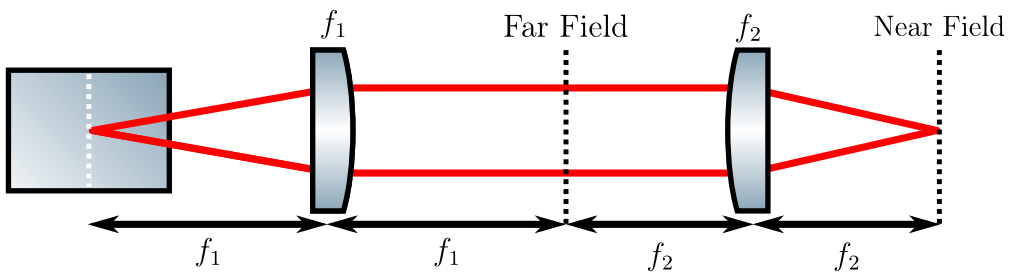

Figure 5.5 Imaging scheme used to obtain near field and far field images of the probe and conjugate beams. The near field image is magnified by a factor of $\frac{f_2}{f_1}$.

spond to pairs of photons originating from the same atoms, as well as the two beams being correlated as a whole. This is what it means for light to be MSM squeezed. Conversely, a single mode squeezed state would not exhibit sub-shot noise fluctuations in localised areas of the beam as the correlations are distributed across the entire beam. Therefore the whole beam must be detected for the intensity correlations to be observed.

In order to observe spatial correlations within the beams we must create either a near field (NF) or far field (FF) image of the beams in the cell. The imaging scheme used to achieve this is shown in figure 5.5. The near field is an image of the intensity profile inside the cell. The correlations are due to each photon pair being made at the same position, therefore the correlated areas of the probe and conjugate beams are on top of one another as illustrated in figure 5.6a. The far field image maps the momentum of the beam at the object plane to a displacement at the image plane. Therefore the image is essentially a map of the momentum correlations. Due to conservation of momentum in the 4WM interaction the correlations are centrally symmetric in the image, as illustrated in figure 5.6b.

5.3.1 Near Field Coherence Length

The correlations in the NF and FF are not arbitrarily small - they are limited in size by the parameters of the 4WM and the properties of the imaging system used. As such we can define a coherence length, x_{coh}, which characterises the smallest area in which independent local squeezing can be observed. The NF coherence length, which is defined orthogonally to the

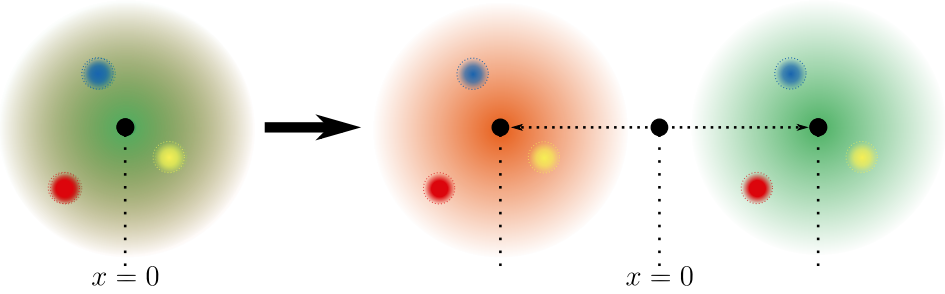

(a) In the near field (NF) correlated areas are in equivalent positions in the cell, due to them being produced at the same time by the same atoms in the cell. Note that the NF images of the probe and conjugate will be overlapped unless separated in the imaging process.

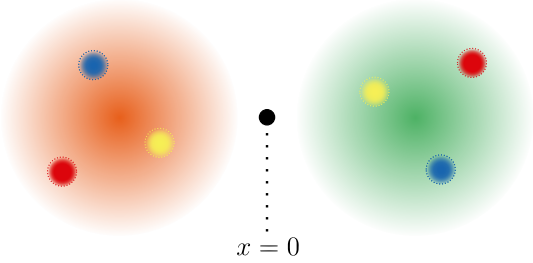

(b) In the far field (FF) the correlations are radially symmetric, due to the conservation of transverse momentum between the probe and conjugate photons.

Figure 5.6 An example of how correlated areas, indicated by matching colours, are positioned in the NF and FF images of the probe and conjugate beams in the cell.

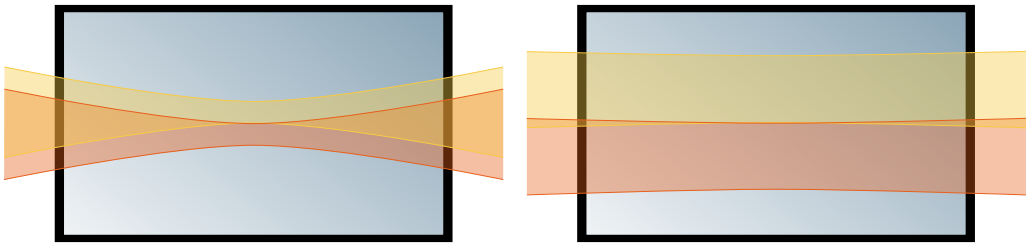

(a) Small areas of the near field image correspond to modes which diverge quickly, creating overlap between adjacent modes inside the gain medium.

(b) Large areas of the near field image correspond to modes which diverge slowly; there is relatively little overlap between adjacent modes inside the gain medium.

Figure 5.7 Looking at a small area of the near field image of the beams can be thought of as looking at a beam with a narrow waist inside the gain medium. The smaller the waist, the faster the beam diverges.

direction of the beam's propagation axis, will be defined at the centre of the cell. The limiting factor is the length of the gain medium: if we were to use an infinitely thin gain medium an MSM squeezed field would be produced where $x_{\text{coh}} \approx \lambda$. However, experimentally the gain medium must have a finite length to produce any gain. The coherence length is limited to the width of modes which do not expand sufficiently within the medium that they become coupled with adjacent modes. This is illustrated in figure 5.7 and quantified below.

To understand the coherence area, we consider the expansion of a beam of waist x in the centre of the cell. The width of the beam increases along the propagation axis, and the smaller the waist the faster this expansion occurs. The coherence length is approximately the size of a mode waist where the width expands to be a factor of $\sqrt{2}$ larger at each end of the cell. Therefore we are looking for the expansion which occurs over the Rayleigh distance, and hence can define the coherence area as the beam waist which has a Rayleigh distance equal to the length of the gain medium

$$x_{\text{coh}} = \sqrt{\frac{\lambda L_g}{\pi n_s}}, \tag{5.7}$$

where L_g is the length of the gain medium, λ is the wavelength of the light, and n_s is

the refractive index of the gain medium. The coherence length is a theoretical limit which can be achieved only if all light emitted from the 4WM process is collected when forming an image of the beam; this is difficult to achieve experimentally.

5.3.2 Far Field Coherence Length

In the FF the coherence length is best understood by considering the size of the beams in the gain medium. In order to have an infinitesimally small coherence area we would require all beams to be plane waves, which is not experimentally possible. In reality the small range of k-vectors in the beams means that if we consider a photon in the far field, there is a small area in the correlated beam in which the correlated photon could lie. This is illustrated in figure 5.8, using the variation in the k-vectors in the pump as an example. The range of k vectors in the pump beam means there are a range of k-vectors the conjugate can possess for a given probe k-vector, leading to an enlarged region in the FF where the conjugate photon can lie. Alternately, one can consider a small area in the far field to diverge quickly when traced back to the cell, and so it corresponds to a beam which is wider than the cell when traced back.

The number of non-overlapping coherence areas, referred to as modes, is the same in the NF and in the FF. This is linked to the spatial bandwidth of the squeezing. For a given probe beam size, a smaller coherence length results in more modes in the beam, and these smaller coherence lengths correspond to higher spatial frequencies. Thus the smaller the coherence length the higher the spatial bandwidth of the squeezing.

5.4 Temporal Bandwidth

There is a finite temporal bandwidth of the squeezing, which can be observed when we measure the frequency spectrum of intensity fluctuations on a squeezed beam using a spectrum analyser. When we analyse frequencies higher than the squeezing bandwidth we no

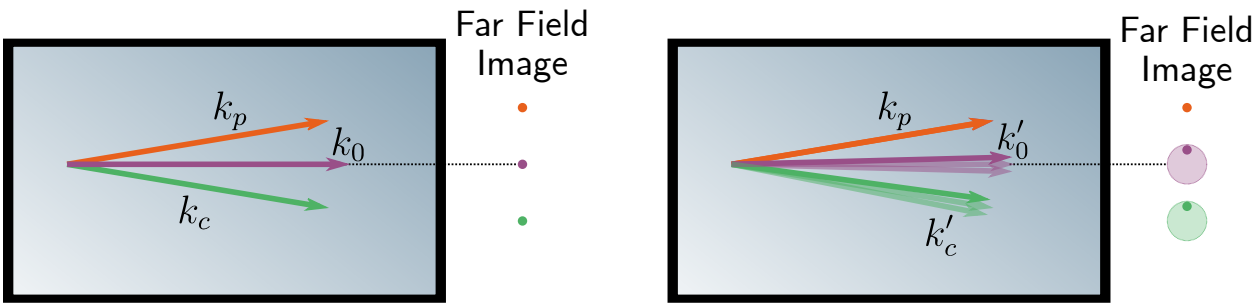

Figure 5.8 Pump, probe and conjugate k-vectors from a single 4WM transition in the gain medium. The left image depicts the case for plane waves, whereas the right is a more realistic experimental case. The corresponding area in which a photon could be seen in the far field are shown by the dots to the right of the gain medium. In the FF the probe and conjugate are symmetric around the pump axis.

longer see a reduction in the quantum fluctuations. It is preferable to analyse at frequencies away from DC, typically at least 100 kHz, as technical noise sources will always dominate at low frequencies. The bandwidth of the squeezing is related to the linewidth of the 4WM transition: vacuum fluctuations with temporal frequencies similar to that of the probe seed also stimulate probe/conjugate pairs to be emitted at slightly different frequencies to those stimulated by the probe seed. The different frequencies present in the beams beat together, and the beat signals generated by the probe and conjugate beams are correlated. This gives the reduction in shot noise we detect which is at MHz frequencies and below. In our case this frequency is approximately 10 MHz. A plot illustrating the frequency spectrum of the various noise sources is shown in figure 5.9. The blue 'subtraction' line shows the temporal noise profile of the squeezed beam if technical noise sources are ignored. The black dashed like shows the temporal noise profile we would expect the squeezing to have in the ideal, but still achievable, experimental case. At low frequencies technical noise will still dominate regardless of whether the light is squeezed; it is only at frequencies where we would otherwise be shot noise limited that we can directly observe a reduced noise power in frequency space by subtracting probe and conjugate. Note that this also means the increased noise on the probe and conjugate beams is only present below this temporal squeezing bandwidth.

We can also consider the spatial noise present on the beam. The plot in figure 5.9 may be

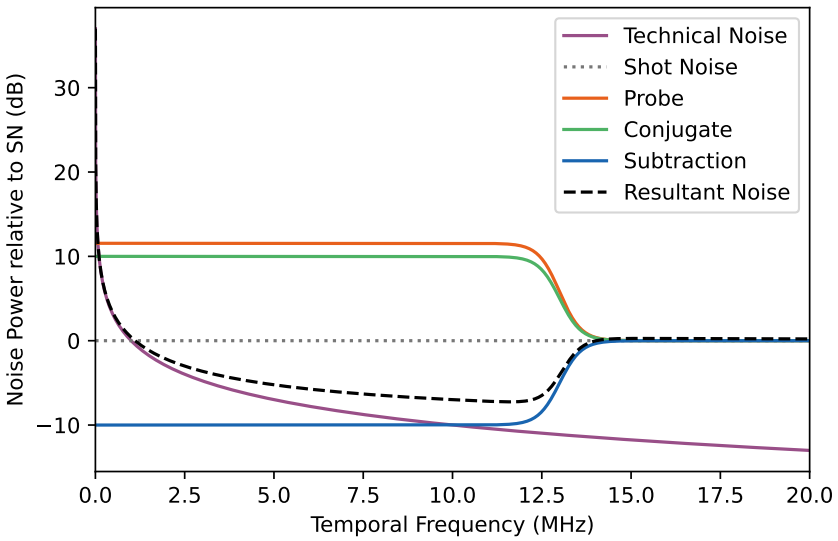

Figure 5.9 An illustration of the noise contributions from the probe beam, the conjugate beam and the classical/technical noise associated with the real experiment where 10dB of squeezing is realised. Shown also is the noise spectrum of the intensity difference (subtraction) of these two beams, ignoring classical noise, and the resultant noise we expect to see on the intensity difference squeezed beam.

thought of as the temporal noise at zero spatial frequency; essentially, this is the noise profile we would expect to see in the case where all of the light from each beam has been captured. Similarly, we could replace the 'Temporal Frequency' axis with a 'Spatial Frequency' axis and the plot would still look extremely similar for some given temporal frequency within the squeezing bandwidth. At low spatial frequencies classical noise would still dominate, and at high spatial frequencies the noise would return to the shot noise level as we move below the size of the coherence area. However, if we were to plot the noise power with respect to spatial frequency for a higher temporal frequency then we would see a much lower level of technical noise present across all spatial frequencies.

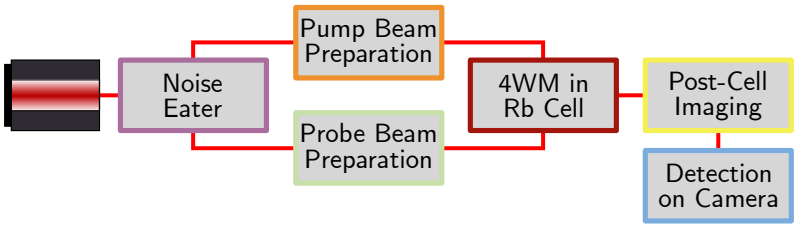

Figure 5.10 A flow diagram outlining the key components of the optical setup used to generate and detect squeezed light via 4WM. The coloured outlines match the sections shown in figure 5.11.

5.5 Experimental Setup

Figure 5.10 outlines the key components of the experimental setup used to produce and analyse the squeezed light, with the corresponding optical setup given in more detail in figure 5.11. Both the probe seed and pump beams are derived from a single laser: an M-Squared SolsTiS titanium-sapphire crystal laser with an output frequency of around 795 nm pumped by a Coherent Verdi laser. This is passed through a 'noise eater', which reduces low frequency technical noise; this is discussed in section 7.2. To generate the detuning between the probe and conjugate a 1.5 GHz AOM is used in a double-pass configuration. To allow rapid and independent switching of the pump beam, an 80 MHz AOM is used in single pass configuration on the pump beam. The pump and probe seed beams are passed through a 12.5 mm rubidium vapour cell heated to approximately 105 °C to create bright probe/conjugate beams via 4WM. A GT polariser is then used after the cell to remove the majority of the pump beam, which is orthogonally polarised to the probe and conjugate. Residual pump beam is blocked in the far-field imaging plane of the cell where the beams are optimally spatially separated relative to their radii. With the pump beam blocked, the correlations in the probe and conjugate beams can then be measured.

This experimental setup was already in place when I joined the experiment, having been designed and modified by previous PhD students. The details of their contributions can be found in their theses[62][61][63]. With the exception of additions discussed explicitly in this thesis, along with modifications to imaging systems throughout to maximise the efficiency

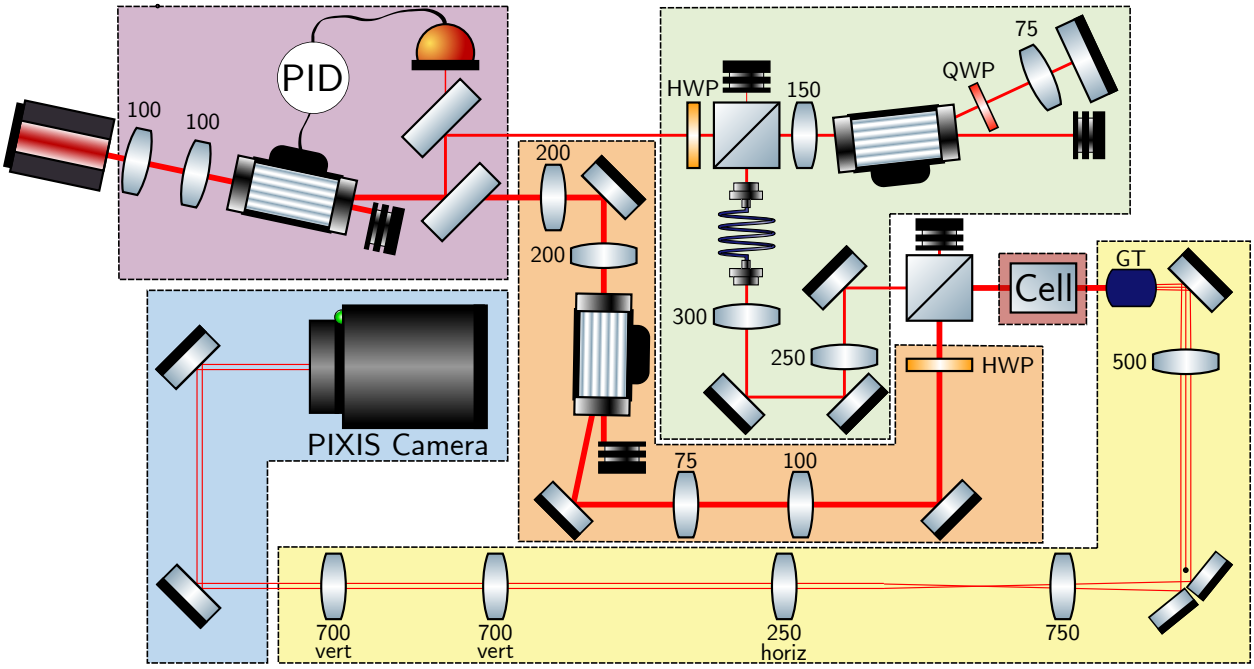

Figure 5.11 A simplified optical diagram of the full experimental setup used to generate 4WM. The colour of the blocks match the outlines in figure 5.10.

of the 4WM process based on optical power available, the core design remained largely unchanged. The experimental setup itself had to be completely realigned shortly after I joined the experiment due to the laser being sent for repairs. This was done by myself, and I took the opportunity to optimise the layout of the experiment minimise scattered light impacting the squeezing measurement.

It is worth acknowledging here that ideally we would like to produce a single beam of light with intensity fluctuations below the quantum noise limit and simply replace classical light in existing experiments with this, however this is very challenging to do. Currently when the intensity difference correlated twin beams produced by the 4WM are overlapped, the fluctuations will add constructively resulting in noise far above the quantum noise limit. It is possible to use an optical cavity to induce a phase shift to one of the beams in such a way that the intensity fluctuations cancel out when the beams are overlapped, however doing this will sacrifice the MSM nature of the light which is essential if it is to be used in imaging applications. Therefore, an experiment using the twin beams to enhance a measurement

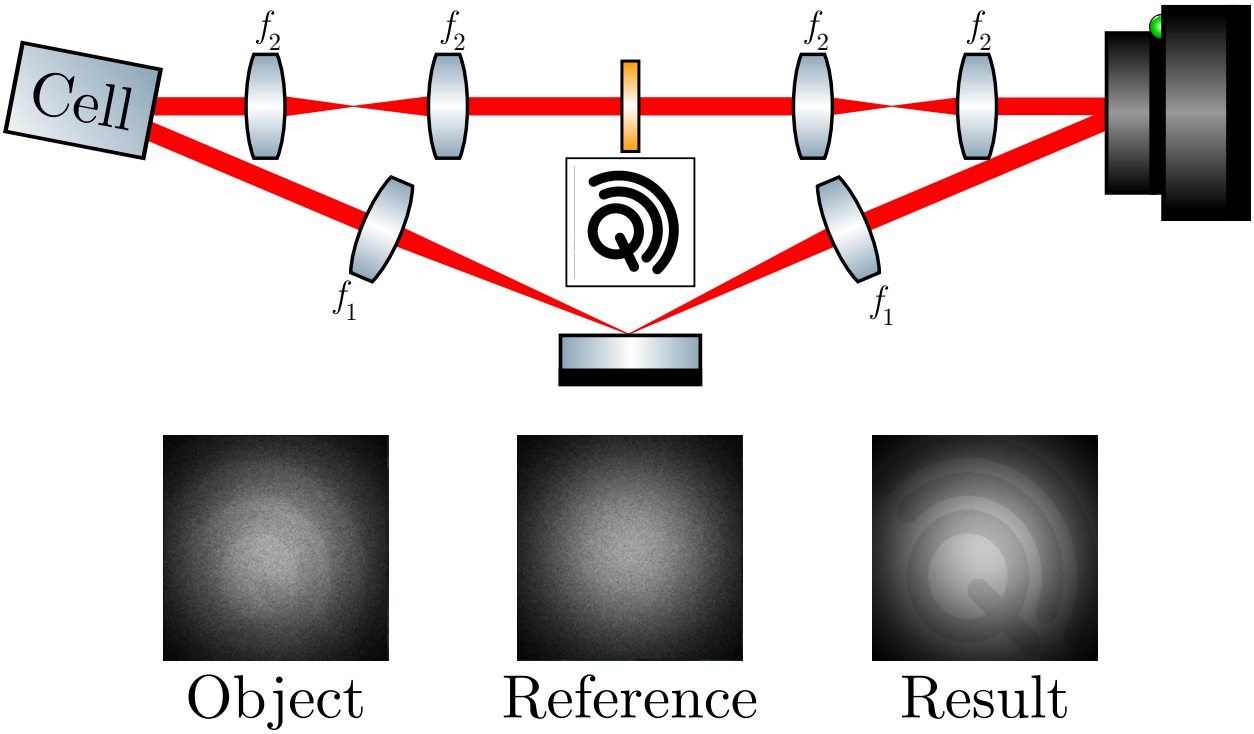

Figure 5.12 An example of a measurement being made using the twin correlated beams. The near-field image of the cell is formed on a partially absorbing plate using one of the beams, the object beam. The image of this plate is then formed on the camera. For the reference beam, a near field image of the camera is formed directly on the camera. Any magnification must be kept the same for both beams. When the reference beam is subtracted from the object beam the result is a clearer image of the absorbing plate. Note that the intensity of the resultant image has been inverted here.

will typically use one of the beams to make the measurement and the other as a reference for the noise. For example, to image a partially transparent object, one beam would be directed through the object while the other would be subtracted from the resultant image, as illustrated in figure 5.12. It is important to note that the use of a reference beam means only half of the light contributing to the noise in the final image is actually used in generating the image. Therefore, to see any benefit from this method the correlations must be sufficient to reduce the noise by at least half, or in other words must provide at least 3 dB of squeezing.

Two main detection schemes are used to measure the correlations in the twin beams. A photodetector can be used at any point in the setup after the cell where the probe and

conjugate are sufficiently spatially separated to measure the intensity difference between the two beams. This is predominantly used to optimise the 4WM parameters to give the highest correlation in the intensity fluctuations, and was well established as a method of measuring the squeezed light produced in the experiment when I joined. A Princeton Instruments PIXIS camera is also used to capture images of the probe and conjugate. This allows the localised correlations to be investigated. This method had seen some success at the point when I joined, which is discussed in Rayne's thesis[63], however the amount of squeezing observed was far lower than expected. These detection methods will be discussed in detail in chapters 6 and 7.

The camera is being used to investigate the correlations in the twin beams in the hope that it is the next step in the application of using quantum light to enhance imaging measurements outside of a quantum optics lab. The multi mode nature of the correlations is evident from existing experiments, such as the generation of arbitrarily shaped entangled twin beams by Boyer et.al[50] or the use of homodyne detection to quantify the spatial modes present[59][60]. However, these all examine the correlations in the continuous regime at a given frequency. Additionally, both methods require relatively elaborate optical setups for this detection and aren't particularly useful for detecting many modes simultaneously as would be required in a setup such as the one in figure 5.12.

A camera is comparatively simple to set up and allows simultaneous detection of many spatial modes, which is essential for effective imaging. Therefore, understanding the limitations of detecting the spatial correlations in the twin beams using a camera motivates a significant portion of this thesis. While spatial correlations have been successfully measured in the FF imaging plane of the cell by Marino et. al.[56] using a camera, the NF correlations have not. Due to the nature of the correlations as illustrated in figure 5.6, using the NF correlations for an imaging measurement is more straight forward as the spatial noise on the reference beam should be identical to that on the object beam.

Chapter Six

Detection: Photodetector

Having used 4WM to produce the correlated probe and conjugate beams it is now necessary to measure the intensity of the beams in order to characterise and quantify the level of squeezing present. In order to do this the light must be converted to an electrical signal which can be analysed and compared to that of a coherent beam. There are two methods by which this was achieved: using a high speed photodetector to convert the light directly to an electrical signal, or alternatively using a high quantum efficiency CCD camera to rapidly capture images of the beam. The photodiode performs a continuous measurement which allows the signal to be analysed in frequency space, thus reducing the difficulties caused by technical noise sources which dominate at low frequencies. The camera method allows for greater flexibility in post processing of the data but is far more sensitive to low frequency noise. The camera detection will be discussed in more detail in chapter 7. It is worth noting that for our purposes the CCD screen can be thought of as an array of photodiodes for which the photoelectrons are stored in 'bins', although there are technical differences between the two[69]. The following discussion will refer only to photodiodes, which are the silicon semiconductor devices used to convert optical power into an electrical current, and photodetectors, which for the purpose of this thesis will refer to a photodiode plus the electronics necessary to allow this photocurrent to be accurately measured.

6.1 Basic Photodetection

We will first discuss the core elements of a simple photodetector, consisting of a photodiode with an appropriate front end to perform a current-to-voltage conversion. Understanding the noise sources introduced by the electronics, and the characteristics such as quantum efficiency and bandwidth of the detector, is essential. The core concepts discussed here will be relevant to all forms of detection discussed in this thesis, however the solution to provide optimised performance will depend on the function of the detector in question. Further details on this can be found in Horowitz and Hill[70], and in particular Hobbs[71] gives an excellent description on how to design low noise photodetectors.

6.1.1 Photodiodes

The photodiode is the core of all photodetectors. It is a semiconductor device which converts incident photons to photoelectron-hole pairs, which are then accelerated by an electric field to create a photocurrent which is proportional in intensity to the power of the incident light.

Silicon photodiodes with a PIN structure, such as that shown in figure 6.1, are commonly used in applications where high sensitivity and signal bandwidth are required. The intrinsic (I) semiconductor region between the P-type and N-type semiconductor junctions increases the efficiency with which incident photons are converted to electron-hole pairs via the photoelectric effect[72]. It also decreases the capacitance of the photodiode compared to one with a PN structure. The generated electron-hole pairs are then swept by the electric field intrinsic to the PIN junction to produce a photocurrent. For fast photodetection, it is generally accepted that photodiodes should be operated in reverse biased mode with a positive bias connected to the N-type junction (cathode) and/or a negative bias to the P-type junction (anode). This increases the size of the intrinsic region, further lowering the capacitance of the photodiode which allows for a higher bandwidth amplification. More details regarding this are given in the next section.

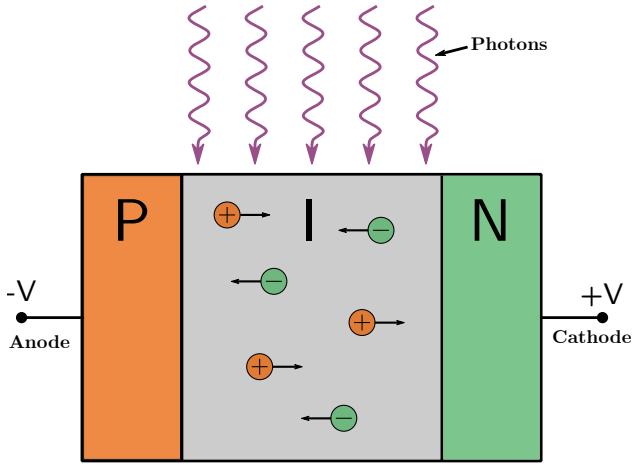

Figure 6.1 A PIN photodiode operated in reverse bias, with a positive and negative bias voltage, V, connected to the cathode and anode respectively. Electron-hole pairs generated in the intrinsic region are swept to the P- and N-type junctions, as indicated by the arrows, to generate a photocurrent proportional to incident light.

When detecting squeezed light, it is crucial that the photodiode has a high quantum efficiency - i.e. the conversion rate of an incident photon to an electron-hole pair should be as high as possible. Each photon has an independent probability of being converted to a photoelectron, meaning any loss during this stage is random and follows Poissonian statistics. This means any loss also destroys correlations between the beams, and thus reduces the measured squeezing level. Therefore an ideal photodiode has a quantum efficiency of 100%. While this is unfeasible in reality, it is possible to achieve very high quantum efficiencies of over 99%.

The photocurrent generated by a photodiode must be converted to a buffered voltage which can be easily monitored without impacting the measurement, and the essence of a good photodetector is in how this conversion is performed. When using bright beams, such as those generated by the seeded 4WM process, the shot noise fluctuations are typically extremely small compared to the average intensity of the light incident on the photodetector and it can be difficult to ensure the technical noise introduced by the electronics of the photodetector does not dominate the shot noise. Therefore, before further discussion of the components of our photodetector, it is helpful to consider the different types of electronic

noise.

6.1.2 Electronic Noise Sources

When designing a photodetector capable of detecting squeezing, the cumulative effect of all electronic noise sources must be significantly lower than the optical shot noise. The current literature pertaining to the design of photodetectors frequently accepts shot noise as a fundamental limit in how low the noise floor of a photodetector needs to be, and it is uncommon for the possibility of pushing below this limit to be addressed. The origin of the various sources of electronic noise will therefore now be discussed.

Flicker Noise

Flicker noise, or pink noise, has a power spectrum which follows a $\frac{1}{f}$ distribution. It is caused by imperfect contact between conductors. It is extremely difficult to avoid flicker noise, and therefore the best way to minimise its impact is to use high frequencies. This means that our analysing frequency should be chosen to be sufficiently high such that the squeezed quantum noise level on the light is greater than the flicker noise level, while still being low enough to lie within the squeezing bandwidth.

Johnson/Thermal Noise

Johnson-Nyquist noise, or thermal noise, is due to thermal agitation of charge carriers. The frequency distribution of the thermal noise of an ideal resistor is approximately white, meaning there is the same noise power in each unit of frequency. Any resistor, R, included in a circuit will introduce a thermal noise current density given by

$$i_{\mathrm{JN}} = \sqrt{\frac{4k_B T}{R}}\ \mathrm{AHz}^{-\frac{1}{2}}, \tag{6.1}$$

where k_B is the Boltzmann constant and T is the temperature of the resistor. Note that

larger resistors have a smaller noise contribution, so it is preferable to use larger resistance values where possible when low noise is of key importance.

Electronic Shot Noise

The concept of electronic shot noise is the same as for optical shot noise: charge is quantised and carried by discrete particles, electrons, so we expect to see statistical fluctuations in the current. Assuming the charges act independently of each other, the fluctuating current's noise density is given by

$$i_{\mathrm{n}} = \sqrt{2qI_{dc}}\,\mathrm{AHz}^{-\frac{1}{2}}, \tag{6.2}$$

where q is the electron charge and I_{DC} is the intensity of the DC current.

It is crucial to appreciate that this formula applies only when the charge carriers act independently, such as charges crossing a barrier in a junction diode where the charges move via diffusion. It is not, however, true for metallic conductors, where long range correlations between the charge carriers suppresses this noise significantly[73].

6.1.3 Photodiode Front Ends

The simplest way to convert the photocurrent generated by a photodiode to a voltage is to pass the photocurrent through a resistance, R. This will convert the shot noise fluctuations in the current, i_{SN}, to a voltage, $V_{\mathrm{SN}} = Ri_{\mathrm{SN}}$, as shown in figure 6.2. Since i_{SN} is typically very small, it is desirable for R to be large, however this results in an RC circuit being formed with the photodiode capacitance, C_{PD}, with time constant $\tau = RC_{\mathrm{PD}}$. This causes the output response to roll off at frequencies greater than

$$f_{\mathrm{RC}} = \frac{1}{2\pi R_f C_{\mathrm{PD}}}, \tag{6.3}$$

severely limiting the bandwidth of the detector. Operating the photodiode in reverse biased configuration, as described above, helps decrease C_{PD} and thus improve the bandwidth

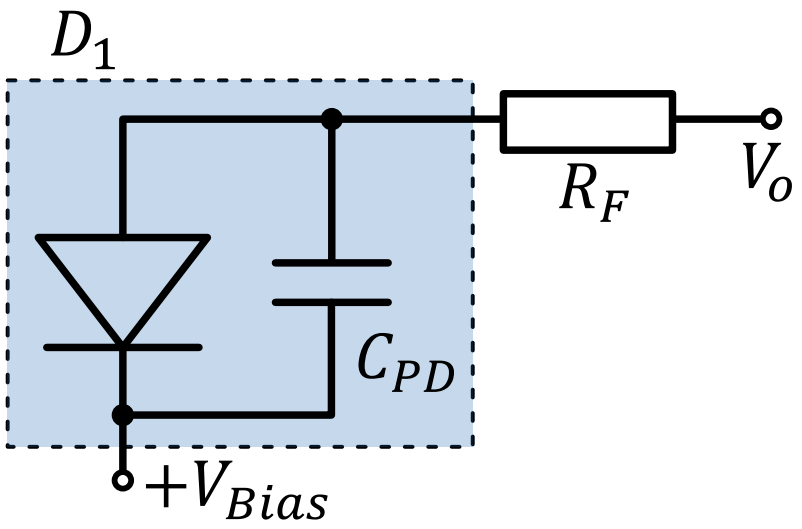

Figure 6.2 Schematic representation of a photodiode, shaded in blue, including the capacitance, C_{PD} across its terminals operated in reverse bias. The generated photocurrent is passed into a resistor, R_F, to produce an output voltage, V_O.

somewhat. However, a small resistance is still necessary to obtain anything close to the MHz bandwidths we desire. For example, the S3883 photodiode by Hamamatsu [74], chosen for its high quantum efficiency and low capacitance of 6 pF, would require a resistance around $R = 2\,\mathrm{k}\Omega$ to operate at a bandwidth of around 10 MHz, without accounting for parasitic capacitances added by soldered connections. Perhaps more significantly, the voltage drop across the resistor would result in a 'build-up' of charge on the anode of the photodiode. This causes the bias of the photodiode to be dependent on the applied optical power, which is highly undesirable as it makes the relationship between incident light and the output of the photodiode non-linear. Clearly another method is needed to reduce the issues caused by the large voltage swing across the photodiode capacitance.

The solution is to use a transimpedance amplifier, which utilises an operational amplifier to hold one side of the photodiode at ground, thus maintaining a constant bias, while also performing a high bandwidth current to voltage conversion.

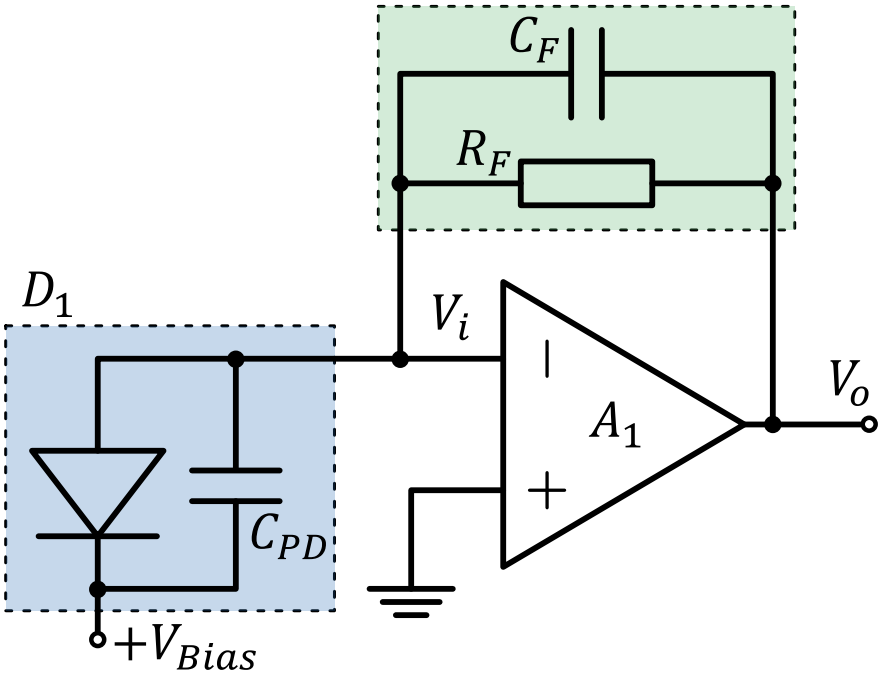

Figure 6.3 A basic transimpedance amplifier, utilising an op amp, $A1$, to convert the photocurrent produced by the reverse biased photodiode, D_1, to an output voltage, V_O, with a transimpedance gain dictated by the feedback loop, shaded in green.

Transimpedance Amplifier

A basic transimpedance amplifier is shown in figure 6.3 as a front end to a photodiode operated in reverse bias with a positive bias voltage, $+V_{\text{Bias}}$. The operational amplifier (op amp) balances the potentials at its inputs by outputting a current from the output pin which cancels any current at the inverting input pin via the feedback resistor R_F, thus forming a feedback loop and holding the unbiased side of the photodiode at a virtual ground. This means the voltages on either side of the photodiode are held approximately constant, so the voltage swing across C_{PD} is close to zero. Exactly how close the swing is to zero is governed by the open-loop gain, A_{OL}, of the op amp: the higher A_{OL} the closer to zero the swing is.

The open-loop gain is frequency dependent, given by

$$A_{\text{OL}}(f) = \frac{A_{\text{DC}}}{(1 + if/f_{\text{dom}})(1 + if/f_2)}, \tag{6.4}$$

where f_{dom} is the dominant pole frequency of the amplifier and A_{DC} is the DC gain. Their product, known as the gain bandwidth product (GBP), provides a reliable metric by which to compare op amps. Intuitively, the GBP is approximately equal to the unity gain crossover frequency, f_T. To create a high-gain high-bandwidth circuit, as we wish to do, an op amp with a high GBP should be selected. Finally the pole at frequency f_2 is representative of other bandwidth limiting effects from other stages of the op amp, often added intentionally to increase stability and damp oscillations which would otherwise occur at high frequency.

The op amp introduces a phase shift to the signal which increases with frequency. Most modern op amps are designed specifically such that their high frequency gain response is (tactically) sacrificed somewhat to ensure the circuit is stable and well-behaved at high frequencies, however care must be taken to ensure the feedback loop does not cause a phase shift sufficiently large that the negative feedback becomes positive and the circuit subsequently oscillates - as a rule it is generally accepted that a phase shift up to 45° is tolerable, in addition to the 180° shift inherent to the inverting amplifier.

The closed-loop gain of the circuit shown in figure 6.3 is given by

$$A_{\mathrm{CL}}(f) = \frac{A_{\mathrm{OL}}(f)}{1 + A_{\mathrm{OL}}(f)G_{\mathrm{fb}}(f)}, \tag{6.5}$$

where $G_{\mathrm{fb}}(f)$ is the frequency dependent gain of the feedback network. When the magnitude of the loop gain, $A_{\mathrm{L}} = A_{\mathrm{OL}}(f)G_{\mathrm{fb}}(f)$, is approximately 1, if the loop's gain has a phase of 180° the denominator of equation 6.5 will go to zero and the closed-loop gain will be infinite. The result is a circuit which oscillates. Therefore the phase shift must be kept sufficiently small that such oscillations cannot occur. It is generally considered that a shift of around 45° to 60° is reasonable, and is achieved by putting a capacitor, C_f, across R_f. The optimum value of the feedback capacitor, C_f, is

$$C_f = \frac{1}{2\pi R_f \sqrt{f_T f_{\mathrm{RC}}}}. \tag{6.6}$$

Generally, it is difficult to know parameters such as the input capacitance, and therefore the value of R_{RC}, precisely. Typically it is better to use a feedback capacitor which is slightly too large to increase stability.

The transimpedance gain of the circuit, which functions as the resistance in the current to voltage conversion, is given by

$$Z_m(f) = \frac{A_{\mathrm{OL}} Z_f}{1 + A_{\mathrm{OL}} + i2\pi f C_d Z_f}, \tag{6.7}$$

where Z_f is the complex impedance of the feedback loop: i.e. for the circuit in figure 6.3 the parallel combination of R_f and C_f. By choosing components carefully and surface mounting the electronics to avoid additional parasitic capacitance, a stable sub shot noise photodetector with a large bandwidth can be designed.

Component Noise Sources

In addition to the noise sources discussed above, there are some more practical sources of noise which must be discussed and mitigated via careful choice of components and equipment.

Power Supply Any noise from the power supply can be coupled into the photodetector's output signal if care is not taken. Choosing a quiet external power supply is the first step in mitigating this, however in terms of circuit design linear voltage regulators should be used to generate the appropriate supply voltage, particularly for powering chips or providing an offset voltage. This is not so crucial for the bias voltage of the photodiode. Additionally capacitors can be added near the supply pins on any chips to provide a low impedance path for AC noise on the DC power supply to ground. The appropriate values for such decoupling capacitors can be found on the relevant datasheets, but typically a pair of decoupling capacitors of 1 µF and 0.1 µF is used.

Op Amp In addition to the high GBP discussed above, the TA op amp should also have suitably low input current and voltage noise. An ideal op amp has perfectly balanced inputs

into which no current flows, however in reality these conditions are not quite met. There is a small offset between the inputs, meaning the potential difference between them is not quite zero. However, this is typically extremely small in modern amplifiers and will be tiny in comparison to the output signal provided our gain is sufficiently high and should also be reasonably well accounted for when calibrating the detector provided it is constant. Of more concern to us are the input current and voltage noise, $i_{N\text{amp}}$ and $e_{N\text{amp}}$. The input voltage noise can be thought of as the variation in the difference the amplifier measures between its two inputs. Since the amplifier only amplifies differential signals it can be modelled as being on either input. The current noise, $i_{N\text{amp}}$, is simply added to the signal and therefore amplified by the same transimpedance gain as the signal current. Since we will be using high gain it is far more likely that the current noise will be the dominant noise source introduced by the op amp. Therefore, the op amp should be chosen to have a current noise (significantly) smaller than that which we expect to see on our photocurrent. The op amp used in the transimpedance stage of all our circuits was the OPA657[75].

Feedback Resistor The feedback resistor R_f is chosen with similar considerations: it will contribute a thermal noise dependent on its value according to equation 6.1, therefore a large value of resistance is preferable. However, care should be taken that R_f remains small when compared to the input impedance of the inverting input of the chosen op amp, which is modelled as infinite.

Non-inverting Input Components It is almost a tradition to add components of equal value to those in the feedback loop to the non-inverting input of the amplifier. This is to ensure the two inputs have close to the same impedance, which helps mitigate any imperfections which may result from current noise caused by the non-infinite impedance of the inputs and from any offset noise which exists between them. Since modern amplifiers often have very well-balanced inputs with high impedance and low voltage offsets this is not so

necessary, but it doesn't hurt to add them!

Finishing the Circuit The output of the TA stage can be input to subsequent amplification or signal processing stages. Manipulating the signal after the TA is generally pretty simple, since we should in theory be working with a relatively large input voltage and are now shielded from the capacitance of the photodiode. Of course, it is still important to ensure any components used have sufficiently high bandwidth to avoid degrading the hard earned TA response, and that the associated electronic noise does not overpower our signal, but this should be straight forward to achieve. A $50\,\Omega$ resistor is added to the output of the photodetector to ensure it is impedance matched to the spectrum analyser to minimise signal reflection from the load. This means the final op amp used in the circuit must be capable of outputting sufficient current that the output voltage can be dropped over the $50\,\Omega$ resistor. This usually means choosing an op amp with a high output current specifically for this purpose, as it is unusual for the low noise high bandwidth op amps ideal for the TA to be capable of outputting enough current.

6.2 Balanced Photodetection

For bright beams, shot noise fluctuations comprise a very small fraction of the DC level of the optical power. This can make it very difficult to detect - especially considering squeezed light has reduced shot noise. Applying a large gain to the transimpedance amplification stage helps ensure the small signal we are trying to see overcomes the electronic noise of the detector, particularly the voltage input noise introduced by the op amp. However, we must also be careful not to saturate the output of the operational amplifier, as it has a limited voltage which it can output, and after this point is no longer sensitive to intensity fluctuations. Therefore, it is beneficial to remove the DC offset before the TA stage.

One method of achieving this is to use a balanced photodetector (BPD), which consists

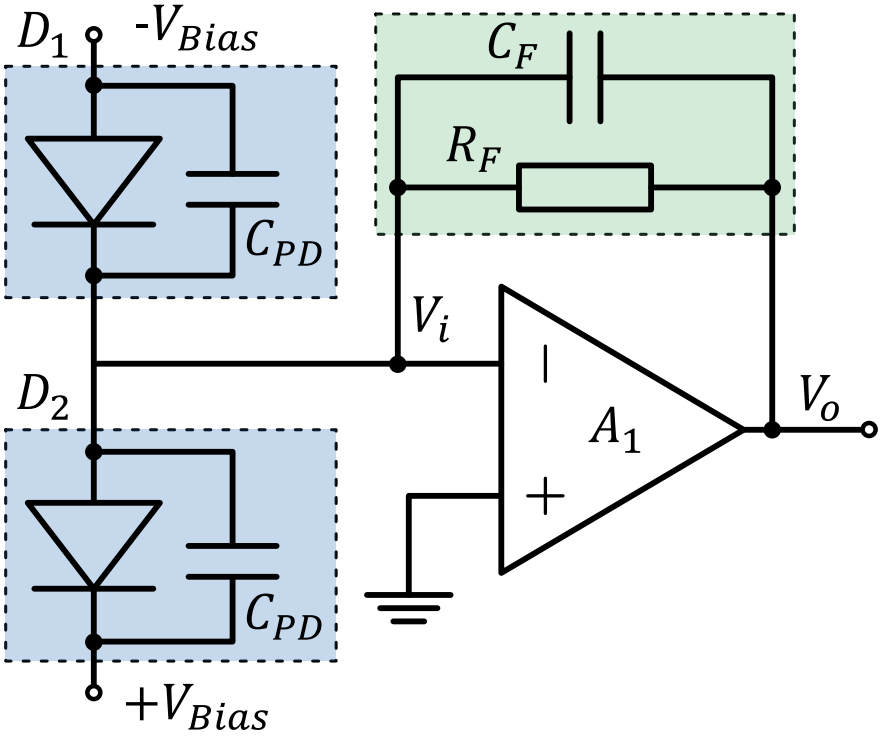

Figure 6.4 The schematic of the BPD, with the two physically separate photodiodes indicated in blue and the feedback loop of the TA in green. Identical photodiodes are used so the capacitance, C_{PD} is the same for both.

of two photodiodes which are oppositely biased and connected anode-to-cathode, allowing their photocurrents to be subtracted, as illustrated in figure 6.4. Since we are interested in the noise on the intensity difference between two beams, this is perfect for determining the degree of squeezing in a single spatial mode. The subtracted photocurrent gives the intensity difference signal which can be amplified using a TA. In addition to allowing greater amplification without saturating the TA stage, this method removes any common mode technical noise on the beams from the signal being measured, making it easier to detect squeezing.

In order for the BPD to be used to measure squeezing, we need to know how much noise we would expect to measure for a pair of coherent beams of the same total power as our squeezed beams. Therefore a calibration of the total optical power incident on the BPD to the noise measured in the intensity difference at the temporal frequency at which the squeezing is being measured must be performed. This calibration is far easier than trying to theoretically calculate what the expected shot noise level would be for a given beam power. To calibrate, a coherent beam is split and one half directed on each of the two photodiodes. Deriving the two beams from the same source helps minimise any technical noise on the final signal as any common mode noise is cancelled and the remaining noise will be at the shot noise limit. The total power incident on the photodiodes is then varied. Since the shot noise is proportional to $\sqrt{N}$, the noise power will increase linearly with optical power, provided we are limited by the shot noise. If we are not at the shot noise limit and are instead limited by a technical noise source, we would expect our noise to increase quadratically with optical power. Plotting measured noise at the chosen analysing frequency against total incident optical power results in a calibration for how much noise we expect to see in a coherent beam of a given power. This in turn allows the noise reduction in a pair of squeezed beams incident on the detector to be determined provided we know the total optical power.

To determine the incident power, one beam is blocked at a time and the two resulting signals are recorded and summed. While this method creates a small delay between the power

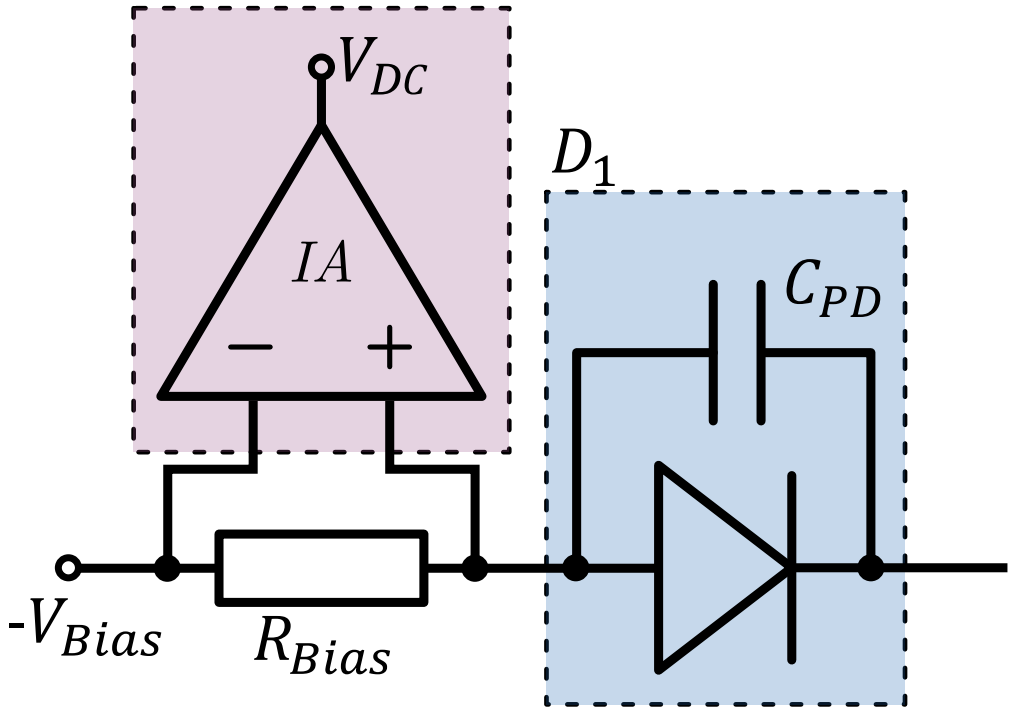

Figure 6.5 One arm of the BPD circuit, with an instrumentation amplifier (IA) added to a resistor placed between the bias voltage and the photodiode to measure the DC optical power.

measurement and the noise measurement, the average optical power in the squeezed beams is generally stable enough that it does not negatively affect the results. However, in newer iterations of the BPD an instrumentation amplifier (IA) has been added to the biased side of each photodiode to allow an instantaneous measurement of the total incident optical power. Figure 6.5 shows this for one of the photodiodes. This measures the voltage drop across a resistor placed between the biased voltage supply and the photodiode, allowing constant monitoring of the total incident optical power without disturbing the noise measurement.

The BPD is a well established tool in our setup used on a daily basis to tune experimental parameters to maximise the level of squeezing present in the twin beams. A drop mirror is used to divert the twin beams so they can be tightly focussed onto the BPD, ensuring the whole of the probe beam falls on one photodiode and the whole of the conjugate falls on the other. This helps to ensure that all light is captured by making sure all light falls

on the photodiodes even if the beams move a little, therefore no intensity fluctuations are introduced by light being lost from the measurement. On a typical day, squeezing of around 5 dB is achievable with relatively minimal effort required to optimise parameters.

6.2.1 Limitations of the BPD

As mentioned previously in chapter 3, one benefit of 4WM over other squeezing methods is that the squeezed beams can be achieved in a single pass of the rubidium vapour without the addition of a cavity to provide sufficient gain. This preserves spatially localised correlations, generating a TMSS which is squeezed across multiple spatial modes.

While the BPD is an invaluable tool in monitoring the squeezing across the whole transverse profile of a pair of beams, difficulties arise when trying to use the BPD to measure part of the beams in order to determine the coherence area of the MSM squeezed light. It is possible to scan a physical aperture, or slit, across the beams and measure the squeezing in the selected portions[52][76], however this introduces a sharp edge into the image of the beam. Since there is some uncertainty in where correlated photons will be spatially located, as discussed in section 5.3.1, due to the finite spatial bandwidth of the squeezing, sharp edges risk losing correlated photons on one detector but not the other. This can be thought of as high spatial frequencies being required to create the sharp edge, and these typically are not within the spatial bandwidth of the squeezing, meaning that when sharp edges are introduced the squeezing is degraded. Fortunately, the ability to analyse the correlations at high temporal frequencies is retained, which means technical noise does not restrict such measurements. Note that the techniques discussed in this chapter are also applicable to the second part of this thesis.

An alternative method of studying the correlations is to capture images of the beams using a camera. While the benefit granted by the BPD of analysing the fluctuations at a particular temporal frequency is lost, the camera allows far more flexibility in the post-

processing of the images, and therefore in the analysis of the correlated modes. This is the topic of the next chapter.

Chapter Seven

Detection: Camera

An alternative method of detection is to capture NF images of the beams using a high quantum efficiency camera. This allows for computational post-processing of the data and therefore far more flexible analysis, including the possibility to analyse multiple distinct modes within a single data set. To effectively characterise the squeezing we must capture multiple images in order to analyse how the intensity difference between the two images varies in time. This is achieved by capturing a series of images in quick succession and calculating the variance in the difference of the intensity difference of the probe and conjugate. Unlike with the BPD, where we can analyse the noise signal in frequency space on a spectrum analyser, when using the camera we are not able to isolate the higher temporal frequency components of the signal. Figure 7.1 gives an example temporal noise profile (note that the frequency values are examples and not necessarily representative of what is seen experimentally). The shaded area between f_1 and f_2 shows the range of temporal frequencies for which the noise is integrated over when capturing images with the camera. The lower limit on this frequency, f_1, is determined by the total time taken to capture all of the images. The upper limit, f_2, is determined by the time taken to capture a single image, as any fluctuations which occur on timescales shorter than this time are averaged over. Ultimately, this means the camera measurement is much more sensitive to technical noise.

To minimise the impact of classical noise is to capture the images as quickly as possible.

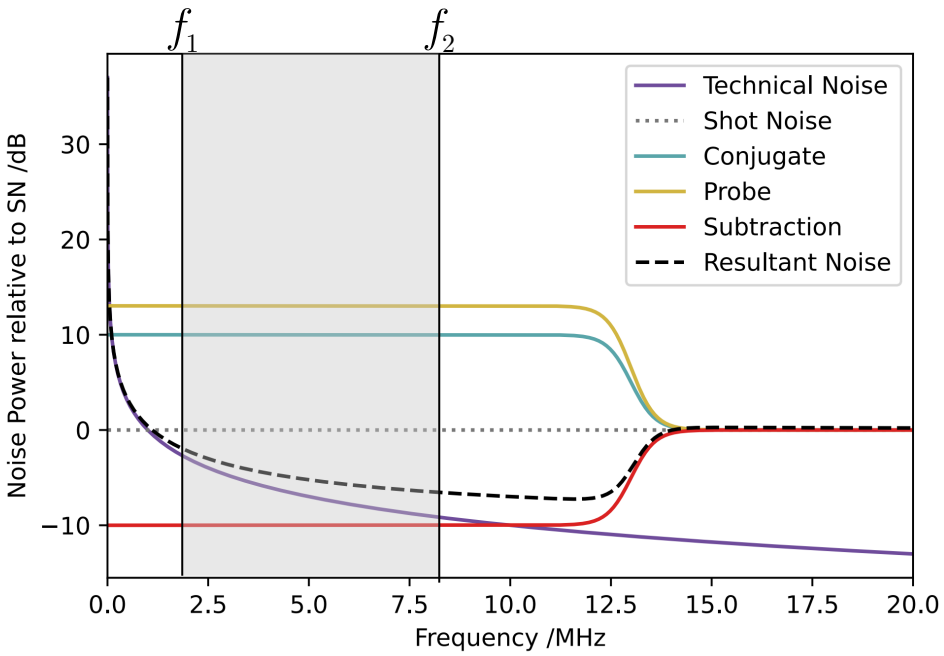

Figure 7.1 The temporal noise power present in the squeezed light. The shaded area between f_1 and f_2 represents the temporal frequencies which are averaged over when capturing an image with the camera.

This increases the value of f_1 and therefore reduces the amount of classical noise which is included in measurement. To facilitate this we use a special kinetic mode of the camera, which provides a workaround for the relatively slow readout time typical of CCDs by capturing several images before readout occurs. The camera shutter opens and a 64*1024 strip of pixels is exposed to one pulse of light, the collected photoelectrons are shifted down by 64 rows, creating a new slice of 64*1024 pixels which are again exposed to another pulse of light. This is repeated until 16 strips are captured, giving a full 1024*1024 images. The camera shutter is then closed, after which the pixel counts are read off one by one. This has the added benefit of allowing the readout to be done by one pixel, which reduces electronic noise added by the readout. As a result, the noise introduced to the images by the camera itself is not the dominant source of noise and does not impact the results.

Note that the duration of the pulse of light determines f_2, the upper limit in the frequency fluctuations we are sensitive to and must be chosen to lie in the squeezing bandwidth.

The camera takes approximately 3.2 µs to shift one row of pixels, and the shift time between images being captured is 196 µs. Each image is exposed for a total of 10 µs, of which the probe seed is on for 1 µs. The difference in these two values is due to the time take for the gain of the 4WM to reach its maximum, and will be discussed later. By contrast the camera's mechanical shutter takes 8 ms to open and the same again to close, meaning we get a significant reduction in the time between images being captured by using the kinetic mode compared to using a traditional shutter based camera. To capture a frame of 16 images takes a total of 19.2 ms, most of which is the time for the shutter to open and close. The reading off of the pixels takes on the order of seconds, depending whether the fast or slow readout mode of the camera is being used. The slow readout mode has the advantage of less digitisation noise in the pixels, meaning a lower electronic noise floor on the signal. The digitisation noise in slow readout mode is 3 counts per pixel. However, this increases the time between frames being taken. This generally is not a problem for us as we do not compare take the variance across slices from different frames. The counts due to dark current are negligible as the camera is cooled to $-70°$C.

In order to avoid blurring of the images as the pixels are shifted on the camera the beams are pulsed such that they are on only when the pixels are stationary. This pulsing is achieved using AOMs with an RF supply controlled by a trigger from the camera such that the beam is on the camera only when the pixels are stationary. This is also how the frequency difference between the probe and pump is achieved as the frequency of the first order beam is shifted by the twice the frequency of the RF signal.

7.1 Technical Limitations

Any source of loss will introduce Poissonian noise into the system which makes correlations hard to detect. Additionally, any additional light incident on the camera will pollute the images with uncorrelated photons and mask the correlations. It is essential to optimise the

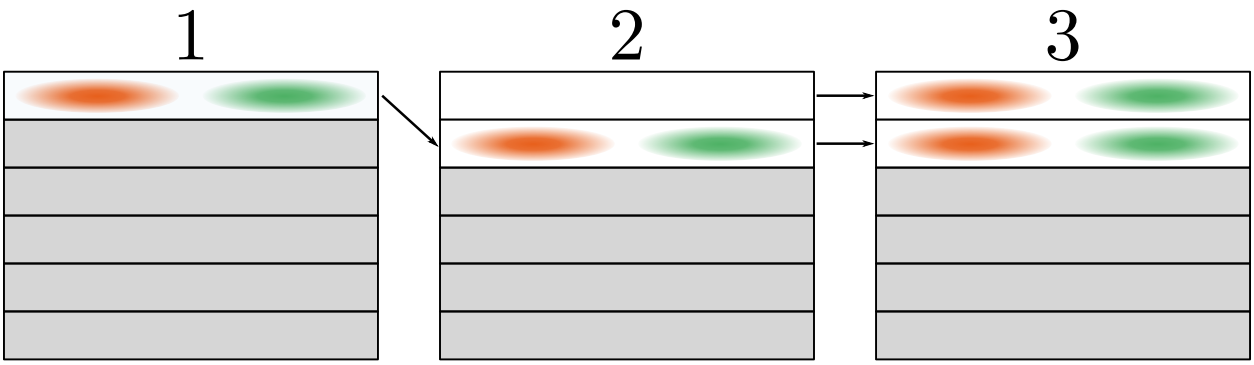

Figure 7.2 The camera CCD is divided into 16 slices (not all shown). After the shutter is opened the pump and probe seed beam are pulsed on and an image of the beams is captured on the top slice (1). The whole CCD screen, including the image of the beams, in then shifted down by 64 pixels to create a new clean slice (2), moving the image down in the process. This is done using the specialised 'kinetic mode' function of the camera. The probe seed and pump are then pulsed on again, exactly as in (1), and an image is captured on the second slice (3). This process is repeated until 16 images have been captured, then the shutter is closed and all pixel values are read by a single 'read-out' pixel.

experimental setup to counteract this as much as possible.

7.1.1 Imaging the Beams

The NF image of the beams inside the cell is captured on the camera using the imaging system shown in figure 5.11 and is comprised of the 5 lenses following the rubidium vapour cell. The first pair of lenses forms a 4f imaging system, with the split mirrors in the FF imaging plane of the cell to allow the optical paths of the probe and conjugate to be displaced slightly from one another. This means the beams are spatially separated in the NF image which is then formed. A pair of cylindrical lenses is then used to image the vertical profile of the beams on the camera, while a single cylindrical lens is used to image the horizontal. This imaging system is carefully aligned using a resolution target to ensure the NF imaging plane of the cell lies on the camera and the hence the correlations are in corresponding regions of the probe and conjugate. The split mirrors can be used to control the positions of the probe

and conjugate beams independently and allows their relative positions on the camera to be easily fine tuned while the experiment is underway.

The relatively large focal lengths on the order of 1 metre used for these lenses allows sufficient separation between the probe and conjugate the pump to be cleanly blocked, however this also reduces the numerical aperture of the imaging system. As mentioned previously, since the higher order spatial modes diverge more quickly the light from these modes is lost if the numerical aperture is not high enough (i.e. for a given focal length if the lenses are not sufficiently large). This leads to the squeezing in higher order spatial modes being significantly reduced, or lost entirely. Large lenses and mirrors (2 inch diameter) are used throughout the imaging system to ensure the numerical aperture is not the limiting factor in our ability to observe spatial correlations in the beams.

7.1.2 Pump Noise

The pump beam power incident on the cell is around 1.5 W; far higher than the probe and conjugate, which are each typically less that 1 mW. Therefore the pump must be cleanly blocked before the camera as in the near field imaging plane it will be on top of the probe and conjugate. While blocking in the far field is the best solution, it is still not perfect: the beams are not perfectly collimated, and as mentioned previously high order spatial modes are comprised of a range of k-vectors, so blocking the pump will almost inevitably also block some light from the probe and conjugate. As correlations in the far field are symmetric, and the pump is in the centre of the probe and conjugate, the ideal case would result in correlated pairs from the probe and conjugate being blocked. The pump block is wedged to limit diffraction effects, however some light is still scattered by the block.

Pump Fluorescence

The pump beam causes some fluorescence from the cell which is emitted in all directions. The fluorescent light which propagates along the same beam path as the probe and conjugate cannot be easily filtered as it is too similar in frequency to the probe and conjugate. Therefore much of this reaches the camera. One might expect from equation 5.6 that the 4WM process should be tuned to give the highest gain in order to optimise the measured squeezing. However, the laser frequency which gives the highest 4WM gain also gives relatively high fluorescence, and this must be taken into account when choosing the optimum frequency for generating squeezed light. Therefore the frequency of the laser is tuned to give the best squeezing rather than the highest gain. In addition to this, the time for which the pump beam is on is kept to a minimum by pulsing it in time with the camera capturing images.

Pulse Optimisation

As mentioned previously in section 5.2, there is a finite time after the pump beam is switched on during which a coherence is established between the relevant ground states of the rubidium atoms, during which the gain of the probe increases to a maximum. As explained previously, maximising the gain for a given amount of fluorescence is desirable as this limits the effect of the noise on the probe seed beam, so the pump is switched on before the probe to allow this coherence to be established. Then, the probe is pulsed on for just long enough that the camera pixels' counts end up just below saturation. Then both beams are switched off while the camera shifts the rows of pixels down to avoid any blurring of the images. This process is controlled by a TTL signal from the camera, and is illustrated in figure 7.3.

7.1.3 Classical Intensity Fluctuations

While using the kinetic mode helps to reduce some of the slower classical fluctuations in the laser, the process is still very sensitive to technical noise, including noise added by the

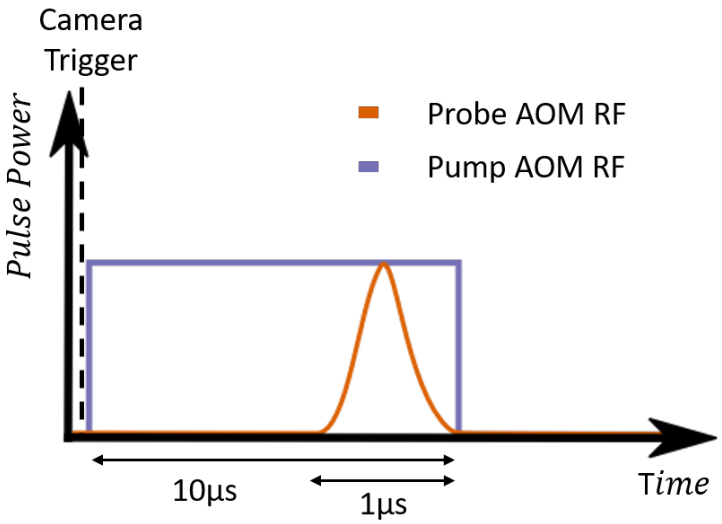

Figure 7.3 An illustration of the duration for which the pump and probe are on whilst a single image is taken using the camera. A TTL signal from the camera is sent to the pump and probe switches. The pump is switched on immediately for a duration of $10\mu s$. The probe RF signal is put through a mixer operated as a variable RF attenuator to create a smooth Gaussian pulse lasting $1\mu s$, chosen to ensure the probe pulse does not contain frequencies higher than the squeezing bandwidth. Both are then switched off whilst the camera shifts the rows of pixels until the next TTL signal from the camera initiates the process again.

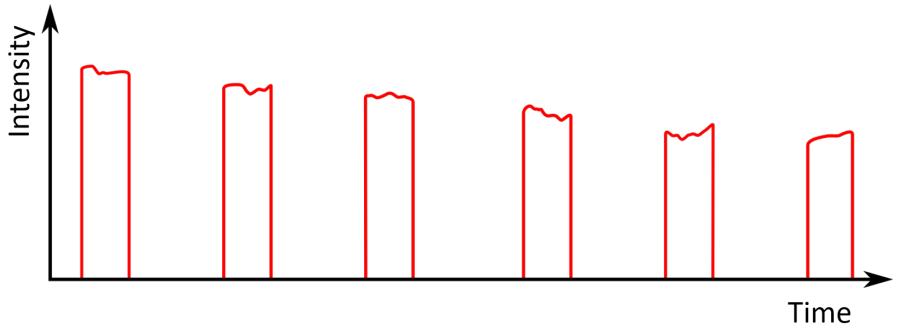

Figure 7.4 If the intensity of the main beam drifts over time, then pulses derived from this beam will have a variance in their intensity which can be much greater than shot noise. The effect has been exaggerated here for clarity.

AOMs. If the intensity of the laser drifts during the span of a single frame of data being taken, the intensity of the light in each pulse will be different, as illustrated in Figure 7.4. This causes fluctuations between the images taken by the camera that are greater than shot noise, and this masks the squeezing. Note that fluctuations which happen within a pulse are averaged over, which reduces their impact.

To quantify the proportion of noise added to the pump and probe beams by their AOMs compared to the noise on the main laser, the optical power in the pump, probe and main laser was monitored by taking a pickoff from each beam and monitoring it on a photodiode. This was done whilst the probe and pump beams were pulsed in sets of 16 pulses, emulating the camera setup depicted in figure 7.3. The pump pulse was high for 10 µs and the probe was high for 1 µs in the same time frame. The sets of 16 pulses were captured using an oscilloscope by triggering off each successive pulse. The average power in each pulse and the laser power in that time frame were measured. This was repeated for multiple sets of 16 pulses, where each pulse represents a slice and a set of 16 pulses represents a frame. Finally the pump and probe powers were each plotted against the corresponding laser power for each slice and across multiple frames. The resulting plots are shown in figure 7.5.

The strong correlation between both the pump and probe powers and the corresponding laser pickoff suggests that the main source of noise is due to intensity fluctuations on the laser

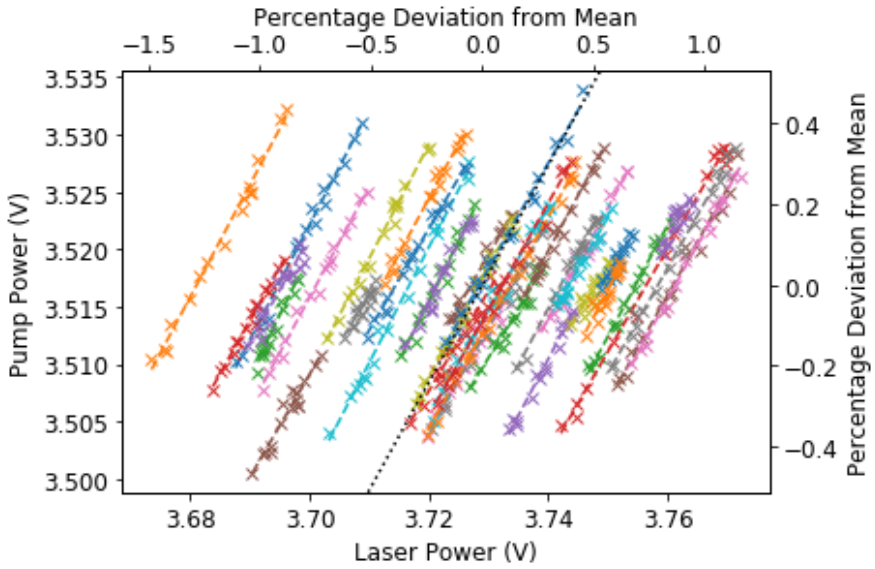

(a) Pump beam results.

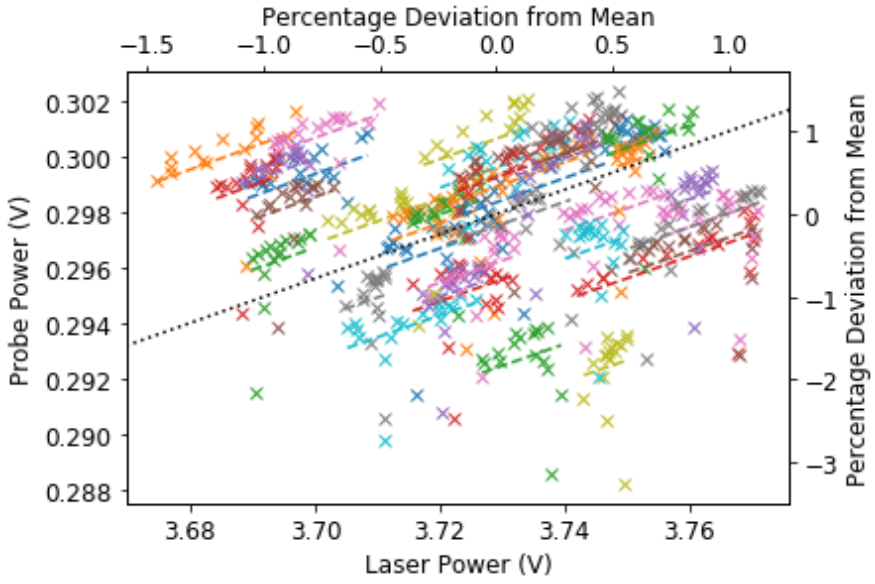

(b) Probe beam results.

Figure 7.5 The power of the probe and pump beams plotted against the power of the laser pickoff for multiple sets of 16 pulses emulating the behaviour of the camera. The 'power' in a given pulse is given by an average taken over a short period of time during the pulse. Each different colour represents a 'frame' and each point is a 'slice'.

power. The x displacement of points between the different frames is likely to do with the way we measured the main beam power: we used a stray reflection off one of the components, so it is possible that something caused the power in the reflection to change in a way that was not representative of the power in the main beam. Note we are only interested in the noise within a frame as we do not compare images taken in different frames, so any fluctuations on this timescale (i.e. the difference between different coloured lines) do not concern us. It simply shows the relatively poor long time stability of the intensity.

To obtain a quantitative measure of the noise remaining if the fluctuations on the main laser beam were removed, the proportion of the intensity fluctuations due to the laser were calculated and compared to those introduced by other sources. If all noise on the pump and probe beams was due to the fluctuations on the laser pickoff, the powers of the pump and probe pickoffs would be perfectly linearly correlated with the laser pickoff power. This is not the case, but by looking at the variance in the residuals from a y=mx fit to each frame of data we can estimate the noise which would remain if all fluctuations due on the main laser beam were removed. These values are given in Table 7.1. For the pump beam in particular, the fluctuations in the residuals are a factor of 6.5 smaller than those in the power. This suggests that reducing the fluctuations in the main beam should result in a significant reduction in the fluctuations on the pump beam. For the probe beam the power fluctuations and fluctuations in the residuals are similar, suggesting the intensity fluctuations measured on the probe beam are predominantly due to the AOM rather than intensity fluctuations on the main beam. Based on these results we decided to implement a noise eater into the system, the results of which are introduced in Section 7.2.

7.2 Noise Eater

In order to reduce the intensity fluctuation on the main laser beam a noise eater was introduced. This consists of an AOM with a pickoff from the first order beam to monitor the

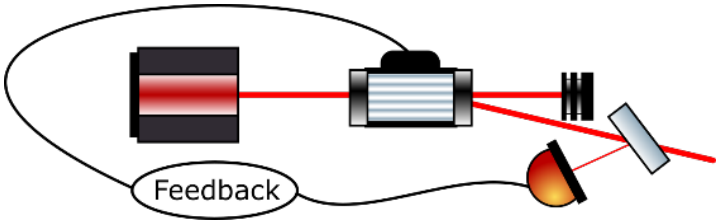

Figure 7.6 An optical diagram of the noise eater showing the pickoff of the deflected (first order) beam .

beam intensity. The remainder of the first order is the output. This RF power to the AOM is controlled via the PID loop supplied with this pickoff so it can correct for any fluctuations in the intensity of the light by altering the RF power. The AOM's RF power is set such that the efficiency of the noise eater is just below maximum, so it is possible to alter the optical power in the first order beam by altering the RF power. This process is illustrated in figure 7.6.

There are two main disadvantages of the noise eater: the first is that power is lost both in the AOM not being 100% efficient and in having to take the pickoff of the beam, and the second is that if the bandwidth is too high noise is added at high frequencies which would otherwise be shot noise limited. To mitigate the first issue the pickoff is kept small, and is taken from a portion of the beam which was previously discarded anyway. The second issue is more difficult: when we take a pickoff of the main beam there are shot noise level fluctuations in the pickoff which are uncorrelated with the main beam and are due to the random selection process of the beam splitter[77]. This can be thought of as mixing vacuum fluctuations with pickoff from the empty port of the beam splitter. The noise eater will try to correct for these fluctuations as though they were in the main beam, meaning it will write noise onto the beam at a level greater than shot noise. Therefore at higher frequencies, where we would otherwise be shot noise limited, the noise eater actually increases the noise present in the main beam. We can compensate for this by limiting the bandwidth of the noise eater. Additionally, using a larger proportion of the beam as the pickoff to monitor the power helps minimise the noise added, to the extent that if 100% of the optical beam was to be used

in the feedback loop the intensity fluctuations of the in-loop light would be sub-Poissonian. This concept of the in-loop optical beam being squeezed by the addition of an electronic feedback loop controlling the intensity has been explored by Tuabman et.al.[78], however it is impossible to extract the light from the loop while retaining its sub-Poissonian nature.

7.2.1 Noise Eater Performance Analysis

To measure the effectiveness of the noise eater at reducing technical intensity fluctuations, the process described in Section 7.1.3 was repeated both with the noise eater lock off and with it on. As we have introduced another AOM into the setup, we would expect the classical fluctuations to be a little worse with the lock off. The results are shown in figure 7.7, with the scales set so they are matched for the lock-on and lock-off cases. It can easily be seen that the fluctuations in the laser pickoff have been reduced quite substantially, and are far less correlated with the pump and probe pickoff intensities in the locked cases, suggesting the feedback loop is operating well and any remaining fluctuations in the pump and probe cannot be attributed to laser pickoff fluctuations. We can quantify the performance of the noise eater by again looking at the variance in the power of the pump and probe beams and the variance of the residuals of the linear fit, as described previously in Section 7.1.3, and comparing them for the case where the noise eater is switched on and switched off. The standard deviations are given in Table 7.1.

	Power Standard Deviation			Residuals Standard Deviation		
	No Lock	Lock Off	Lock On	No Lock	Lock Off	Lock On
Pump	0.13%	0.15%	0.07%	0.02%	0.06%	0.06%
Probe	0.46%	0.14%	0.05%	0.44%	0.04%	0.04%

Table 7.1 A table of the standard deviation on the power of the probe and pump as a percentage of the mean power in the beam, and of the residuals of the $y = mx$ fit between the laser pickoff power and each of the probe and pump powers. 'No lock' is before the noise eater was implemented in the experiment, 'lock on' and 'lock off' are with the noise eater in place with the feedback switched on and off respectively.

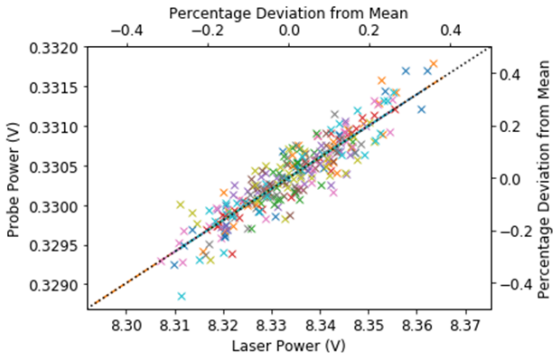

(a) The relationship between the probe power and the main beam power, noise eater lock off.

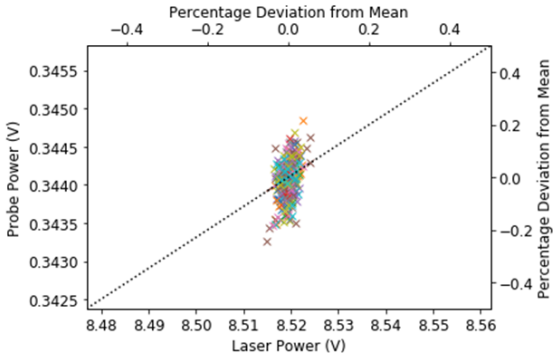

(b) The relationship between probe power and laser pickoff power, noise eater lock on.

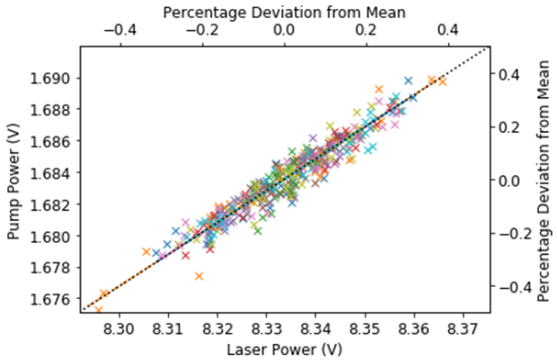

(c) The relationship between pump power and laser pickoff power, noise eater lock off.

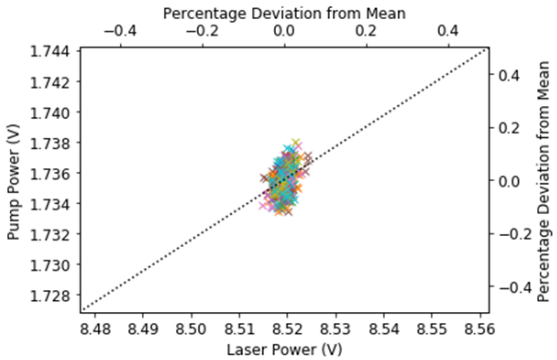

(d) The relationship between pump power and laser pickoff power, noise eater lock on.

Figure 7.7 Plots showing the relationship between the pump and laser pickoff powers and the probe and laser pickoff powers with the noise eater switched off and on. Each colour represent a different 'frame', i.e. a set of 16 pulses, while each cross represents a 'slice', i.e. a single pulse. Note the average power in each frame has been normalised as we are not converned with fluctuations between frames.

There is clearly an improvement when the noise eater is switched on compared to when it is off, and it can be seen that the standard deviation of the power is almost equal to that of the residuals when the noise eater is switched on. This suggests the noise eater is performing almost optimally, and any remaining variance in the probe and conjugate intensities can be attributed to sources other than fluctuations on the laser pickoff, such as the AOM. Therefore it is not necessary to manipulate the bandwidth of the noise eater to avoid writing excess noise onto the signal at high frequencies.

There is a rather significant difference, particularly for the probe beam, in the standard deviation of the power and residuals when the noise eater was not in place compared to when it was implemented. The addition of the noise eater to the setup involved realigning the vast majority of the optics, so this inconsistency between the probe and pump behavior when the noise eater was added could suggest the alignment of the AOMs may significantly impact the noise on the beams.

Currently, the noise eater feedback loop uses a standard PID lockbox. To improve the performance of the noise eater, a specialised PID circuit has been designed to have an improved noise performance and a bandwidth which can be limited to avoid writing additional noise onto the light at high frequencies. It will also be capable of locking the noise eater and optimising the lock parameters automatically, which should help ensure a more consistent day-to-day performance. This has not yet been implemented into the experiment.

7.3 Fourier Analysis of Beam Fluctuations

From the camera we obtain a set of near field images of the probe and conjugate in the cell, displaced slightly such that they are positioned adjacent to one another, such as those shown in figure 7.8. Of the 16 'slices' captured by the camera, only the centre 12 are used. The first two images have a high variance in the difference between the probe and conjugate counts relative to the others due to the AOMs establishing a thermal equilibrium, while the final

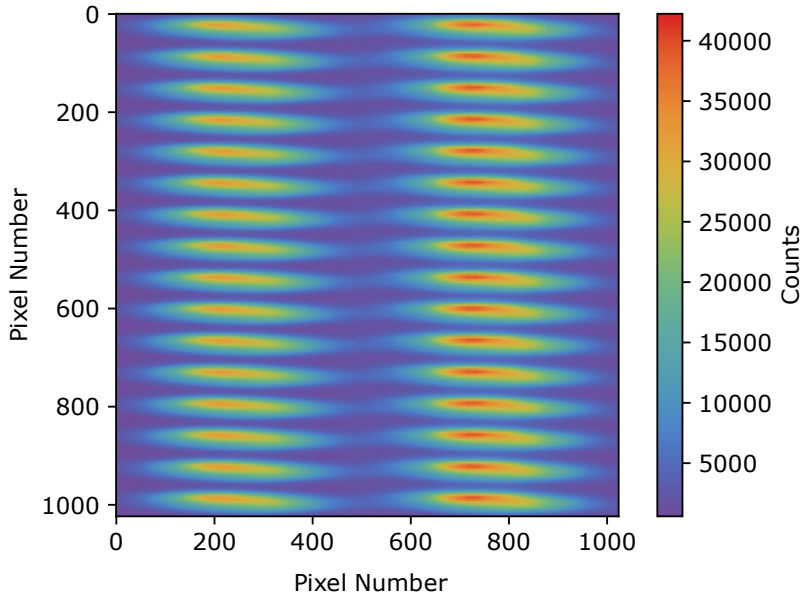

Figure 7.8 A typical 'frame' captured by the camera of the probe and conjugate beams, with the first and last two 'slices' removed. Here the probe beam is on the right side and is brighter than the conjugate.

two images are close to the beam path while the shutter is closed and are therefore exposed to background noise for the longest. This leads to an increased variance in these slices which makes it difficult to see squeezing above shot noise.

We analyse the spatial characteristics of the beam fluctuations using Fourier analysis. This examines the variance of the power in each of the spatial frequencies in the image. In principle this allows the spatial squeezing bandwidth, and by extension the coherence area, to be deduced. The whole image is used to determine the noise at each spatial frequency, which is good from the perspective of averaging over a larger quantity of data but has the disadvantage that the edges of the images where background noise dominates and the beam is very weak pollutes the data. This is evident from figure 7.9, where it can be seen that the noise power relative to shot noise is significantly higher around the edges of the beam.

The process of the Fourier analysis is outlined in figure 7.10. The result of the analysis is a plot of the noise power present in each spatial frequency. When using the full range of

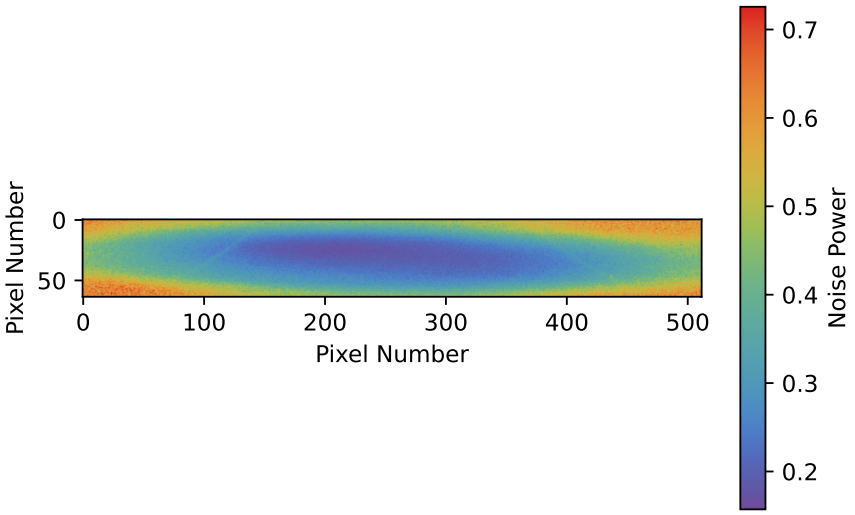

Figure 7.9 The variance in each slice across a frame of data captured by the camera, not including the first or last 2 slices to be captured, normalised to the mean power in each pixel.

spatial frequencies available from the data, at very high frequencies the noise drops below the shot noise limit. This is caused by a small leakage between adjacent pixels on the CCD: the counts in one pixel can 'bloom' out into other pixels, creating correlations between adjacent pixel counts which looks like squeezing. We therefore restrict the analysis to much lower frequencies where we expect squeezing to be seen.

Figure 7.11 shows the 1D noise spectrum averaged over many frames of images. In addition to the intensity difference noise (subtraction), this plot also shows the noise on each beam individually and on the intensity sum (addition). At low frequencies classical noise dominates, however the noise on the intensity difference is clearly lower than on the beams individually or on the intensity sum, which indicates a significant proportion of the low frequency intensity fluctuations are common to both beams and are removed by the subtraction. The intensity difference noise dips below shot noise for only one point, and only slightly, despite the BPD indicating approximately 5 dB squeezing. This occurs at a very

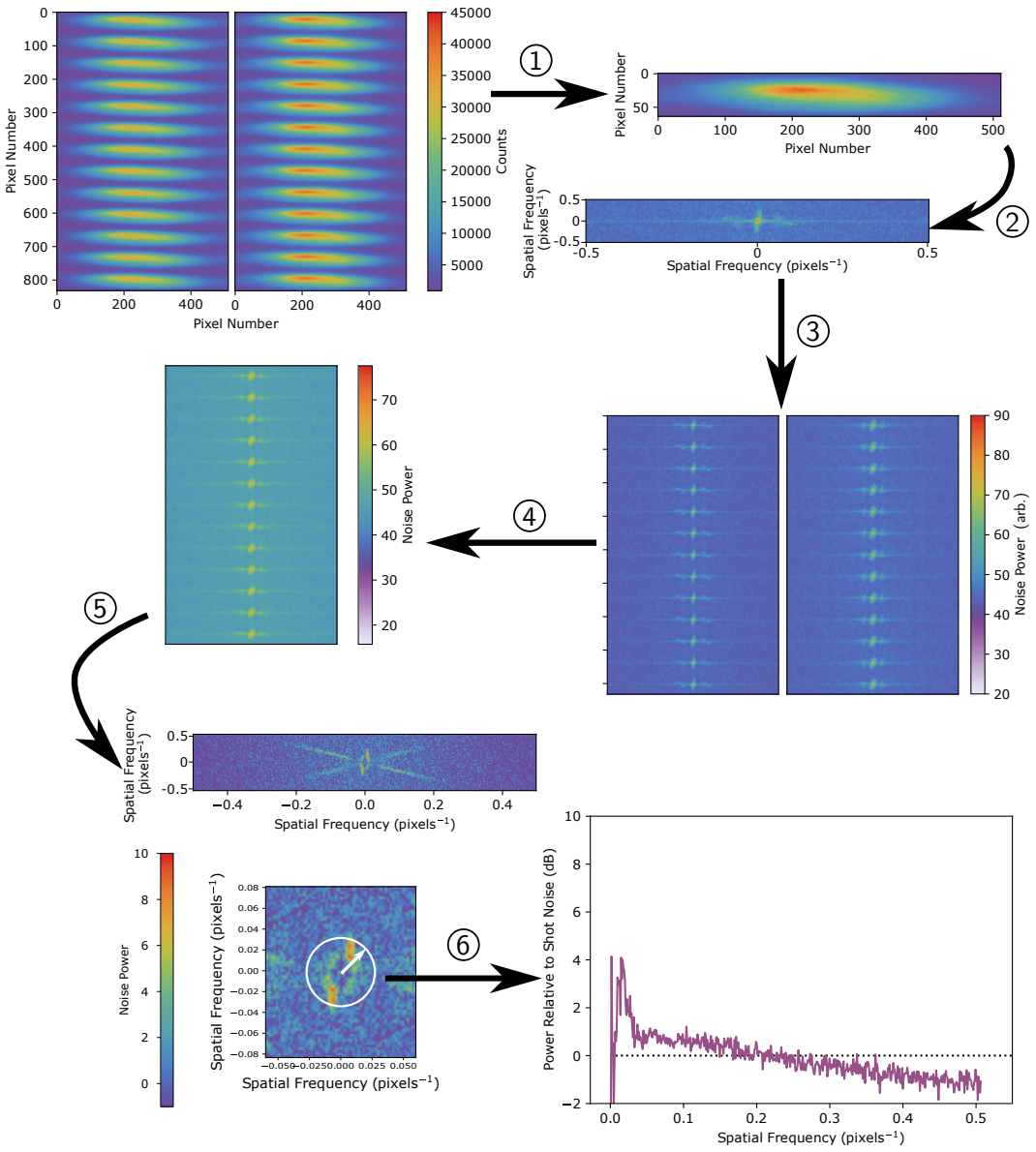

Figure 7.10 A step-by-step illustration of the Fourier analysis. (1) A frame of images is taken and divided into 24 separate beam images: 12 of each beam. (2) The Fourier transform of an image is taken. (3) This is repeated for all 24 images. (4) The probe and conjugate images in Fourier space are subtracted from one another. (5) The variance across the 12 slices in Fourier space is taken, giving a 2D map of the variance which is the size of a single slice. (6) An average is taken over all points in the Fourier space variance map which correspond to the same frequency, giving a 1D plot of the noise present in each spatial frequency in the beam.

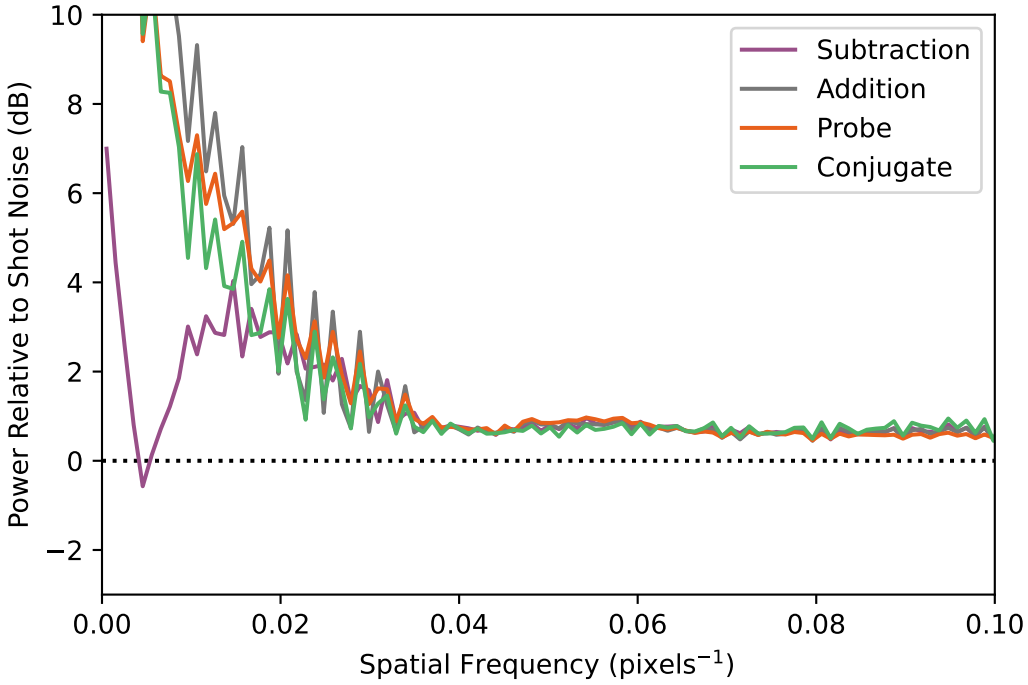

Figure 7.11 The noise present at each spatial frequency of the images of the probe and conjugate beams captured by the camera, restricted to low spatial frequencies where we expect to see squeezing. Note the spatial frequency is in units of inverse pixels in the x direction.

low spatial frequency before the noise increases again, peaking at a spatial frequency just below 0.02pixels^{-1}.

If we were seeing the limit of the squeezing bandwidth we would expect to see the intensity difference noise dip below 0 dB before increasing again to the shot noise limit, but not to go above shot noise again. This behaviour suggests the presence of correlations which are correlated at low spatial frequencies but then become anti correlated at higher spatial frequencies, driving the noise above the shot noise limit in this region. One possible explanation is misalignment of the beams: at low spatial frequencies a small misalignment doesn't significantly affect the results because on average the region we are examining is aligned correctly, however at higher analysing frequencies the region we are examining is far smaller and the misalignment is more significant. However, the 'bump' seen in the noise profile seems quite resilient to the alignment of the beams, and the 2D noise profile suggests something more complex may be occurring. Where a misalignment would cause 'lobes' of noise around DC in the spatial noise profile, which are seen in figure 7.10, there is also a ring of noise which appears which cannot be explained by a simple misalignment. This ring appears at the same spatial frequencies as the noise bump in the 1D profile. Therefore, we have reason to suspect a more complex misalignment or distortion of the beams is impacting the results. This suspicion is what lead me to investigate the spatial correlations generated in the 4WM process further. A more careful investigation of how the 4WM process works, and more specifically how the beams propagate through the cell, is the topic of the next few chapters.

Chapter Eight

Spatial Propagation Model

It is common to consider a thin gain medium when considering 4WM, thus avoiding any issues to do with the transverse displacement of the beams as they propagate through the gain medium. We took one step away from this when discussing coherence areas, however this did not address the full impact of the finite length of the gain medium on the beam as a whole. Alternately, when modelling 4WM the beams are often considered to be co-propagating. However, in reality there is a small angle between them - a requirement to ensure phase matching of the probe, conjugate and pump. This angle is a potential source of this additional noise. Since the probe and conjugate are both capable of seeding the 4WM process, one would expect their transverse profiles to overlap as they pass through the cell. The effect would be for the two beams to be 'locked together' in any transverse movement. This is reminiscent of the temporal 'locking together' of the probe and the conjugate, as described by Boyer et.al.[79], in which a pulsed probe seed incident on a Rb85 vapor cell pumped by a strong pump beam generates probe-conjugate pairs via 4WM. There is a delay between the conjugate and probe pulses emerging from the cell, with the conjugate emerging first due to having a higher group velocity in the medium. One may expect this delay to increase as cell length increases, with the distance travelled by probe and conjugate also increasing, however the results show that after a certain effective cell length, corresponding to a 4WM gain of 1, the probe and conjugate become 'locked together' and the differential

delay does not increase any more. We suspect a similar effect to occur spatially, with the probe and conjugate beams being spatially 'locked together' as they propagated through the cell.

This chapter will investigate this matched propagation and the distortion it causes in the NF images of the beams. First, I developed a theoretical model for beam propagation which used propagation equations obtained via the method used by Turnbull et al. [53] but with a few modifications to correctly account for transverse motion of the beams. This allows for the angle between the probe and conjugate to be accounted for when modelling the position of the beams as they propagate through the 4WM medium. I then used this model to simulate the 4WM process, then verified it experimentally by designing an experiment to measure the displacement between the probe and conjugate at the output of the cell.

We will first detail the first step of developing a model of the beams as they pass through the gain medium. This model will aim to approximate the position of the probe and conjugate beams on the output face of the rubidium cell for a range of experimental parameters. The model will then be verified experimentally where possible.

8.1 Propagation Equations

The computational model will use the propagation equations, which give the transverse profiles of the probe or conjugate beams after passing through Rb vapor for a certain distance.

The first step is to consider the wave equation for an electric field of mode n, $\underline{E}_n(\underline{r},t)$, in a non-linear medium:

$$\nabla^2\underline{E}_n(\underline{r},t) - \frac{1}{c^2}\frac{\partial^2\underline{E}_n(\underline{r},t)}{\partial t^2} = \frac{1}{\epsilon_0 c^2}\frac{\partial^2\underline{P}_n(\underline{r},t)}{\partial t^2}, \tag{8.1}$$

where $\underline{P}_n$ is the full polarisation of mode n, including the linear part, c is the speed of light and ϵ_0 is the vacuum permittivity. We consider the beam to be propagating in the z direction, with a small angle between the probe seed and pump beams in the transverse

x direction, as is the case in our experimental setup described in chapter 5. Since we are interested primarily in the behaviour induced by this angle we shall ignore the y direction. This means we assume there for be no angle between the probe and pump beam in the y-direction. Therefore $\underline{r} = a\hat{\underline{x}} + b\hat{\underline{z}}$.

Since $\underline{E}_n(\underline{r},t) = \underline{E}_n(\underline{r})e^{i\underline{k}_n\cdot\underline{r}}e^{i\omega_n t}$, where ω_n is the optical frequency and $|k|_n = {}^{\omega_n}/_c$ is the wave vector of mode n, defined in vacuum, we may write the wave equation in an altered form which we shall eventually solve in reciprocal space:

$$\nabla^2 E_n(\underline{r},t) + \frac{\omega_n^2}{c^2}E_n(\underline{r},t) = \frac{1}{\epsilon_0 c^2}\frac{\partial^2 P_n(\underline{r},t)}{\partial t^2}. \tag{8.2}$$

The vector notation for $\underline{E}$ has been dropped because fields we are considering are each of one linear polarisation, with the probe and conjugate being the same and the pump being orthogonal.

Next, we can move the x-dependence into the envelope by letting $E_n(\underline{r})e^{i\underline{k}_n\cdot\underline{r}} = \varepsilon_n(x,z)e^{ik_n z}$:

$$\frac{\partial^2\varepsilon_n(x,z)}{\partial x^2} + 2ik_n\frac{\partial\varepsilon_n(x,z)}{\partial z} = \frac{1}{\epsilon_0 c^2}\frac{\partial^2 P(\underline{r},t)}{\partial t^2}e^{-ik_n z}e^{-i\omega_n t}. \tag{8.3}$$

We now consider the polarisation of the non-linear media. From [53], the polarisation for the probe and conjugate beams can be expressed as

$$P_p(\underline{r},t) = \epsilon_0\chi_{pp}\varepsilon_p(\underline{r})e^{\underline{k}_p\cdot\underline{r}}e^{i\omega_p t} + \epsilon_0\chi_{pc}\varepsilon_c^*(\underline{r})e^{i(2\underline{k}_0-\underline{k}_c)\cdot\underline{r}}e^{i(2\omega_0-\omega_c)t}, \tag{8.4}$$

$$P_c(\underline{r},t) = \epsilon_0\chi_{cc}\varepsilon_c(\underline{r})e^{\underline{k}_c\cdot\underline{r}}e^{i\omega_c t} + \epsilon_0\chi_{cp}\varepsilon_p^*(\underline{r})e^{i(2\underline{k}_0-\underline{k}_p)\cdot\underline{r}}e^{i(2\omega_0-\omega_p)t}, \tag{8.5}$$

where χ_{pp} and χ_{cc} are the direct susceptibilities of the probe and conjugate respectively, χ_{cp} and χ_{pc} are the cross susceptibilities and the subscripts 0, p and c indicate a property of the pump, probe and conjugate beam respectively. Note that these are subtly different to the linear and third-order susceptibilities as their dependence on the pump field is to all orders. This level of accuracy is necessary as the 4WM transition is resonant, especially

when compared to similar schemes such as parametric down conversion, which means the higher order terms in the pump power are still significant.

Rearranging the form of the electric field in the same way as used for equation 8.3 and noting that $2k_0 - k_p = k_c$, we obtain

$$P_p(\underline{r},t) = \left(\epsilon_0\chi_{pp}\varepsilon_p(x,z)e^{ik_pz} + \epsilon_0\chi_{pc}\varepsilon_c^*(x,z)e^{ik_pz}\right)e^{i\omega_pt} \tag{8.6}$$

$$P_c(\underline{r},t) = \left(\epsilon_0\chi_{cc}\varepsilon_c(x,z)e^{ik_cz} + \epsilon_0\chi_{cp}\varepsilon_p^*(x,z)e^{ik_cz}\right)e^{i\omega_ct}. \tag{8.7}$$

Substituting equations 8.6 and 8.7 into equation 8.3 we obtain wave equations for the probe and the conjugate

$$\frac{\partial^2\varepsilon_p(x,z)}{\partial x^2} + 2ik_p\frac{\partial\varepsilon_p(x,z)}{\partial z} = -k_p^2\chi_{pp}\varepsilon_p(x,z) - k_p^2\chi_{pc}\varepsilon_c^*(x,z) \tag{8.8}$$

$$\frac{\partial^2\varepsilon_c^*(x,z)}{\partial x^2} - 2ik_c\frac{\partial\varepsilon_c^*(x,z)}{\partial z} = -k_c^2\chi_{cc}^*\varepsilon_c^*(x,z) - k_c^2\chi_{cp}^*\varepsilon_p(x,z) \tag{8.9}$$

which we now must solve to find their propagation equations.

The first step is to transform to Fourier space to allow us to deal with the x-derivative. The transform for the probe is straightforward:

$$\rightarrow \quad \varepsilon_p(x,z) = \int_{-\infty}^{\infty}\tilde{\varepsilon}_p(k_x,z)e^{ik_xx}dk_x \tag{8.10}$$

For the conjugate we must taken the complex conjugate of the Fourier transform, as this is used in equation 8.9:

$$\begin{aligned}
\varepsilon_c(x,z) &= \int_{-\infty}^{\infty}\tilde{\varepsilon}_c(k_x,z)e^{ik_xx}dk_x, \\
\varepsilon_c^*(x,z) &= \int_{-\infty}^{\infty}\tilde{\varepsilon}_c^*(k_x,z)e^{-ik_xx}dk_x, \\
\rightarrow\ \varepsilon_c^*(x,z) &= \int_{-\infty}^{\infty}\tilde{\varepsilon}_c^*(-k_x,z)e^{ik_xx}dk_x.
\end{aligned} \tag{8.11}$$

Therefore, equations 8.8 and 8.9 become

$$-k_x^2\tilde{\varepsilon}_p(k_x,z)+2ik_p\frac{\partial\tilde{\varepsilon}_p(k_x,z)}{\partial z}=-k_p^2\chi_{pp}\tilde{\varepsilon}_p(k_x,z)-k_p^2\chi_{pc}\tilde{\varepsilon}_c^*(-k_x,z), \tag{8.12}$$

$$-k_x^2\tilde{\varepsilon}_c^*(-k_x,z)-2ik_c\frac{\partial\tilde{\varepsilon}_c(-k_x,z)}{\partial z}=-k_c^2\chi_{cc}^*\tilde{\varepsilon}_c^*(-k_x,z)-k_c^2\chi_{cp}^*\tilde{\varepsilon}_p(k_x,z). \tag{8.13}$$

Next, we introduce some shortened notation (temporarily dropping the (k_x,z) and $(-k_x,z)$ for convenience):

$$\frac{\partial\tilde{\varepsilon}_p}{\partial z}=(-\Delta k+a_{pp})\tilde{\varepsilon}_p+a_{pc}\tilde{\varepsilon}_c^* \tag{8.14}$$

$$\frac{\partial\tilde{\varepsilon}_c^*}{\partial z}=(\Delta k-a_{cc})\tilde{\varepsilon}_c^*-a_{cp}\tilde{\varepsilon}_p, \tag{8.15}$$

where $a_{pp}=\frac{ik_p}{2}\chi_{pp}$, $a_pc=\frac{ik_p}{2}\chi_{pc}$, $a_{cc}=\frac{ik_c}{2}\chi_{cc}^*$, $a_cp=\frac{ik_c}{2}\chi_{cp}^*$ and $\Delta k=\frac{ik_x^2}{2k_p}=\frac{ik_x^2}{2k_c}$.

These linear differential equations with constant coefficients can be written as a matrix of the form $\underline{X}^{'}=\mathbf{M}\underline{X}$:

$$\begin{pmatrix}\partial\tilde{\varepsilon}_p/\partial z\\ \partial\tilde{\varepsilon}_c^*/\partial z\end{pmatrix}=\begin{pmatrix}-\Delta k+a_{pp} & a_{pc}\\ -a_{cp} & \Delta k-a_{cc}\end{pmatrix}\begin{pmatrix}\tilde{\varepsilon}_p\\ \tilde{\varepsilon}_c^*\end{pmatrix} \tag{8.16}$$

We seek a solution of the form $\underline{X}=\underline{C}e^{\lambda z}$. When substituted into the form of equation 8.16 this gives $\lambda\underline{C}e^{\lambda z}=\mathbf{M}\underline{C}e^{\lambda z}$. Non-trivial solutions to this equation will have the form $\det\{\mathbf{M}-\lambda\mathbf{I}\}=0$.

Therefore, we find the determinant of $\mathbf{M}-\lambda\mathbf{I}$, as given in equation 8.16, by first writing

$$\begin{aligned}\begin{vmatrix}-\Delta k+a_{pp}-\lambda & a_{pc}\\ -a_{cp} & \Delta k-a_{cc}-\lambda\end{vmatrix}&=-\Delta k+(a_{pp}-\lambda)(-a_{cc}+\Delta k-\lambda)+a_{cp}a_{pc}\\ &=\lambda^2+\lambda(a_{cc}-a_{pp})+\Delta k(a_{pp}+a_{cc})-a_{cc}a_{pp}-\Delta k^2,\end{aligned} \tag{8.17}$$

and then solving equation 8.17 quadratically:

$$\begin{aligned}\lambda &= \frac{1}{2}(a_{pp} - a_{cc}) \pm \sqrt{(a_{cc} - a_{pp})^2 - 4[\Delta k(a_{pp} + a_{cc}) - a_{cc}a_{pp} - \Delta k^2 + a_{cp}a_{pc}]} \\ &= \frac{1}{2}(a_{pp} - a_{cc}) \pm \frac{1}{2}\sqrt{(a_{cc} + a_{pp} - 2\Delta k_z)^2 - 4a_{cp}a_{pc}} \\ &= \delta a \pm \xi, \end{aligned} \tag{8.18}$$

where $\delta a = \frac{1}{2}(a_{pp} - a_{cc})$, $\xi = \sqrt{a^2 - a_{cp}a_{pc}}$ and $a = \frac{1}{2}(a_{cc} + a_{pp} - 2\Delta k_z)$.

Next we must find the eigenvectors for the eigenvalues given in equation 8.18. First, for $\delta a + \xi$, we find

$$(a_{pp} - \Delta k - \delta a - \xi)\tilde{\varepsilon}_p + a_{pc}\tilde{\varepsilon}_c^* = 0$$

$$\tilde{\varepsilon}_p = \frac{-a_{pc}}{-\Delta k + a_{pp} - \delta a - \xi}\tilde{\varepsilon}_c^* == A_1\tilde{\varepsilon}_c^* \tag{8.19}$$

$$v_1 = \begin{pmatrix} A_1 \\ 1 \end{pmatrix}, \tag{8.20}$$

where $A_1 = \frac{a_{pc}}{\xi - a}$.

For $\delta a - \xi$ we find

$$(a_{pp} - \Delta k - \delta a + \xi)\tilde{\varepsilon}_p + a_{pc}\tilde{\varepsilon}_c^* = 0$$

$$\tilde{\varepsilon}_p = \frac{a_{pc}}{-\Delta k + a_{pp} - \delta a + \xi}\tilde{\varepsilon}_c^* = A_2\tilde{\varepsilon}_c^* \tag{8.21}$$

$$v_2 = \begin{pmatrix} A_2 \\ 1 \end{pmatrix} \tag{8.22}$$

where $A_2 = \frac{-a_{pc}}{\xi + a}$.

Therefore, the general solution to equation 8.16 is

$$\begin{pmatrix} \tilde{\varepsilon}_p \\ \tilde{\varepsilon}_c^* \end{pmatrix} = c_1 \begin{pmatrix} A_1 \\ 1 \end{pmatrix} e^{(\delta a + \xi)z} + c_2 \begin{pmatrix} A_2 \\ 1 \end{pmatrix} e^{(\delta a - \xi)z}. \tag{8.23}$$

From this we can extract equations for $\tilde{\varepsilon}_p$ and $\tilde{\varepsilon}_c^*$:

$$\tilde{\varepsilon}_p = c_1 A_1 e^{(\delta a+\xi)z} + c_2 A_2 e^{(\delta a-\xi)z} \tag{8.24}$$

$$\tilde{\varepsilon}_c^* = c_1 e^{(\delta a+\xi)z} + c_2 e^{(\delta a-\xi)z}. \tag{8.25}$$

To deduce the values of c_1 and c_2 we must consider the initial conditions of the experiment. We will be using a seed beam, $\varepsilon_s(k_x)$ of the probe frequency, w_p, meaning at $z = 0$ the probe field is equal to the seed field and the conjugate field is zero. Applying these initial conditions gives,

$$\tilde{\varepsilon}_c^*(-k_x, 0) = c_1 + c_2 = 0 \rightarrow c_1 = -c_2 \tag{8.26}$$

$$\tilde{\varepsilon_p}(k_x, 0) = c_1(A_1 - A_2) = \tilde{\varepsilon}_s(k_x) \rightarrow c_1 = \frac{\tilde{\varepsilon}_s(k_x)}{A_1 - A_2}, \tag{8.27}$$

where we recall $\tilde{\varepsilon_c^*}$ is a function of $-k_x$ thanks to the form of the Fourier transform of the complex conjugate of $\varepsilon(x, z)$ given in equation 8.13 and equation 8.12.

We may simplify $(A_1 - A_2)$ to give

$$\begin{aligned} A_1 - A_2 &= \frac{a_{pc}}{\xi - a} + \frac{a_{pc}}{\xi + a} \\ &= \frac{2a_{pc}\xi}{\xi^2 - a^2} \\ &= \frac{2a_{pc}\xi}{-a_{cp}a_{pc}} \\ &= -\frac{2\xi}{a_{cp}}. \end{aligned} \tag{8.28}$$

Substituting this back into equations 8.27 and 8.26 we find the values of our constants to be

$$c_1 = -\frac{\varepsilon_s a_{cp}}{2\xi} \tag{8.29}$$

$$c_2 = -c_1 = \frac{\varepsilon_s a_{cp}}{2\xi}. \tag{8.30}$$

Finally, we can substitute equations 8.29 and 8.30 into the general form of the probe and conjugate fields given in equations 8.24 and 8.25:

$$\begin{aligned}
\tilde{\varepsilon}_c^* &= -\tilde{\varepsilon}_s \frac{a_{cp}}{2\xi}\left(e^{(\delta a+\xi)z} - e^{(\delta a-\xi)z}\right) \\
\tilde{\varepsilon}_c^* &= -\tilde{\varepsilon}_s e^{\delta a z}\frac{a_{cp}}{\xi}\sinh \xi z \qquad (8.31) \\
\tilde{\varepsilon}_p &= -\tilde{\varepsilon}_s \frac{a_{cp}}{2\xi}\left(\frac{a_{pc}}{\xi - a}e^{\xi z} + \frac{a_{pc}}{\xi + a}e^{-\xi z}\right)e^{\delta a z} \\
&= -\tilde{\varepsilon}_s \frac{a_{cp}}{2\xi}e^{\delta a}\left(\frac{a_{pc}(2\xi\cosh \xi z + 2a\sinh \xi z}{-a_{pc}a_{cp}}\right) \\
\tilde{\varepsilon_p} &= \tilde{\varepsilon}_s e^{\delta a}\left(\cosh \xi z + \frac{a}{\xi}\sinh \xi z\right). \qquad (8.32)
\end{aligned}$$

Therefore the final equations for the probe and conjugate fields in k-space are

$$\tilde{\varepsilon}_c^*(k_x, z) = -\tilde{\varepsilon}_s(-k_x)e^{\delta a z}\frac{a_{cp}}{\xi}\sinh \xi z \tag{8.33}$$

$$\tilde{\varepsilon}_p(k_x, z) = \tilde{\varepsilon}_s(k_x)e^{\delta a}\left(\cosh \xi z + \frac{a}{\xi}\sinh \xi z\right), \tag{8.34}$$

where we have replaced k_x with $-k_x$ in equation 8.33, and

$$\begin{aligned}
\delta a &= \frac{1}{2}(a_{pp} - a_{cc}), \\
\xi &= (a^2 - a_{cp}a_{pc})^{\frac{1}{2}}, \\
a &= \frac{1}{2}(a_{cc} + a_{pp}) - \Delta k, \\
\Delta k &= \frac{ik_x^2}{2k_p} = \frac{ik_x^2}{2k_c}, \\
a_{pp} &= \frac{ik_p}{2}\chi_{pp}, \\
a_{pc} &= \frac{ik_p}{2}\chi_{pc}, \\
a_{cp} &= \frac{ik_c}{2}\chi_{cp}^*, \\
a_{cc} &= \frac{ik_c}{2}\chi_{cc}^*.
\end{aligned}$$

These equations tell us how to propagate plane waves in k-space in the rubidium medium, giving the transverse profile of the beams after they have propagated through the medium for a distance z. Propagating the beams in reciprocal space allows us to account for different Fourier components experiencing different phase matching conditions. The profile of the beam in real space after such a propagation can then be found by taking the inverse Fourier transform. Note the probe is a proportional to $\varepsilon(k_x)$ while the conjugate is proportional to $\varepsilon(-k_x)$, which makes physical sense when one considers the beams themselves with have opposite transverse momenta.

8.1.1 Changing Parameters

We will be using the model to change the gain by changing the following parameters:

- One-photon detuning, Δ_1: controlled experimentally by changing the laser lock frequency;

- Two-Photon detuning, δ: controlled experimentally by changing the probe AOM RF signal frequency;

- Pump power, Ω: controlled experimentally by changing the pump AOM RF signal power (to allow excess power to be dumped while minimising scattered light).

Additionally the gain is affected by changing the temperature of the cell, however this is more difficult to model due to the atom density and ground state coherence both being changed simultaneously by changing temperature.

To understand how these parameters affect the gain of the 4WM process, it is helpful to first look directly at how they impact the direct and cross susceptibilities: χ_{pp}, χ_{cc}, χ_{cp} and χ_{pc}. As mentioned previously, the real components of the direct susceptibilities, χ_{pp} and χ_{cc}, are responsible for the index of refraction while the imaginary component controls the absorption. Similarly, the real components of the cross susceptibilities, χ_{pc} and χ_{cp}, control the gain of the 4WM while the imaginary components contribute to the de-phasing of the beams should the phase matching condition not be met. We assume the phase matching to be well met and refraction to have minimal impact due to the index being very small and the beams being very close to normal, therefore absorption and gain are the most relevant quantities to us.

We shall first investigate the effect of two-photon detuning. The susceptibilities controlling the absorption and the gain are plotted in figure 8.1 for the approximate experimental parameters typically used to optimise squeezing, with the two-photon detuning varied, for both the probe and the conjugate in figure 8.1. The first thing to note is that the resonance, indicated by a very high absorption, is not at a two-photon detuning of zero. This is due to the significant light shift induced by the strong pump beam causing the energy levels in the dressed atom to be shifted from their bare positions. Changing Ω shifts the resonance feature towards zero when decreased and further from zero when increased. Linked to this is the effect of the one-photon detuning: a greater one-photon detuning moves the resonance

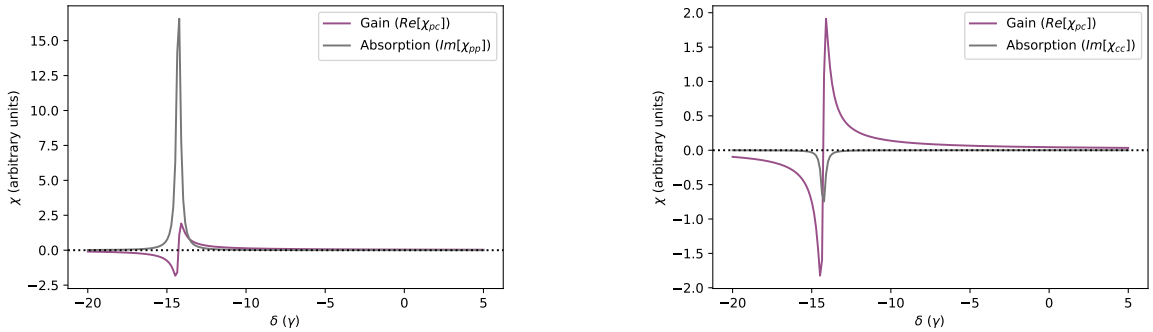

(a) Probe **(b)** Conjugate

Figure 8.1 The modelled real and imaginary components of the cross and direct susceptibilities respectively, plotted with respect to changing two-photon detuning, δ. Note that while the units of χ are arbitrary, they are the same between the probe and conjugate plots.

closer to zero. This is effectively equivalent to decreasing the pump power, as it reduces the light shift experienced by the atom since the pump beam inducing the shift is further from resonance. Note the absorption parameter of the probe beam is far higher than that of the conjugate, by around a factor of 10. For this reason, we assume absorption of the conjugate beam to be negligible. Finally, we see the absorption feature is far larger than the gain feature. This is why it is generally better to be away from resonance when choosing parameters to optimise squeezing.

Figure 8.2 shows a zoomed in version of figure 8.1a, and illustrates the effect of the ground state decoherence, γ_c, on the susceptibilities. It can be seen that a larger decoherence value causes broadening of the resonance and decreasing the maximum gain. As a result it is necessary to operate quite far from the resonance where absorption has almost dropped to zero if we wish to see good squeezing. Typically a two-photon detuning of around 1 to 2γ, where $\gamma = 2\pi \times 5.75\,\text{MHz}$[67] is the natural linewidth of the rubidium 85 D1 transition, is found to give optimum squeezing.

Realistically, it is very difficult to know the value of the ground state decoherence we have experimentally. However, based on Turnbull et.al. [53] we may assume it lies between

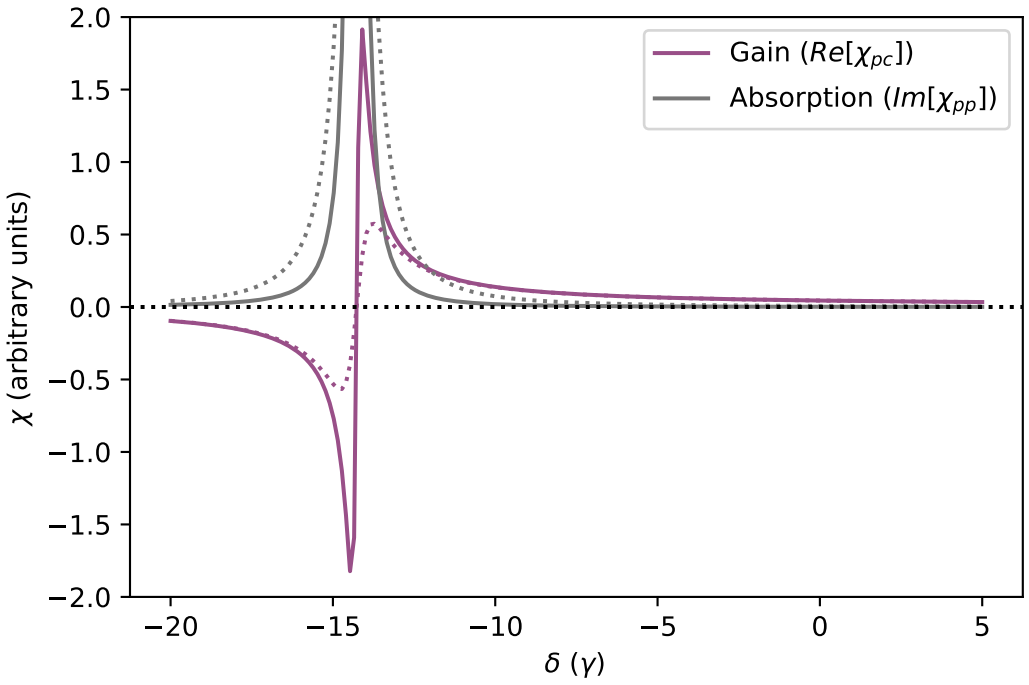

Figure 8.2 The modelled real and imaginary components of the cross and direct susceptibilities respectively, plotted with respect to changing two-photon detuning, δ. The solid lines are with a ground state decoherence of $\gamma_c = 0.1\gamma$, whereas the dashed lines are with a decoherence of $\gamma_c = \gamma$.

the two values used in figure 8.2.

8.2 Modelling the Propagation of the Beams

In order to determine the transverse profiles of the beams as they pass through the cell, equations 8.34 and 8.33 were used to model the profiles after various propagation distances, z by taking the Fourier transform of equation 8.34 and equation 8.33. This was done for a range of experimental parameters. Since experimentally we can only measure the profiles of the beams on the output of the cell, the focus of the simulation results will mostly be on the beam profiles at this point as it is comparable to experimental data.

8.2.1 Setup

There is a high degree of complexity in the model in that equations 8.34 and 8.33 contain many variables, many of which affect the beam profiles dramatically. To make the model more manageable and make it easier to study the impact of experimental parameters on the matched propagation effect we are studying we have assumed the pump beam to be of constant intensity, meaning it is not depleted as it passes through the gain medium. This is a reasonable assumption for the majority of the cases we will look at as the pump beam is significantly more intense than any of the other beams, making its depletion from the 4WM process negligible. We will also model the pump beam as a plane wave. While experimentally this is not accurate, it will help understand the impact of altering different experimental parameters individually without always having the impact of varied pump power present. It also means non-linear effects such as cross-Kerr lensing are not taken into account. The seed, $\varepsilon_s(k)$, will be modelled as a Gaussian beam with a tilt applied by adding a position dependent phase in the x direction. The equation used to generate the seed beam for the probe in real space is given by

$$\varepsilon_s(x) = \exp\left\{-\left(\frac{x^2}{2 * \sigma^2} - ix\alpha\right)\right\}. \tag{8.35}$$

To ensure the seed waist is in the centre of the cell both the x- and z-direction this is then back-propagated by half the cell length. The result is used as the seed in equation 8.34.

8.2.2 Deciding Parameters

The parameters used in the model, given in table 8.1, were chosen to be as close to those used experimentally as possible. They were determined as follows:

Density The atom density in the cell is dependent on the temperature of the coldest point of the cell. The cell used was a standard cylindrical vapour cell which was heated.

It was wrapped in aluminium foil to help retain heat and stabilise the temperature, with a 'cold finger' left exposed in the centre of the cell to ensure the rubidium condensed away from the end windows. There was a large experimental error associated with measuring the temperature of this cold point with a probe, as it was difficult to access due to the foil and also hard to secure the temperature probe. Additionally, the temperature is very sensitive to fluctuations in the temperature of the lab itself over a long period of time. The value given in table 8.1 is based on a temperature range of approximately $100\,^{\circ}\mathrm{C} - 110\,^{\circ}\mathrm{C}$, and is taken from Wolfram[80].

Cell Length The cell length is one of the most well defined parameters. It's important to consider that for the purpose of this particular set of measurements a longer cell than usual was used: 20 mm as opposed to the usual 12.5 mm to maximise the impact of the matched propagation on the probe and conjugate beam and therefore make it easier to measure experimentally.

Pump Power (Ω) The pump power as used in the simulation is expressed as a resonant Rabi frequency. This is calculated using the definition of the Rabi frequency:

$$\Omega_{ij} = \frac{d_{ij} \cdot E_0}{\hbar}, \tag{8.36}$$

where d_{ij} is the dipole matrix element for the $i \rightarrow j$ transition. Since the transitions are both to far detuned virtual states, we assume the far-detuned dipole matrix element, $d_{\mathrm{det}} = 1.73 a_0 e$, as calculated by Steck [67], can be used for both and thus they both have the same resonant Rabi frequency. Uncertainties arise as to what the 'correct' value of intensity is due to the finite size of the pump beam experimentally despite it being modelled as a plane wave in addition to the uncertainties in the size and power of the pump beam. A Gaussian beam of power P has a peak intensity of

$$I_p = \frac{2P}{\pi w^2}, \tag{8.37}$$

where w is the waist of the beam. Its field is related to its intensity by

$$E = \sqrt{\frac{2I}{c\epsilon_0 n}}, \tag{8.38}$$

where we will assume the refractive index, n, to be 1 as the pump frequency is relatively far from resonance.

Equations 8.37 and 8.38 can be substituted into equation 8.36 to give

$$\omega = \frac{d_{\text{det}}}{\hbar}\sqrt{\frac{4P}{\pi w^2 c\epsilon_0}}. \tag{8.39}$$

For a power of 2 W, which is an upper limit on the experimental pump power, and a beam waist of 0.75 mm, which is an underestimate, we find an upper estimate for the Rabi frequency to be around 145γ. For a power of 1.25 W and a beam waist of 1.5 mm we find a Rabi frequency of around 60γ. Considering also the assumption that we may use the d_{det} as the dipole matrix element for both transitions we are left with a wide range of potential pump values. For simplicity, the parameter Ω will be referred to simply as pump power for future discussions.

1-Photon Detuning (Δ_1) The 1-photon detuning is controlled by altering the frequency of the main laser which is controlled via a reference cavity. Unfortunately, this is measured in terms of a voltage applied to the piezo in the cavity, meaning it is not possible to know the exact frequency of the laser itself. We expect Δ_1 to be on the order of 1 GHz; Turnbull et.al. [53] determined a value of 144γ, and so this was used as an initial estimate.

2-Photon Detuning (δ) The 2-photon detuning, δ, is controlled by the difference in the frequencies of the probe and pump beams. Both the probe and pump beams are controlled

by AOMs which shift their frequencies in opposite directions relative to that of the main laser, f_0. The probe frequency is given by

$$f_{\mathrm{pr}} = f_0 - 2\Delta f_{\mathrm{pr}}, \tag{8.40}$$

where Δf_{pr} is the RF frequency applied to the probe AOM, which is operated in double pass configuration. The pump frequency is given by

$$f_{\mathrm{pu}} = f_0 + \Delta f_{\mathrm{pu}}, \tag{8.41}$$

where Δf_{pu} is the RF frequency applied to the pump AOM, which is operated in single pass configuration.

The frequency difference between the probe and pump beams is therefore equal to equation 8.41 - equation 8.40:

$$f_{\mathrm{diff}} = \Delta f_{\mathrm{pu}} + 2\Delta f_{\mathrm{pr}}. \tag{8.42}$$

The one-photon detuning is equal to the difference between the ground state separation, $\Delta = 3.036\,\mathrm{GHz}$[67], and the frequency difference between the pump and probe beams. Therefore,

$$\delta = \Delta f_{\mathrm{pu}} + 2\Delta f_{\mathrm{pr}} - \Delta. \tag{8.43}$$

The pump AOM is fixed at a value of 80 MHz, as any change in this would deflect the beam, and the 2-photon detuning is controlled solely from the probe AOM frequency which does not suffer from the issue of the beam path being changed by altering the RF frequency thanks to the double pass configuration. Typically, the value is set to 1482 MHz, as this has been found to achieve a good level of squeezing, which gives a 2-photon detuning of 8 MHz, or about 1.4γ. This parameter is the most well know and well controlled experimental

Parameter	Symbol	Calculated Value	Comments
Density	ρ	$1\text{–}5 \times 10^{18}\,\mathrm{m}^{-3}$	Based on cell temp 100 °C–110 °C
Cell Length	L	$20 \times 10^{-3}\,\mathrm{m}$	Experimental Parameter
Dipole Matrix Element	d_{14}, d_{23}	$2.44 a_0 e$	Calculated from Steck [67]
Pump Power	Ω	60γ–145γ (varied)	Experimental Parameter
1 Photon Detuning	Δ_1	144γ (varied)	Taken from paper [53]
2 Photon Detuning	δ	1.4γ (varied)	Experimental Parameter
Ground State Decoherence	γ_c	$0.05\gamma - 0.5\gamma$	Taken from paper [53]

Table 8.1 A table showing the parameters used in the simulation, where a_0 is the Bohr Radius and e is the charge of an electron. Note the pump power is expressed as a resonant Rabi frequency.

parameter, as it can be calculated exactly from the RF frequencies applied to the AOMs which are well known.

Ground State Decoherence The ground state decoherence represents the atoms falling out of the coherent superposition they must be in for the 4WM process to occur. This is due to multiple effects such as collisions with other atoms or with the wall of the cell. It is very difficult to quantify and is largely determined based on other experimental parameters. Turnbull et.al. [53] gives an estimate of its value to be between 0.1γ and 0.5γ, although this depends on the temperature of the cell. Unfortunately, this means altering the temperature of the cell not only changes the atom density but also the ground state decoherence, making it difficult to accurately model a temperature change.

8.2.3 The Simple Case Using Typical Experimental Parameters

The computational model of the 4WM is complex and has a range of outputs. Extracting the data we need to study the matched propagation of the probe and conjugate involves several steps. Before progressing to this we shall first look at a typical set of fixed experimental parameters and discuss the outputs of the simulation. As mentioned previously, the primary focus will be on studying the transverse profiles of the beams on the output face of the cell,

as this is what we measure experimentally. However, there is also benefit to studying the propagation of the beams through the cell as determined by the model: it is interesting to see how much gain there is at each step, and also to check momentum is conserved throughout propagation through the cell. All following results will use a cell length of 20 mm and a probe-pump angle of 8 mrad unless otherwise stated. The density and ground state decoherence values have been chosen within the margins indicated in table 8.1 to give a gain close to that seen experimentally given the other values stated.

The transverse profiles of the beams as output by the model are shown in figure 8.3. The values of the detunings, δ and Δ_1, as well as the pump power, Ω, will be the most commonly varied parameters experimentally and as such are displayed on the plot. For ease of comparison it is helpful to also plot the position on the seed beam on the input face of the cell, as this is approximately where one would expect the conjugate beam to be due to the transverse momentum of the probe and conjugate being conserved. To study the matched propagation effect the relationship between beam position and gain were investigated.

In the following plots, the intensity profiles are normalised such that the peak intensity of the seed is 1. However, for future analysis it will be useful to have a single numerical value for the gain, representative of the total power in the beam rather than the power relative to the peak amplitude of the probe. This is determined by dividing the total power in the probe/conjugate by the total power in the probe seed. This method was chosen over using the maximum intensity of the beams because the distortion of the probe and conjugate that we see as they pass thought the cell leading to them often having a very different shape to the seed. This is particularly relevant in extreme cases such as when the gain is very small (<2), as the beam sometimes splits in two. An example of this is shown in figure 8.5

The centre of mass (COM) of the probe beam, which average position weighted by the intensity, is skewed somewhat from the maximum amplitude of the beam; a result of the asymmetric profile of the beam. It was chosen to use centre of mass rather than peak positions for the same reasons described above for using total power as opposed to maximum intensity.

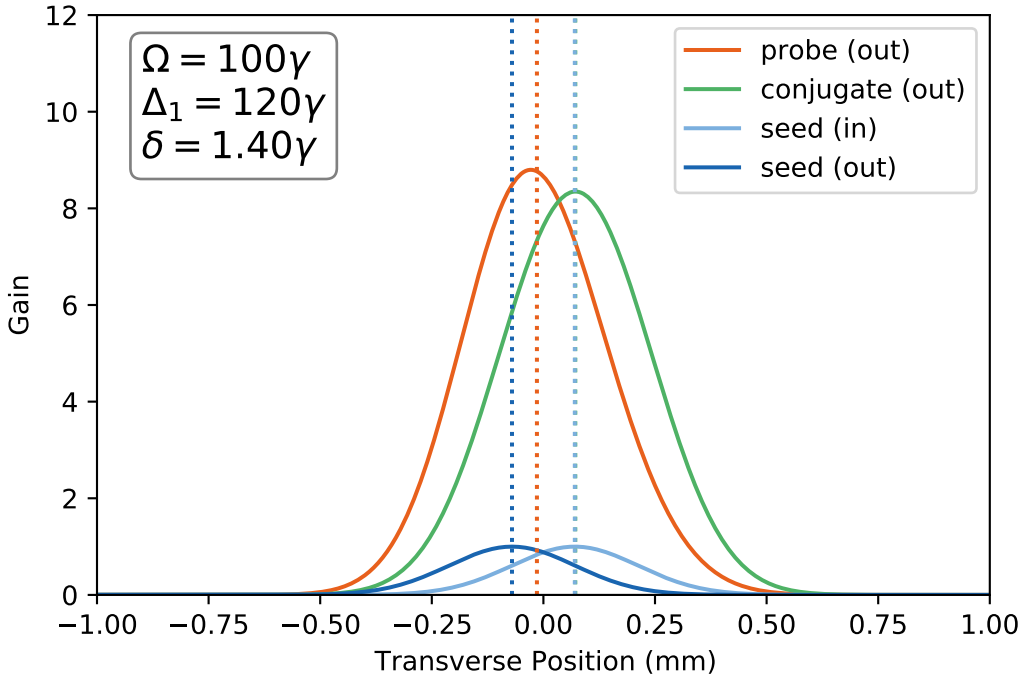

Figure 8.3 A plot showing the transverse profiles of the beams generated by the 4WM model. Whether they correspond to the input or output face of the cell is indicated in brackets. The vertical dotted lines indicate the centre of mass of the beams.

It can be seen that the conjugate centre position lies on top of the seed input position, which is what would be expected with perfect conservation of transverse momentum with no refraction or absorption. These assumptions hold well for the conjugate as it is very far from single photon resonance compared to the probe.

Figure 8.4 shows the transverse profiles of the probe and conjugate beams at various positions in the 20 cm cell, with the seed positions on the input and output face being shown for reference. While this cannot be simply replicated experimentally without changing the cell, it is still interesting to look at the behaviour of the beams as they pass through the cell. One notable feature is that the conjugate COM appears to be the same as the probe seed input position for all points in the cell, although it should be noted that it is not actually identical. Also, it appears the probe COM moves in the $-x$-direction initially before slowing

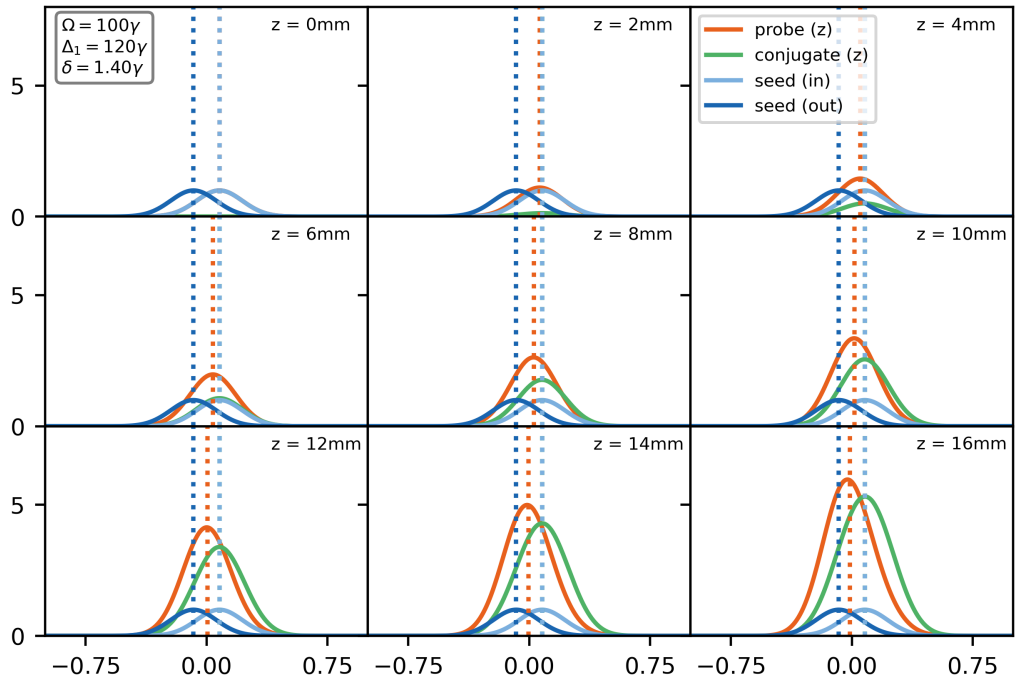

Figure 8.4 The transverse profiles of the probe and conjugate beams at multiple z positions in the cell, with the probe seed position on the input and output face of the cell for reference. The weighted mean position of each beam is indicated by a dotted line.

when the centre of the cell is reached, barely moving past the transverse centre point.

If we adjust the pump power such that the gain of the 4WM is very low, as has been done in figure 8.5, we see that in extreme cases the position of the beams can be difficult to define as they no longer retain their Gaussian shape. The conjugate beam has split in two, and the centre of mass is no longer on top of that of the probe seed input. This splitting is reminiscent of the effect seen at low probe gain in the matched pulse propagation experiment by Boyer et al. [79]. This splitting effect is never seen in figure 8.4, therefore we should not expect the relationship between gain and the COM of the beams to be independent of the variable changed to control the gain.

A more complete image of the beams' path through the cell can be plotted by modelling

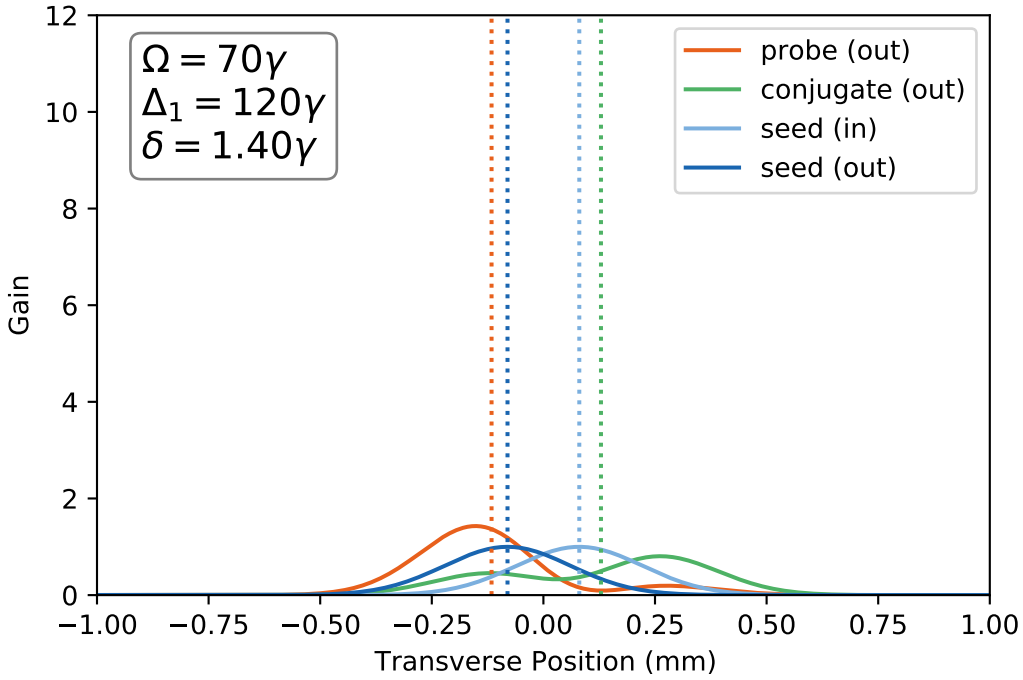

Figure 8.5 The transverse profiles with the pump power lowered in the model to give a low gain (<2). Splitting of the conjugate beam can be observed.

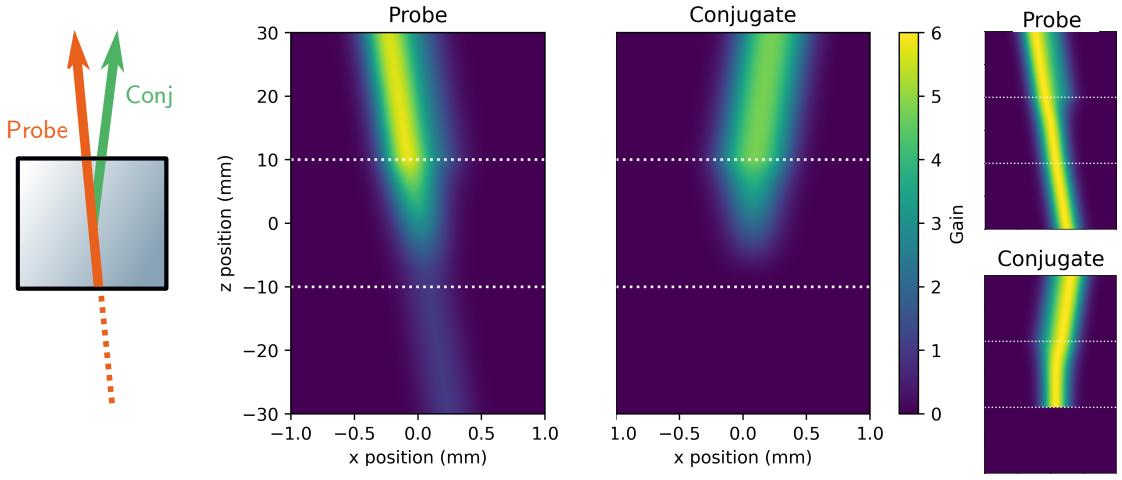

Figure 8.6 Simulation of the probe and conjugate beams passing through the rubidium cell. The 20 mm cell is in the z direction, centred at $z = 0$ with boundaries indicated by white dotted lines, and in all x. The beams propagate in the positive z direction in free space ($z < -10$), in the rubidium cell ($-10 < z < 10$) and in free space again ($10 < z$), as indicated in the schematic on the left. On the right images with the amplitude of the beams normalised for each step in z are shown to better illustrate the path of the probe and conjugate through the cell.

the transverse profiles at many z values and plotting them as a 2D image, as shown in figure 8.6. This helps emphasise that a great deal of the gain occurs in a relatively short distance at the end of the cell: to be expected from an exponential process. One can also see that the gain on the probe beam is slightly weighted to the centre x-axis of the cell - the beam becomes broadened in one direction, causing the centre of mass to move towards the centre of the cell. Also of interest is the behaviour of the conjugate through the cell and at the cell boundary: after appearing to take a relatively straight path through the cell it appears to quite dramatically change direction at the output. One might question whether momentum is conserved in the cell, as from figure 8.6 the conjugate seems to have little or no transverse momentum component in the cell. however, the path of the conjugate in free space after the cell, which is approximately symmetric about $x = 0$ to that of the probe, is indicative that the conjugate does in fact have a net transverse momentum component.

We can also calculate the net transverse momentum component numerically. This is

relatively straight forward, as propagation of the beams is already performed in k-space so we need only sum all momentum components in the beams at each stage. The net transverse momentum of a beam is given by

$$P_{\text{x}} = \sum_{k_x} k_x |E_k|^2, \tag{8.44}$$

where E_k is the transverse profile of the beam in k-space, with $k = 0$ being the transverse momentum of the plane pump wave. If momentum is conserved, we expect the net momentum of the probe and conjugate, given by

$$P_{\text{x-net}} = P_{\text{x-probe}} + P_{\text{x-conj}} - P_{\text{x-seed}} \tag{8.45}$$

to be equal to zero.

Unfortunately, calculating the momentum in the manner shown in figure 8.44 does not take into account momentum loss due to absorption. Since the absorption of the probe is far higher than that of the conjugate, this leads to a discrepancy in the net transverse momentum as output by the model. Therefore, to accurately determine whether the model conserves the transverse momentum of the beams as expected we must remove absorption from the model.

The parameter responsible for absorption in the propagation equations, equation 8.24 and equation 8.25, are the direct susceptibilities, χ_{pp} and χ_{cc} respectively. Specifically, the imaginary components of χ_{pp} and χ_{cc} control the absorption while the real components dictate the refractive index. By setting the imaginary components of the direct susceptibilities to zero the absorption is effectively 'switched off' in the model and we expect momentum to be conserved. Due to a numerical rounding error in the code we see the momentum is conserved to within 1 part in 10^{-14}. It is worth noting that the difference between the gain with and without absorption present also given an insight into the amount of absorption occurring which is difficult to obtain purely with experimental data.

Having created a model capable of mapping the gain and the transverse position of the probe and conjugate beams with respect to a variety of parameters, and checked momentum is conserved as one would expect, we will now aim to verify the model with experimental data. The model shows that the position of the COM of the beams in the cell varies with gain, and this variation differs depending on which parameter is used to control the gain. We have observed that at very low gains the transverse profiles of the beams begins to break apart. Additionally, we expect the absorption of the probe beam in particular to increase rapidly when the detunings are altered such that they they are closer to the light-shifted resonance.

Chapter Nine

Investigating the Spatial Propagation Model

Now we've established the capabilities of the model we will explore its outputs and use experimental data to verify its predictions. For our fixed length 20 mm cell, we expect to see the probe and conjugate displacements from the optical axis vary as a function of gain. The relationship between this displacement and the gain will depend on the parameter used to control the gain: either one-photon detuning, two-photon detuning or pump power.

The output of the model gives the transverse profiles of the beams at the end of the cell. These positions will be measured experimentally as a function of gain, with the gain changed by varying the parameters discussed previously in section 8.2.2. A pump beam of waist 1 mm is used. This provides a reasonably collimated beam which is required to match the plane wave pump assumption of the model. The total power in the pump beam is 1.5 W, ensuring the no depletion requirement is satisfied.

9.1 Experimental Setup

To image the probe and conjugate beams on the output face of the cell a $4f$ imaging system was used and the image was captured on a beam profiler, as illustrated in figure 9.1. To

ensure good alignment of the imaging plane, a resolution target was positioned in place of the edge of the cell and the focus of the imaging system was set using this. As the displacement of the beams we are trying to measure is very small a large numerical aperture was desirable. Therefore, the lenses were chosen such that they were as large as physically possible without capturing the pump beam deflected by the GT polariser. The first lens was chosen to have the shortest focal length which still gave a reasonable separation of the beams in the far field to allow any residual pump beam not filtered by the polariser to be physically blocked. Since the pump is approximately a plane wave in the cell, it is small in the FF and therefore should be easy to block. However, the waist of the probe beam in the cell was chosen to be small: specifically, it was chosen to represent the size of the coherence area by determining the near field beam waist which would completely occupy the range of squeezed k-vectors according to the gain seen in the far field. This meant the probe seed was large in the FF and therefore easily clipped when blocking the pump. A magnification of 4 was used to allow a greater probe power to be incident on the beam profiler before saturation occurred, minimising the impact of background noise sources such as scattered pump beam or fluorescence.

In order to avoid having to capture multiple images with different beams blocked, the probe and conjugate were spatially separated in the imaging plane by using a pair of mirrors in the FF, as shown in figure 9.1, to change their relative optical paths. This technique is the same as the one used for the camera, described in chapter 7, and allowed them both to be captured in the same image. Unfortunately, this meant the position of the beams relative to one another on the edge of the cell had to be calibrated.

9.1.1 Imaging System Calibration

Ultimately, we need a way of comparing the experimental data to that in the model. To do this, we need to identify the position of the optical axis and the seed (in) and seed (out) axes which were used in the simulation in the real data. The positions of these in the experimental

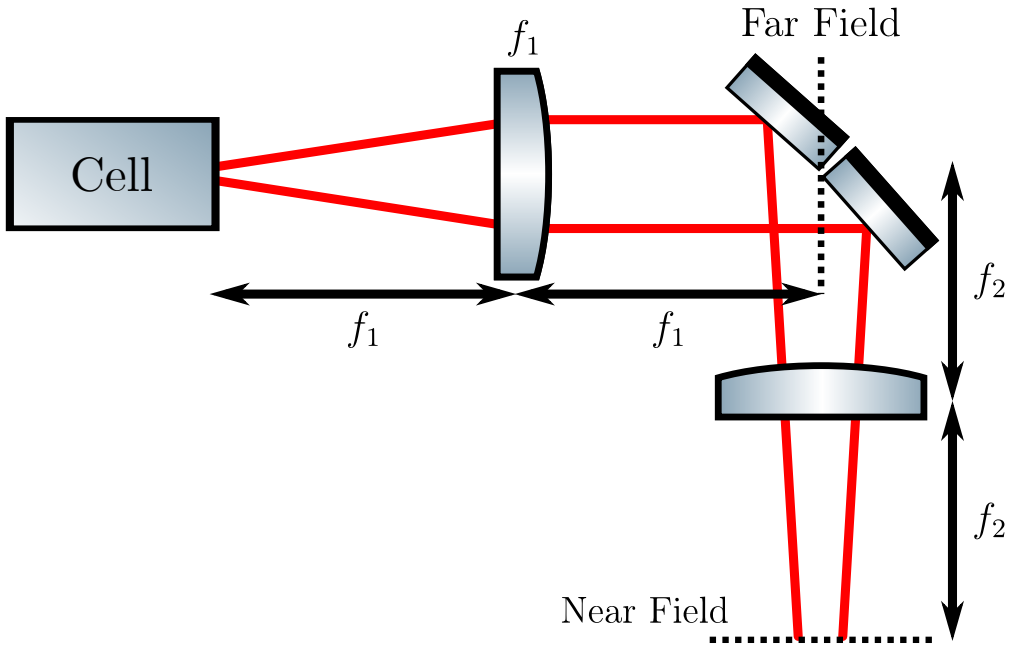

Figure 9.1 The imaging system used to capture the transverse positions of the probe and conjugate beams at the end of the cell. The pump beam was blocked in the FF, and split mirrors were used in the FF to separate the probe and conjugate NF images. A beam profiler was placed in the NF to capture the image of the beams.

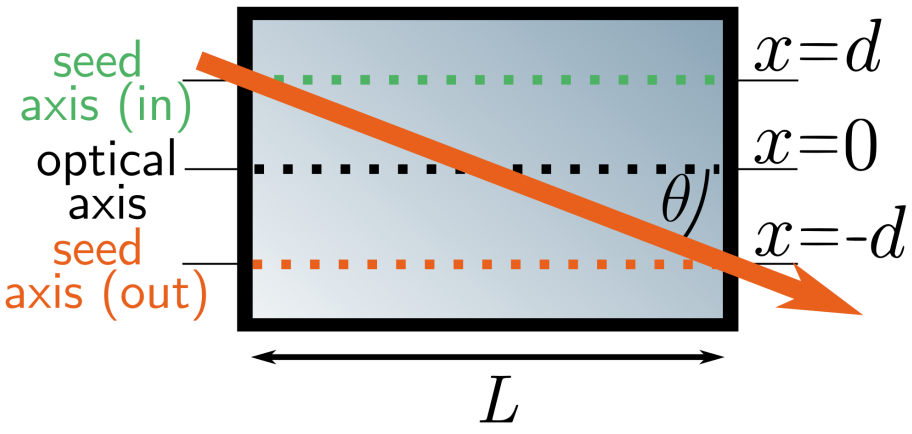

Figure 9.2 A top schematic view of the cell showing the path of the probe seed beam when far detuned (orange). The calculated displacement, d, between either seed beam and the optical axis of the pump at the end of the cell is $L\theta/2$, assuming θ to be small. Note the angle is exaggerated in this schematic.

data are illustrated in figure 9.2.

The process of determining the positions of these axes involved several steps. The COM of the probe seed beam, far detuned from resonance and with no pump beam present, is first determined to give the position of the seed (out) axis. This is defined by the transverse position of the probe seed at the z position of the output face of the cell if the cell were removed, as shown in figure 9.2. The main source of error in determining this axis was due to fluctuations in the background light which was subtracted from the image prior to the COM being determined. The optical axis on the probe image is then d away from this, as can be seen from figure 9.2.

The position of the optical axis on the probe image was determined by imaging a resolution target with the attenuated pump beam. It was first steered so that it was reflected off the mirror usually hit by the probe beam, giving the position of the resolution target through the optical path of the probe split mirror. The same was then repeated for the conjugate mirror. Each produced the same image of the resolution target on the beam profiler but displaced slightly. Determining the displacement between these two images is what provides us with the calibration to identify the position of the probe and conjugate beams relative to

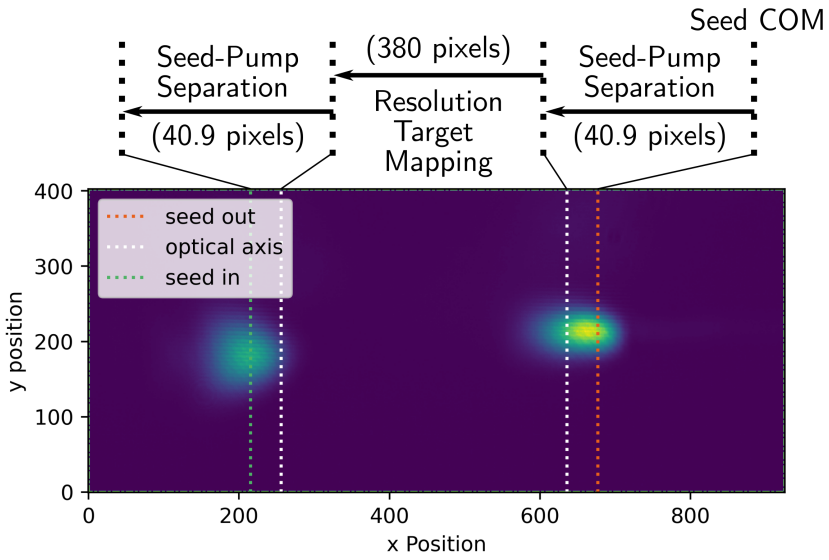

Figure 9.3 A typical image of the probe and conjugate, with lines representing the position of the optical axis and the seed position on the input and output faces of the cell, including arrows to indicate how these were calculated. Seed-Pump separation refers to the separation between the centre of the beams, where the centre of the pump is considered to be on the optical axis. Note that the seed COM was calculated from an image of just the seed beam; this image is just for reference.

one another.

After this the position of the seed (in) axis on the conjugate image was determined from the ange between the probe and pump beams. This whole process, and the positions of the various axes, is illustrated in figure 9.3.

It should be noted that it was difficult to guarantee the imaging system captured the edge of the cell precisely: it was not possible to put a resolution target on, or even close to, the end of the cell because the heating element of the cell extends past the cell wall. Instead, the cell was moved and the resolution target placed in approximately the correct position.

Figure 9.4 shows an example of the two images of the resolution target formed during the calibration, produced using an attenuated pump beam as described above. By identifying the difference between the same part of the resolution target on the two images we can determine the relative positions of the two images and how to map a known point on the

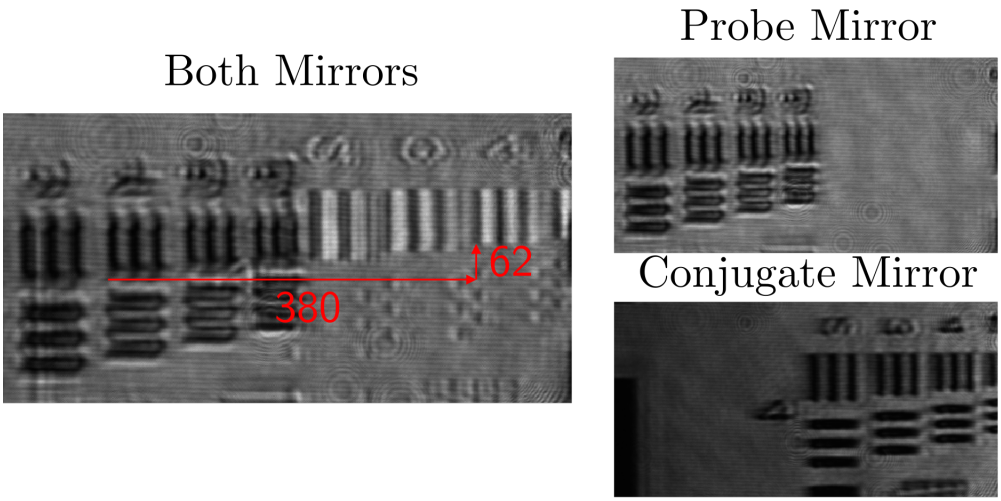

Figure 9.4 Images of the resolution target captured by reflecting the pump beam off each mirror in turn with the other mirror blocked. For 'both' the pump primarily hits the conjugate mirror, but a small amount of light still hits the probe mirror which allows a weak image to form. The arrows indicate the path to the same point on the resolution target in both images.

probe image to that same point on the conjugate. The position of the optical axis on the conjugate image was determined according to this translation. Finally, the position of the seed (in) axis was then d away from the optical axis on the conjugate image.

Unfortunately, the method described here is relatively unreliable as errors are accumulated at each stage. For the seed axis (out), the uncertainty is representative of the fluctuations in the background which is subtracted from the seed image and the impact this has on the COM position of the beam. Also, the angle between the probe and pump is difficult to measure due to the probe seed waist being small in the cell, which means that it is large in the FF, making it more difficult to accurately determine the angle. The uncertainty in the angle between the seed and pump introduces an additional source of error which is added to the error in the COM of the probe position when determining the position of the optical axis. The error in transforming the optical axis on the probe image to that on the conjugate image is considered negligible compared to the uncertainty on the angle. Unfortunately, the same uncertainty on the angle once again contributes cumulatively to the uncertainty in the position of the seed (in) axis on the conjugate image.

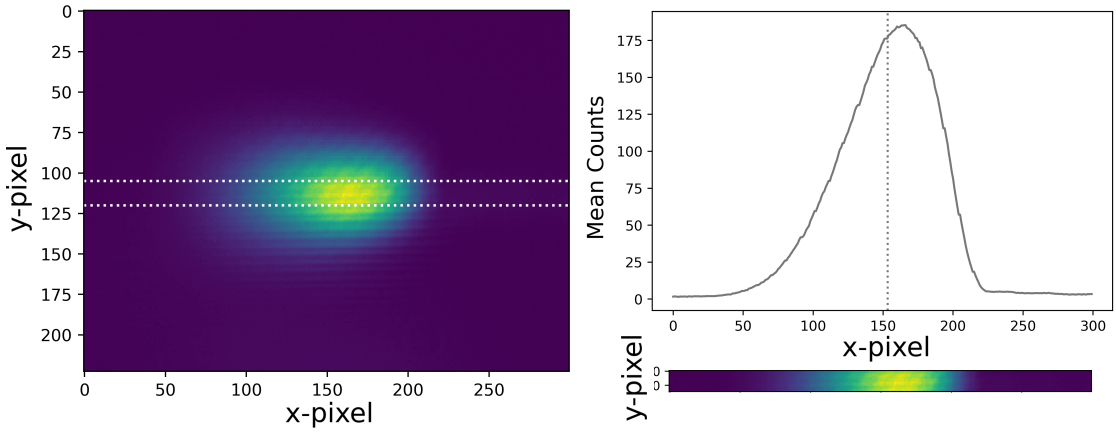

Figure 9.5 An example image of the probe beam. A horizontal slice of the beam, centred about the maximum in the vertical direction, is taken and the mean counts in the y-direction is then found to give the profile shown with COM indicated by the dotted line. The gain and horizontal position of the beam is then calculated from this profile.

The axis positions determined above will be used on the following plots showing the experimental data to help give context to the magnitude of the observed beam displacements and to allow for easier comparison to the modelled results, however an effort will be made to make the uncertainties on their exact positions clear.

9.2 Image Processing

After capturing an image of the beams, the necessary information about the beam position and power was extracted. This was done via the process illustrated in figure 9.5 which focuses here only on the probe. A horizontal strip, centred around the maximum value in the y-direction, is taken and the sum along the y-axis is taken. The x-position of the beam is determined by calculating the centre of mass of this strip. The gain of the beam is then found by first integrating the strip, which gives a value proportional to the power. For a given data set, the strip used is always the same, meaning the gain is found by taking an image of the seed beam and determining its value via this same method then dividing the two values.

9.3 Stability

Before making measurements, the stability of the setup was determined to ensure there were no drifts in the gain or displacement which could impact the measurement. Both the short-term and long-term stability were checked by capturing a series of sets of images of the probe with the experimental parameters set to those typically used for optimal squeezing. Possible sources of instability include drifts in experimental parameters, such as pump power or cell temperature, over a long period of time or movement of the beams affecting their measured position, which could occur over a shorter time frame.

The probe beam was imaged on the beam profiler, with images being captured for approximately 30 s per set, with approximately 5 minutes in between measurement sets. The power of the probe seed was also monitored during each of these sets by measuring the power in a pickoff of the seed beam, obtained using a PBS and waveplate. The results are all normalised to the seed power.

Figure 9.6 shows the displacement from the initial position with respect to gain calculated from the stability measurements, with displacement and gain determined as above. We see the position of the probe varies more than that of the conjugate. The probe positions with respect to gain also mostly follow a trend of increasing gain and decreasing displacement, which indicated a drift in an experimental parameter. However, this drift is relatively small over a period of an hour compared to that which we expect to see based on the distance between the seed (in) axis and the optical axis. The first two sets taken are slight outliers in this trend, indicating a position drift which is not dependent on gain, however this drift is still small compared to the displacements we are hoping to measure, which will be closer to 100 µm. Finally, the outlying point with very high gain present in both shots was likely due to the beam profiler over-exposing the image due to a software glitch. For the real data, multiple images will be captured for each set of parameters to ensure this can be mitigated.

Overall, the percentage variance in the gain and position of the probe and conjugate are

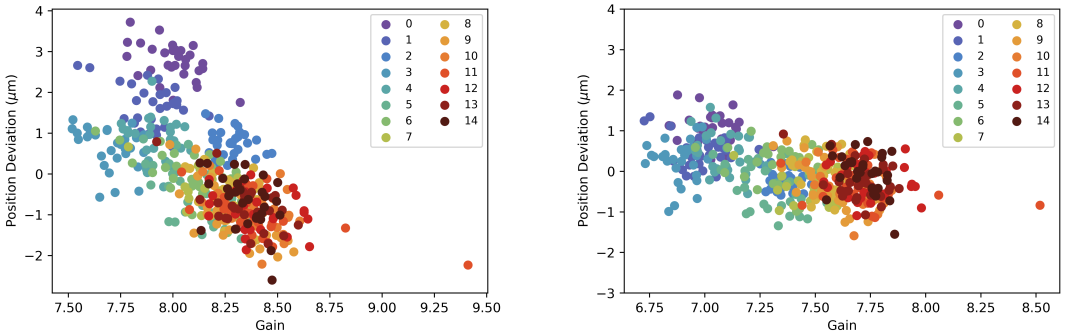

(a) Probe. **(b)** Conjugate.

Figure 9.6 The deviation from the mean position with respect to gain. Each colour represents a dataset of 30 images taken over 30 s, with each point being a single image. These datasets were taken approximately 5 minutes apart, with set 0 being captured first.

	Gain		Position	
	Set	All	Set	All
Probe	0.22%	0.74%	0.4%	2.0%
Conjugate	0.17%	1.16%	0.2%	0.5%

Table 9.1 The percentage variance of the gain and position of the probe and conjugate, calculated over the full set of data shown in figure 9.6 (All) and also as an average of the variances of each 30 s set of data. The variance of the position is expressed as a percentage of the distance between the seed (out) and optical axis, 70 μm.

mostly below 1% over the time these measurements were taken and are given in table 9.1. It is interesting to note that the fluctuations in the position of the probe within a set are twice as large as those for the conjugate, which already suggests the idea of being able to trivially correlate parts of the probe and conjugate with a simple mapping is a flawed concept.

9.4 Example Experimental Procedure

The temperature of the cell is a difficult parameter to model due to it impacting both atom density and ground state coherence simultaneously. It is also not well controlled experimentally, as it takes time for the cell temperature to stabilise and it is also difficult to measure

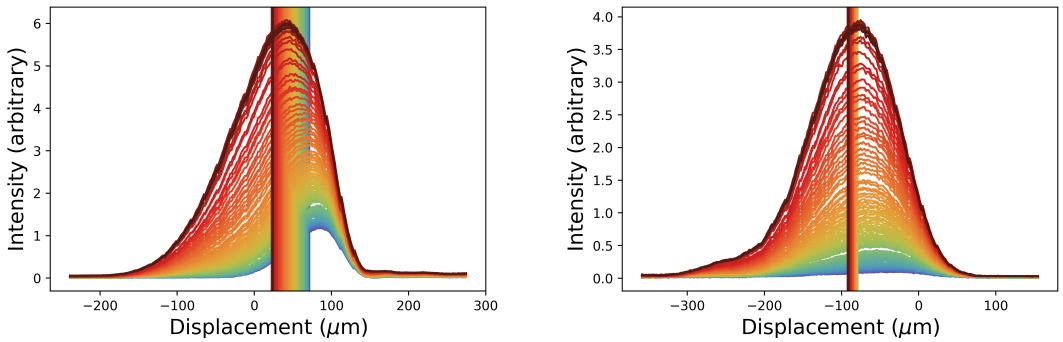

(a) Probe. **(b)** Conjugate.

Figure 9.7 The transverse profiles of the probe and conjugate beam, captured 2 s apart as the cell was allowed to cool after the heater being switched off, with red captured first and purple last. The centre of mass of each beam is also shown. At very low temperatures only the seed beam remains.

the temperature accurately. It will therefore be used as a qualitative example for how the experimental data was captured.

The camera was set to capture an image every 2 s for 240 s, with the cell heater turned off after the first couple of seconds. This creates a set of data where the temperature decreases in an uncontrolled way throughout. The transverse profiles of the beams are shown in figure 9.7. It can be seen that the probe moves significantly more than the conjugate, mirroring the observed results from the stability measurement. Also the gain on the left side of the seed beam in figure 9.7a is significantly greater than that on the right side of the beam. We see the probe pulled towards the pump axis at higher gains values.

It is helpful to look at the position of each beam with respect to the probe gain, which is shown in figure 9.8. At low gains, particularly for the conjugate, the contribution of background noise is significant and so these results are less reliable. This potentially explains why the conjugate seems to curve back on itself when the gain is small.

It is interesting that, certainly for gains greater than 2, the beams move in the same direction. This is not what one would typically expect, as conservation of transverse momentum would make one think the beams propagate through the cell in opposite transverse

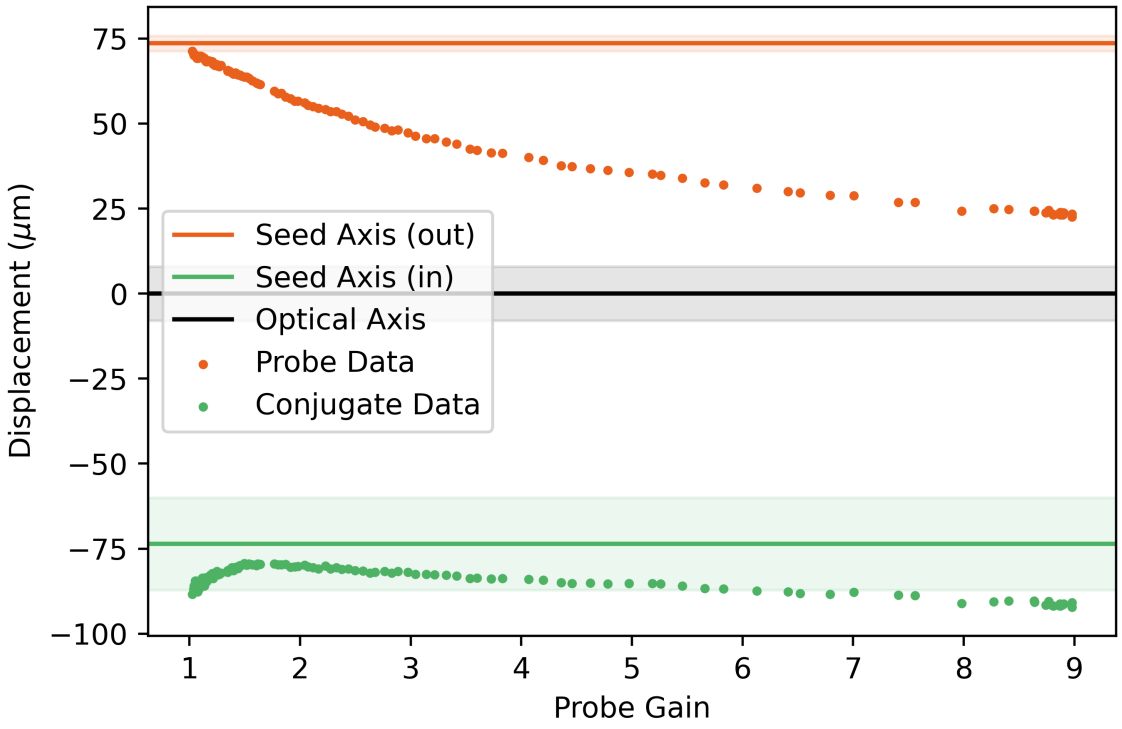

Figure 9.8 Scatter plots of the displacement of the probe and conjugate beams from the pump axis with respect to gain, taken as the cell cools down. The horizontal lines represent the positions on the end of the cell illustrated in figure 9.2, calculated as shown in figure 9.3. The shaded area around these lines indicates the uncertainty of the various axes.

directions, as they do in free space, and therefore their displacements would be approximately symmetric about the optical axis. However, this behaviour is similar to that seen in the simulation, where we can computationally verify that when absorption is 'switched off' the transverse momentum of the beams is still conserved. It should also be noted that the shapes of the beams are distorted compared to that of the seed: the gain is certainly not uniform across the transverse profile of the beam. This non-uniform gain profile, combined with absorption, is the primary driver of the movement of the COM of the beams as opposed to a straightforward translation of a Gaussian profile.

9.5 Parameter investigations

Having used the somewhat qualitative example of changing temperature to establish how the experimental results are analysed, we will now use a range of other parameters to vary the gain and compare these to the computational model discussed previously in chapter 8.

As with the model, the gain can be changed experimentally by several parameters:

One-photon detuning, Δ_1: this is adjusted via changing the laser frequency. While this is controlled precisely, it is hard to determine an absolute value for the wavelength of the light which is consistent between experimental sessions, and is likely to change dramatically during the course of the experimental run if the laser falls out of lock. Additionally, it is difficult to guarantee that each step of adjustment on the laser control corresponds to an equal step in beam frequency. Furthermore, altering the one-photon detuning slightly alters the power of the beams. All measurements where one-photon detuning is altered were taken over a single session, and the detuning was measured relatively rather than absolutely.

Two-Photon detuning, δ: this is controlled via the frequency of the probe AOM, and is stable and well defined. As the two-photon detuning is already quite close to resonance, the results of changing it can be quite dramatic. Also, changing the RF signal frequency will alter the efficiency of the probe AOM, meaning the power of the probe seed will be altered.

Pump power, Ω: This is relatively straight forward to control by adjusting the RF power input to the pump AOM, allowing it to be controlled independently of the probe and without adding excess noise as the high power portion of the beam is blocked a comfortable distance from the post cell imaging system.

The investigations will primarily focus on the position of the probe beam, as at low powers it becomes very difficult to accurately determine the position of the conjugate. Furthermore, the uncertainty on the position of the seed axis (in) makes it difficult to match the conjugate's experimental absolute position to the computational model, whereas knowing the position of the seed axis (out) makes this far easier for the probe beam.

9.5.1 Varied Pump Power

The pump power was varied by changing the RF power supplied to the pump AOM. An image of the probe and conjugate was captured for each pump power and the horizontal position of the beams were determined by calculating the COM position of the beam, as with the temperature example. The gain was determined by integrating the total powe over the transverse profile of the beam. The resulting displacement plot is shown in figure 9.9. Note the pump power was not varied linearly for the whole range of values - as it was controlled by an AOM there was a middle-region where the power change was linear but around the saturation and minimum RF power the change in pump power was much smaller per step, which is why the points at the highest and lowest gains are closer together.

Broadly speaking, the probe beam behaves as it did for gain controlled by temperature: the position of the probe beam gets closer to the optical axis for higher gains. Unfortunately, the gain achieved in this particular data set is not as high as for the temperature data set (this is simply due to another parameter not being tuned quite optimally), however we still see the position starting to level out at higher gains as it did in figure 9.8. We see that the

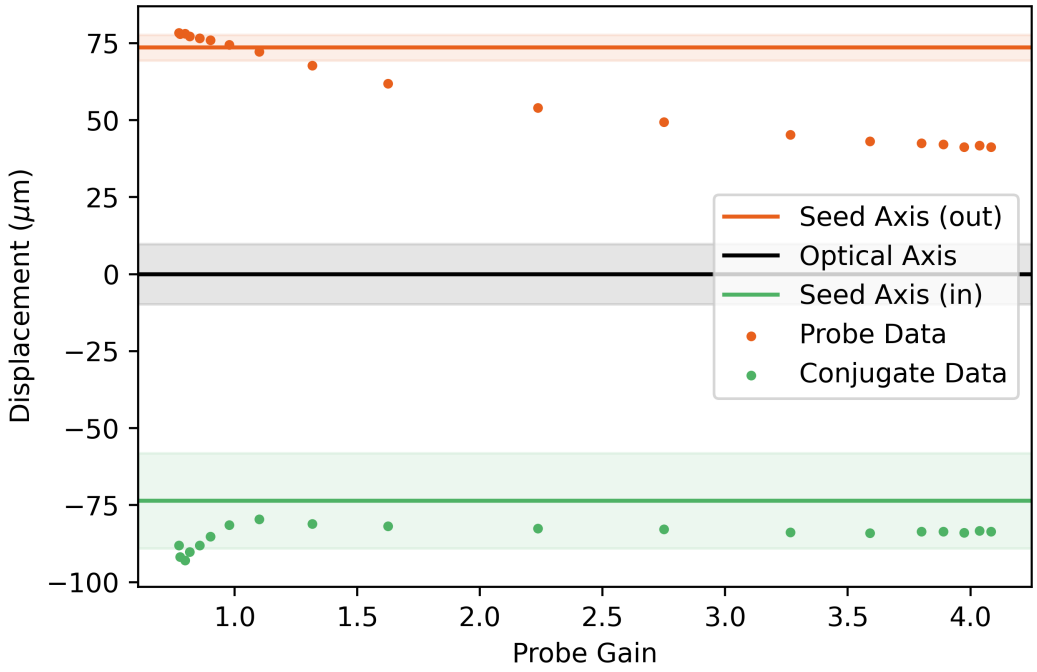

Figure 9.9 The position with respect to gain of the probe beam, with pump power used to alter the gain. The seed and optical axes, with shaded areas representing uncertainties, are shown.

conjugate is displaced from the appropriate seed axis by significantly less than the probe, particularly at high gains.

Interestingly, at a gain of around 1 the beam displacement crosses the seed axis and continues to be displaced below 1. The gain below 1 is indicative of absorption, and it would seem the absorption of the probe is asymmetric. However, it should be remembered that there will still be some 'gain' in this region. The gain we measure experimentally is a combination of pure gain and absorption - as we cannot measure absorption we must base the gain only on the power of the probe beam. Assuming the absorption occurs evenly across the transverse profile of the beam we would then expect the gain at which the probe position crosses the seed (out) axis to be slightly less than 1. Therefore the axis position in figure 9.9 is possibly a little lower than it should be, but still within the indicated error.

9.5.2 Varied One-Photon Detuning

The one-photon detuning was controlled by changing the frequency of the TiSaph laser using the internal reference cavity. Unfortunately, it was not possible to know the absolute value of the one-photon detuning. The step size when changing the cavity length was also only known approximately as it was given as a voltage applied to the piezo crystal controlling the size of the the cavity rather than as an absolute value of the change in cavity size.

The gain peak as a function of Δ_1 is highly asymmetric, with one side having a much higher gradient than the other. From figure 9.10 it can be seen that there is a difference in probe and conjugate behaviour on the low gradient of the gain which is particularly noticeable at low gain values, where the probe moves towards the seed axis (out) while the conjugate moves away from the seed axis (in). However, both are moving away from the optical axis as gain decreases.

It can be seen on the low detuning/high gradient of the plot that the data crosses the seed axis at a gain of much greater than 1. This suggests there is a significant amount of

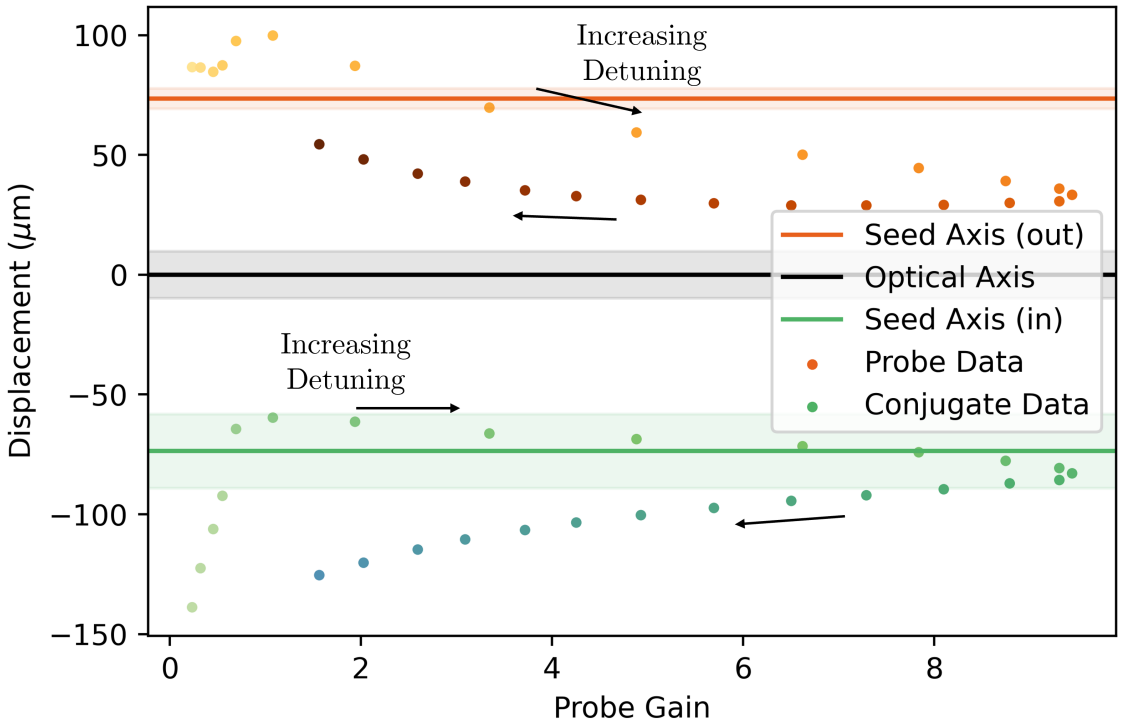

Figure 9.10 The position with respect to gain of the probe and conjugate beams, with one-photon detuning used to alter the gain. The seed and optical axes, with shaded areas representing uncertainties, are shown.

absorption present. This is supported by the minimum gain on this arm, which is well below 1. It also supports what we know from the camera data: for optimum squeezing results Δ_1 is set to be on the low gradient side of the gain peak. Presumably the best squeezing is seen here because at detunings smaller than this the absorption starts to significantly increase. It seems as though the data on the low gradient side is approaching a crossing of the seed axis at around a gain of 1, suggesting the absorption on this side is not as significant.

It is also interesting that a single gain value can correspond to (at least) two different displacements. This again links to the idea of absorption playing an important role: on one side of the point of maximum gain the absorption is different to on the other, and this will likely also impact the position of the beam. It could be hypothesised that, with no absorption, the position with respect to gain on either side of the resonance would be the same.

9.5.3 Varied 2-photon Detuning

Figure 9.11 shows the experimental results for varied 2-photon detuning, δ. As with pump power, the beam is displaced towards the optical axis at higher gains. However, the gain achieved here is significantly higher than when altering the other parameters.

As mentioned previously, the two-photon detuning resonance is relatively much closer to the resonance than the other parameters in terms of how much it is varied in this experiment. Unfortunately, at the high gains seen here the beams become extremely distorted as there is a large amount of absorption as well as high gain. It is interesting that the beam crosses the optical axis: again it should be emphasised that the probe beam at these points is quite distorted, but from the beam profiles it can be seen that the gain is heavily biased to the optical axis side of the beam with the other side barely changing, which is what results in this movement.

At gains below 1 we once again see the position of the probe beam cross the seed axis,

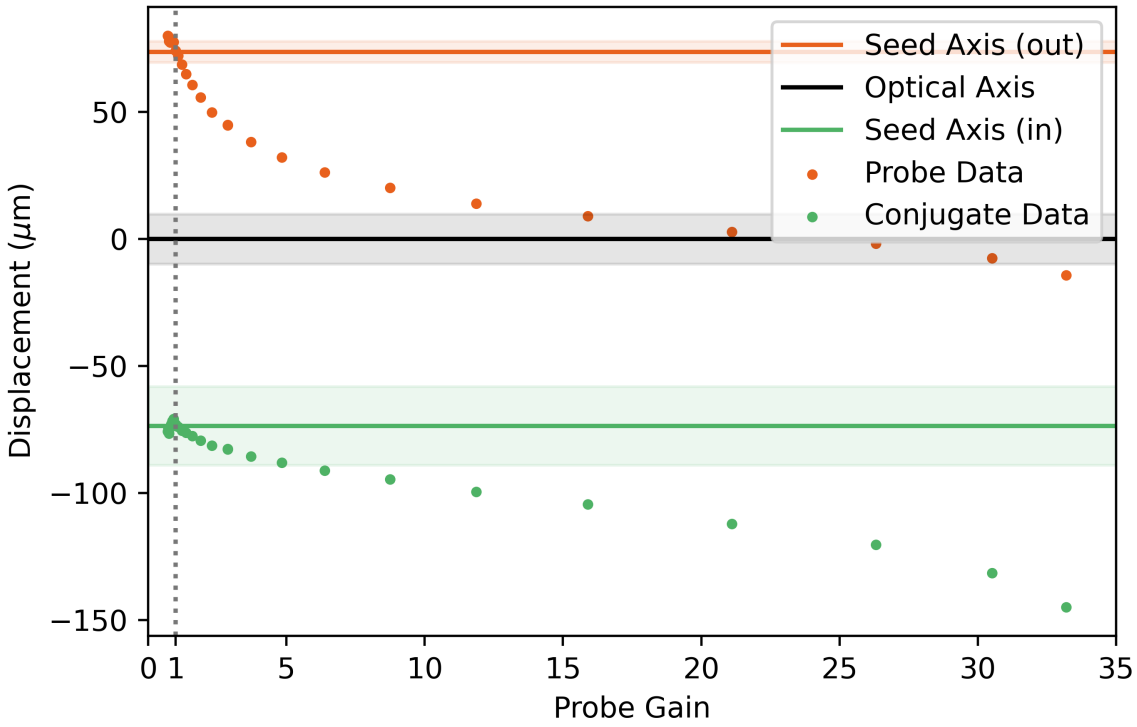

Figure 9.11 The position with respect to gain of the probe and conjugate beams, with two-photon detuning used to alter the gain. The seed and optical axes, with shaded areas representing uncertainties, are shown.

indicating there is absorption of the beam present. This crossing occurs at a gain of around 1, suggesting gain across the transverse profile of the beam is relatively uniform here such that the beam shape is not distorted.

We see here that the displacement of the probe and conjugate follows a very similar trend, although at very high gains the displacement of the conjugate becomes quite large after the probe has crossed the optical axis. This is a contrast to the pump power, where the conjugate stayed approximately on the seed axis (in).

9.6 Fitting the Model to the Data

Qualitatively, the experimental data matches what is seen in the computational model: the position of the beams on the output face of the cell varies with gain of the beam, being pulled closer to the optical axis at higher gains. Furthermore, the motion depends on the variable used to control the gain and is consistently more significant for the probe beam compared to the conjugate. The next step is to verify the model matches what we see experimentally more quantitatively. As there are values in the simulation which are difficult to predict, such as the ground state decoherence and one-photon detuning, the aim here will be to fit the model discussed in chapter 8 to the data discussed in sections 9.4 to 9.5.2. This will allow us to determine these unknown parameters with more accuracy, and verify that the model performs as expected.

Table 8.1 gives a summary of the model parameters which are unknown, or difficult to know precisely. Thanks to the large number of unknown parameters there is a significant risk of over-fitting. Additionally, the range over which a parameter can be controlled is often limited, either by experimental limitations (such as a finite available pump power) or by limitations made in the model (such as the assumption we are far from resonance, which limits the range of detunings which can be used). It is not possible to fit multiple separate sets of data simultaneously as there are parameters (such as density and one-photon detuning) we expect to change slightly between data sets. Therefore, we will fit the data for varied pump power, one-photon and two-photon detunings separately, but restrict the parameters such that any variation between sets is representative of fluctuations we would expect to see experimentally. Additionally, only the probe beam data and model will be used as the data for the probe, particularly at low gains, is more reliable than that for the conjugate.

It is worth acknowledging at this point that to reliably use the model to guide an experimental process it would be necessary to know the majority of the experimental parameters

with reasonably good certainty. With the current experimental setup there is a large error on the certainty to which we know the one-photon detuning and temperature, which would have to be known if we wished to use the model to predict outcomes of particular experimental runs. This would require significant enhancements to the experimental setup, but would be an interesting subject of further study.

9.6.1 Varying Single Parameters

Two-Photon Detuning, δ

As discussed previously, the two-photon detuning, δ, is experimentally well known and well controlled. The least-squares fitting algorithm, which is a constrained version of a Lavenberg-Marquardt algorithm, takes a set of initial guess parameters along with the set of δ values used to generate the experimental data and runs the computational model to extract the position and gain of the probe beam corresponding to each of these δ values. It then determines the difference between these modelled values and the experimental data, and re-runs the model with varied parameters until this difference is minimised. The fitting parameters are each limited to be within a particular range which has been determined to be physically reasonable. The result of the fit is shown in figure 9.12. The data was restricted to gains above 1, as at low gain the background can significantly influence the centre of mass position of the beam, and below 20, as this is the region closest to resonance where the beam shape becomes badly distorted.

We see that at low gain in particular the displacement is slightly smaller than would be expected based on the fit. This could be due to the influence of the background light: the region of the beam profiler containing the probe beam is chosen at high gain and fixed for all analysis, meaning the beam is off-centre from the region of interest at low gain so the background may pull the centre of mass of the beam towards the centre slightly. While the broad shape of the model is matched by the data, it clearly does not match exactly.

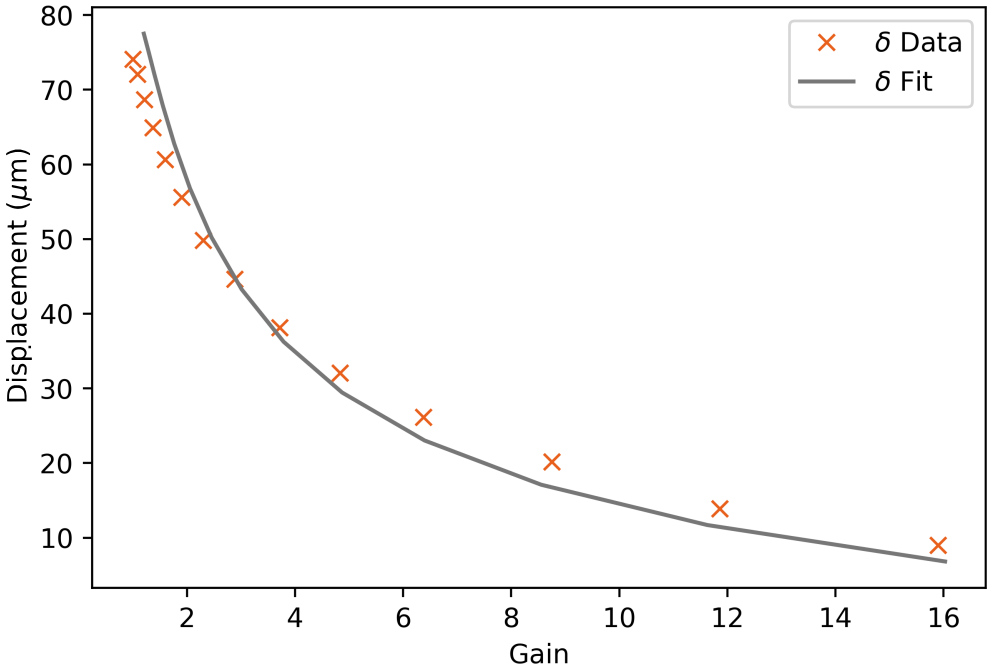

Figure 9.12 The data set varying two-photon detuning, δ, fitted with the numerical model. The parameters used for this fit are given in table 9.2.

One-Photon Detuning, Δ_1

The one-photon detuning is controlled by changing the laser cavity width, which we assume to provide an approximately linear change in frequency. As mentioned previously there is no absolute measurement for the laser frequency, and we do not even know the absolute value of the frequency change as it is too small to be measured on a wavemeter, so can only be approximated based on the number of steps required to cause a 1 pm change in wavelength. Therefore, additional parameters were added to the objective function used to fit the data to scale and offset the approximated experimental values of Δ_1 in the form $\Delta_1 = a\Delta_{1\text{guess}} + c$. Additionally, the range of data it was possible to fit was restricted by assumptions made in the model: namely, in the model the atoms were assumed to be stationary. That is to say that the Doppler profile of the atoms was not accounted for, and this is a reasonable assumption provided our virtual state is sufficiently far detuned from the excited state. Decreasing the detuning brings us closer to resonance and into a region where the model is not capable of describing the behaviour we see experimentally. For this region, all data around the turning point in gain we see in figure 9.10 and on the high gradient side (greater displacement) was rejected for the purpose of the fit, as in these regions there is a significant amount of absorption due to the Doppler broadening which the model does not account for. The resultant fit is shown in figure 9.13. Note the typical parameters used for an experimental run would correspond to a gain of around 6 in figure 9.13, so this is the value of Δ_1 which should be considered when comparing to the other fits. Again, this fit matches the broad shape of the model despite clearly matching exactly. It is, however, a better fit than the data for the two-photon detuning, although this could simply be a result of overfitting due to the additional fitting parameter.

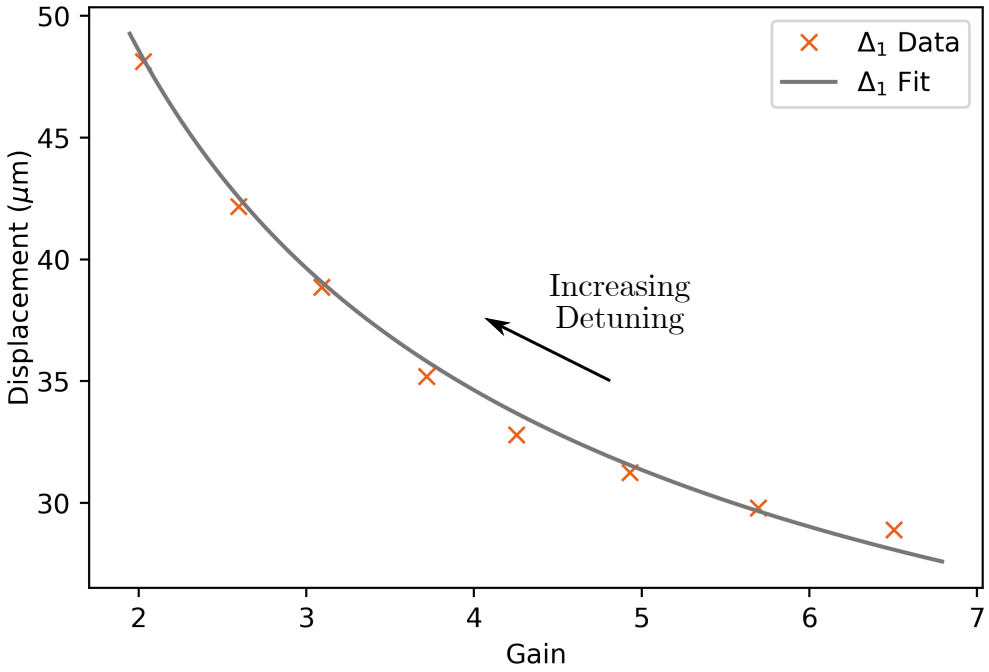

Figure 9.13 The data set varying one-photon detuning, Δ_1, fitted with the numerical model. The parameters used for this fit are given in table 9.2.

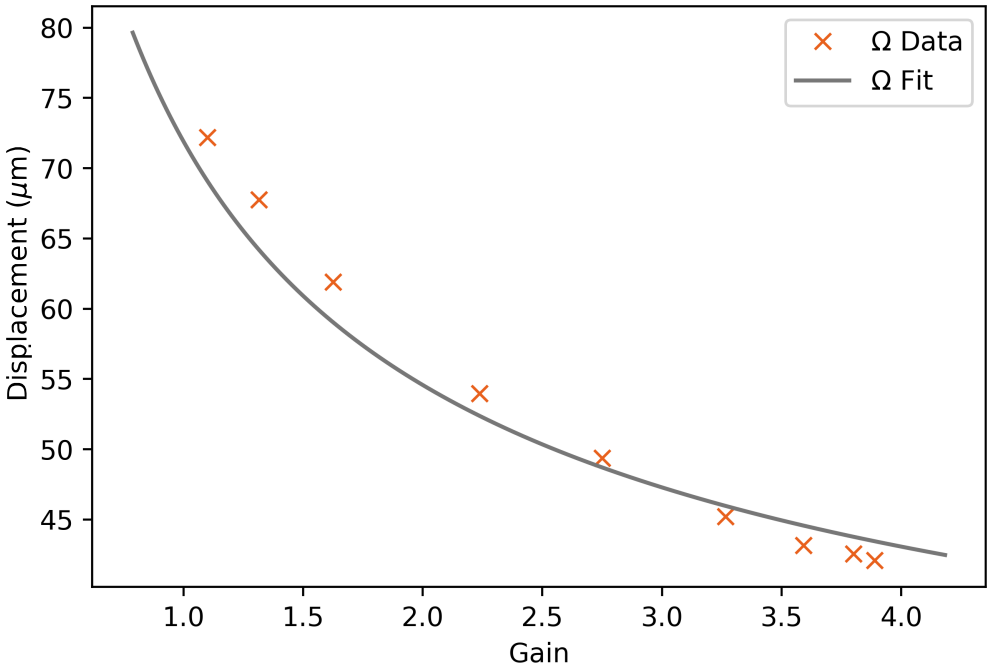

Figure 9.14 The data set varying pump power, Ω, fitted with the numerical model. The parameters used for this fit are given in table 9.2.

Pump Power, Ω

The pump power is expressed as a resonant Rabi frequency, and uncertainty in this parameter arises primarily from the uncertainty in the measured waist of the pump beam and in the value used for the dipole matrix element; these are considered together as one fitting parameter. At high RF power, changing the RF power by 1 dBm causes a change in optical power which is not measurable with our power meter but is sufficient to induce a change in the gain of the 4WM. These points are removed from the fit, as otherwise several data points would falsely be fit using the same pump power. Additionally, data points with gain below 1 are also removed.

Table 9.2 gives the fitted parameters for the 3 data sets described above. Generally, the fitted parameters are reasonably consistent for the three sets. Some deviation in the one-photon detuning is expected as this has to be manually set each time 4WM is obtained.

Parameter	Varied Ω	Varied Δ_1	Varied δ
Pump Power, Ω	$67\gamma \rightarrow 52\gamma$	83γ	88γ
One-Photon Detuning, Δ_1	170γ	$79\gamma \rightarrow 160\gamma$	180γ
Two-Photon Detuning, δ	1.39γ	1.39γ	$0.32\gamma \rightarrow 4.75\gamma$
Atom Density (per mm^3)	2.7×10^9	2.3×10^9	2.4×10^9
Ground State Decoherence, γ_c	0.24γ	0.5γ	0.1γ
Angle, α (in mrad)	6	6	6
Probe waist, σ (in μm)	70	98	70
Position Offset (in μm)	0	34.5	10.9

Table 9.2 Fitting parameters used in figures (9.12-9.14).

Similarly, the atom density and ground state decoherence both depend on the cell temperature, which in turn will vary slightly throughout the day and therefore between data sets.

The most troubling parameter is the probe waist, which should be the same between the 3 data sets. However, it is possible that this appears different between the 3 to account for variations in other parameters.

Also shown in the table is a parameter to allow a position offset to be added to the data to account for the uncertainty in where the optical axis lies in the experimental data.

The angle between the beams is consistently on the smaller side of that which was measured. Since both experimentally and in the model we are using relatively small beams there's a wide range of k-vectors in the probe seed, which effectively means there's a range of angles between the pump and probe seed. The gain is dependent on the angle between the probe and pump beams due to the phase matching condition. This is taken into account in the simulation. The dependence is not symmetric - i.e. there is an ideal angle for maximum gain, but the gain does not decrease evenly on either side of this angle. Experimentally the angle between the beams is set to be slightly larger than this optimum, as this helps with blocking the pump and separating the beams in the far field as it increases the distance between them. Unfortunately, we also see experimentally that more gain occurs at the smaller

angles, as in the far field it can clearly be seen that there is more gain closer to the optical axis. When looking at the experimental data, this increased gain at smaller angles could make the angle between the pump and probe seed seem smaller than it actually is. This also introduces additional error in the location of the probe seed axis, which is where the variation in the position offset originates from, and also increase the perceived probe waist as not all momentum components experience gain equally. In summary, the probe waist, angle and position offset variables are likely tied together.

9.7 Modelling Changes in Multiple Parameters

We can also investigate changes in multiple parameters at once. Experimentally, this must be done in a single data taking session due to the drifts in temperature and the uncertainty in the absolute value of the one-photon detuning discussed previously. This somewhat limits the extent to which we can explore the full parameter space, but we can comfortably explore pairs of parameters changing. The advantage to considering multiple parameters simultaneously is that it increases the number of data points obtained per degree of freedom (fitting parameter). This reduces the risk of overfitting.

Changing Pump Power and Two-Photon Detuning

Figure 9.15 shows experimental data for changing the probe gain via changing the pump power for a range of two-photon detunings. The seed axis and optical axis are shown as before. The typical two-photon detuning used when optimising for squeezing is 1.39γ. We see at lower detunings the gain is generally larger as we move towards resonance, and the position of the probe beam is typically closer to the optical axis. At higher detunings we see the gain decrease and the data typically follows the same line of gain against displacement, while higher detuning curves move away from this somewhat. This is likely linked to the higher levels of absorption present at lower detunings closer to resonance.

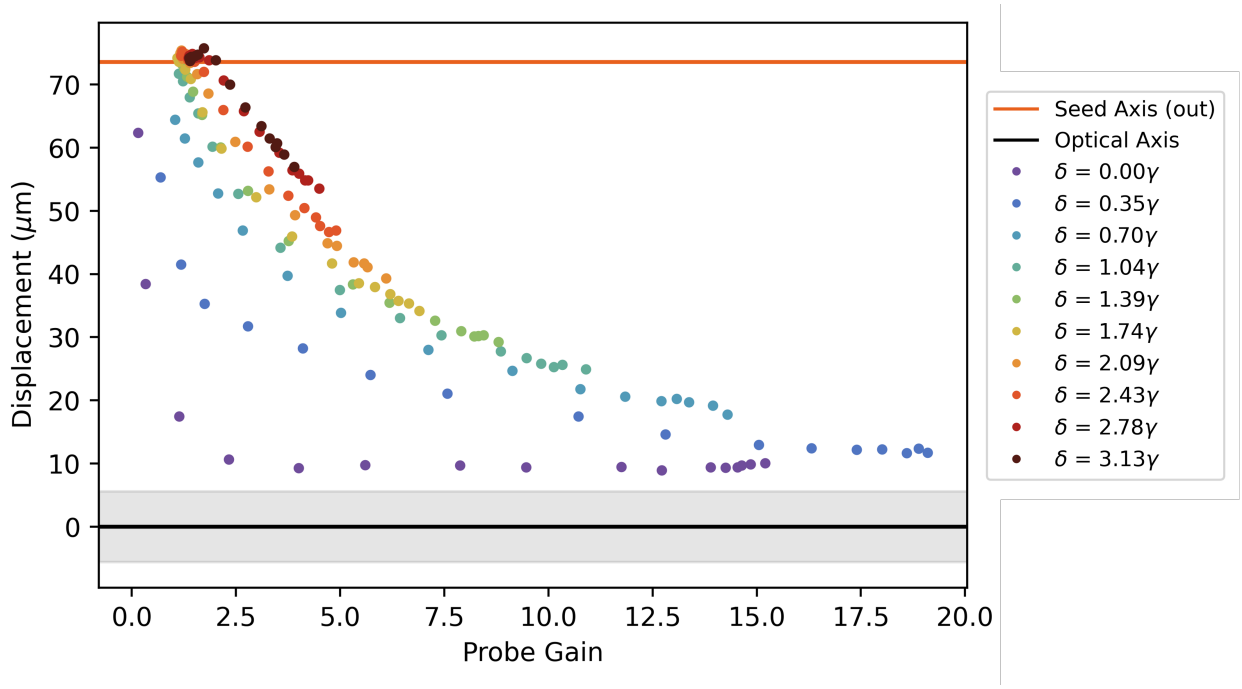

Figure 9.15 Experimental data for the displacement with respect to gain of the probe beam for a range of pump powers at a number of two-photon detunings, δ.

We can use the model to produce a similar data set, shown in figure 9.16, although as explained previously it is difficult to precisely know several of the experimental parameters so this discussion will focus primarily on the qualitative shape of the results. Again, we see at higher detunings the gain is generally higher, although we do not see the decrease in gain in the model that we see in the experimental data. The model becomes less accurate closer to the light-shifted resonance as it assumes the population of the excited state to be small, which is not the case close to the two-photon detuning resonance when there is very high absorption (as can be seen in figure 8.1.

As with the experimental data, the model outputs plotted in figure 9.16 also shows at higher detunings the shape of the displacement vs gain curves are pulled away from the trend they follow at lower detunings. Using the model the absorption can be switched off, and this 'no absorption' case is shown on the right side of figure 9.16. We see that without absorption the two-photon detuning still affects the gain, however it does not affect the gain vs displacement relationship caused by changing pump power.

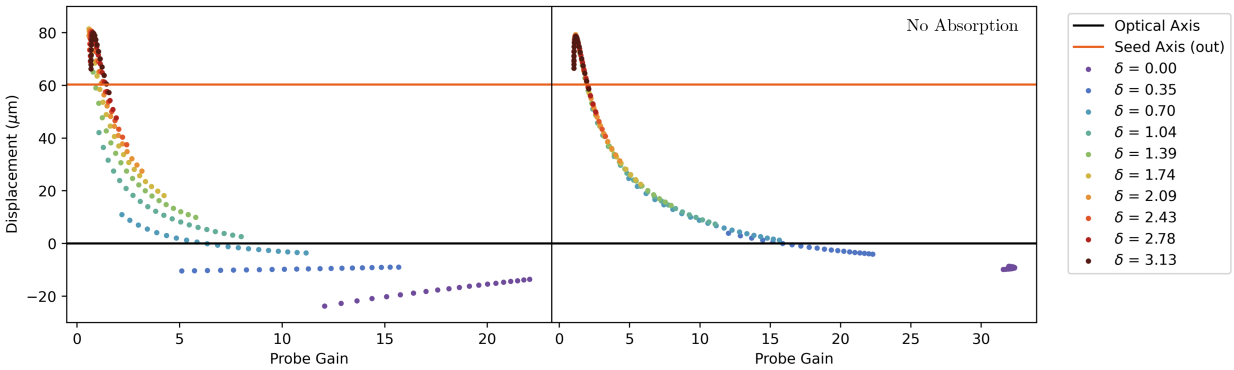

Figure 9.16 Modelled data for the displacement with respect to gain of the probe beam for a range of pump powers at a number of two-photon detunings, δ. The plot on the right shows the results with no absorption, obtained by setting the imaginary component of the direct susceptibilities to zero.

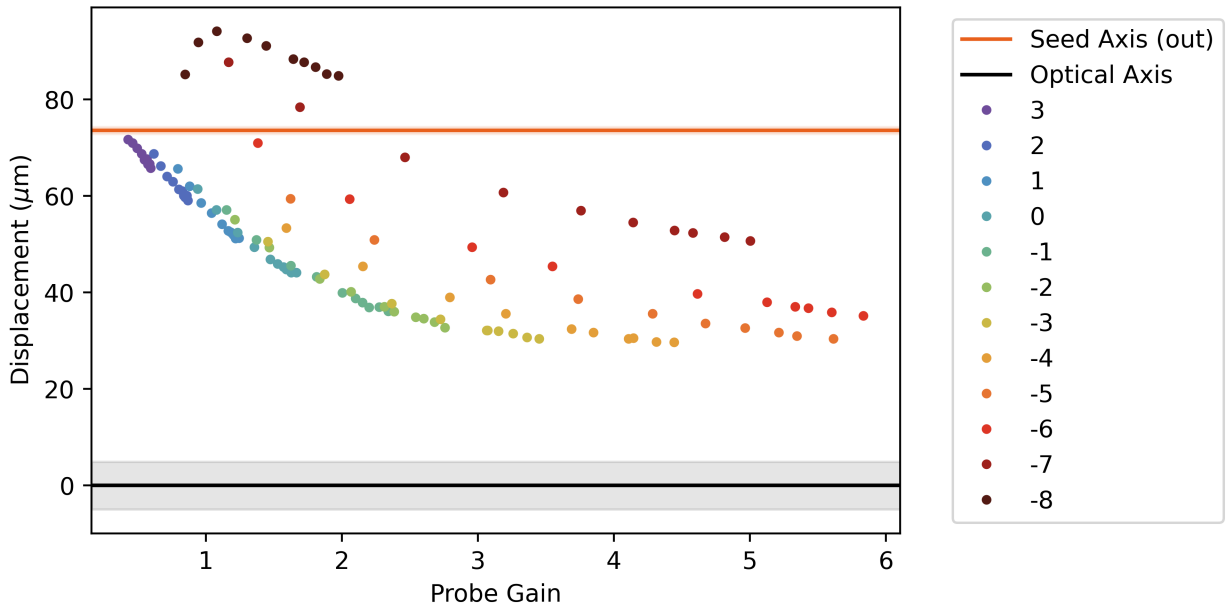

Figure 9.17 Experimental data for the displacement with respect to gain of the probe beam for a range of pump powers at a number of one-photon detunings, Δ_1. The value of Δ_1 is arbitrary, but expressed as a number of steps in the laser cavity control from the usual experimental value used for generating squeezing, with 0 indicating the (approximately) value for optimum squeezing.

9.7.1 Changing Pump Power and One-Photon Detuning

Figure 9.17 shows experimental data, this time with the pump power and one-photon detuning being altered. The value of the one-photon detuning is defined in terms steps of the frequency of the TiSaph laser, as controlled by the laser cavity, with '0' being the approximate value at which optimum squeezing is seen. We see from the peak gain in each one-photon detuning set that the positive values correspond to the high gradient side of the gain while the negative correspond to the low gradient side, with 0 being the typical value used experimentally when generating squeezed light. Unfortunately, it is more difficult to generate a modelled dataset to replicate these results with no absorption as we did in figure 9.16 due to the model becoming invalid as we get closer to resonance, as discussed previously.

We see a similar trend to the two-photon detuning and pump power case. There is a common curve of displacement with respect to gain the data mostly follows at detunings above 0. For smaller detunings the gain-displacement relationship varies, with a broadly higher displacement. If we assume, as before, that this is indicative of higher absorption at these detunings then we may infer that if absorption was removed all data would lie along this common line and we would see a one-to-one mapping between gain and absorption. It is reassuring that we see the best squeezing in the region where we also see the smallest displacement, and this further reinforces that this region experiences less absorption of the probe beam as we know from previous discussion that high absorption reduces the levels of squeezing for a given gain.

Chapter Ten

Conclusion

This part of the thesis has focused on investigating the matched propagation of the probe and conjugate beams when undergoing 4WM in a rubidium vapour cell, and the impact this has on our ability to detect localised correlations in the NF images of the beams. A model has been produced, and this has been verified qualitatively using experimental data. As there are high levels of uncertainty in some of the modelled experimental parameters, we fitted these during the verification. A more thorough verification of the model will require reducing these experimental uncertainties. While currently the model approximates the pump as a plane wave, it could be easily adapted to include a Gaussian pump beam in order to be more representative of the experimental setup.

It is clear from the model and from the experimental data that there is a nontrivial relationship between the position of the probe and conjugate beams and the gain from the 4WM process. This relationship also varies depending on which parameter is altered to control the gain. Cell temperature, one-photon detuning, two-photon detuning and pump power were all explored as methods of controlling the gain. In a typical setup the pump power will vary significantly across the transverse profile of the beams due to its finite size. As a result, it is reasonable to expect that different portions of the transverse sections of the probe and conjugate beams, which 'see' different pump intensities as they pass through the cell, will experience different displacements from the optical axis on the output of the

cell. Crucially, this displacement is also different for the probe and conjugate, which means it is reasonable to expect the correlations to be distorted in the near field image of the cell. Additionally the spatial propagation of the beams is something which has not been studied previously, and is currently in the process of being written up as a paper.

The understanding gained of the matched propagation of the probe and conjugate beams indicates that the trivial subtraction of the images used in the Fourier analysis is too simple to account for these details. However, it also provides an explanation as to why a peak in the spatial noise profile was observed in the Fourier analysis, and opens up the possibility of using different techniques to create a 'map' of the correlations. Such methods are primarily based on the idea of convolving different windowing functions across the beams. The windowing functions can be designed to probe different spatial frequencies. An example of this is using Morlet wavelets, which can be used identify correlated areas. In preliminary investigations some squeezing has been observed using such analysis. Currently the classical noise on the images is the limiting factor in such analysis.

Having gained awareness that the correlations may be distorted by the matched propagation of the beams through the cell, the experimental setup can be re-optimised with this in mind. Minimising the classical noise on the image is arguably more important than ever: improvements to the noise eater, such as designing new electronic feedback circuit which reduces the electronic noise while also allowing a larger optical power to be sampled, are already underway, which would help reduce classical fluctuations on the laser further. Additionally, where the Fourier analysis took into account noise in the image as a whole an analysis making use of windowing functions could examine a subset of the images of the beams. This means we can focus on the centre of the images where the intensity of the beams is the greatest, and as such they can be expanded more and therefore be of greater power before saturating the camera. As a result the impact of fluorescence and other sources of noise from the pump will be reduced, again helping to decrease the classical noise. Finally, while there are issues with classical noise when using the camera due to the limited speed at

which is can operate, the BPD operates in the continuous regime and can be used to directly measure noise at frequencies where classical noise is insignificant. Therefore, a physical aperture can be used to select a portion of the probe and conjugate and a continuous detection scheme can be used to measure the correlations present. While this has been done before with vertical slits, and it is possible to observe localised correlations using such a method, the precise positions of the correlated regions in the two beams has not been verified in detail. With the addition of the instrumentation amplifier to the BPD, as discussed in section 6.2, making simultaneous measurements of the total incident optical power and the noise on the intensity difference of the two beams possible,

Assuming the issue of the classical noise can be overcome, from the matched propagation simulation and the experimental data it should be possible to produce a map of the real space correlated regions of the probe and conjugate beams which would mean they could be used in sub-shot noise spatial measurements and this will lead to a publication. Unfortunately, the model currently considers the pump to be a plane wave of constant intensity, whereas in reality it is likely the variation in pump intensity across the transverse profile of the pump beam seen by the probe and conjugate as they propagate through the cell which causes the distortion in the correlations. Rather than including a non-plane wave pump beam in the model, which would require re-calculating the propagation equations, it would be simpler to model the position of the probe and conjugate beam a number of times for a range of pump power values and use the outputs to build a picture of the position of the correlations generated by a more realistic pump beam. This would not account for any variation in the transverse momentum of the pump, but would account for the variation in pump power which is the more significant effect. Most importantly, to reduce the significance of the distortion caused by this effect the intensity of the pump beam should be kept as uniform as possible across the transverse profile of the probe and conjugate beams. While it has always been known that the pump width in the cell should be as large as possible to ensure the gain across the transverse profile of the probe is as constant as possible, the displacement of the

beams which goes hand-in-hand with this gain was previously not considered. Currently the maximum width of the pump beam is limited by the total power in the laser: with more power it would be possible to increase the size of the pump while maintaining a sufficiently high intensity. Alternatively, the waist of the probe beam in the cell could be decreased slightly, as this is currently not the limiting factor in the size of the coherence area. Finally, the model has indicated that it may be preferable to operate in a region with some absorption. While this will decrease the overall squeezing, it may also reduce the distortions and make it easier to observe correlations between the probe and conjugate beams. With this in mind, it should be possible to improve upon the current MSM squeezing observed.

Part II

Position Detection

Chapter Eleven

Introduction and Literature Review

Increasingly there are applications even outside the field of physics research, which are limited by the shot noise on light, and it is desirable to have ways of improving these measurements which do not require advanced optical setups. Detecting small transverse displacements of a beam is an example which is of particular use in the field of high speed atomic force microscopy (AFM), which has reached nanometric sensitivity[81] and operates at the shot noise limit[82][83][84]. To improve such a measurement, techniques utilising MSM squeezed light, such as that discussed in Part 1 of this thesis, can be employed. A beam with a position which could be determined beyond the shot noise limit, a quantum laser pointer, was experimentally realised in 2003[85], squeezed light has been used to enhance measurements made with micro-electro-mechanical systems (MEMS)[86] and Homodyne detection techniques have been used with squeezed light to achieve position detection with sensitivity beyond the quantum noise limit.

Using squeezed light to further improve the SNR of such a shot noise limited measurement is one option, however this typically requires complex experimental techniques which are not easily available outside of a quantum optics lab. Before investing in such methods, is can be beneficial to investigate whether the measurement itself can be improved using classical techniques. The vast majority of applications where detecting the position of a beam is necessary use a TEM00 mode, shown in figure 11.1, which from this point, will be referred

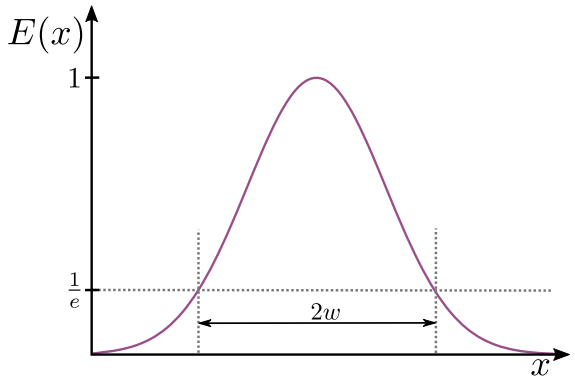

Figure 11.1 The transverse profile of a Gaussian beam of radius w.

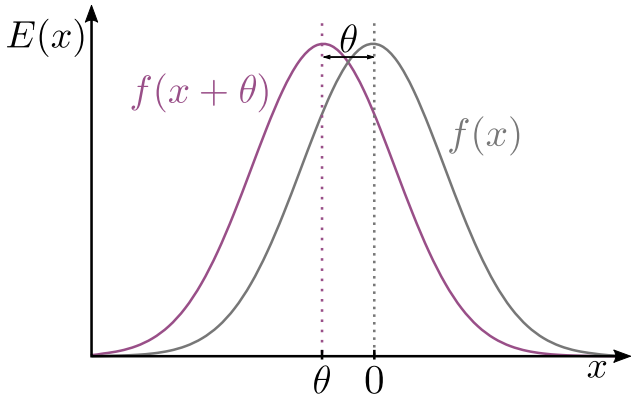

Figure 11.2 The transverse profile of a Gaussian beam (grey), and that of one displaced by θ in the x-direction (purple).

to as a Gaussian beam. Discussion will be restricted from this point to small displacements of a Gaussian beam, such as that shown in figure 11.2. For such a displacement, to first order the signal is all contained within the TEM01 mode, as we will see, therefore intuitively an ideal detector will be sensitive to this mode.

We will restrict the discussion to a rather specific application: measuring the small oscillating tilt of a reflector, such as the cantilevers used in atomic force microscopy (AFM). As such, we are interested in measuring displacement at rates of around $100\,\mathrm{kHz} - 1\,\mathrm{MHz}$; it is therefore necessary for the detection method to have a bandwidth of at least $100\,\mathrm{kHz}$. Furthermore, the heating of the microcantilever of the AFM caused by the incident beam means the optical power is limited, typically to under $1\,\mathrm{mW}$, which is why increasing the SNR by increasing the power is not possible.

While part 1 of this thesis focused on improving the SNR of a measurement by decreasing the quantum noise on the light used to make the measurement, this part will be concerned with selecting an optimum measurement scheme to maximise the SNR for a given beam intensity without altering the quantum nature of the light itself, with the particular case of the AFM in mind.

The aim of this work is to improve upon the current method of using a split photodetector

to determine the displacement of the beam by designing a new detector with a carefully chosen detection mode. The idea for such a detector resulted from considering ways of constructing detectors sensitive to higher order modes or squeezed light, such as the TEM01 mode, in a continuous regime. It was something I first worked on as a masters student in the research group, specifically designing and initial detector using an array of photodiodes capable of detecting a range of different spatial modes at the shot noise limit using the BPD circuit design as a starting point.

This new detector will be shown to saturate the Quantum Cramer-Rao bound for detecting a small displacement of an optical beam. Much of the theoretical work calculating the SNR of the detectors follows the example of Barnett et.al.[87], adapted for our optimised detector. Furthermore, the design and construction of the new detector will be discussed, and its performance compared to that of a split detector. The potential enhancement when using squeezed light with this new detector will also be discussed.

Chapter Twelve

Position Detection Theory

12.1 Ideal Detection of a Gaussian Mode

We begin by asking what is the 'ideal' measurement we would like our detector to make in order to maximise sensitivity to small displacements? To answer this, first consider the transverse x-direction electric field profile in 1D of a TEM00 mode,

$$E_0(x) = \varepsilon_0 \frac{w_0}{\sqrt{\pi} w} e^{\frac{-x^2}{w^2}}, \tag{12.1}$$

where ε_0 is the amplitude of the field and w is the beam radius, defined as shown in figure 11.1. w_0 is the beam waist radius, which is the radius at the focus of the beam.

If the beam is displaced by a small amount, θ, in the x-direction, as illustrated in figure 11.2, we can approximate its new transverse field profile as

$$E_0(x-\theta) \approx E_0(x) - \theta \frac{dE_0(x)}{dx}, \tag{12.2}$$

and from this we determine the change in our field introduced by this small displacement to be

$$E(x) - E_0(x-\theta) \approx \theta \frac{dE_0(x)}{dx}. \tag{12.3}$$

We shall refer to ${}^{dE_0(x)}/_{dx}$ as the displacement mode, which for our TEM00 mode is given by

$$\frac{dE_0(x)}{dx} = -E_0 \frac{2xw_0}{\sqrt{\pi}w^3} e^{-\frac{x^2}{w^2}}. \tag{12.4}$$

To measure θ we use a photodetector with a detector profile $g(x)$. The detector profile is essentially a position dependent conversion factor which tells us by how much light falling on a particular part of the photosensitive region of the detector is amplified. For simplicity we assume the photosensitive region to be infinite in space. As an example, a simple photodiode has a constant detector profile, $g(x) = c$, where the constant provides a conversion from input optical power to output electronic signal. The quantum efficiency of the photodiode, transimpedance gain of the following detector electronics, and any additional operations performed on the signal are all taken into account in this detector profile.

The photodiode produces a current proportional to optical intensity, with the generated electronic signal given by

$$S = \int S_\theta(x)dx = \int g(x)E_0^2(x-\theta)dx. \tag{12.5}$$

Since the change we are trying to measure is proportional to the derivative of the field, we should choose $g(x)$ such that our signal is sensitive to ${}^{dE_0}/_{dx}$. This way, all the detected light will contribute to the evaluation of the displacement.

The signal density of the output of a detector with detection profile $g(x)$ detecting a small displacement, θ, of a Gaussian beam displaced by θ is given by

$$S_\theta(x) = g(x)(E_0(x-\theta))^2 \approx g(x)\left(E_0^2(x) - 2\theta E_0(x)\frac{dE_0(x)}{dx}\right), \tag{12.6}$$

where we have kept only terms to first order in θ.

We choose $g(x)$ to be odd, meaning the term proportional to $E_0^2(x)$ will be zero when integrated over the full profile of the detector. Therefore, removing this term we find the signal

$$S_\theta(x) = -2g(x)\theta E_0(x)\frac{dE_0(x)}{dx}, \tag{12.7}$$

which is an overlap integral between the detection mode, $g(x)E_0(x)$, and the displacement mode, ${}^{dE_0(x)}/_{dx}$. To maximise the SNR, the signal should be maximised at a fixed shot noise, which means maximising the overlap integral with normalised modes. Therefore we should choose $g(x)$ such that $g(x)E_0(x)$ is proportional to ${}^{dE_0}/_{dx}$ to maximise our sensitivity to the displacement, θ.

It is worth noting here that this is proportional to the TEM01 mode. Therefore, our ideal detection mode for a small movement, θ, of a Gaussian beam in the TEM00 mode, $E_0(x)$, is one proportional to the TEM01 mode.

12.2 Saturating the Quantum Cramer-Rao Bound

The quantum Cramer-Rao Bound (QCRB) is a quantity frequently used in quantum metrology to quantify the quality of a measurement. For our purposes, it is essentially a measure of the smallest precision to which displacement can be measured within our quantum system as allowed by quantum mechanics, and is the inverse of the quantum Fisher information. In our case specifically, it is a measure of the information about the displacement of the beam contained within the beam itself, irrespective of the detection scheme used to extract such information. It is the quantum equivalent of the Cramer-Rao bound, which expresses a lower bound on the variance of an unbiased estimator of a deterministic parameter; in our case the photocurrent. Proving that the QCRB is saturated by the chosen detection scheme is therefore proof that an optimum detection mode has been chosen, as all possible Fisher information is extracted from the quantum state. A more thorough explanation of the QCRB and its relevance to the optimal measurement of quantum states is undertaken by Braunstein et al. [88], while the original theoretical derivation was performed by Helstrom [89][90].

The use of a photodetector as described previously can be considered analogous to Ho-

modyne detection, with the detector plus field acting as a local oscillator to the signal times the derivative of the field as shown in equation 12.7. We can therefore apply the theory derived for Homodyne detection schemes to determine whether our detection scheme is the best possible - i.e. to show that the quantum Cramer-Rao bound is saturated. The QCRB for a displacement measurement using a Homodyne detection scheme is derived by Sun et al. [91], following the work by Pinel et al. [92]. Ultimately, Pinel finds the QCRB for a displacement measurement using a coherent beam in the TEM00 mode with waist w as

$$\theta_{\min}^{\mathrm{QCRB}} = \frac{w}{2\sqrt{N}}, \tag{12.8}$$

where N is the number of photons. We will need to match this in order to prove we have saturated the QCRB with our displacement measurement. Intuitively, this follows what we would expect from a shot noise limited measurement in that a greater number of photons leads to a smaller minimum measurement. Decreasing the waist would benefit the measurement, however the minimum waist size is controlled by the size of the microcantilever: the beam in the far field where the detection is performed gets smaller when the beam on the cantilever gets larger, and the maximum size of the beam on the cantilever is limited by the size of the cantilever itself. Therefore, the smallest the beam can be on the detector depends on how large the cantilever itself is.

12.3 Available Detection Modes

Next we consider how well the detectors available to us match this ideal detection mode. As mentioned previously we will be considering two main types of detector: a split photodetector (SD) and a resistive position sensitive detector (PSD). Diagrams of these detectors are given in figure 12.1. We shall now discuss each in detail.

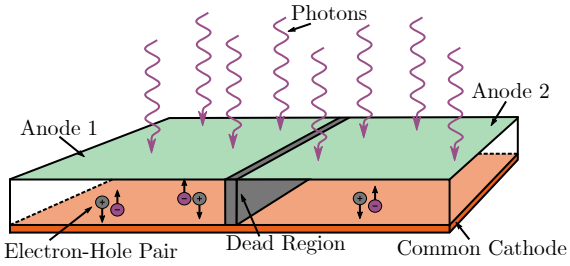

(a) The SD, for which a 'dead region' separates the left and right side and cannot be crossed.

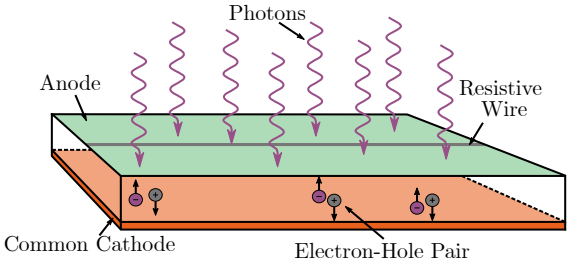

(b) The PSD, which has a resistive 'P' region (green) between the two anodes.

Figure 12.1 Diagrams of the two detectors showing incident light generating electron-hole pairs in the photosensitive region. Physical connections to the anodes (grey) and cathodes (orange) are show as thin wires.

12.3.1 Split Detector

The SD comprises two separate photodiodes which are connected by a small 'dead region' on a single chip with a common cathode, as illustrated in figure 12.1a. The photocurrents produced by these two photodiodes are subtracted from one another by the subsequent electronics, resulting in a signal which should, on average, be zero when a Gaussian beam is centred perfectly on the chip.

The detected mode is a product of both the mode of the incident light, in our case the TEM00 mode, and the detector mode, $g(x)$, of the photodetector being used. In the case of the split detector this is a step function, with the centre being the meeting point of the two diodes. For simplicity, the dead region between the two photodiodes is considered to be of negligible width for now. The detected mode is given by the product of the TEM00 Gaussian beam mode and this detector mode, as is shown in figure 12.2a. The heights of the two sides of the step function are controlled by the gain on the electronics following the photodiode chip. For all following discussions they will be considered to always be equal and opposite.

12.3.2 Position Detector

The PSD consists of a single photodiode with a resistive surface between the two anode connections, as shown in figure 12.1b[93]. Light incident on the PSD creates a photocurrent which then experiences a resistance proportional to the position of the incident beam. When perfectly centred, the resistance of each path (to the two anodes) is equal, so the generated photocurrent is split equally between the two anodes. However, when the beam moves closer to one of the two anodes the resistance of the path to that anode falls, and to the other subsequently increases, meaning a greater proportion of the photocurrent will travel along the path of least resistance - i.e. to the anode to which it is closest.

The detector mode, $g(x)$, of the PSD is linear as the resistance is directly proportional to the distance from the anode[93]. The detected mode, $g(x)E(x)$, is shown in figure 12.2b. It can be seen that this is proportional to the ideal mode described previously, and therefore we expect the PSD to out perform the SD. Any nonlinearity which may occur near the edges of the PSD, for example asymmetries caused by physical imperfections, will be ignored for this theoretical treatment.

12.4 Theoretical SNR

In order to predict precisely how the PSD should perform in measuring a small displacement compared to the SD, we must consider the signal and noise of a beam translated by a small amount, θ, as measured by each detector and compare their SNRs when operating at the shot noise limit.

The derivation for the theoretical SNR of the PSD was developed through collaboration with Jacob Beckey and Haixing Miao. It follows the work presented in Beckey's masters thesis, with some corrections applied.

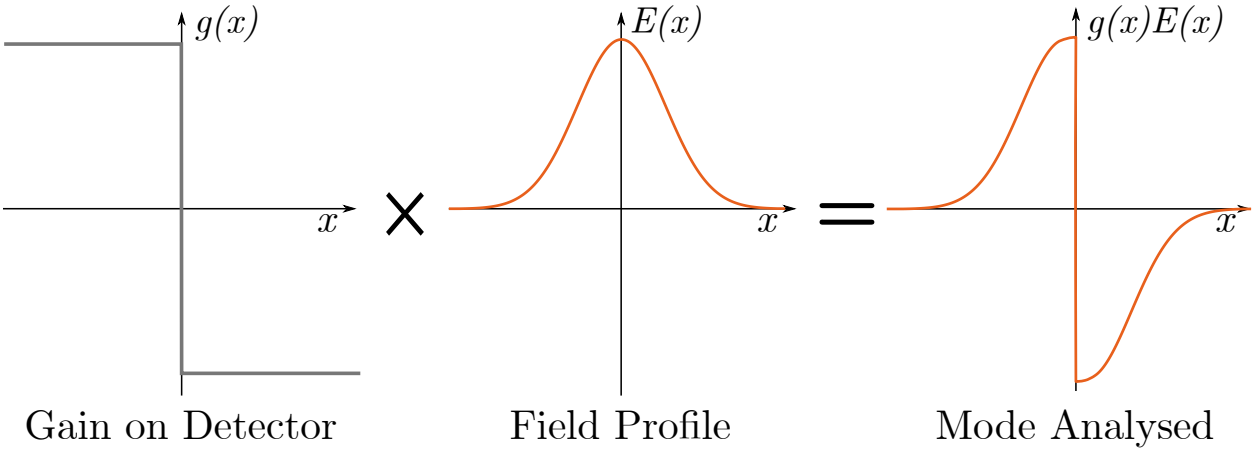

(a) The split detector mode combined with a Gaussian beam.

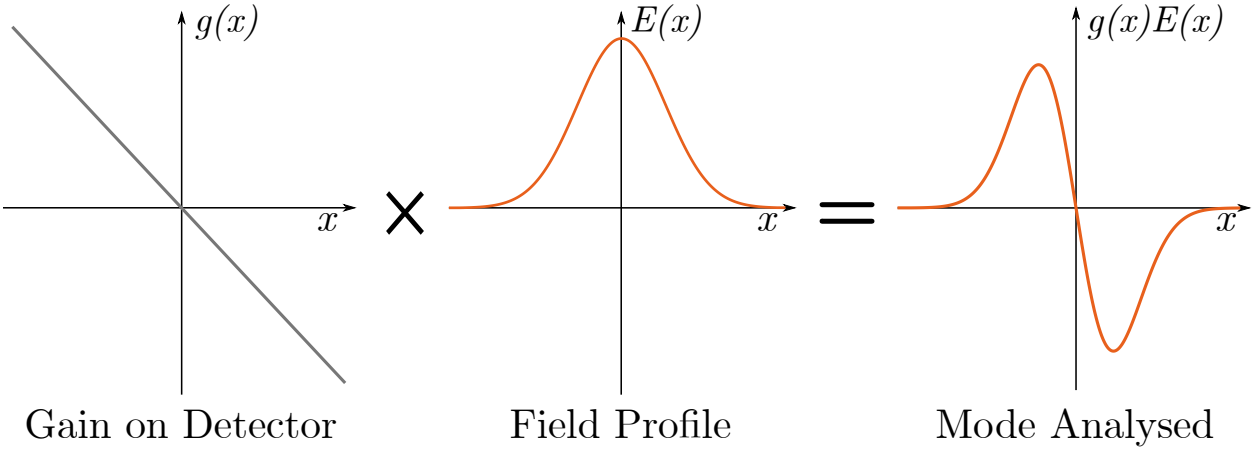

(b) The position sensing detector mode combined with a Gaussian beam.

Figure 12.2 The gain on each detector combined with a Gaussian beam mode to give the mode analysed.

12.4.1 Oscillating Beam Wavefunction

The first step is to find a convenient way of mathematically representing an electric field displaced by a small amount, θ. It is useful to first express the electric field density operator, $\hat{\psi}(x, y)$, as a sum of orthogonal modes:

$$\hat{\psi}^{(+)}(x, y) = \sum_{i}^{\infty} u_i(x, y)\hat{a}_i, \tag{12.9}$$

where $u_i(x, y)$ denotes the 2D profile of mode i and $\hat{a}_i$ is the annihilation operator for that mode. Note that $u_i(x, y)$ is considered to be real, such that $u_i^*(x, y) = u_i(x, y)$.

Since the $u_i(x, y)$ are orthogonal,

$$\hat{a}_i = \iint_{-\infty}^{\infty} u_i(x, y)\hat{\psi}^{(+)}(x, y)dxdy. \tag{12.10}$$

For the case we are interested in the TEM modes are the most convenient to use. We are concerned with primarily the u_0 mode, which is in the coherent state, and u_1 mode, in which most of our signal lies to first order. The normalised forms of these are

$$u_0(x, y) = \frac{\sqrt{2}w_0}{\sqrt{\pi}w} e^{-\frac{(x^2+y^2)}{w^2}}, \tag{12.11}$$

$$u_1(x, y) = \frac{2\sqrt{2}w_0}{\sqrt{\pi}w^2} x e^{-\frac{(x^2+y^2)}{w^2}}. \tag{12.12}$$

The TEM00 mode is considered to be in a coherent state, $|\alpha\rangle$, and all other modes are in the vacuum state, $|0\rangle$. Our initial state vector is therefore

$$|\psi\rangle = |\alpha\rangle_0 |0\rangle_1 |0\rangle_2 .... \tag{12.13}$$

To model the small displacement introduced to the beam we shall define a unitary operator, $\hat{U}(\theta)$, which displaces the wavefunction in the transverse direction by a small amount, θ. We assume this displacement is induced by a passive component, such as a micro-cantilever, and therefore $\hat{U}^{\dagger}(\theta)|0\rangle = |0\rangle$. Thus we can write our displaced field vector as

$$|\psi(\theta)\rangle = \hat{U}(\theta)\,|\psi\rangle \tag{12.14}$$

$$= \hat{U}(\theta)\,|\alpha\rangle_0\,|0\rangle_1\,|0\rangle_2 \ldots \tag{12.15}$$

$$= \hat{U}(\theta)e^{\alpha\hat{a}_0^\dagger - \alpha^*\hat{a_0}}\,|0\rangle_0\,|0\rangle_1\,|0\rangle_2 \ldots \tag{12.16}$$

$$= \hat{U}(\theta)e^{\alpha\hat{a}_0^\dagger - \alpha^*\hat{a_0}}\hat{U}^\dagger(\theta)\,|0\rangle_0\,|0\rangle_1\,|0\rangle_2 \ldots \tag{12.17}$$

$$= e^{\alpha\hat{U}(\theta)\hat{a}_0^\dagger\hat{U}^\dagger(\theta) - \alpha^*\hat{U}(\theta)\hat{a_0}\hat{U}^\dagger(\theta)}\,|0\rangle_0\,|0\rangle_1\,|0\rangle_2 \ldots . \tag{12.18}$$

From equation 12.10 we have

$$\hat{U}(\theta)\hat{a}_0\hat{U}^\dagger(\theta) = \iint_{-\infty}^{\infty} u_0^*(x,y)\hat{U}(\theta)\hat{\psi}^{(+)}(x,y)\hat{U}^\dagger(\theta)dxdy \tag{12.19}$$

$$= \iint_{-\infty}^{\infty} u_0^*(x,y)\hat{\psi}^{(+)}(x-\theta,y)dxdy. \tag{12.20}$$

Next, we make the substitution $x' = x - \theta$:

$$\hat{U}(\theta)\hat{a}_0\hat{U}^\dagger(\theta) = \iint_{-\infty}^{\infty} u_0(x'+\theta,y)\hat{\psi}^{(+)}(x',y)dx'dy \tag{12.21}$$

$$\approx \iint_{-\infty}^{\infty} \left(u_0(x',y) + \theta u_0'(x',y)\right)\hat{\psi}^{(+)}(x',y')dx'dy, \tag{12.22}$$

where we have used the knowledge that the displacement, θ, is small.

Since we are working with the TEM modes we can substitute $u_0'(x,y) = \frac{1}{w}u_1(x,y)$ to obtain

$$\hat{U}(\theta)\hat{a}_0\hat{U}^\dagger(\theta) = \iint_{-\infty}^{\infty} \left(u_0(x',y) + \theta\frac{u_1(x',y)}{w}\right)\hat{\psi}(x',y)dx'dy \tag{12.23}$$

$$= \hat{a}_0 + \frac{\theta}{w}\hat{a}_1. \tag{12.24}$$

Substituting this back into equation 12.18 gives

$$|\psi(\theta)\rangle = |\alpha\rangle_0 \otimes \left|\frac{\theta\alpha}{w}\right\rangle_1 \otimes |0\rangle_2 \otimes ..., \tag{12.25}$$

which is the state vector for a beam with a small displacement θ.

12.4.2 Signal Operator

Now that we have an appropriate representation of the state, we must consider the signal detected by the SD and PSD when a displaced beam is incident. In each case, the signal density at x, $S(x)$, is given by the product of the relevant detector mode with the photon number density at that point in space. For simplicity, we assume the detector to have a quantum efficiency of 1. While this is not a realistic assumption, it simplifies the calculation to the ideal case:

$$\hat{S}(x,y) = g(x)\hat{\psi}^{(-)}\hat{\psi}^{(+)} \tag{12.26}$$

$$= g(x)\left(u_0(x,y)\hat{a}_0^\dagger + u_1(x,y)\hat{a}_1^\dagger + \sum_{i>1} u_i(x,y)\hat{a}_i^\dagger\right) \tag{12.27}$$

$$\times \left(u_0(x,y)\hat{a}_0 + u_1(x,y)\hat{a_1} + \sum_{i>1} u_i(x,y)\hat{a_i}\right), \tag{12.28}$$

where $u_i(x,y)$ are real.

Since all terms for which $i \neq 0, 1$ are operating on the vacuum state, there are relatively few terms with non-zero contribution when the expectation value is calculated. Hence the signal density operator with all terms relevant to our oscillating beam can be simplified to

$$\hat{S}(x,y) = g(x)\left(u_0(x,y)u_1(x,y)\left(\hat{a}_0^\dagger\hat{a}_1 + \hat{a}_1^\dagger\hat{a}_0\right) + u_0^2(x,y)\hat{a}_0^\dagger\hat{a}_0 + u_1^2(x,y)\hat{a}_1^\dagger\hat{a}_1\right). \tag{12.29}$$

The signal detected by the photodetector is found by integrating over x and y. This expression is simplified by assuming $g(x)$ to be an odd function, which is the case for both the SD and the PSD:

$$\hat{S} = \iint_{-\infty}^{\infty} g(x)u_0(x,y)u_1(x,y)\left(\hat{a}_0^\dagger\hat{a}_1 + \hat{a}_1^\dagger\hat{a}_0\right)dxdy. \tag{12.30}$$

Using the state defined in equation 12.18, the expectation value of the signal is therefore

$$\left\langle \hat{S} \right\rangle = \iint_{-\infty}^{\infty} g(x)u_0(x,y)u_1(x,y)\left\langle \left(\hat{a}_0^\dagger\hat{a}_1 + \hat{a}_1^\dagger\hat{a}_0\right)\right\rangle dxdy \tag{12.31}$$

$$= \iint_{-\infty}^{\infty} g(x)u_0(x,y)u_1(x,y)\frac{2N\theta}{w}dxdy, \tag{12.32}$$

where N is the total number of photons detected.

12.4.3 Noise Operator

The noise on the signal measured by the detector is given by the square root of the variance in the signal:

$$\Delta S = \sqrt{\left\langle \hat{S}^2 \right\rangle - \left\langle \hat{S} \right\rangle^2}. \tag{12.33}$$

Since the oscillation is small, we approximate $\theta = 0$ for the purpose of calculating noise, meaning we consider the beam to be as in equation 12.13. This means $\left\langle \hat{S} \right\rangle = 0$, and so

$$\Delta S = \sqrt{\left\langle \hat{S}^2 \right\rangle}. \tag{12.34}$$

When calculating $\hat{S}^2$ it is necessary to look back at equation 12.28 as the higher order modes have a non-zero contribution to the noise. Therefore

$$\hat{S}^2 = \left(\iint_{-\infty}^{\infty} g(x)\left(u_0(x,y)a_0^\dagger + \sum_{i\neq 0} u_i(x,y)a_i^\dagger\right)\left(u_0(x,y)a_0 + \sum_{i\neq 0} u_i(x,y)a_i\right)dxdy\right)^2. \tag{12.35}$$

To calculate this it is helpful to consider that only terms with operators in the order $\hat{a}_0^\dagger\hat{a}_\alpha\hat{a}_\alpha^\dagger\hat{a}_0$ will have a non-zero contribution when $\left\langle \hat{S}^2 \right\rangle$ is calculated using a coherent state, as will be the case here. Thus,

$$\hat{S}^2 = \iint_{-\infty}^{\infty} g(x) \left(u_0(x,y)\hat{a}_0^\dagger \sum_{i\neq 0} u_i(x,y)\hat{a}_i \right) dxdy \tag{12.36}$$

$$\times \iint_{-\infty}^{\infty} g(x') \left(\sum_{i\neq 0} \left(u_i(x',y')\hat{a}_i^\dagger \right) u_0(x',y')\hat{a}_0 \right) dx'dy', \tag{12.37}$$

where it should be noted that the sums are over the same i.

The expectation value of $\hat{S}^2$ when operating on a coherent state is therefore

$$\left\langle \hat{S}^2 \right\rangle = \left\langle \iint_{-\infty}^{\infty} g(x) \left(u_0(x,y)\hat{a}_0^\dagger \sum_{i\neq 0} u_i(x,y)\hat{a}_i \right) dxdy \right. \tag{12.38}$$

$$\left. \times \iint_{-\infty}^{\infty} g(x') \left(\sum_{i\neq 0} \left(u_i(x',y')\hat{a}_i^\dagger \right) u_0(x',y')\hat{a}_0 \right) dx'dy' \right\rangle \tag{12.39}$$

$$= N \iint_{-\infty}^{\infty} g(x)u_0(x,y) \left(\sum_{i\neq 0} u_i(x,y) \left\langle 0 \right|_i \hat{a}_i \right) dxdy \tag{12.40}$$

$$\times \iint_{-\infty}^{\infty} g(x')u_0(x',y') \left(\sum_{i\neq 0} u_i(x',y')\hat{a}_i^\dagger \left| 0 \right\rangle_i \right) dx'dy' \tag{12.41}$$

$$= N \iiiint_{-\infty}^{\infty} g(x)g(x')u_0(x,y)u_0(x',y') \sum_{i\neq 0} u_i(x,y)u_i(x',y')dxdydx'dy'. \tag{12.42}$$

We now use the knowledge that u_i are a complete orthonormal basis set and so

$$\sum_i u_i(x,y)u_i(x',y') = \delta(x-x')\delta(y-y'). \tag{12.43}$$

Since the contribution from the $i = 0$ term is zero we can consider the sum in equation 12.42 to be over all i, and therefore equation 12.42

$$\left\langle \hat{S}^2 \right\rangle = N \iint_{-\infty}^{\infty} g^2(x)u_0^2(x,y)dxdy. \tag{12.44}$$

Finally, the general expression for the noise on our signal is found by taking the square root of equation 12.44:

$$\Delta S = \sqrt{N \iint_{-\infty}^{\infty} g^2(x) u_0^2(x,y) dx dy}. \tag{12.45}$$

Intuitively, we see that when both $g(x)$ and $u_0(x,y)$ are large the noise contribution is also very large. Therefore it is beneficial to choose $g(x)$ such that it is small where $u_0(x,y)$ is large to minimise the noise.

Now that we have expressions for the expectation value of the signal, equation 12.32, and the noise, equation 12.45, we can find the SNR of our two detectors.

12.4.4 Split Detector SNR

For the split detector, $g(x) = \Theta(x) - \Theta(-x)$. Therefore the signal is

$$\left\langle \hat{S}_{\mathrm{SD}} \right\rangle = \iint_{-\infty}^{\infty} u_0(x,y) u_1(x,y) \frac{2N\theta}{w} dx dy \tag{12.46}$$

$$= \frac{2N\theta}{w} \frac{4}{\pi w^3} \frac{\sqrt{\pi} w}{\sqrt{2}} \frac{w^2}{2} = \frac{2\sqrt{2} N\theta}{\sqrt{\pi} w}, \tag{12.47}$$

and the noise is

$$\Delta S_{\mathrm{SD}} = \sqrt{N \iint_{-\infty}^{\infty} u_0^2(x,y) dx} \tag{12.48}$$

$$= \sqrt{N}. \tag{12.49}$$

Hence the SD has an SNR of

$$\mathrm{SNR}_{\mathrm{SD}} = \frac{2\sqrt{2}\theta}{\sqrt{\pi} w} \sqrt{N} \tag{12.50}$$

12.4.5 PSD SNR

Similarly for the PSD, which has a detector mode $g(x) = \frac{x}{L}$, where L is the length of the detector, the signal is

$$\left\langle \hat{S}_{\mathrm{PSD}} \right\rangle = \iint_{-\infty}^{\infty} \frac{x}{L} u_0(x,y) u_1(x,y) \frac{2N\theta}{w} dxdy \tag{12.51}$$

$$= \iint_{-\infty}^{\infty} \frac{w}{2L} u_1^2(x,y) \frac{2N\theta}{w} dxdy \tag{12.52}$$

$$= \frac{N\theta}{L}, \tag{12.53}$$

and the noise is

$$\Delta S_{\mathrm{PSD}} = \sqrt{N \iint_{-\infty}^{\infty} \frac{x^2}{L^2} u_0^2(x,y) dxdy} \tag{12.54}$$

$$= \sqrt{N \iint_{-\infty}^{\infty} \frac{w^2}{4L^2} u_1^2(x,y) dxdy} \tag{12.55}$$

$$= \frac{w}{2L}\sqrt{N}. \tag{12.56}$$

Therefore, the SNR of the PSD is

$$\mathrm{SNR}_{\mathrm{PSD}} = \frac{2\theta}{w}\sqrt{N}. \tag{12.57}$$

From this we see that the minimum displacement which can be measured with the PSD, corresponding to an SNR of 1, is

$$\theta_{\min} = \frac{w}{2\sqrt{N}}, \tag{12.58}$$

which is equal to the minimum given by the QCRB in equation 12.8. Therefore, we see that the PSD saturates the QCRB and provides the best possible measurement of the displacement of our laser beam for our given optical setup.

We expect the PSD to have an SNR which is better than that of the SD when detecting the intensity of a signal corresponding to a small displacement, θ, by a factor of $\sqrt{\frac{\pi}{2}}$. Since we will generally be using a spectrum analyser to monitor the output of the detectors, which measures the power at the noise and signal frequencies, we expect the ratio of the measured SNRs to be $\frac{\pi}{2}$, which is approximately 2 dB.

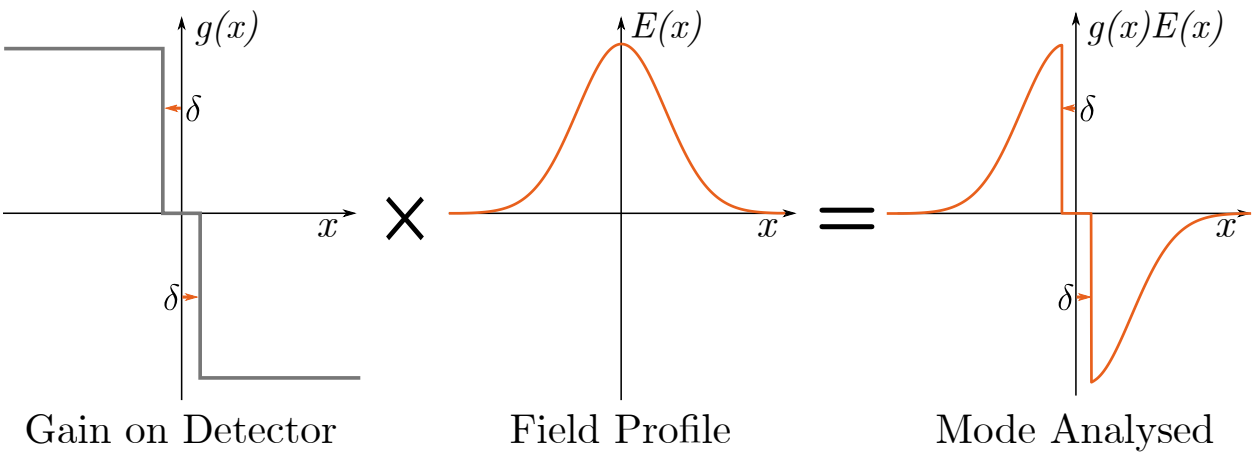

Figure 12.3 A more realistic resultant profile of the detector mode combined with the beam mode results in the detected, or analysed, mode for the split detector including the dead region.

12.5 Split Detector Dead Region

Until this point we have considered the dead region in the centre of the split detector to be negligible, and assumed the gain on the detector a step function shown in figure 12.2a. However in reality there is a small portion in the centre where the gain is zero as no light is detected; a more realistic detector mode is shown in figure 12.3. Since this new, more accurate detected mode is actually a little closer to the shape of the TEM01 mode there is reason to believe the SNR of the actual split detector may be slightly better than the theoretical prediction which ignores the dead region might indicate.

Including the dead region we find, using equation 12.32 and the result from equation 12.47, that the expectation value for the signal of the split detector with dead region of size 2δ is

$$\left\langle \hat{S}_\delta \right\rangle = \frac{2\sqrt{2}\theta}{\sqrt{\pi}w}N - \int_{-\delta}^{\delta}\int_{-\infty}^{\infty}\Theta(x)u_0(x,y)u_1(x,y)\frac{2\theta}{w}Ndxdy \tag{12.59}$$

$$= \frac{2\sqrt{2}\theta}{\sqrt{\pi}w}N - \frac{16\theta N}{\pi w^4}\int_{0}^{\delta}\int_{-\infty}^{\infty} xe^{-\frac{2(x^2+y^2)}{w^2}}dxdy \tag{12.60}$$

$$= \frac{2\sqrt{2}\theta}{\sqrt{\pi}w}N - \frac{16\theta N}{\pi w^4}\left(\frac{w^2}{4}\frac{w\sqrt{\pi}}{\sqrt{2}}(1-e^{-\frac{2\delta^2}{w^2}}\right) \tag{12.61}$$

$$= \frac{2\theta}{\sqrt{\pi}w}Ne^{-\frac{2\delta^2}{w^2}} \tag{12.62}$$

Similarly, using equation 12.45 we find the noise on the signal of the split detector with the dead region to be

$$\left\langle \hat{S}_\delta{}^2 \right\rangle = N - N\int_{-\delta}^{\delta}\int_{-\infty}^{\infty} u_0^2(x,y)dxdy \tag{12.63}$$

$$= N - \frac{4N}{\pi w^2}\int_{0}^{\delta}\int_{-\infty}^{\infty} e^{-\frac{2(x^2+y^2)}{w^2}}dxdy \tag{12.64}$$

$$= N\left(1-\mathrm{erf}(\frac{\sqrt{2}\delta}{w})\right) \tag{12.65}$$

$$\approx N\left(1-\frac{2\sqrt{2}}{\sqrt{\pi}w}\delta\right). \tag{12.66}$$

This results in an SNR which depends on the size of the dead region, 2δ, and is given by

$$SNR_\delta = \frac{2\theta}{\sqrt{\pi}w}\sqrt{N}\frac{e^{-\frac{2\delta^2}{w^2}}}{\sqrt{1-\frac{2\sqrt{2}}{\sqrt{\pi}w}\delta}} \tag{12.67}$$

$$\approx \frac{2\theta}{\sqrt{\pi}w}\sqrt{N}\left(1-\frac{2\delta^2}{w^2}\right)\left(1+\frac{\sqrt{2}}{\sqrt{\pi}w}\delta\right), \tag{12.68}$$

valid for small values of $\frac{\delta}{w}$, which is plotted in figure 12.4. We see that for small dead region, 2δ, the SNR is actually improved over the case with no dead region, with the maximum SNR occuring at a dead region with of around 0.45. Therefore, we would expect to see an SNR ratio between the SD and PSD which is slightly lower than the value predicted previously.

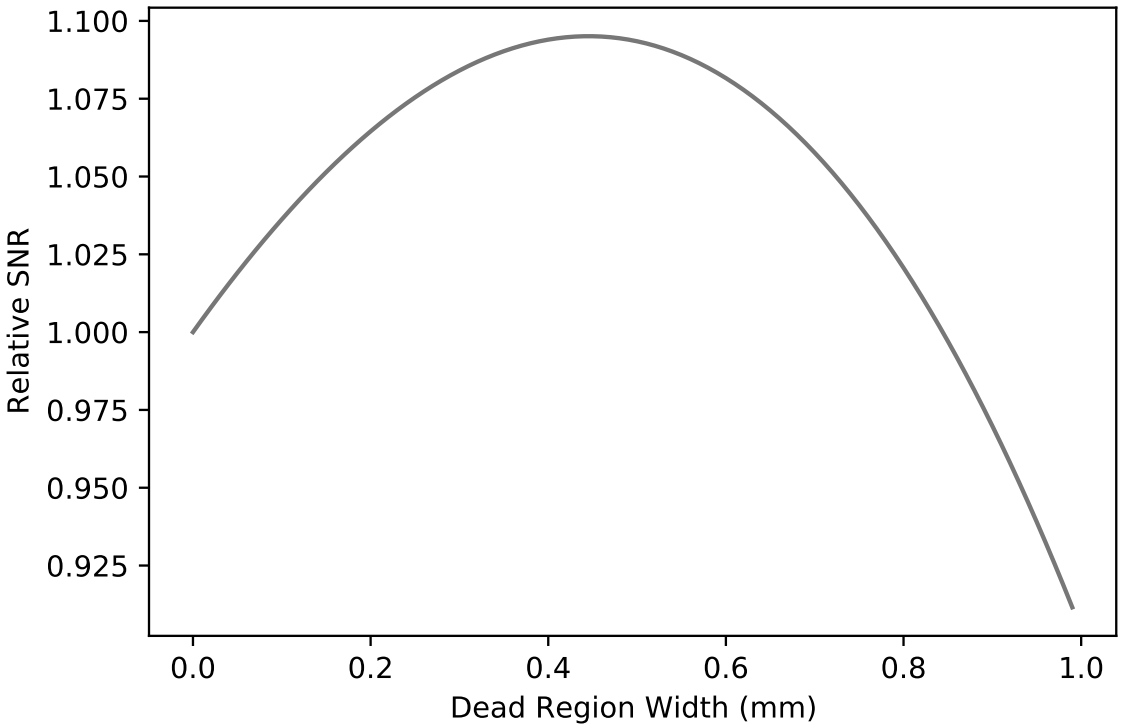

Figure 12.4 Modelled results for how the SNR of the split detector varies with the size of the dead region, relative to the SNR with no dead region. Interestingly, we see that a small dead region actually improves the SNR.

Chapter Thirteen

Building and Characterising Detectors

In order to experimentally verify the theoretical prediction for the SNR ratio between the two position detectors, they had to be built and tested. As was the case with the BPD, it was important for both detectors to be shot noise limited in the range of measurement parameters for which we are interested: again it was necessary to use relatively high analysing frequencies of at least 100 kHz to avoid the classical noise which dominates at low frequencies.

The circuit schematic, component selection and PCB layout for an initial detector design to test the AC filter and instrumentation amplifiers was done by myself. This prototype was then assembled and debugged by two masters students, Carlton French and Lucas Rushton, with my assistance. They also added to the design the SD and PSD chips and assembled the final version of the circuit. The calculations for and final selection of the components for the Ac filter was done by myself, as was the circuit characterisation discussed in this section.

13.1 Building the Detectors

When designing the TA circuits for the PSD and SD chips, the design used for the BPD (discussed in section 6.2) was used as a basis. Unfortunately, the split photodiode and position detection chips both have a common cathode. This prevents the photocurrents from being subtracted before the transimpedance amplifier, as was done for the BPD by

oppositely biasing the two photodiodes, as the two halves of the detector must be biased in the same direction due to their shared cathode. This meant that a separate TA was required for each half of the photodetector. With the DC component of the signal still present the output voltage of the op amps used in the transimpedance stage saturates at a relatively low gain, making it difficult for the shot noise to overcome electronic noise introduced by the op amp itself. In particular, the voltage input noise introduced by the op amp was problematic as this is often relatively high for high bandwidth, low noise op amps. The reason for this is simply that the applications of such chips commonly involve large gains, and it is unusual to be limited by the voltage noise. Instead, the current noise (which is amplified along with the signal input current) is usually the limiting factor and therefore low current noise characteristics are preferable. It is almost always the case that, in the amplifiers considered, at gains low enough to not saturate the output of the op amps the voltage input noise severely limited performance. Note that while it is possible to choose an op amp with a higher supply voltage, and therefore a greater maximum output voltage, typically the ones with the low noise, high GBP characteristics needed for sub-shot-noise photodetection have an operating voltage of 5V and a maximum output voltage closer to 4V. This is typically the limiting factor on our gain for a signal with the DC component still present. Therefore it was necessary to make a few modifications to the original BPD circuit.

The core elements of the new circuit are represented in figure 13.1. The key idea is that the addition of an AC filter immediately after each side of the photodetector chip allows the DC component of each signal to be significantly attenuated before the TAs, greatly increasing the tolerable gain before the op amps are saturated and ensuring the voltage input noise of the op amps is not the most significant source of noise in the circuit. Assuming this to be the case, we must now simply ensure the dominant noise current on the input is that of the shot noise.

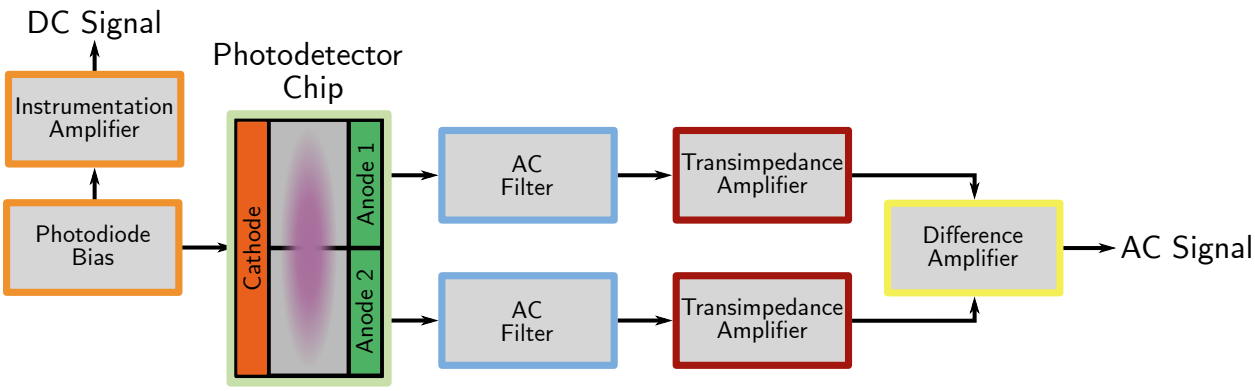

Figure 13.1 A flow diagram of the position detector circuit. The photodetector chip used here is the SD, but the electronics used for the PSD is completely equivalent.

13.1.1 Circuit Modifications

AC Filter

An AC filter consists of a resistor, R_{AC}, and capacitor, C_{AC}, connected as shown in figure 13.2. The addition of this filter causes any components of the generated photocurrent with frequency lower than the cutoff frequency,

$$f_c = \frac{1}{2\pi R_{\mathrm{AC}} C_{\mathrm{AC}}}, \tag{13.1}$$

to be attenuated. When choosing an appropriate resistance value for the AC filter both the thermal noise introduced and the voltage drop across the resistor must be considered. It is clear that this thermal noise current must not be greater than the shot noise current, and since the thermal noise current of a resistance is given by

$$i_n = \sqrt{\frac{4k_B T}{R}}, \tag{13.2}$$

where T is the temperature of the resistor and k_B is the Boltzmann constant, larger values of R are called for to minimise the added thermal noise. Unfortunately, the voltage drops across the filter resistors also cause the photodiode to de-bias as incident optical power was increased. To understand this, consider the circuit diagram in figure 13.2, where the

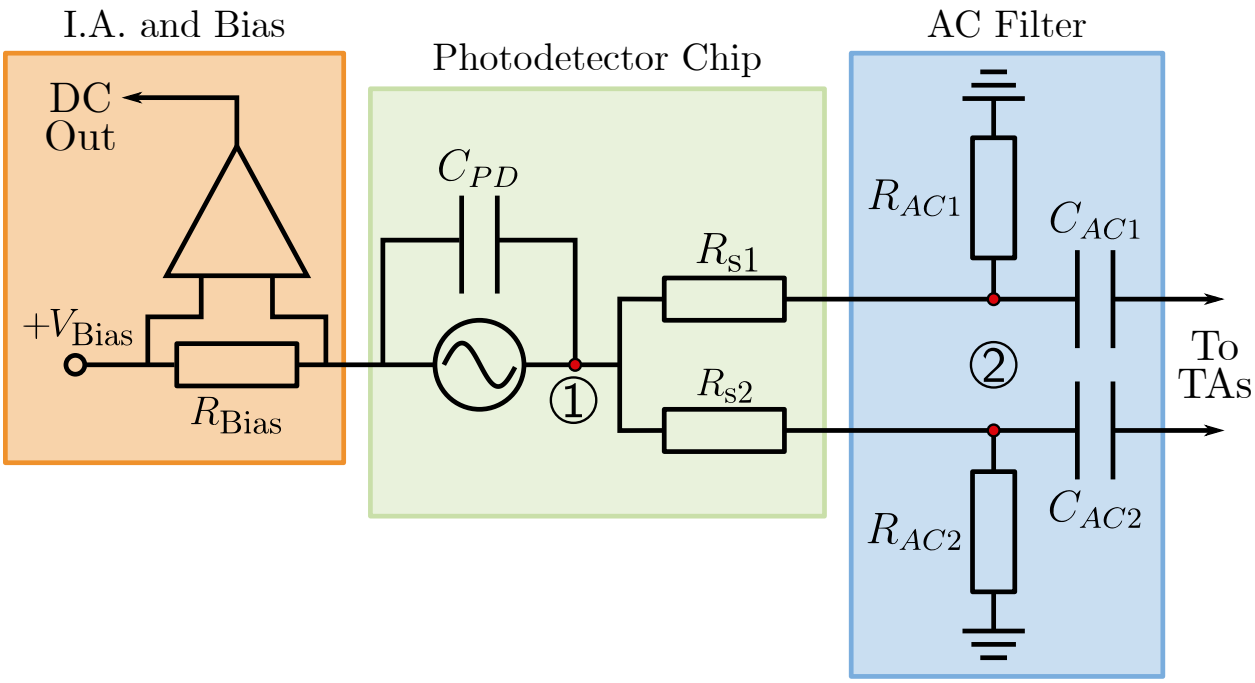

Figure 13.2 An equivalent circuit diagram of the key components of the front end of both the PSD and SD chips. The instrumentation amplifier measures the voltage drop across the bias resistor, R_{bias} to monitor the combined DC power on both sides of the chip. An AC filter has been added to each anode to remove the DC component of the signal before it is passed to the transimpedance amplifier. Red dots indicate key points in the circuit which will be discussed.

components of the AC filter are shown. For now, the series resistance of the photodetector chip is assumed to be negligible. Low frequency components of the current produced by the photodetector chip cannot flow through the AC filter capacitors, and instead flows across the AC filter resistors. The resultant voltage drop across these resistors cause a non-zero voltage at point 2. As the photocurrent increases this potential also increases, and when this becomes equal to the bias voltage applied to the chip it will no longer be biased and no longer respond correctly to changes in optical power. At this point, the AC filter has caused the photodetector to become de-biased.

Therefore, when adding an AC filter to our photodetector, it is desirable to use a large resistance to reduce thermal fluctuations, but a small resistance to increase the optical power at which de-biasing of the detector occurs. In fact, continuing to ignore the internal series

resistance for a moment, these two effects balance one another, meaning provided the Johnson noise introduced by the AC filter is the dominant source of electronic noise then from the perspective of optimising the ratio of shot noise to electronic noise the AC resistor value is irrelevant.

Series Resisitance The internal series resistance of the photodiode, R_{s1} and R_{S2}, are represented in figure 13.2 explicitly. Note that each anode has a separate series resistance associated with it. For the SD, this value is small, fixed and equal for the two sides of the detector. For the PSD these resistances are larger, on the order of $\approx 100\,\mathrm{kHz}$, and vary with the point of the chip surface one considers. The voltage drop across the internal series resistance of the photodetector chip will cause a voltage to be present at point 1 in figure 13.2. Typically this voltage drop is negligible due to the small value of the internal series resistance, however in the case of the PSD the series resistance must be considered when choosing appropriate component values as its thermal noise contributes to the electronic noise on the subtracted signal.

Including the contribution of the series resistances, if the voltage at point 1 becomes equal to the bias voltage the photodiode will no longer be biased and will become unresponsive. This occurs when the incident optical power is sufficient to generate a photocurrent, i_{PC}. and assuming the beam is centred such that the generated photocurrent, i_{PC}, is divided equally between the two anodes, and the series resistance of the two anodes is equal, this de-biasing occurs when

$$\frac{i_{\mathrm{PC}} R_s}{2} = V_{\mathrm{Bias}}, \tag{13.3}$$

where $R_s = R_{s1} = R_{s2}$.

Therefore, the de-biasing can be overcome by increasing the bias voltage, and it will always be preferable to have a larger bias voltage for the purpose of improving our SNR as this helps increase both detector bandwidth and optical power at saturation.

It is important here to note that when discussing the series resistance of the PSD there are two different regiemes to consider: when discussing electronic noise, the total resistance between the two anodes (the interelectrode resistance) is the important quantity; however, when considering the voltage drop across the series resistance we should consider the resistance between the point on the chip where the photoelectrons are generated and the anodes. This second series resistance will always be smaller, and is always impacted by the beam size. Since we want to maximise the voltage at which de-biasing occurs, it is preferable to make the beam as large as possible on the chip to make the series resistance which causes the voltage at point 1 in figure 13.2 to be produces as small as possible.

While the internal series resistance is a property of the chip and is not easy to change, the AC filter components can easily be set to any value required. A smaller value of R_{AC} results in a smaller voltage drop, which means the de-biasing of the photodiode will occur at a higher optical power. Unfortunately this also results in increased Johnson-Nyquist noise, which has noise current density for a given resistance, R, as given in equation 13.2.

Generally, the benefit of using a higher power beam is an increased shot noise level, which makes it easier for the shot noise limit to be above the electronics noise floor. Since shot noise is proportional to $\sqrt{N}$, where N is the number of photons, the shot noise current, i_{SN}, is proportional to the square root of the total photocurrent, i_{PC}. Assuming we operate just below the point where the detector debiases, and with equal power on either side of the detector, the total shot noise current at saturation is given by

$$i_{\mathrm{SN}} = \sqrt{i_p} = \sqrt{\frac{V_{\mathrm{Bias}}}{R_{s1} + R_{\mathrm{AC}}} + \frac{V_{\mathrm{Bias}}}{R_{s2} + R_{\mathrm{AC}}}}. \tag{13.4}$$

An optimum value of R_{AC} for a given internal resistance can be found by maximising the ratio the shot noise current given in equation 13.4 to the electronic/thermal noise introduced by the resistors, assuming this to be the dominant source of electronic noise. As the internal resistance of the PSD is the more complex of the two cases due to to series resistance connecting the two halves of the circuit together, the value chosen for R_{AC} for both circuits

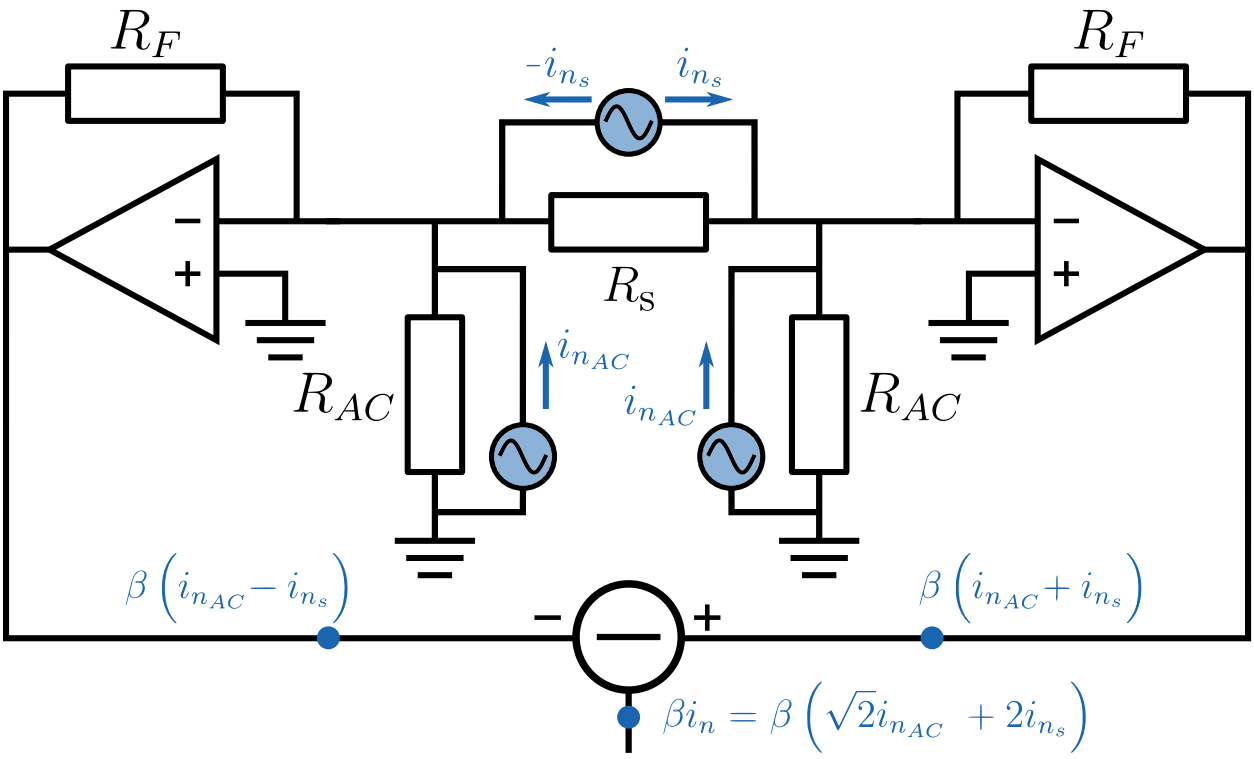

Figure 13.3 A simplified schematic of PSD circuit for the purpose of analysing the noise current introduced by the series resistance of the PSD, R_s, and the resistors used in the AC filters, R_{AC}. The capacitors in the AC filter have not been included, as the each act as a short circuit for the high frequencies we are interested in.

will be based of the internal resistance, R_{s1}, of the PSD.

From figure 13.3 we can calculate the expected noise contribution from the PSD and AC filtering resistors, which is treated as a current source in parallel with the resistances, producing a current which is given by equation 13.2. We assume we are only concerned with noise around our analysing frequency, which will be significantly high that the capacitance of the AC filters can be treated as a short circuit, as in the diagram. Additionally, we assume the feedback resistors, R_F, to be significantly large that their contribution to the thermal noise is negligible. The feedback capacitors are not shown in this diagram as their role is primarily in the stability of the transimpedance stage and their effect on the noise is not significant, and the transimpedance gain is simply β.

The series resistance of the PSD, R_s, produces equal and opposite noise contributions to

the two anodes. This current experiences a transimpedance gain of β. The noise currents are perfectly anticorrelated, which means when the subtraction is performed we see a total contribution from the series resistor to the noise voltage of $2\beta i_{n_s}$[94]. Meanwhile, each of the AC resistors, R_{AC}, contribute a noise current, $i_{n_{\mathrm{AC}}}$, which also experiences a transimpedance gain of β. Note that this current does not flow across R_s due to either side of R_s being held at 0 V by the transimpedance amplifiers. Since this noise is random and uncorrelated, when the signals are subtracted the noise voltage contribution is $\beta\sqrt{2}i_{n_{\mathrm{AC}}}$.

Therefore, the total thermal noise contribution from the series and AC resistances is

$$\beta i_n = \beta\left(\sqrt{2}i_{n_{\mathrm{AC}}} + 2i_{n_s}\right). \tag{13.5}$$

To maximise the ratio of shot noise at saturation power, calculated in equation 13.4, we consider the case where the beam is positioned centrally on the detector such that $R_{s1} = R_{s2} \approx {}^{R_s}/_{n}$, where n is a value which depends on the waist of the beam on the PSD. We must maximise

$$\frac{i_{\mathrm{SN}}}{i_n} = \frac{\sqrt{2}\sqrt{\frac{V_{\mathrm{bias}}}{R_{\mathrm{AC}}+\frac{1}{3}R_s}}}{\sqrt{2}\sqrt{\frac{4k_BT}{R_{\mathrm{AC}}}} + 2\sqrt{\frac{4k_BT}{R_s}}}, \tag{13.6}$$

where we have divided through by the gain factor, β, which is common to both the shot noise and the electronic noise.

Taking the derivative of equation 13.6 with respect to the AC resistance, R_{AC}, we find the maximum ratio of shot noise current to electronic noise current occurs when $R_{\mathrm{AC}} = \left(n\sqrt{2}\right)^{-\frac{2}{3}} R_s$. We expect the series resistance experienced by photoelectrons on average to be around a third of the total series resistance, R_s. For this case, i.e. $n = 3$, we find the value of R_{AC} should be about 40% that of R_s. A value of 50 kΩ was used.

Note that the de-biasing also affects the capacitance of the photodiode, meaning as the bias changes the characteristics of the whole circuit changes due to this change in capacitance. Therefore the circuit must be designed considering the capacitance of the photodiode for a

Characteristic	**SD** (S3096-02)	**PSD** (S458406-06)
Photosensitive Area	(1.2×3) mm	(1×3.5) mm
Dead Region Width	30 µm	N/A
Photosensitivity	0.5 A/W	0.48 A/W
Capacitance	5 pF	15 pF
Dark Current	0.05 nA	0.05 nA
Interelectrode Resistance	N/A	140 kΩ*

Table 13.1 Key specifications of the SD and PSD.
∗Typical resistance between the two anode pins.

small bias voltage, ensuring that the bandwidth is sufficiently high even at this capacitance. However, the capacitance given in the datasheets[94][95] and in table 13.1 are for a reverse bias of 1 V so this is a reasonable value to use when deciding component values for the rest of the circuit.

Generally, the two photodiodes are relatively similar in their characteristics. The small difference in size and responsivity can be mostly negated with a calibration to ensure the optical power detected by each chip is the same, although it should be ensured that the beam is not significantly larger than the chip as this will affect the mode of the beam detected by each chip.

Instrumentation Amplifier

Unfortunately, removing the DC component of the signal means we were no longer able to measure the DC power in the optical beam by blocking one eye of the photodetector at a time, as was done with the BPD. Therefore, to allow the total optical power incident on the photodetector to be measured, an instrumentation amplifier was added across the resistor, $R1$, as shown in figure 13.2. This allowed the small voltage drop across this resistor, proportional to the total photocurrent generated in the photodiodes, to be measured with reasonable accuracy. The bandwidth of the instrumentation amplifier was quite low, however we expect the optical power to remain relatively constant so this was not an issue.

Unfortunately, due to the common cathode, this method could not be used to measure the power on each half of the photodetector independently.

Subtraction Stage

As the photocurrents can no longer be subtracted, a difference amplifier was added to the circuit, as illustrated in figure 13.1. At this stage it was possible to relax the requirements on the noise characteristics of the chosen op amp slightly as the input signal was already quite large, making it far easier to overcome the electronic noise of the op amp itself. The greatest barrier here lay in choosing an op amp which could accept a sufficiently high common mode input, as the signals out of the transimpedance stage were between -3 V and 3 V. The OPA657 was used for this purpose as it was easily accessible to us and had a comfortably sufficient noise and bandwidth performance. It is possible that a chip could have been chosen with a higher saturation power, allowing for additional amplification and pushing us further from electronic noise.

Circuit Performance Analysis

It must be mentioned that the improvement in performance gained by adding the AC filter was marginal, so it is worth asking if it was really a necessary addition in the first place. The higher gain possible in the TA stage with the addition of the filter comes at the cost of the introduction of an additional saturation point in the form of the de-biasing of the photodiode and additional thermal noise introduced by the AC filters' resistors. In short, the main benefit of the AC filter is the ability to overcome the input voltage noise of the op amps used in the TAs. As explained before, op amps for applications such as this are typically poorly optimised for low gain, and being limited by voltage noise is generally a rather bad place to be. However, in hindsight it may have been possible to find a better optimised op amp which would have functioned as well as the AC filters without the need for a new circuit design. However, it is also worth noting that the additional difference amplifier

would still have been necessary, and the instrumentation amplifier is useful even without the AC filter as then grant the ability to instantly measure the DC power incident on the chip without disturbing the noise measurement.

13.2 Detector Characterisation

To verify that the detectors were shot noise limited, measurements were conducted to characterise their behaviour and determine the experimental parameters for which they were limited by quantum noise. This was achieved by characterising the detectors' noise and DC voltage outputs with respect to varied incident optical power. A beam with an optical power which could be varied using a PBS and HWP was centred on the photosensitive surface of the photodetector. The noise output of the photodetector was then measured using a spectrum analyser, and the DC output of the instrumentation amplifier was measured using an oscilloscope. From this DC measurement a separate calibration could be used to determine the optical power incident on the detector. For a shot noise limited device, we expect the relationship between incident optical power and measured noise to be linear as the noise power is proportional to the number of photons, N, or the intensity of the beam. If the detector is limited by electronic noise, however, the relationship will not be linear.

It is important to use approximately the same beam size for the characterisation as will be used in any subsequent measurements for the PSD, as the saturation power will depend on beam size due to the dependence of the internal resistance on beam size. As the characterisation will only be used to determine a saturation power and will not be used directly in calculating the SNR there is some tolerance in how well the beam size must match that used in when measuring the SNR. This should allow for slight variation in the physical position of the photodetector relative to the imaging system between the two cases.

The large beam characterisations were performed at several different analysing frequencies, with the RBW and VBW set to 1 kHz and 30 Hz respectively, to gain insight into the

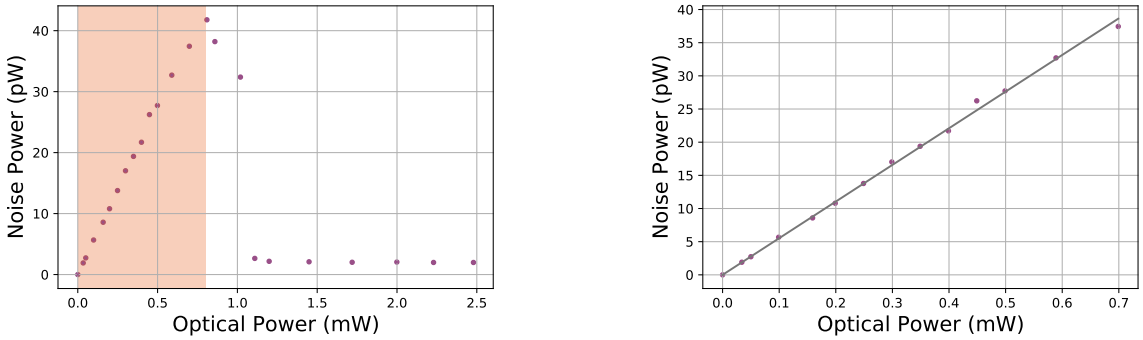

(a) All powers. **(b)** Linear region.

Figure 13.4 Split detector noise with respect to optical power at 500 kHz analysing frequency.

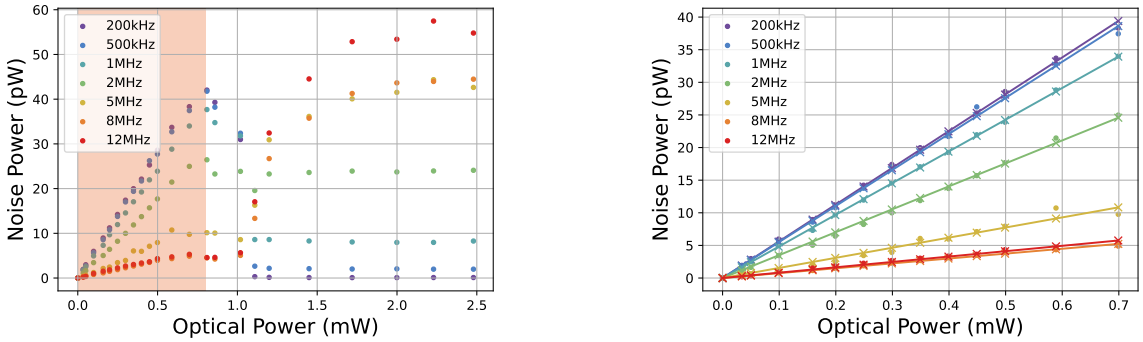

(a) All powers. **(b)** Linear region.

Figure 13.5 Split detector noise with respect to optical power at various analysing frequencies.

bandwidth of the detector and allow an optimum signal frequency to be chosen for the SNR measurement. A 5 s zero span measurement of noise power at the chosen analysing frequency was taken for each optical power and the average value of the trace used.

The optical power to noise plots for the split detector and PSD are given in figures 13.4a to 13.6b. The left hand plots are the 'full' data sets, showing the saturation points, whereas the right hand plots correspond to the linear region, indicated in orange on the left hand plots, with linear fits applied. We expect the plots to go through the origin since a background subtraction is performed to remove electronic noise.

From these plots, shown in figures (13.5- 13.7), we see that both detectors are comfortably

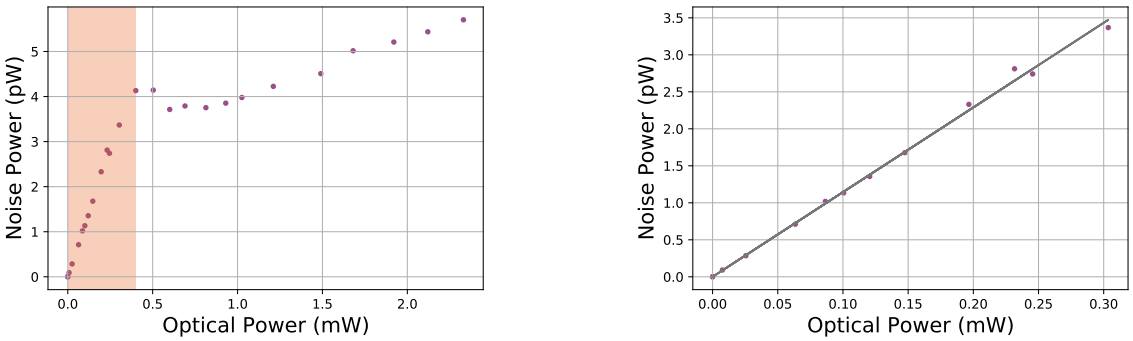

(a) All powers. **(b)** Linear region.

Figure 13.6 PSD noise with respect to optical power at 500 kHz analysing frequency.

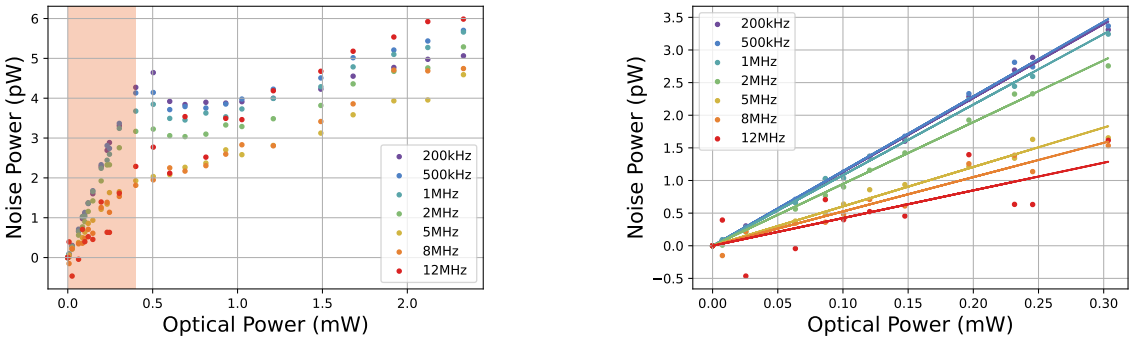

(a) All powers. **(b)** Linear region.

Figure 13.7 PSD noise with respect to optical power at various analysing frequencies.

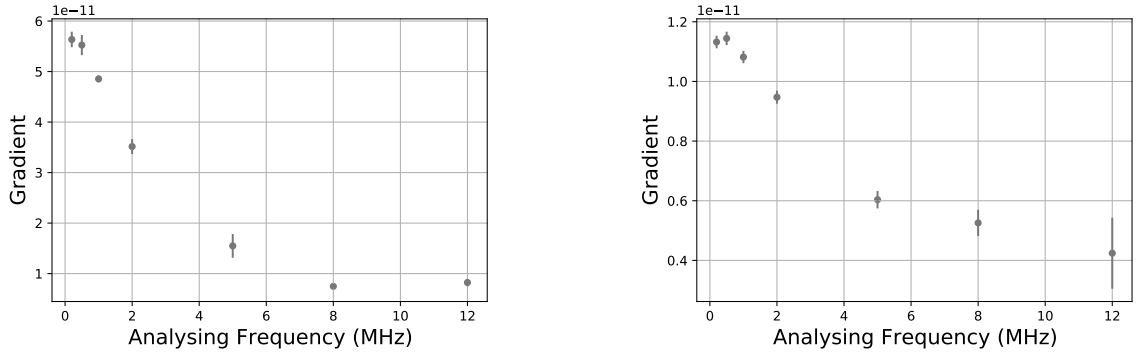

(a) Split detector. **(b)** PSD.

Figure 13.8 The linear region gradient with respect to analysing frequency of each detector.

shot noise limited up to an optical power of around 0.4 mW for an analysing frequency of 1 MHz or under. Therefore, the SNR measurements will be performed using parameters which lie within this range.

Figure 13.8 shows how the gradient of the linear response region of the PSD and split detectors, effectively the gain of the detector, varies with analysing frequency. The gradient of the linear section for both detectors decreases with increasing analysing frequency. This higher gain at lower frequencies is normal, as it is governed by the bandwidth of the detector as explained previously. For the split detector, the response remains linear even at 12 MHz analysing frequency. For the PSD this is not the case due to the higher capacitance of the photodiode, made even more significant by the faster de-biasing due to the higher internal resistance, which results in a much lower bandwidth for this detector.

Since the detectors are slightly different sizes, if the beams are any larger than the photodiodes they will detect different powers. To determine whether this is occurring, a second measurement was performed using a small beam, which ensured all optical power was detected by the photodiode. From this the detectors could each be calibrated to allow the detected optical power to be accurately determined from the voltage output of the instrumentation amplifier. The calibration plots are given in figures 13.9a to 13.10b.

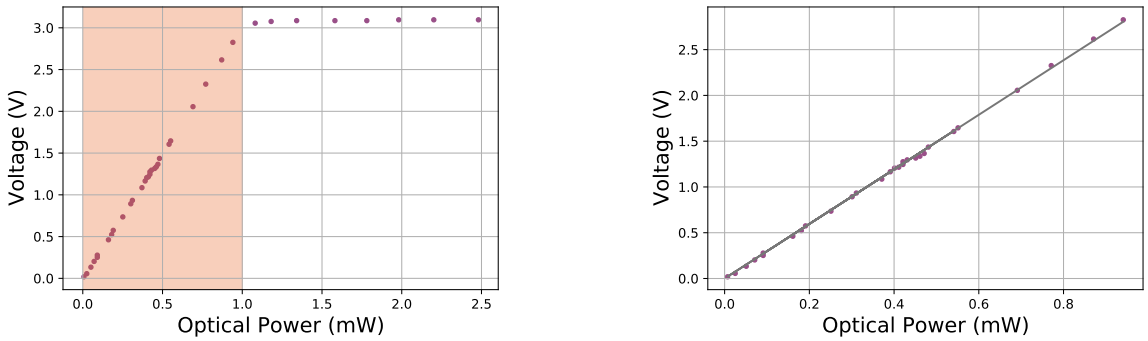

(a) All powers. **(b)** Linear region.

Figure 13.9 Split detector voltage with respect to optical power, taken using a small beam waist on the detector.

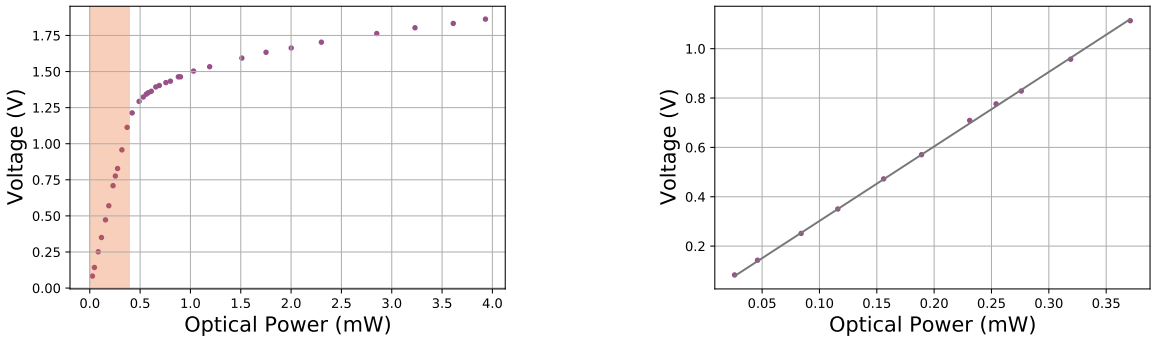

(a) All powers. **(b)** Linear region.

Figure 13.10 PSD voltage with respect to optical power, taken using a small beam waist on the detector.

With the smaller beam, the PSD saturates at a much lower optical power than the SD: around 0.4 mW compared to 1 mW. This is due to the higher internal resistance of the PSD, which is even greater with a small beam size. To allow these voltage calibrations to be used, and to ensure we are in the shot noise limited regime for both detectors throughout measurements, optical powers below 0.4 mW will always be used when making SNR measurements.

Chapter Fourteen

SNR Measurement

To determine the SNR of each detector, we must provide a signal in the form of a beam oscillating about its transverse centre position at a chosen analysing frequency. Effectively, we want to displace the beam by a small amount in the horizontal transverse direction. This must be done at a stable and relatively high frequency (100s of kHz) in order to ensure the signal is in a region where the detectors are shot noise limited. Measuring the spectral power density at this frequency gives the 'signal', and the noise is determined by measuring the spectral power density at a frequency away from the signal frequency.

There were several experimental parameters which were difficult to know experimentally, predominantly the displacement of the beam at the surface of the photodetector. Therefore, instead of making a measurement of the absolute SNR of each detector, it was decided to measure the ratio of their SNRs. This eliminated the need to know many experimental parameters; instead, we just had to ensure the parameters were kept constant for both detectors. In doing this, the assumption was made that the SD performed experimentally exactly as we predicted theoretically, with an SNR equal to that given in equation 12.50. Therefore, if the ratio between the SNR measured experimentally for the SD and PSD was equal to the theoretical ratio, $\pi/2$ when measuring the noise and signal power, we can infer that the SNR of the PSD is equal to that which we calculated in equation 12.57 and that the detector is capable of saturating the QCRB.

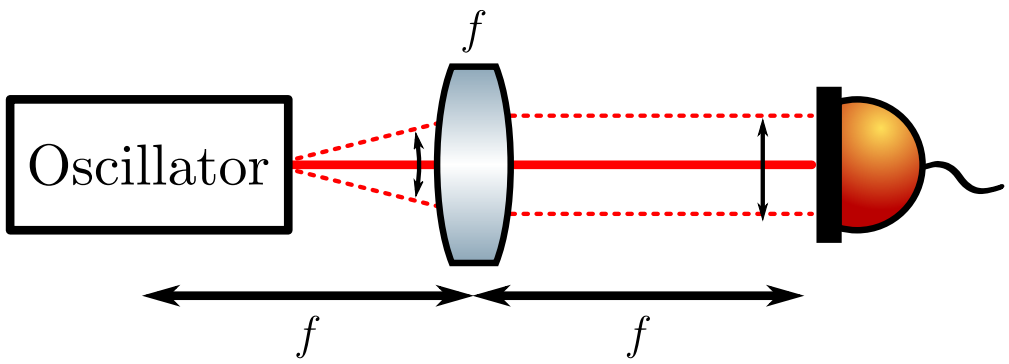

Figure 14.1 The imaging scheme used to capture the motion of the beam. The single lens placed one focal lens away from the oscillation source forms a far-field image one focal length away on the detector.

14.1 Creating a Test Signal

The first consideration when creating an ideal signal with which to measure the SNR of the two detectors is the mode of the beam itself. The laser used in this experiment was a Toptica DL Pro Diode laser at 794 nm[96]. To ensure the beam was as close to a theoretical TEM00 mode as possible, the beam was coupled into a single mode optical fibre before being used in the optical setup.

The next step was to determine how to generate a suitable deflection of the beam to be measured which functions in a manner equivalent to a microcantilever in an AFM. The result is a displacement in the far field of the source of deflection, which is maximised by using a single lens placed one focal length away from both the source and the detector, thereby imaging the far field of the source of oscillation. This is illustrated in figure 14.1.

14.1.1 An Oscillating Mirror

The first source I tested was an oscillating mirror to introduce a horizontal transverse oscillation to the beam. The mirror oscillation was achieved by adding a solid stack piezo chip [97] to the mirror mount, as shown in figure 14.2c. Applying a voltage to the piezo caused it to expand, which in turn caused the mirror to tilt about the vertical axis. This resulted in a

slight deflection of a beam reflected off the mirror. By applying an oscillating voltage, offset such that the applied voltage was always above zero to avoid damaging the piezo, the mirror would oscillate about the vertical axis and the beam's transverse position is oscillated as a result. It was essential that the piezo was applied to the correct 'corner' of the mirror so as to keep the number of degrees of freedom in the movement the same. As can be seen in figure 14.2c one corner has a hole in which the screw sits, restricting its movement in the plane of the mirror completely. The second has a slot in which the screw sits which allows it to slide in one dimension. The third corner, on which the piezo is placed, was completely flat and movement of the screw is not restricted.

This method is relatively easy to set up, and has very low optical losses assuming the mirror has a high reflectivity. The amplitude of the oscillation was very unstable as the mirror was forced to oscillate off-resonance, meaning a second reference detector was necessary to independently monitor the oscillation amplitude. Unfortunately, forcing the mirror to oscillate at a frequency much higher than the resosnant frequency of the mount also caused high order deformation modes to be induced which had a significant vertical component. The reference detector was relatively insensitive to this vertical motion, but the PSD and SD both were due to being narrow in the vertical direction. A more robust mirror mount which had the piezo mounted in the centre would likely have helped minimise the vertical component and make this method of oscillating the beam useful, however we did not have access to this.

14.1.2 An Acousto-Optical Modulator (AOM)

The second source of deflection I considered was an AOM with a frequency modulated RF signal. While this introduces some additional restrictions on the beam size, and any loss through the AOM also reduces the level of squeezing if squeezed light should be used later, it is far more stable than the mirror. Additionally, the modulation frequency and amplitude

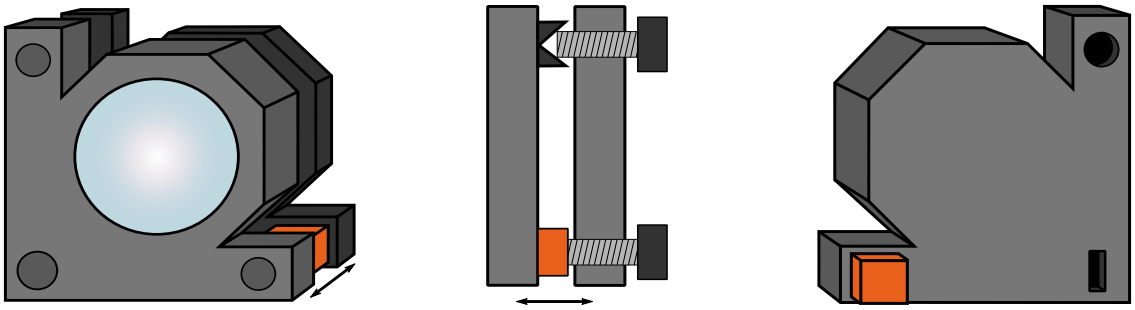

(a) Front View **(b)** Side View **(c)** Back View

Figure 14.2 A schematic view of the front, side and back of the mirror mount with the piezo (shown in orange) attached. When a voltage is applied to the piezo it expands in the direction indicated by the arrows.

can be controlled much more precisely and consistently than with the mirror, meaning there should be no need for a reference detector and no significant vertical component to the beam's motion. For these reasons, the AOM was used.

In order to make an accurate comparison of the SNR of the two detectors we must ensure the same optical power, signal frequency and signal amplitude are used when determining the SNR of each detector. One possibility would be to split the beam equally between the two detectors, thereby guaranteeing the signal is the same for both, however this method would require two (preferably identical) spectrum analysers for the measurement to be made simultaneously. Additionally, if the same test were to be performed with squeezed light later on to measure the improvement seen by the two detectors, splitting the beam would reduce the level of squeezing. Therefore a drop mirror was used to re-direct the beam from one detector to the other between measurements. However, while the source of the oscillating beam is the same, the way the source is imaged onto the surface of the detector can also impact the signal. An imaging system was implemented such that the FF of the AOM was imaged onto the surface of each detector.

Noise on the Signal

As always with shot noise limited measurements, it is vital to ensure technical noise sources are kept to a minimum. For the position detection measurement, we benefit inherently from a huge reduction in any common mode noise sources as we are subtracting one half of the beam from the other. Any fluctuations in the power of the beam as a whole (or any even TEM mode) will be cancelled, provided the beam is centred perfectly on the detector. It is important to study how good the common mode noise rejection is, and to consider any noise sources which are not common mode and will therefore not be removed by the subtraction.

Common Mode Noise Rejection The common mode rejection ratio (CMRR) of the SD was measured using an intensity modulated beam, generated by applying an amplitude modulated RF signal to the AOM, which was split equally in two and focused on either side of the SD. The SD was chosen as its behaviour is more predictable than that of the PSD and it has essentially no dependence on the size of the beam used provided the waist is smaller than the photodiode. With both beams on the detector, the modulation amplitude was increased until a small signal could be seen at the modulation frequency, then one of the beams was blocked to determine the signal power. This allowed the CMRR to be determined as the difference between the signal with one beam blocked and that with both unblocked. The CMRR was found to be so good that it was difficult to measure, as the power in the signal with one beam blocked saturated the spectrum analyser, however it was found to be at least 65 dB at 100 kHz,and at least 35 dB at 900 kHz. Crucially for both cases, the amplitude noise present with both beams incident of the detector was below the electronic noise floor of the detector even for noise amplitudes far greater than those we expect to see. We may therefore assume any common mode amplitude noise will not limit our measurement.

For the small oscillations we are considering, any reduction in the common mode noise rejection introduced by the displacement of the beam is a second order effect. Additionally, operating at high frequencies already helps render many technical noise sources irrelevant.

However, care should still be taken to minimise any amplitude fluctuations which may be introduced to the beam by using the AOM. For example, fluctuations in the power of the frequency modulated RF signal will in turn cause power fluctuations in the first order beam which is being used in the measurement. Even though most whole-beam intensity fluctuations will be cancelled by the subtraction performed in the position detection it is still sensible to keep this noise to a minimum with careful design of the RF chain used to supply the AOM.

Additional Noise Sources: Modulation Frequency and AOM Bandwidth In an ideal system, the AOM would cause the whole first order beam to be deflected at once and without any distortion, leading to a smooth transverse displacement in the Fourier plane. However, in reality this is not quite the case. For a simple case with no modulation, an AOM uses acousto-optics to diffract a portion of the input optical beam into the first order beam using an input acoustic (RF) signal. This also shifts the frequency of the light by the RF signal frequency, however for this application the frequency shift is irrelevant as the photodiode response is independent of such small frequency changes. The angle by which the beam is deflected is dependent on the frequency of the RF signal, therefore by modulating this frequency it is possible to vary the angle of deflection of the beam and cause it to oscillate transversely when observed in the far field.

Frequency modulation is achieved by altering the frequency of a signal in time. In general, a frequency modulated signal is described by

$$y(t) = A_c \cos\left(2\pi f_c t + \frac{\Delta f}{f_m}\sin(2\pi f_m t)\right), \tag{14.1}$$

where f_c is the carrier frequency, A_c is the amplitude of the carrier, Δf is the peak frequency deviation and f_m is the highest frequency component present in the modulating signal. For this application the value of the carrier frequency, $f_c = 80\,\text{MHz}$, is dictated by the specifications of the AOM. The frequency of the oscillation of the beam is controlled by

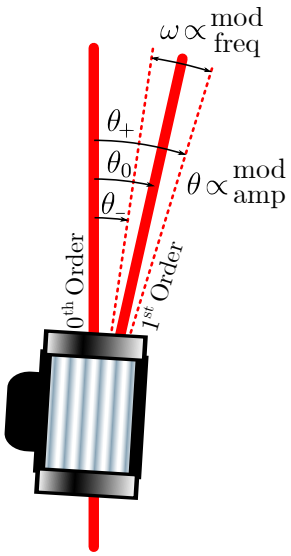

Figure 14.3 A diagram illustrating the dependence of the position of the 1st order beam out of the AOM on the modulation applied to the RF signal. The larger the amplitude of the modulation, the greater the maximum displacement. The frequency at which the beam position oscillates is equal to the modulation frequency.

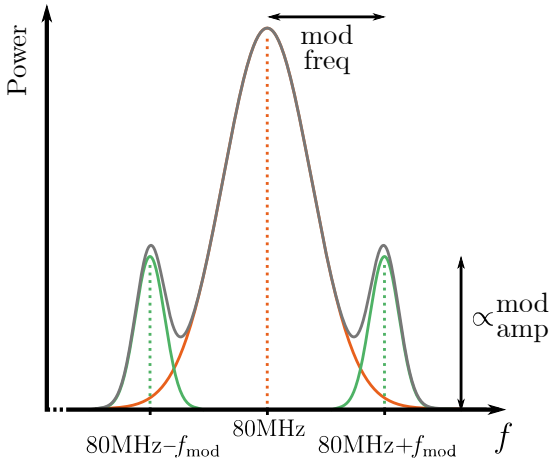

Figure 14.4 An example frequency space representation of the RF signal supplied to the AOM to generate the lateral displacement. The two sidebands on the carrier frequency are introduced via frequency modulation, so are out of phase with one another. Their position is dependent on the carrier frequency and modulation frequency, while their amplitude is proportional to the amodulation amplitude. The width of the carrier frequency peak was on the order of 1 MHz.

the modulation frequency, f_m, and must be chosen to lie within the range of operation of the detector, so $(0.1-1)$ MHz. The amplitude of the oscillation is governed by Δf. Figure 14.3 illustrates how the first order beam responds to the frequency modulated signal. The lowest frequency component of the RF, $(f_c - \Delta f)$, defines the minimum deflection angle, θ_{min}, and the highest frequency component, $(f_c + \Delta f)$, defines the maximum deflection angle, θ_{min}. The carrier frequency, f_c governs the average deflection angle, θ_0. The frequency at which the beam oscillated between minimum and maximum deflection is controlled by the modulation frequency, f_m, of the RF signal. The result is a beam which oscillates about a centre position with amplitude governed by Δf at a frequency given by f_m.

When the frequency modulated signal is applied to the AOM, a diffraction grating is

generated in the AOM crystal which depends on the instantaneous frequency of the RF signal in the crystal at that time. For relatively slow modulation frequencies, where the instantaneous frequency varies slowly, the diffraction grating can be considered to be constant across the transverse profile of the beam in the crystal as the transition time of the RF wave is small in comparison to the period over which the frequency is changing. However, as the modulation frequency increases, the period of modulation becomes comparable to the transit time of the RF wave across the beam in the crystal, meaning different parts of the transverse profile of the beam are deflected by different amounts. This is illustrated in figure 14.5. As a result, the translation of the beam in the far field becomes more complex than a simple translation of a TEM00 mode. The distortions introduced by this effect are not likely to not be symmetric. While we can expect excellent common mode rejection of any fluctuations in the overall intensity of the beam, any fluctuations in odd spatial modes will not see the same benefit. In fact, fluctuations in the TEM01 mode, for example, will add constructively - entirely by design, as this is how the displacement is detected. Therefore, it is important to avoid modulating too fast so as to not introduce high-order distortions into the displaced beam.

To set an upper limit for the modulation frequency, the AOM switch on/off time was measured for the beam sized used in the SNR measurements, shown in figure 14.6. It can be seen that the time for the RF wave to traverse the beam is approximately 300 ns. Note that the RF signal is sampled poorly as the bandwidth of the oscilloscope is very close to the frequency of the RF signal, however this does not matter as we are only interested in seeing when the signal is switched off. The delay between the RF being turned off and the beam power starting to decrease is indicative of the time taken for the RF signal to travel through the electronics and through the portion of the crystal without the beam passing through, and will not impact our measurement as the frequency modulated signal will be applied continuously. From this measurement we see that modulation frequencies on the order of a few MHz will see maximum difference in the RF amplitude from one side of the beam to the

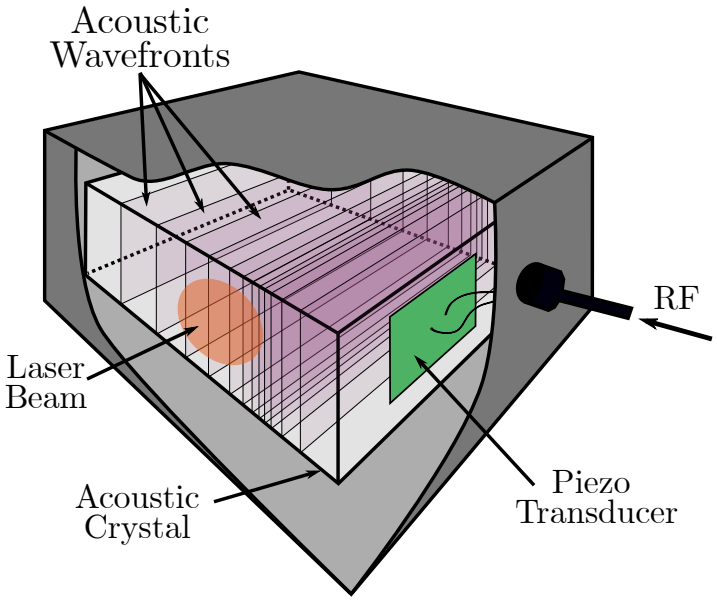

Figure 14.5 A spatially varying diffraction grating is formed in the AOM by the frequency modulated RF signal. A faster modulation or larger beam will cause a greater variation in the spacing between adjacent high pressure areas across the width of the beam.

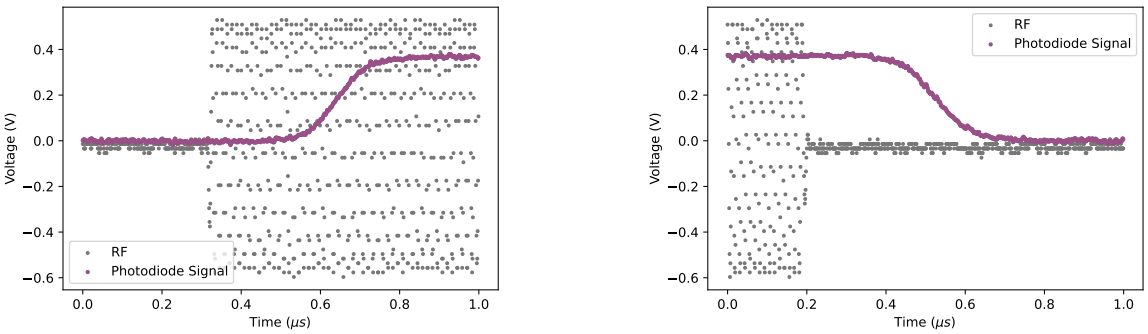

(a) Switching on time.

(b) Switching off time.

Figure 14.6 The switching time of the AOM was measured by monitoring the power of the first order beam as the RF signal was switched off. Note that this value is dependent on the size of the beam and therefore the data was taken using the same beam size which was later used for SNR measurements.

other so it is preferable to make measurements with modulation frequencies that are much lower: nominally we will use frequencies in the 100 kHz range.

14.2 Making an SNR Measurement

Having taken into account and minimised any noise sources, an SNR measurement can be taken for the two detectors. This was done one detector at a time, using a drop mirror to alter the beam path and direct all light to one detector or the other. The total optical power incident on the detector throughout each measurement set was monitored using the instrumentation amplifier output. Using the voltage calibration, it was possible to check the same optical power was incident on both detectors despite them being slightly different sizes and the measurements being made at different times.

Due to the internal resistance of the position detector being smaller for a larger beam size, it was desirable for the beam waist of the surface of the photodetector to be as large as possible. Since the beam on the photodetector is a FF image of the beam in the AOM its size is somewhat dictated by the size of the beam in the AOM, which needs to be relatively large to get a good diffraction efficiency. Therefore, an imaging system was introduced after the AOM to increase the size of the FF image. The SNR measurements were then made for each photodetector by taking a 'wide' (40 kHz) span measurement centred on the signal frequency. The average value of the background with the signal region removed was used as a noise value, and a Gaussian was fitted and the peak amplitude (minus noise) provided the signal measurement. Care was taken to keep all parameters of the spectrum analyser consistent between measurements, in particular the RBW and VBW. A background subtraction of data taken with the beam blocked was performed for each set of results to remove the electronic noise of the detectors.

14.2.1 A Typical SNR Measurement

As explained previously, the SNR measurement for each detector was calculated for the signal produced by an oscillating beam incident on the detector. As the beam oscillation was relatively fast, on the order of at least a few kHz, the voltage signals output by the two detectors were observed using a spectrum analyser to analyse a range of frequencies around the signal frequency. An example is given in figure 14.7. The large peak in the centre of the two signal plots is due to the oscillation of the beam. The noise in the signal around this peak are due to shot noise fluctuations in the light. It can be seen that the electronic noise floor of the two detectors is relatively similar, with the PSD being slightly higher. This is to be expected due to the extra internal resistance present in the PSD compared to the SD. Additionally, the optical noise seen on the PSD is far lower than on the SD. This is due to some cancellation in shot noise which is gained from the splitting of the current in the PSD being resistive. While the signal produced by the PSD is also lower than that of the SD, the shot noise measured is lower by a greater amount. This ultimately means that the SNR of the PSD is better than that of the SD, however it is difficult to see this for certain from figure 14.7.

To obtain a qualitative measurement of the SNR, the amplitude of each peak shown in figure 14.7 was taken to be the signal. The noise was obtained by taking an average of the shot noise, excluding a wide area surrounding the peak to ensure this did not artificially increase the noise. The ratio of these two values were then taken to provide an SNR for each detector.

14.2.2 Determining the SNR of the SD and PSD

The SNR of each detector was measured for a range of modulation frequencies. The results are shown in figure 14.8. The SNR increases approximately quadratically as the oscillation amplitude of the signal is increased. This is to be expected, as we are measuring the power

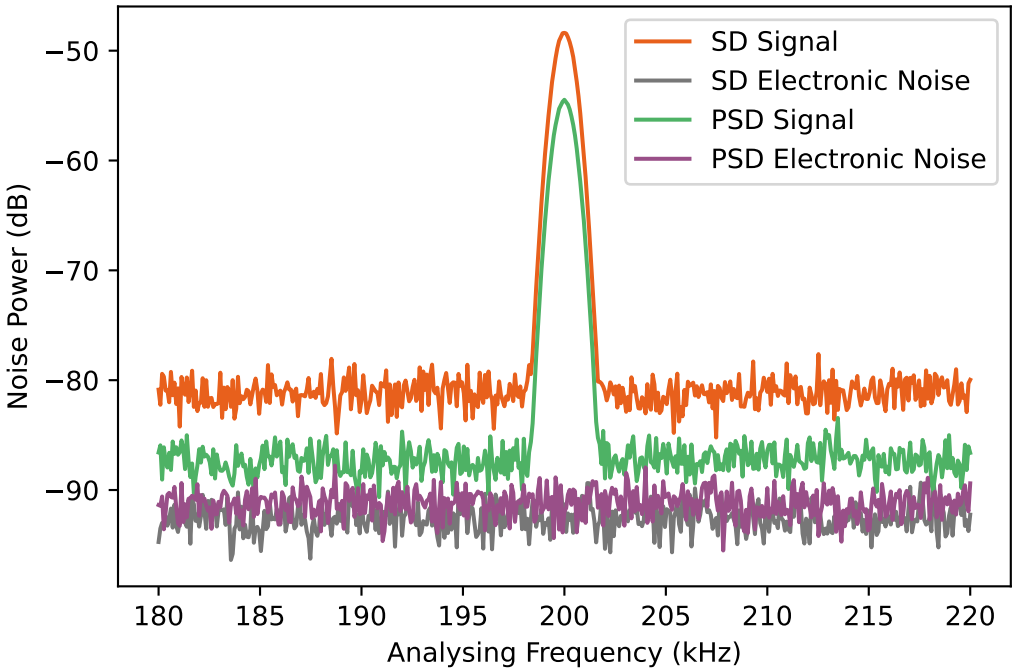

Figure 14.7 A typical example of a noise power spectrum captured for the PSD and SD. For the 'signal' measurement, an oscillating beam generated as described previously was incident on the detector. For the electronic noise measurement no light was incident on the detector. The amplitude of the incident signal and optical power used was the same for both detectors.

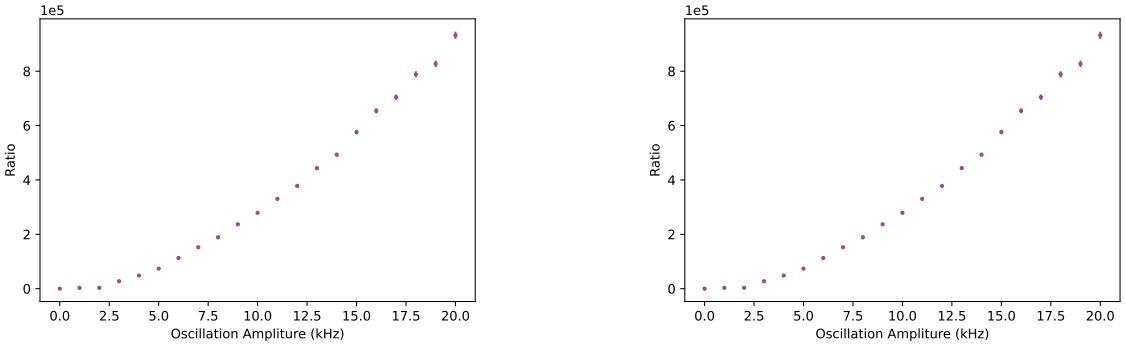

(a) Split Detector. **(b)** Position Sensing Detector.

Figure 14.8 The Signal to Noise Ratios (SNR) of the SD and the PSD, measured for a range of oscillation amplitudes.

of the signal, and the intensity of the signal changes linearly with oscillation amplitude.

The ratio of the PSD SNR to the SD SNR was found to decrease with increasing modulation frequency, as shown in figure 14.9. This is due to the switch time of the AOM described previously. At higher frequencies, the diffraction grating formed in the AOM by the RF signal significantly varies across the transverse profile of the beam. This results in additional noise being coupled into the beam at the signal frequency which is not symmetric and therefore not cancelled by the subtraction of one side of the photodetector from the other. Based on these results it can be assumed that the SD is more sensitive to such fluctuations, which contribute to the signal more than to the noise thereby increasing the SNR of the SD and decreasing the SNR ratio between the PSD and SD. This makes sense given the detection mode of the PSD is proportional to the TEM01 mode exactly, whereas that of the SD is comprised of higher order modes so will be more sensitive to higher order fluctuations.

It should be noted that the modulation amplitude was constant throughout these measurements, meaning the modulation index decreases at higher frequencies. This corresponds to less power in the sidebands at higher modulation frequencies. However, since the same set of conditions was used for both detectors one would not expect any such effects to have an impact on the SNR ratio between the two detectors.

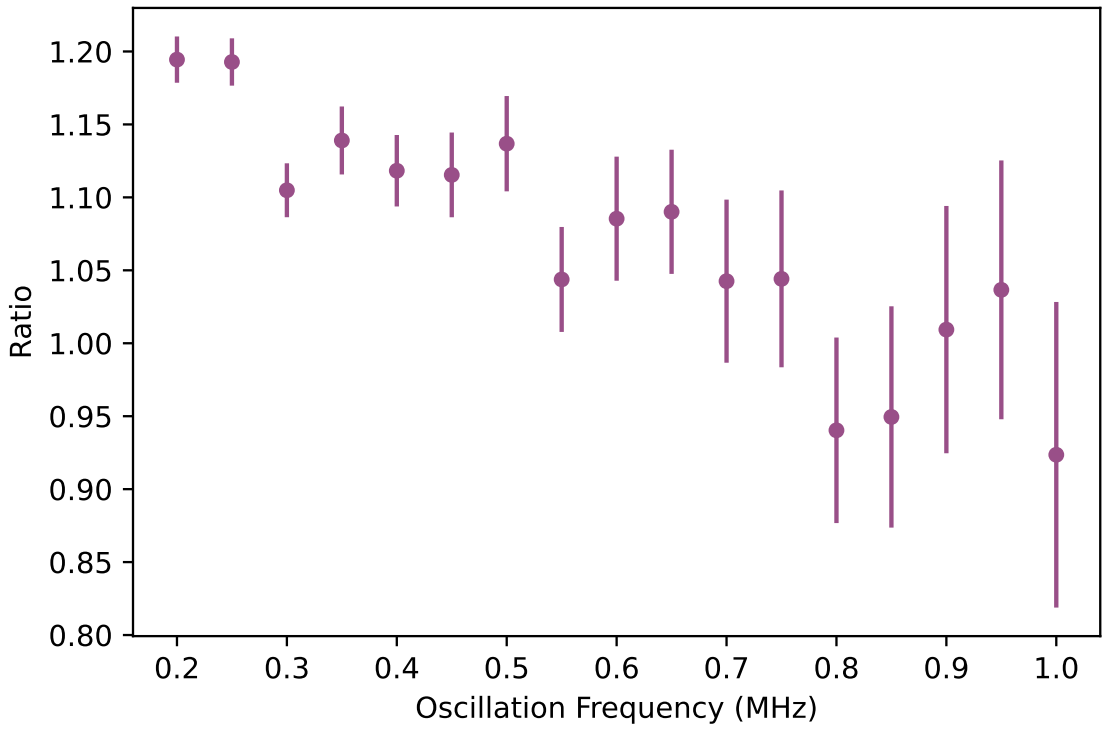

Figure 14.9 The SNR of the PSD relative to that of the SD for a range of modulation frequencies.

Figure 14.10 shows the SNR ratio of the detectors for varied modulation amplitude at a fixed modulation frequency. The results are shown for 200 kHz, 500 kHz and 1 MHz modulation frequencies.

It can be seen from figure 14.10 that at lower modulation frequencies, where noise due to the switching time of the AOM should be at a minimum, the SNR ratio is close to that predicted by the theory. However, even at low modulation frequencies, higher modulation amplitudes seem to cause the SNR ratio to degrade, as increasing the modulation amplitude has the same effect as increasing the modulation frequency in terms of increasing the variation in the diffraction grating across the profile of the beam in the AOM crystal. The 'step' in SNR ratio values which seems to happen at around 10 kHz modulation amplitude may be indicative of an additional electronic noise source at these frequencies, likely from the RF function generator.

To confirm whether the SD was indeed more sensitive to additional amplitude fluctuations introduced at higher modulation frequencies, the SNR ratio was recorded for an amplitude modulated signal. To first order, an amplitude modulation introduced by modulating the power of the RF signal should not be detected by either the SD or PSD, as any amplitude fluctuations in the overall beam should be cancelled perfectly by the subtraction provided the beam is centred on the detector. However, due to the finite time taken for the RF signal to propagate across the transverse profile of the beam, we expect to see similar distortions to the first order beam as those described for the case of frequency modulation.

Figure 14.11 shows such a data set, where the amplitude modulation was applied with a fixed amplitude of 5 kHz. The SNR is seen to decrease for higher modulation frequencies, which indicated the PSD becomes less sensitive to amplitude noise at higher frequencies compared with the SD. Note that as the modulation amplitude was kept fixed throughout these measurements, the modulation index will vary for different modulation frequencies. As before, this should not impact the results as both detectors will still see the same signal.

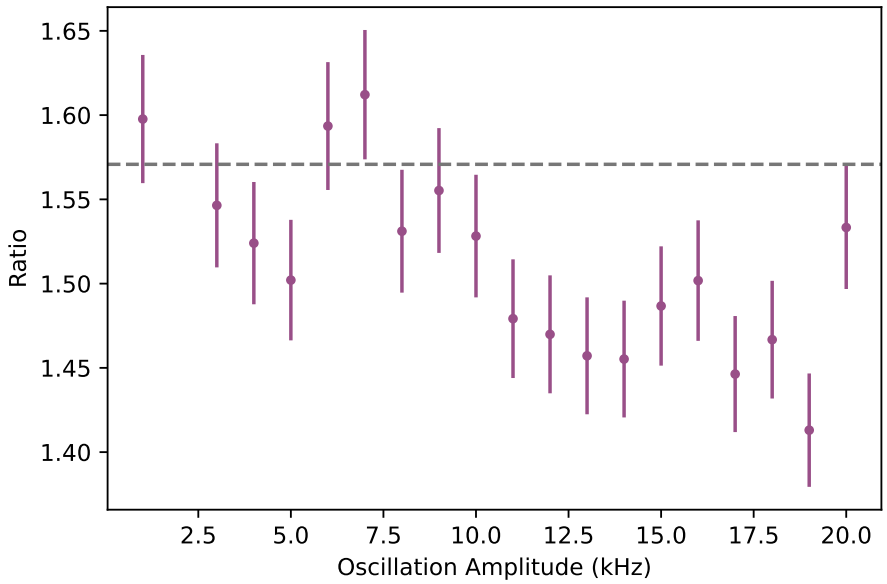

(a) 200 kHz modulation frequency.

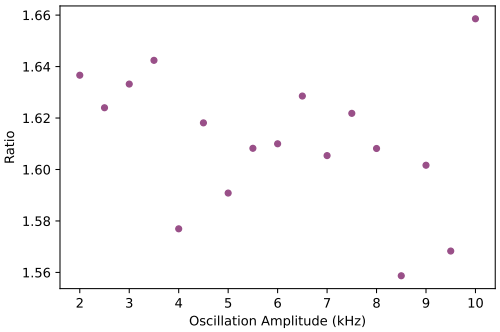

(b) 500 kHz modulation frequency.

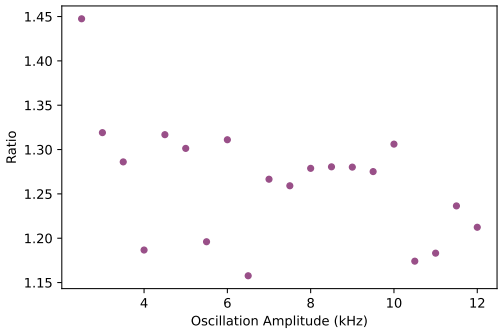

(c) 1MHz modulation frequency.

Figure 14.10 Plots of the SNR ratio with respect to oscillation amplitude between the PSD and SD at various modulation frequencies. At 200 kHz modulation frequency this is compared to the theoretical SNR ratio of $\pi/2$, indicated by the grey dashed line. At higher modulation frequencies the results are less reliable due to the noise introduced by the finite time taken for the RF wave to transit the beam in the crystal of the AOM.

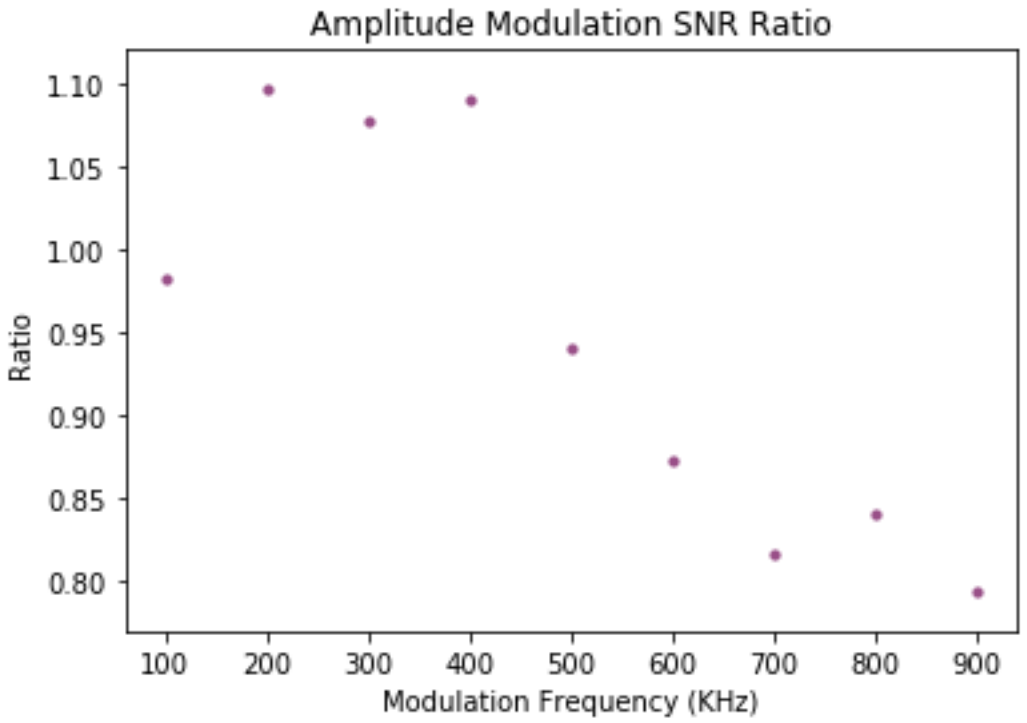

Figure 14.11 The SNR ratio between the PSD and SD for an amplitude modulated RF signal at a range of modulation frequencies.

14.3 SD Dead Region

It was previously discussed in section 12.5 that the SNR of the SD is slightly increased by the presence of the dead region. While it is not possible to alter the size of the dead region on the SD, using the split mirrors and the BPD in a configuration such as that in figure 14.12 results in a detector with a variable dead region. It should be noted that when varying the size of the dead region the block, indicated by '$*$' in figure 14.12, it was also necessary to adjust the position of the beam on the splitting mirror using the mirror immediately after the AOM such that the power on the two eyes of the detector remained balanced. This also ensured the effective dead region size was altered in a way which was symmetric. The block used was a slit with the beam positioned off-centre such that only one side of the beam was blocked was blocked. This was positioned just after the splitting mirror, which was in the far-field imaging plane of the AOM.

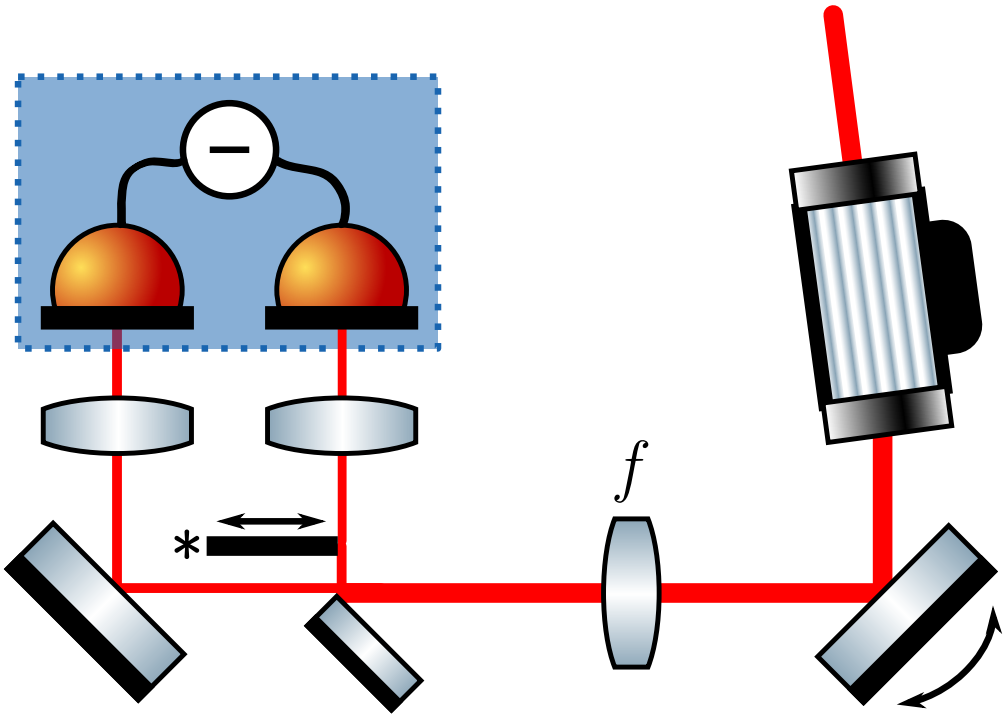

Figure 14.12 The optical setup used to determine the impact of the size of the dead region of a split detector on its SNR when measuring the position of an oscillating beam. To create a variable dead region the beam is optically split and a block, indicated by '$*$', is used on one side. The movable mirror is then altered to re-centre the beam on the dead region.

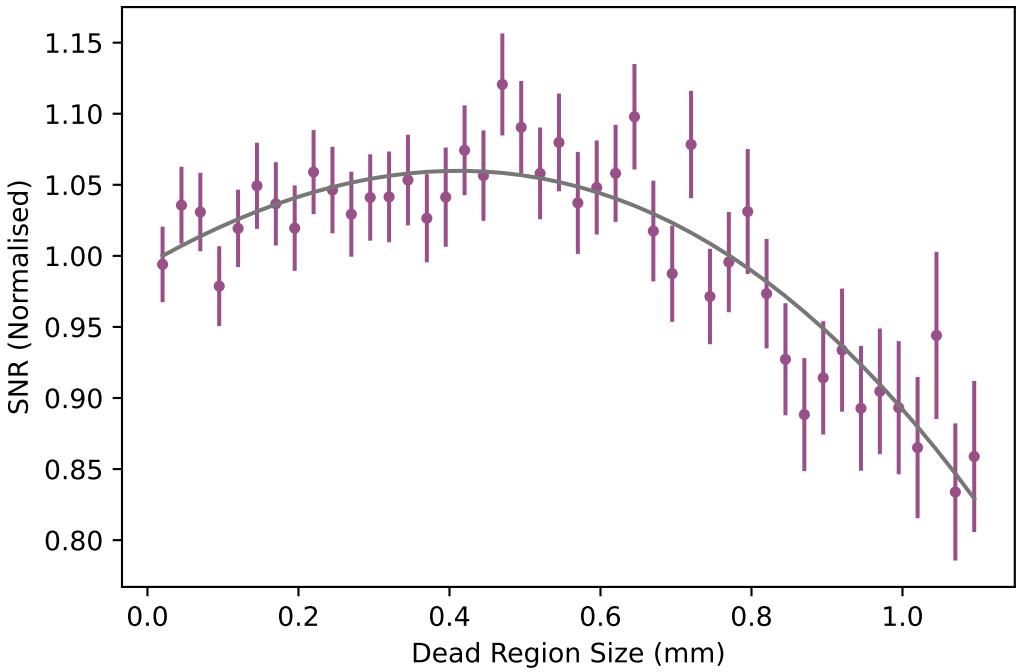

Figure 14.13 The SNR of the BPD with varied effective dead region size, taken with a modulation frequency of 200 kHz and a modulation amplitude of 10 kHz.

The SNR of the BPD was measured for varying dead region size, the data for which is shown in figure 14.13 fitted with equation 12.68. The SNR given is normalised to that with no dead region, and is the ratio of signal to noise power. We see an improvement of $5-10\%$ for a dead region size of around 0.5 mm. For the split detector chip used the dead region has a size of around 30 µm, which is sufficiently small that it should barely impact the measured SNR.

Chapter Fifteen

Conclusion

In this part we have theoretically determined the optimum detection mode for measuring a small displacement of a beam to be one proportional to the derivative of the transverse beam profile. For a Gaussian (TEM00) beam, this is proportional to the TEM01 mode. Such a measurement has been shown to saturate the QCRB. Compared to the usual way of detecting such a displacement, using a split photodetector, this was calculated to provide an improvement in the SNR of the power of the signal of $\pi/2$. A detector with this optimum detection mode was designed and constructed, and the improvement in the SNR over using a conventional SD was shown to be $\pi/2$, as was calculated theoretically. The theoretical derivation and results presented in this part are currently being prepared for submission.

The greatest challenges in making this measurement were in ensuring the noise of the constructed detectors were shot noise limited, meaning the SNR measurement was a result only of the detection profile and noise on the light rather than of the electronic noise, and in creating a signal which was stable and fast enough with which to characterise the performance of the circuit. For the latter, it was found that, intuitively, the most important characteristic in the performance of the PSD is arguably the maximum bias voltage that can be applied to the photodetector chip used; the internal resistance fundamentally limits the maximum optical power which cab be used before the detector de-biases, but thanks to the thermal noise contribution changing this resistance has little or no impact on the electronic noise

of the detector relative to the shot noise on the light at de-biasing power. The only way to improve the performance is to increase the bias, thereby increasing the optical power at which de-biasing occurs, and therefore increasing the shot noise, without affecting the electronic noise.

The PSD provides an improved SNR for position detection measurements over the conventional SD. It is no more difficult to align than the SD, and could feasibly replace SDs in existing AFM systems to give an improved performance with no other parameters needing to change aside from potentially needing additional optics to manipulate the beam on the detector. Furthermore, the PSD should perform better than the SD if used with squeezed light. When using squeezed light with either detector, the detection mode itself should be squeezed to see maximum improvement. Technically, this means that for the SD the flipped Gaussian mode, shown in figure 12.2a, should be squeezed and for the PSD the TEM01 mode, shown in figure 12.2b, should be squeezed. It is possible to squeeze only the relevant mode for each detector, and thus MSM squeezing is not strictly necessary. However practically when using 4WM, all spatial modes up to a certain order are squeezed. The detection mode of the PSD is proportional to the TEM01 mode, which is low order and therefore we expect to see intensity correlations in this mode. Contrasting this, the straight edge of the detection mode of the split detector introduces high spatial frequencies, or equivalently higher order modes, into the signal. It is far harder to observe intensity correlations in these higher order modes, as diffraction prevents them from being coupled by 4WM in a thick medium, as discussed in section 5.6. Therefore in the case of the SD the signal is polluted with noise from these non-squeezed higher order modes. Ultimately, this means the PSD should perform better than the SD not only because of its detection mode is optimised for detecting a small displacement of a Gaussian beam, but also because the detection mode is better suited for use with squeezed light.

Finally, we have seen that the dead region of an SD can have a beneficial impact on the SNR of the detector. Controlling the size of the dead region can be achieved by changing

the size of the beam on the detector. Through this, small improvements in the SNR of a position measurement could be seen in existing systems without needing to make any other alterations to the detector. Also, a mask could be used to modify the size of the dead region on the chip itself which would be cheap and easy to implement.

References

[1] T. H. MAIMAN. "Stimulated Optical Radiation in Ruby". In: *Nature* 187.4736 (Aug. 1960), pp. 493–494. DOI: 10.1038/187493a0.

[2] L. Fallani and A. Kastberg. "Cold atoms: A field enabled by light". In: *EPL (Europhysics Letters)* 110.5 (June 2015), p. 53001. ISSN: 1286-4854. DOI: 10.1209/0295-5075/110/53001.

[3] John Kitching, Svenja Knappe, and E.A. Donley. "Atomic Sensors – A Review". In: *Sensors Journal, IEEE* 11 (Oct. 2011), pp. 1749–1758. DOI: 10.1109/JSEN.2011.2157679.

[4] Jorge L. Cervantes-Cota, Salvador Galindo-Uribarri, and George F. Smoot. "A Brief History of Gravitational Waves". In: *Universe* 2.3 (2016). ISSN: 2218-1997. DOI: 10.3390/universe2030022.

[5] Prachi Sharma and Mandeep Singh. "A Review of the Development in the Field of Fiber Optic Communication Systems". In: (Aug. 2018).

[6] Nathaniel Fried and Pierce Irby. "Advances in laser technology and fibre-optic delivery systems in lithotripsy". In: *Nature Reviews Urology* 15 (June 2018). DOI: 10.1038/s41585-018-0035-8.

[7] Edward Manche and Joshua Roe. "Recent advances in wavefront-guided LASIK". In: *Current Opinion in Ophthalmology* 29 (Apr. 2018), p. 1. DOI: 10.1097/ICU.0000000000000488.

[8] Ludovic Thobois, Jean Cariou, and Ismail Gultepe. "Review of Lidar-Based Applications for Aviation Weather". In: *Pure and Applied Geophysics* 176 (May 2019). DOI: 10.1007/s00024-018-2058-8.

[9] M. Fox. "Quantum Optics: An Introduction". In: Oxford Master Series in Physics. OUP Oxford, 2006, pp. 78–81.

[10] R. E. Slusher et al. "Observation of Squeezed States Generated by Four-Wave Mixing in an Optical Cavity". In: *Phys. Rev. Lett.* 55 (22 Nov. 1985), pp. 2409–2412. DOI: 10.1103/PhysRevLett.55.2409.

[11] Min Xiao, Ling-An Wu, and H. J. Kimble. "Precision measurement beyond the shot-noise limit". In: *Phys. Rev. Lett.* 59 (3 July 1987), pp. 278–281. DOI: 10.1103/PhysRevLett.59.278.

[12] "A gravitational wave observatory operating beyond the quantum shot-noise limit". In: *Nature Physics* 7.12 (Sept. 2011), pp. 962–965. ISSN: 1745-2481. DOI: 10.1038/nphys2083.

[13] L. McCuller et al. "Frequency-Dependent Squeezing for Advanced LIGO". In: *Phys. Rev. Lett.* 124 (17 Apr. 2020), p. 171102. DOI: 10.1103/PhysRevLett.124.171102.

[14] V. Delaubert et al. "Quantum limits in image processing". In: *EPL (Europhysics Letters)* 81.4 (Jan. 2008), p. 44001. DOI: 10.1209/0295-5075/81/44001.

[15] Fan Yang et al. "Fisher information for far-field linear optical superresolution via homodyne or heterodyne detection in a higher-order local oscillator mode". In: *Phys. Rev. A* 96 (6 Dec. 2017), p. 063829. DOI: 10.1103/PhysRevA.96.063829.

[16] C Gerry and P Knight. *Introductory Quantum Optics*. Cambridge University Press, 2004.

[17] M. Fox. *Quantum Optics: An Introduction*. Oxford Master Series in Physics. OUP Oxford, 2006.

[18] M.O. Scully and M.S. Zubairy. *Quantum Optics*. Cambridge University Press, 1997. ISBN: 9780521435956.

[19] Stephen M Barnett and John A Vaccaro. *The quantum phase operator: a review*. Taylor & Francis, 2007.

[20] Eric W. Weisstein. *Paraxial Approximation*. https://scienceworld.wolfram.com/physics/ParaxialApproximation.html. (Visited on 12/20/2021).

[21] Amnon. Yariv. *Quantum Electronics*. 2nd ed. John Wiley & Sons, 1975, pp. 22–28.

[22] Anthony E. Siegman. *Lasers*. University Science Books, 1986.

[23] William H. Carter. "Spot size and divergence for Hermite Gaussian beams of any order". In: *Appl. Opt.* 19.7 (Apr. 1980), pp. 1027–1029.

[24] Michael A. Taylor et al. "Biological measurement beyond the quantum limit". In: *Nature Photonics* 7.3 (Mar. 2013), pp. 229–233. ISSN: 1749-4893. DOI: https://doi.org/10.1038/nphoton.2012.346.

[25] Jun Miyazaki and Yasunobu Toumon. "Experimental evaluation of temperature increase and associated detection sensitivity in shot noise-limited photothermal microscopy". In: *Optics Communications* 430 (2019), pp. 170–175. ISSN: 0030-4018. DOI: https://doi.org/10.1016/j.optcom.2018.08.007.

[26] Mikhail I. Kolobov, ed. *Quantum Imaging*. Springer, 2007.

[27] Mikhail I. Kolobov. "The spatial behavior of nonclassical light". In: *Rev. Mod. Phys.* 71 (5 Oct. 1999), pp. 1539–1589. DOI: 10.1103/RevModPhys.71.1539.

[28] Guilherme Xavier and Gabrela Lima. "Quantum information processing with space-division multiplexing optical fibres". In: *Communications Physics* 3 (Dec. 2020), p. 9. DOI: 10.1038/s42005-019-0269-7.

[29] Benjamin J. Puttnam, Georg Rademacher, and Ruben S. Luís. "Space-division multiplexing for optical fiber communications". In: *Optica* 8.9 (Sept. 2021), pp. 1186–1203. DOI: 10.1364/OPTICA.427631.

[30] Marco Genovese. "Real applications of quantum imaging". In: *Journal of Optics* 18.7 (June 2016), p. 073002. DOI: 10.1088/2040-8978/18/7/073002.

[31] Ling-An Wu et al. "Generation of Squeezed States by Parametric Down Conversion". In: *Phys. Rev. Lett.* 57 (20 Nov. 1986), pp. 2520–2523. DOI: 10.1103/PhysRevLett.57.2520.

[32] T. Sh. Iskhakov et al. "Heralded source of bright multi-mode mesoscopic sub-Poissonian light". In: *Optics Letters* 41.10 (May 2016), p. 2149. ISSN: 1539-4794. DOI: 10.1364/ol.41.002149.

[33] T.B. Pittman, B.C. Jacobs, and J.D. Franson. "Heralding single photons from pulsed parametric down-conversion". In: *Optics Communications* 246.4 (2005), pp. 545–550. ISSN: 0030-4018. DOI: https://doi.org/10.1016/j.optcom.2004.11.027.

[34] O. Jedrkiewicz et al. "Detection of Sub-Shot-Noise Spatial Correlation in High-Gain Parametric Down Conversion". In: *Phys. Rev. Lett.* 93 (24 Dec. 2004), p. 243601. DOI: 10.1103/PhysRevLett.93.243601.

[35] Jean-Luc Blanchet et al. "Measurement of Sub-Shot-Noise Correlations of Spatial Fluctuations in the Photon-Counting Regime". In: *Phys. Rev. Lett.* 101 (23 Dec. 2008), p. 233604. DOI: 10.1103/PhysRevLett.101.233604.

[36] Matthew Edgar et al. "Imaging high-dimensional spatial entanglement with a camera". In: *Nature communications* 3 (Aug. 2012), p. 984. DOI: 10.1038/ncomms1988.

[37] Matthew Reichert, Hugo Defienne, and Jason W. Fleischer. "Massively Parallel Coincidence Counting of High-Dimensional Entangled States". In: *Nature communications* 8 (May 2018). DOI: 10.1038/s41598-018-26144-7.

[38] L. A. Lugiato and A. Gatti. "Spatial structure of a squeezed vacuum". In: *Phys. Rev. Lett.* 70 (25 June 1993), pp. 3868–3871. DOI: 10.1103/PhysRevLett.70.3868.

[39] M. Marte et al. "Spatial patterns in optical parametric oscillators with spherical mirrors: classical and quantum effects". In: *Opt. Express* 3.2 (July 1998), pp. 71–80. DOI: 10.1364/OE.3.000071.

[40] M. Lassen et al. "Tools for Multimode Quantum Information: Modulation, Detection, and Spatial Quantum Correlations". In: *Phys. Rev. Lett.* 98 (8 Feb. 2007), p. 083602. DOI: 10.1103/PhysRevLett.98.083602.

[41] Benoît Chalopin et al. "Direct generation of a multi-transverse mode non-classical state of light". In: *Opt. Express* 19.5 (Feb. 2011), pp. 4405–4410. DOI: 10.1364/OE.19.004405.

[42] L. Lopez et al. "Multimode quantum properties of a self-imaging optical parametric oscillator: Squeezed vacuum and Einstein-Podolsky-Rosen-beams generation". In: *Phys. Rev. A* 80 (4 Oct. 2009), p. 043816. DOI: 10.1103/PhysRevA.80.043816.

[43] M. D. Levenson, R. M. Shelby, and S. H. Perlmutter. "Squeezing of classical noise by nondegenerate four-wave mixing in an optical fiber". In: *Opt. Lett.* 10.10 (Oct. 1985), pp. 514–516. DOI: 10.1364/OL.10.000514.

[44] Alberto M. Marino et al. "Entangled Images from 4-Wave Mixing in Rubidium Vapor". In: *Conference on Lasers and Electro-Optics/Quantum Electronics and Laser Science Conference and Photonic Applications Systems Technologies*. Optical Society of America, 2008, QFB3. URL: http://www.osapublishing.org/abstract.cfm?URI=QELS-2008-QFB3.

[45] Da Zhang et al. "Enhanced intensity-difference squeezing via energy-level modulations in hot atomic media". In: *Phys. Rev. A* 96 (4 Oct. 2017), p. 043847. DOI: 10.1103/PhysRevA.96.043847.

[46] C. F. McCormick et al. "Strong low-frequency quantum correlations from a four-wave-mixing amplifier". In: *Phys. Rev. A* 78 (4 Oct. 2008), p. 043816. DOI: 10.1103/PhysRevA.78.043816.

[47] M. Jasperse, L. D. Turner, and R. E. Scholten. "Relative intensity squeezing by four-wave mixing with loss: an analytic model and experimental diagnostic". In: *Opt. Express* 19.4 (Feb. 2011), pp. 3765–3774. DOI: 10.1364/OE.19.003765.

[48] Zhongzhong Qin et al. "Experimental Generation of Multiple Quantum Correlated Beams from Hot Rubidium Vapor". In: *Phys. Rev. Lett.* 113 (2 July 2014), p. 023602. DOI: 10.1103/PhysRevLett.113.023602.

[49] Paul-Antoine Moreau, Fabrice Devaux, and Eric Lantz. "Einstein-Podolsky-Rosen Paradox in Twin Images". In: *Phys. Rev. Lett.* 113 (16 Oct. 2014), p. 160401. DOI: 10.1103/PhysRevLett.113.160401.

[50] Vincent Boyer et al. "Entangled Images from Four-Wave Mixing". In: *Science* 321.5888 (2008), pp. 544–547. DOI: 10.1126/science.1158275.

[51] Mohammadjavad Dowran et al. "Quantum-enhanced plasmonic sensing". In: *Optica* 5.5 (May 2018), pp. 628–633. DOI: 10.1364/OPTICA.5.000628.

[52] Joshua Hordell et al. "Transport of spatial squeezing through an optical waveguide". In: *Opt. Express* 26.18 (Sept. 2018), pp. 22783–22792. DOI: 10.1364/OE.26.022783.

[53] M. T. Turnbull et al. "Role of the phase-matching condition in nondegenerate four-wave mixing in hot vapors for the generation of squeezed states of light". In: *Physical Review A* 88.3 (Sept. 2013). ISSN: 1094-1622. DOI: 10.1103/physreva.88.033845.

[54] Ashok Kumar, Hayden Nunley, and A. M. Marino. "Observation of spatial quantum correlations in the macroscopic regime". In: *Phys. Rev. A* 95 (5 May 2017), p. 053849. DOI: 10.1103/PhysRevA.95.053849.

[55] M. W. Holtfrerich and A. M. Marino. "Control of the size of the coherence area in entangled twin beams". In: *Phys. Rev. A* 93 (6 June 2016), p. 063821. DOI: 10.1103/PhysRevA.93.063821.

[56] Ashok Kumar and A. M. Marino. "Spatial squeezing in bright twin beams generated with four-wave mixing: Constraints on characterization with an electron-multiplying charge-coupled-device camera". In: *Phys. Rev. A* 100 (6 Dec. 2019), p. 063828. DOI: 10.1103/PhysRevA.100.063828.

[57] Quentin Glorieux et al. "Quantum correlations by four-wave mixing in an atomic vapor in a nonamplifying regime: Quantum beam splitter for photons". In: *Phys. Rev. A* 84 (5 Nov. 2011), p. 053826. DOI: 10.1103/PhysRevA.84.053826.

[58] Jeffrey H. Shapiro and Asif Shakeel. "Optimizing homodyne detection of quadrature-noise squeezing by local-oscillator selection". In: *J. Opt. Soc. Am. B* 14.2 (Feb. 1997), pp. 232–249. DOI: 10.1364/JOSAB.14.000232.

[59] Prasoon Gupta et al. "Effect of imperfect homodyne visibility on multi-spatial-mode two-mode squeezing measurements". In: *Opt. Express* 28.1 (Jan. 2020), pp. 652–664. DOI: 10.1364/OE.379033.

[60] Christopher S. Embrey et al. "Bichromatic homodyne detection of broadband quadrature squeezing". In: *Opt. Express* 24.24 (Nov. 2016), pp. 27298–27308. DOI: 10.1364/OE.24.027298.

[61] Matthew Turnbull. "Multi-Spatial-Mode Quadrature Squeezing from Four-Wave Mixing in a Hot Atomic Vapour". PhD thesis. School of Physics and Astronomy, University of Birmingham, 2013.

[62] Christopher Embrey. "Controlling Local Quantum Fluctuations of Light Using Four-Wave Mixing in an Atomic Vapour". PhD thesis. School of Physics and Astronomy, University of Birmingham, 2015.

[63] Joshua Rayne. "Multi-mode squeezing of light via four-wave mixing in a hot rubidium vapour". PhD thesis. School of Physics and Astronomy, University of Birmingham, 2019.

[64] Robert W. Boyd. *The Nonlinear Optical Susceptibility*. Third Edition. Burlington: Academic Press, 2008.

[65] R. C. Pooser et al. "Low-Noise Amplification of a Continuous-Variable Quantum State". In: *Phys. Rev. Lett.* 103 (1 June 2009), p. 010501. DOI: 10.1103/PhysRevLett.103.010501.

[66] R. C. Pooser et al. "Quantum correlated light beams from non-degenerate four-wave mixing in an atomic vapor: the D1 and D2 lines of 85Rb and 87Rb". In: *Opt. Express* 17.19 (Sept. 2009), pp. 16722–16730. DOI: 10.1364/OE.17.016722.

[67] Daniel A. Steck. *Rubidium 85 D Line Data*. http://steck.us/alkalidata. (Visited on 12/17/2021).

[68] *AOMO 3080-125*. https://gandh.com/wp-content/uploads/2013/12/3080_125_97_01598_01rC.pdf. Gooch & Housego. (Visited on 07/27/2021).

[69] Kenneth R. Spring and Michael W. Davidson. *Concepts in Digital Imaging Technology: Quantum Efficiency*. https://hamamatsu.magnet.fsu.edu/articles/quantumefficiency.html. (Visited on 12/17/2021).

[70] "The art of electronics". In: ed. by Paul Horowitz and Winfield Hill. Third. Cambridge: Cambridge Univ. Pr., 1991. Chap. Chapter 8.

[71] P.C.D. Hobbs. *Building Electro-Optical Systems: Making It all Work*. Wiley Series in Pure and Applied Optics. Wiley, 2011. ISBN: 9781118211090.

[72] Hamamatsu Photonics. *SI Photodiodes*. https://www.hamamatsu.com/resources/pdf/ssd/si_pd_kspd9001e.pdf. (Visited on 12/16/2021).

[73] "The art of electronics". In: ed. by Paul Horowitz and Winfield Hill. Third. Cambridge: Cambridge Univ. Pr., 1991. Chap. Chapter 8, p. 476.

[74] *SI PIN Photodiodes*. https://www.hamamatsu.com/resources/pdf/ssd/s3071_etc_kpin1044e.pdf. Hamamatsu Photonics. (Visited on 07/27/2021).

[75] Texas Instruments. *OPA657*. Accessed: 14-05-2021.

[76] V. Boyer, A. Marino, and P. Lett. "Generation of Spatially Broadband Twin Beams for Quantum Imaging". In: *Physical Review Letters* 100.14 (Apr. 2008). ISSN: 1079-7114. DOI: 10.1103/physrevlett.100.143601.

[77] B. Huttner and Y. Ben-Aryeh. "Influence of a beam splitter on photon statistics". In: *Phys. Rev. A* 38 (1 July 1988), pp. 204–211. DOI: 10.1103/PhysRevA.38.204.

[78] Matthew S. Taubman et al. "Intensity feedback effects on quantum-limited noise". In: *J. Opt. Soc. Am. B* 12.10 (Oct. 1995), pp. 1792–1800. DOI: 10.1364/JOSAB.12.001792.

[79] V. Boyer et al. "Ultraslow Propagation of Matched Pulses by Four-Wave Mixing in an Atomic Vapor". In: *Phys. Rev. Lett.* 99 (14 Oct. 2007), p. 143601. DOI: 10.1103/PhysRevLett.99.143601.

[80] Gianni Di Domenico and Antoine Weis. *Vapor Pressure and Density of Alkali Metals*. 2011. URL: https://demonstrations.wolfram.com/VaporPressureAndDensityOfAlkaliMetals/.

[81] Shinji Kamimura. "Direct measurement of nanometric displacement under an optical microscope". In: *Appl. Opt.* 26.16 (Aug. 1987), pp. 3425–3427. DOI: 10.1364/AO.26.003425.

[82] D. P. E. Smith. "Limits of force microscopy". In: *Review of Scientific Instruments* 66.5 (1995), pp. 3191–3195. DOI: 10.1063/1.1145550.

[83] Constant A. J. Putman et al. "A detailed analysis of the optical beam deflection technique for use in atomic force microscopy". In: *Journal of Applied Physics* 72.1 (1992), pp. 6–12. DOI: 10.1063/1.352149. eprint: https://doi.org/10.1063/1.352149.

[84] Takeshi Fukuma et al. "Development of low noise cantilever deflection sensor for multienvironment frequency-modulation atomic force microscopy". In: *Review of Scientific Instruments* 76.5 (2005), p. 053704. DOI: 10.1063/1.1896938. eprint: https://doi.org/10.1063/1.1896938.

[85] Nicolas Treps et al. "A Quantum Laser Pointer". In: *Science* 301.5635 (2003), pp. 940–943. DOI: 10.1126/science.1086489. eprint: https://www.science.org/doi/pdf/10.1126/science.1086489.

[86] Raphael C. Pooser and Benjamin Lawrie. "Ultrasensitive measurement of microcantilever displacement below the shot-noise limit". In: *Optica* 2.5 (May 2015), pp. 393–399. DOI: 10.1364/OPTICA.2.000393.

[87] S.M. Barnett, Claude Fabre, and Agnes Maitre. "Ultimate quantum limits for resolution of beam displacements". In: *The European Physical Journal D* 22 (Mar. 2003), pp. 513–519. DOI: 10.1140/epjd/e2003-00003-3.

[88] Samuel L. Braunstein and Carlton M. Caves. "Statistical distance and the geometry of quantum states". In: *Phys. Rev. Lett.* 72 (22 May 1994), pp. 3439–3443. DOI: 10.1103/PhysRevLett.72.3439.

[89] C.W. Helstrom. "Minimum mean-squared error of estimates in quantum statistics". In: *Physics Letters A* 25.2 (1967), pp. 101–102. ISSN: 0375-9601. DOI: https://doi.org/10.1016/0375-9601(67)90366-0.

[90] Carl W. Helstrom. *Quantum detection and estimation theory*. English. Academic Press New York, 1976, ix, 309 p. : ISBN: 0123400503.

[91] Hengxin Sun et al. "Small-displacement measurements using high-order Hermite-Gauss modes". In: *Applied Physics Letters* 104 (Mar. 2014), pp. 121908–121908. DOI: 10.1063/1.4869819.

[92] Olivier Pinel et al. "Ultimate sensitivity of precision measurements with intense Gaussian quantum light: A multimodal approach". In: *Physical Review A* 85.1 (Jan. 2012). ISSN: 1094-1622. DOI: 10.1103/physreva.85.010101.

[93] Hamamatsu Photonics. *PSD (Position Sensitive Detectors)*. https://www.hamamatsu.com/resources/pdf/ssd/psd_kpsd9001e.pdf. (Visited on 05/14/2021).

[94] Hamamatsu Photonics. *One-Dimensional PSD*. https://docs.rs-online.com/1334/0900766b81540439.pdf. (Visited on 11/22/2021).

[95] Hamamatsu Photonics. *SI PIN Photodiodes*. https://www.hamamatsu.com/resources/pdf/ssd/s3096-02_s4204_kpin1039e.pdf. (Visited on 11/22/2021).

[96] Toptica Photonics. *DL Pro*. URL: https://www.toptica.com/products/tunable-diode-lasers/ecdl-dfb-lasers/dl-pro/ (visited on 12/21/2021).

[97] Piezomechanik. *Piezomechanik Actuators*. https://www.piezomechanik.com/fileadmin/content_files/products/actuators/actuators-1-cofired-monolithic-ceramic-stacks-rings-chips.pdf. (Visited on 11/03/2021).